12-2021

High-Magnification Digital Image Correlation Techniques for Aged Nuclear Fuel Cladding Testing

Robert Scott Hansen
Utah State University

HIGH-MAGNIFICATION DIGITAL IMAGE CORRELATION TECHNIQUES FOR AGED NUCLEAR FUEL CLADDING TESTING

by

Robert Scott Hansen

A dissertation submitted in partial fulfillment
of the requirements for the degree

of

DOCTOR OF PHILOSOPHY

in

Mechanical Engineering

Approved:

_____	_____
Ryan Berke, Ph.D. Major Professor	Tadd Truscott, Ph.D. Committee Member
_____	_____
Ling Liu, Ph.D. Committee Member	Hailei Wang, Ph.D. Committee Member
_____	_____
Nicholas Roberts, Ph.D. Committee Member	D. Richard Cutler, Ph.D. Interim Vice Provost for Graduate Studies

UTAH STATE UNIVERSITY
Logan, Utah
2021

ABSTRACT

High Magnification Digital Image Correlation Techniques for
Aged Nuclear Fuel Cladding Testing

by

Robert Scott Hansen
Utah State University, 2021

Major Professor: Dr. Ryan B. Berke
Department: Mechanical and Aerospace Engineering

A comprehensive understanding of the anisotropic behavior of nuclear fuel cladding is vital for ensuring the safety of light water reactors in nuclear power plants. Safety design often relies on accurate computer modelling of this zirconium alloy cladding, which in turn requires experimental validation of those modelling tools. It is increasingly important to expand those modelling capabilities to include the microstructure. A particularly influential set of microstructural features is the brittle hydride precipitates which naturally form during reactor use. Thus, to allow these safety gains to be made, efforts must be made to better understand the effect these hydrides have on the mechanical behavior of zirconium alloy cladding. As a result, high-temperature full-field strain measurement techniques of directional tests with increased measurement resolution must be developed to enable these efforts.

This dissertation work explored the expansion of capability through several main objectives, which supported the final objective of hydride strain mapping. First, the ability to take high-temperature, high-magnification full-field strain measurements using a custom lens for digital image correlation (DIC) was demonstrated. Second, the pairing of super resolution imaging techniques with DIC for increased measurement resolution was explored. Third, the aperture

setting was optimized to balance the tradeoff between poor depth of field and deblurring from the diffraction limit of light. Fourth, several hoop-direction anisotropic testing methods were investigated to find the optimal ring hoop tension test arrangement. Finally, the developed techniques were used to produce full-field strain measurements of cladding with varying hydride orientations and concentrations in hoop tension tests, allowing validation of evolving cladding models.

(242 pages)

PUBLIC ABSTRACT

High Magnification Digital Image Correlation Techniques for Aged Nuclear Fuel Cladding Testing

Robert Scott Hansen

Nuclear fuel cladding in light water reactors, often made of zirconium alloys, is naturally made more brittle by exposure to the water coolant during normal reactor operation. However, this embrittlement by zirconium hydrides changes the mechanical behavior of the cladding material, affecting how it will deform and what may cause it to fail. Because the cladding already has different properties in different material directions, mechanical testing also needs to be direction specific. In addition, to understand the effects that these microscale hydride features have, measurements of deforming cladding need to be at a microscale. This dissertation describes several high-magnification innovations and advancements in digital image correlation (DIC), a non-contact method for measuring displacement and strain of test specimens during experiments. First, a high-magnification UV lens is demonstrated to be capable of DIC measurements with improved spatial resolution and at high temperatures. Second, previously developed super resolution imaging techniques are applied to DIC measurements of directional ring test specimens, again improving resolution and measurement quality. Third, image capture settings are optimized to balance a tradeoff between poor depth of field and the diffraction of light, both of which cause blurred images and poorer DIC measurements. Fourth, several test arrangements are analyzed with computer modelling to determine the best method for directional tests of the cladding. Finally, the techniques are used to perform high-magnification tension tests for hydrided ring cladding specimens.

ACKNOWLEDGMENTS

Firstly, I would like to thank my advisor, Dr. Ryan Berke. I owe much of my success to his support. He has encouraged, taught, and assisted me from the beginning of my research through to this point. His technical expertise and his commitment to assisting me with my personal goals have made possible this journey of research, through every setback and success.

I would be remiss if I did not thank my lab mates over the years. In them I have found new ideas and invaluable contributions to my work, as well as friendships. Their tireless help in editing and re-editing my papers has doubtlessly made for more refined work. I also thank the staff in the MAE department, from graduate program coordinators ensuring I never miss a deadline to the machinist Terry Zollinger for always machining yet another grip or specimen.

I would also like to acknowledge funding through from the Department of Energy, Nuclear Engineering University Program. This material is based upon work supported under an Integrated University Program Graduate Fellowship. Any opinions, findings, conclusions, or recommendations expressed in this publication are those of the author and do not necessarily reflect the views of the Department of Energy Office of Nuclear Energy.

Also, I would like to thank David Kamerman, Dave Swank, and their coworkers at Idaho National Laboratory for their help in procuring zirconium cladding samples for testing. This work would not have been possible without their help.

Finally, I am very grateful to my wife Karlie, my parents, and my family and friends. There is no greater reward in life than the love of a family, and with this I have been greatly blessed. It is both because of them and for them that I have been able to accomplish this and every other notable achievement in my life. Their support cannot be overstated.

Robert S. Hansen

CONTENTS

Page

LIST OF TABLES

Page

LIST OF FIGURES

Page

CHAPTER 1
INTRODUCTION

1.1. Motivation

The design and maintenance of nuclear reactors in commercial power plants presents several multi-faceted challenges that draw on such varied fields as material science, mechanical design, structural engineering, chemistry, nuclear physics, heat transfer, and many others. In light water reactors (LWRs), the nuclear fuel cladding or nuclear fuel rods are the intermediary barrier between the radioactive fuel and the primary coolant [1]. Considerations in the design and maintenance of cladding include neutron cross sections, thermal conductivity, mechanical behavior, and chemical properties [2]. As a result, understanding the behavior of cladding is particularly important to the safety and function of nuclear reactors.

In order to provide better understanding of cladding behavior, a large effort has been made in developing tools which can be used to model the multiphysics associated with nuclear fuel cladding, both under operating and accident conditions [3]. These tools are useful for modeling fuel-cladding performance, but they still rely on experimental validation [4]. As additional improvements and continued developments such as multiscale and multiphysics coupling press forward [5], the need for additional in-pile and out-of-pile thermomechanical data from validation experiments grows as well [4,6].

The purpose of this dissertation is to provide experimental data of aged cladding to be used in validation of these models. In order to provide needed experimental validation to better understand thermomechanical behavior, current measurement techniques should be improved to expand the accuracy, precision, and temperature range. This will allow better testing to determine constitutive relationships, plasticity behavior, and deformation to failure of nuclear fuel cladding.

The subsequent subsections provide an overview of the state of cladding behavior, testing and relevant measurement techniques which form the basis of this work.

1.2. Research Background

1.2.1. Hydrogen Embrittlement of Nuclear Fuel Cladding

Light Water Reactors (LWRs) are the most common reactor type in service in today's nuclear energy fleet [7]. The majority of those LWRs are Pressurized Water Reactors (PWRs), which made up about two-thirds of operational nuclear plants across the world in 2019, as seen in Figure 1.1[8]. These reactors heat the water in the primary coolant loop which then transfers the heat through an exchanger to the steam generating loop. The other common type of LWR is the Boiling Water Reactor (BWR), which accounted for 16% of operating plants worldwide in 2019 [8]. BWRs feature a single coolant loop, which allows direct boiling above the reactor to generate the steam. The coolant loops for both types of LWRs operate in a temperature range of roughly 280-330°C, but the PWR operates at 15 MPa and a typical BWR operates at 7MPa [9]. Other less-common reactor types in use include Pressurized Heavy Water Reactors, Graphite-moderated Water-cooled Reactors, Gas Cooled Reactors, and Sodium Fast Neutron Reactors [8].

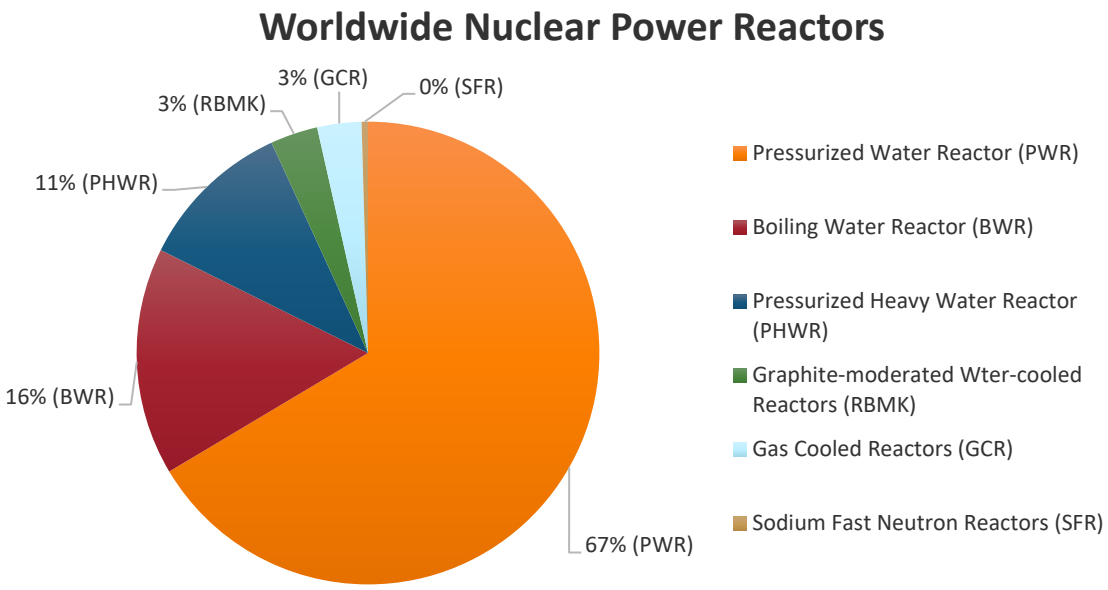

Figure 1.1: Breakdown of worldwide commercial power reactor types in use in 2019. Data from [8].

Typical LWR fuel comes in the form of UO_2 pellets, roughly 1 cm in diameter and 2 cm tall. Several fuel pellets are placed within a single cladding tubing with a slightly larger diameter and a length of roughly 4 m [10]. These fuel pins, consisting of the fuel and cladding, are placed in bundles to form the fuel assembly of the reactor. The material of choice for LWR fuel cladding has been Zirconium alloys, due in part to their low neutron cross section and desirable mechanical properties, along with corrosion and radiation damage resistance at elevated temperatures [9]. However, the crystal structure of zirconium is hexagonal close packed (hcp), and the limited slip systems of hcp crystals give the material anisotropic behavior [11]. This directionality is exaggerated in material processing methods used to fabricate cladding, which create texture as plastic deformation causes grains to reorient in a similar direction [12]. As a result, mechanical behavior such as creep and stress corrosion cracking, as well as fatigue and yield strength, are

anisotropic as well [11,13,14]. This anisotropy has led to careful testing of behavior in the axial and hoop directions, as well as experiments on the effect of biaxial stress and strain states [15,16]. Despite the added complexity of anisotropy, zirconium alloys have been the mainstay for cladding in LWRs for over 60 years [17].

A negative aspect of zirconium alloy cladding is its chemical pickup of undesired elements such as nitrogen, oxygen and hydrogen, which can degrade mechanical behavior. Alloying elements have been added to develop Zircaloy-1, -2, and -4 to address corrosion, nitrogen pickup, and hydrogen pickup respectively [18]. However, the formation of zirconium hydrides in particular has caused several challenges, as the added hydrides cause embrittlement of the zirconium alloy and pose the greatest threat to the mechanical integrity of the fuel cladding [19]. This embrittlement can be especially problematic in accident conditions, including loss-of-coolant accidents (LOCA) and reactivity-initiated accidents (RIA), due to loss of strength and ductility [20].

Hydrides form in the zirconium alloy as hydrogen is released during the oxidation of the cladding with the cooling water. The freed hydrogen can migrate through the protective oxide layer on the water side of the cladding, entering the metal [21]. At small concentrations, the hydrogen remains in solid solution. However, once the concentration exceeds a temperature-dependent solubility limit (roughly 100-150 wt. ppm at LWR operating conditions), hydride precipitation occurs [22]. These hydrides are predominantly in the face-centered cubic (fcc) δ-hydride phase, although at higher concentrations the face-centered tetragonal (fct) γ-hydride phase can form as well [23].

Because of the crystallographic texture of the fabricated cladding, the hydrides form as platelets in one of two orientations: along the axial-circumferential plane, known as circumferential hydrides as seen in Figure 1.2 , or along the axial-radial plane, known as radial

hydrides [24]. When there is little to no stress in the cladding, the hydrides tend to form in the circumferential direction [25]. However, because hydrides can migrate due to stress gradients [26], some conditions can cause their reorientation into radial hydrides [27]. These radial hydrides form primarily when the cladding is subject to thermal cooling or thermal cycling while undergoing stress [28,29], and thus they are more likely to form in LOCA conditions [30]. Due to the high mobility of hydrogen in the zirconium matrix, hydrides tend to migrate towards and form in areas of colder temperatures. This often leads to higher hydride concentrations towards the waterside surfaces and even the formation of hydride rims or blisters [31]. Additionally, hydrides can migrate due to stress gradients within the cladding.

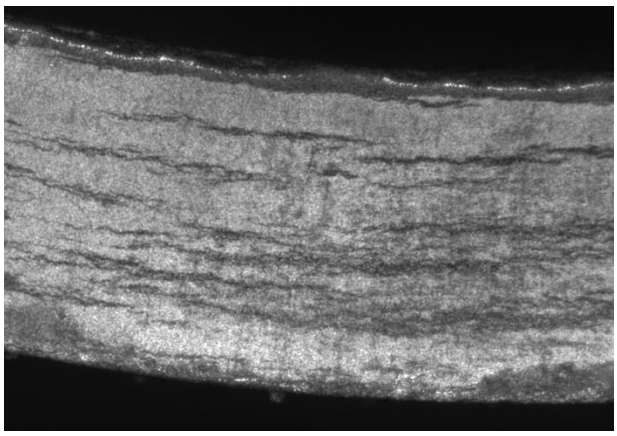

Figure 1.2: Sample of circumferential hydrides formed in zirconium alloy cladding.

These hydrides can have a great impact on the mechanical behavior of the cladding. Fatigue behavior [33], creep and plasticity [34], and strength and ductility [35] are all affected by the presence of hydrides. If there are localized concentrations of hydrogen in the form of hydride rims or blisters, the cladding will undergo brittle rather than ductile failure due to the initiation of cracks in these hydride features which then propagate through the cladding [36–38]. Local stresses caused

by hydride concentrations can cause low-temperature fracture in the hydrides even when the hydrides would otherwise have a higher strength than the surrounding matrix [31]. The length, orientation, and concentration of the hydrides all impact mechanical behavior, although that effect can vary at different temperatures [35,39]. The temperature the cladding is subjected to also has a significant effect on the ductile or brittle behavior of the hydrides within the cladding, both for radial and circumferential orientations [31].

The anisotropy of the cladding, combined with the hydride effects, make material modeling of cladding in nuclear reactors an effort that is dependent on directionality, hydride morphology and concentration, temperature, and stress/deformation state. Thus, experimental work to determine mechanical behavior must account for these different factors, even if the effect of only one variable is being investigated.

1.2.2. Motivations and Methods for Mechanical Testing of Fuel Cladding

During normal operation of nuclear reactors, the cladding is exposed to operating temperatures of roughly 300°C, and external pressurization on the order of tens of MPa with internal pressurization on the order of MPa to tens of MPa [40,41]. Cladding in operation may undergo thermomechanical deformation due to thermal expansion, thermal creep, irradiation creep, increase in internal pressurization, and contact with the fuel pellet [42]. Throughout the life of the fuel pin assembly, the burnup pellet can cause swelling and cracking. As this deformation of the pellet exceeds the gap between the pellet and the cladding, it creates a pellet-cladding mechanical interaction (PCMI) which can cause deformation of the cladding in the hoop or circumferential direction [43].

These cladding deformation mechanisms can become much more pronounced under accident conditions. The increase in the fission rate during RIA conditions causes an abrupt

temperature spike in the pellets which swell almost instantaneously, causing PCMI and potential cladding failure [44]. The thermal energy increase can lead to cladding outer surface temperatures of roughly 1200°C [45]. A biaxial stress state is created in the cladding in RIA conditions, with hoop stress as the dominant stress and axial stress roughly 70-80% of the hoop stress [46]. Because cladding at failure may undergo significant axial and hoop stress, and because of the anisotropy of zirconium alloy cladding, evaluation of the mechanical behavior of the cladding must consider stresses in the axial and circumferential directions independently of each other. This work focuses on circumferential, or hoop direction, testing.

Circumferential testing of cladding and similar tubing has been performed with a variety of methods. Expansion Due to Compression (EDC) tests involve placing a pellet or plug inside the cladding, which is then compressed axially so that it expands outward and exerts a force on the inside edge of the cladding [47]. Original versions of the test created a uniaxial hoop stress, but variations have produced a biaxial stress state by constraining the ends of the cladding to prevent contraction, approaching biaxiality of RIA conditions [48]. It has been adapted for various temperatures using different pellet materials, with capabilities up to 900°C [43].

A more traditional test of hoop direction material properties is the burst test. The burst test has been used to determine material behavior ranging from fracture of large-diameter gas line pipes [49,50] to testing for explosion criteria in CO_2 pressure vessels [51]. In all cases, a fluid is used to pressurize a vessel or pipe in order to cause deformation and potentially failure. A static burst test involves pressurization to some level less than failure, which pressure is maintained for some period of time to check for structural integrity [52]. Alternatively, a dynamic burst test involves increasing the pressure until failure occurs to evaluate failure conditions and behavior [53]. The time scale of the pressure increase may vary, depending on whether dynamic response or quasi-

static failure is under investigation. Burst testing of fuel cladding has been done extensively, whether to obtain purely hoop direction properties through an open-end test [54], to observe failure behavior in rapid pressurization [55], and to study creep behavior at elevated temperatures [56,57]. Variations of burst testing have also been developed which utilize an intermediary interface to apply the pressure to the inside of the cladding, such as rubber tubing [58] or a thin-walled driving tube which mimics PCMI under RIA conditions [59,60]. However, one of the shortcomings of burst testing is the uncertainty of where failure will occur, due to the lack of a gauge region.

Early researchers performed a uniaxial tension tests (UTT) in the hoop direction by cutting a thin slice in the hoop direction (machining a ring, then making an axial cut or cuts through the width of the ring) and then flattening out the curvature [61]. However, doing so introduces artificial strains during the flattening which significantly alter the behavior of the material. Instead, Ring Hoop Tension Tests (RHTT) have been used to study hoop properties of cladding and other tubular materials [62]. These tests use two mandrels in the shape of hemicylinders which hook inside a ring specimen, as seen in Figure 1.3; as the mandrels are pulled apart, they press against the inner surface of the ring, which applies a tensile stress in the hoop direction. Original versions of the test used a simple ring cut from cladding without any gauges [63]. Further modifications used a notched specimen which features a gauge region to focus deformation on a specific location [62].

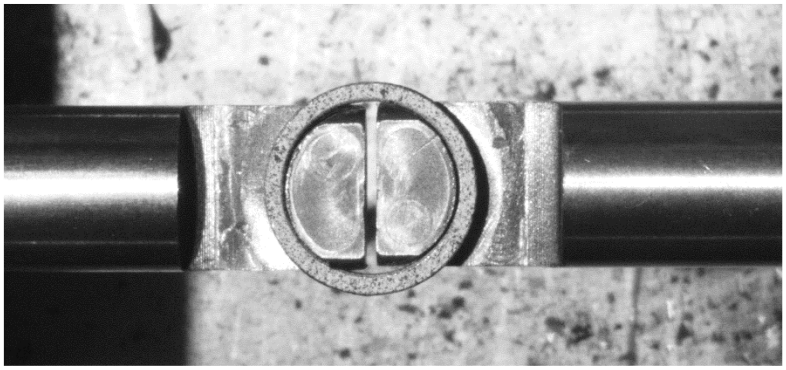

Figure 1.3: Ring Hoop Tension Test (RHTT) setup: two hemicylindrical grips are placed on the inside of the ring, then pulled apart to cause ring tension.

Some researchers place the gauge at the top and bottom of the grips, as shown in arrangement A of Figure 1.4. One of the most common gauge arrangements is to place the gauge region at the gap between the mandrels, as seen in arrangement B, [65] in order to reduce friction between the grips and the ring. However, this arrangement causes some bending moment in the gauge region as the ring deforms to the shape of the grips. To combat this, some researchers have rotated the gauge 45 degrees towards the direction of loading, as seen in arrangement C [32,66]. Alternatively, others have used an insert between the mandrel grips to prevent the inward bending of the ring, shown in arrangement D. [67,68]. These different arrangements seek to find a balance between uniform hoop tension and the effects of friction in order to obtain the desired hoop tensile behavior.

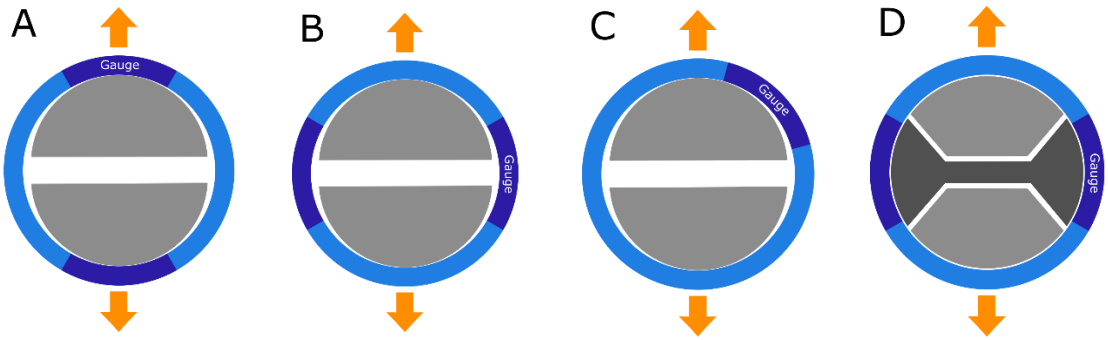

Figure 1.4: Potential test arrangements for RHTT. Direction of loading is shown by arrows, grips are shown in gray, the ring is shown in blue with the gauge section in dark blue.

1.2.3. Digital Image Correlation and High-Temperature Measurements

The material characterization of cladding samples through the previously described test methods relies on quality strain measurements. Digital Image Correlation (DIC) is a method for producing full-field displacement measurements on a surface being inspected [69]. It involves placing a trackable pattern on the surface, taking images before and after some displacement or deformation, and then processing those images with software that tracks the motion of individual pattern segments. DIC has become a popular strain measurement in part because of three distinct advantages over other methods: (1) it is a non-contact measurement, only requiring a thin layer of paint or other pattern [70], (2) it can be adapted to different length scales depending on the lens and camera used [71], and (3) it can provide full-field strain data for a surface, rather than a single data point averaged over some area [69]. These advantages make it a prime choice for measuring heterogeneous strain in materials characterization, such as the testing of nuclear fuel cladding.

First, any specimens to be investigated using DIC must feature a trackable pattern on the surface. There are several important aspects of an ideal pattern: it must have sufficiently high contrast [72], it must be a random pattern (non-periodic and non-repetitive) in order to provide unique subsets [73], and it must be isotropic and non-directional [74]. Although a naturally occurring pattern on the surface may be available in cases where the specimen has some texture or other inhomogeneous pattern [75], these requirements often necessitate the application of a contrasting black-and-white speckle pattern [73]. It is also important to ensure that speckles are appropriately sized for the scale of the measurement. Speckle size, as well as density of the speckle pattern, must be chosen based on the specific application [76].

Once a pattern is in place, images of the specimen are taken before and after some motion or deformation. This is accomplished by a camera and lens combination which can capture the pattern at the appropriate time and length scale [77]. The motion of the pattern is then tracked

between the reference and deformed images by a correlation algorithm, which searches for the same regions between the two images [78]. This may be accomplished by either local or global DIC. Local, or subset-based DIC, breaks the image into subsets of multiple pixels, and then searches for the pixel subsets individually [79]. The Global, or finite-element-based DIC approach, tracks the motion of all pixels in the region of interest simultaneously, ensuring that continuity constraints between portions of the image are maintained [80]. Global DIC measures the motion of the complete mesh [81], and while this can allow for more accurate measurements, it also increases computation time significantly [82]. As a result, local DIC is often the preferred approach and can be found in many commercial codes.

Using the reference and deformed images, the correlation algorithm tracks the motion of specific subsets in the image. Subsets sizes are defined by the DIC software user, along with the step size, or offset spacing between the center pixels of subsets [83]. The speckle pattern ensures that each subset has a unique 'fingerprint' of grayscale values, which allows the algorithm to begin searching for the same unique subset in the deformed image. If a speckle is too large, it will dominate a subset and make it indistinguishable, and if a speckle is too small then the difference between speckles becomes indistinguishable. A variety of shape functions can be used, which map between the reference and deformed subsets and include the position and displacement parameters which are to be solved for based on the correlation criteria [84]. Algorithms which use the cross-correlation (CC) criteria, such as the sample in Equation 1.1, seek to maximize a correlation coefficient which measures the similarity between two sets of pixels. Those which employ sum of squared differences (SSD), such as those in Equation 1.2, seek to minimize the difference between two subsets, meaning if they are perfectly matched, the difference in pixel values will be zero (see Equation 1.2) [85,86]. These correlation algorithms can be adjusted to account for changes in

lighting by normalizing the distribution of pixels and setting the mean to zero to further improve accuracy and noise robustness [85].

$$C_{CC}\left(x, y, u, v, \frac{du}{dx}, \frac{du}{dy}, \frac{dv}{dx}, \frac{dv}{dy}\right) = \sum_{i,j}[F(x,y) * G(x', y')] \quad (1.1)$$

$$C_{SSD}\left(x, y, u, v, \frac{du}{dx}, \frac{du}{dy}, \frac{dv}{dx}, \frac{dv}{dy}\right) = \sum_{i,j}[F(x,y) - G(x', y')]^2 \quad (1.2)$$

where F is grasycale values of original image, G is grayscale values of deformed image, x and y are the original position coordinates, u and v are displacements between images, $\frac{du}{dx}, \frac{du}{dy}, \frac{dv}{dx}$, and $\frac{dv}{dy}$ are partial derivatives, and x' and y' are displaced position coordinates.

Unlike strain gauges, the non-contact nature of DIC measurements allows for use at higher temperatures, given the camera and lens can capture the speckle pattern clearly. However, to capture clear images in elevated temperature tests, the lens and camera must deal with the emitted light from the heated specimen. As a specimen approaches roughly 600°C, it begins to emit Planck radiation in the form of visible light [87]. The intensity of the light being emitted varies with the emissivity of the surface, meaning lower emissivity surfaces may lessen the effect, but the varying emissivity of the speckle pattern becomes problematic if not dealt with [88]. One solution is to selectively filter the wavelengths of light illuminating the specimen and sensed by the camera. From Planck's law, it is known that at this threshold of visible emitted light, the emission intensity is higher at longer wavelengths. Therefore, relying on shorter-wavelength blue light sources to illuminate the specimen in conjunction with filters which block out all visible light other than blue can extend the upper temperature limit of DIC [89–93] by preserving the speckle quality and contrast in images.

The temperature range of DIC has been stretched even further by employing UV light [94]. Because UV has shorter wavelengths than visible, light in that spectrum is emitted at minimal levels at even higher temperatures. However, this necessitates the use of both cameras that are sensitive to UV light and lenses that can transmit UV light [95]. It may also be necessary to use UV filters to block all visible light if the camera is sensitive to both UV and visible wavelengths. This combination of UV optics and cameras has allowed measurements to be taken at temperatures up to 1600°C [96] with potential to reach much higher temperatures, limited by the melting temperature of the specimen.

1.2.4. Considerations for High-Magnification and High-Resolution DIC

In applying DIC techniques to strain measurements of a hydrided cladding specimen undergoing some deformation, the need to make small-scale measurements becomes apparent. With cladding hydrides measuring as little as a few microns across [97], full-field strain maps of cladding tests must be similarly small-scale in order to capture the material behavior. As previously mentioned, DIC can be adapted to any length scale as long as the equipment can take clear images of the speckled surface [71]. The ability to take an accurate measurement at a given scale depends on the resolution of the camera, the magnification and working distance of the lens, and how those factors interact to produce the field of view of the image. These all impact the resolution and size of the image, and therefore the quality of DIC small-scale measurements. Although DIC is capable of accurately detecting sub-pixel displacements [98,99], increasing resolution (decreasing the physical area on the surface represented by an image pixel) will allow even smaller-scale measurements to be made.

In the quest for small-scale DIC measurements, it is important to acknowledge that spatial resolution of measurements, or the area represented by a single measurement data point, is not the

same as image resolution. Because the measurement is subset-based, each displacement data point from a subset is averaged over the region covered by that subset. Thus, minimizing subset size improves the spatial resolution of displacement data, ensuring that inaccurate approximations of nonuniform displacement fields are not made [100]. However, this must be balanced against the uncertainty that comes with smaller subset sizes; a smaller collection of pixels equates to a 'less-unique' fingerprint for each subset, which can make correlation more challenging [101]. This balance limits the lower range of subset sizes and causes the effective displacement field resolution to be worse than the image pixel resolution.

Compounding this further, strain calculations rely on more than one subset. The strains are calculated as first-order partial derivatives of the displacement field. These partial derivatives are calculated from the Taylor series approximation of the displacement field, which necessarily uses more than one subset [102]. This results in averaging the strain measurement over areas larger than a single subset [103], causing some spatial filtering or smoothing of the strain data [104]. The averaging effect at both the subset displacement level and the strain calculation level requires that even further resolution improvement be achieved to make small-scale DIC strain measurements.

Researchers using DIC methods often improve spatial resolution by increasing the magnification of the lens. Microscale measurements have been made by taking reference and deformed images using an optical microscope [105] or scanning electron microscope (SEM) [106–108]. This has allowed measurements on the nanoscale, able to capture strain across very small structural features. However, this limits in-situ experiments to environments which can be supported by the SEM, thereby often limiting DIC to ex-situ measurements of pre- and post-deformation rather than allowing the live mapping of evolving deformation and strain fields during a test. Some microscopy setups have been specially fitted to allow loading of the specimen while

under the microscope at room temperature [109–111], but high temperature tests with this level of magnification are generally limited to ex-situ measurements [112]. For high-temperature in-situ tests, often a long stand-off distance, or working distance, between the specimen and the optical equipment is required to enable viewing through an environmental chamber window, but this generally limits the magnification of the lenses.

Even in the case where zoom lenses with long working distances allow in-situ measurements, the increase in magnification due to lens or microscope selection also limits the field of view. For a given number of pixels on a camera sensor, increasing resolution by decreasing the physical size represented by a pixel will also cause the field of view to decrease. In cases where good resolution and large fields of view are required together, high-magnification images with small fields of view have been stitched together to create a single image with a large field of view [113]. This has been done with optical microscopes [114,115] as well as SEMs [116,117].

As an alternative to image stitching, the technique of super resolution (SR) imaging shows potential to be paired with DIC for high resolution measurements. SR has been developed in other fields and used as a method of increasing the resolution of an image while maintaining the field of view. As seen in Figure 1.5, the technique involves combining several overlapping images to form a single higher resolution image of the common field of view [118]. SR can be used either in the absence of high magnification optics or in conjunction with them to produce an image with increased resolution.

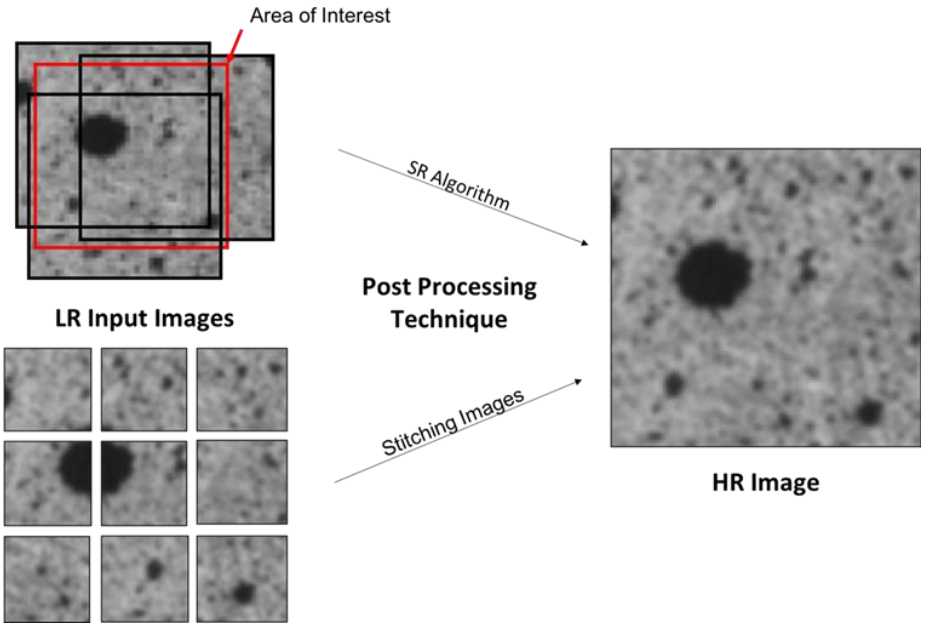

Figure 1.5: Comparison of super resolution with image stitching.

The technique has its roots in mathematical models used to improve image quality and resolution beyond the diffraction limit of light [119]. There have been several distinct algorithms proposed [118,120–125] and applications have ranged from biochemistry [126] and telemedicine [127] to smartphone technology [128] and astronomy [129]. Because SR imaging is a post-processing method, it can be paired with any image capture method, including the potential use of SR imaging with high-magnification, high-temperature DIC measurements to further improve resolution. To our knowledge, this dissertation includes the first demonstration of combined super-resolution imaging and DIC.

Another important consideration in high magnification DIC measurements is the diffraction limit of light, and the defocusing of an image that can result. This diffraction of light is particularly relevant when environmental factors necessitate longer working distances [130], such as the in-situ measurement cases noted previously. Consideration of this effect is important when

determining the parameters of image capture such as working distance, magnification, aperture, and lighting.

For a beam of light passing through a circular iris or aperture, a two-dimensional diffraction pattern is produced. The central bright disk of this pattern, called the Airy disk, is a key limit to the spatial resolution of imaging small features [131]. The size of this Airy disk is directly proportional to the wavelength of the lighting source and the working distance, and inversely proportional to the diameter of the aperture. Thus, after employing the shortest wavelengths of light allowable by the camera system and shortest working distances allowable by the testing environment, the size of the Airy disk is mainly controlled by the aperture. For most applications, the Airy disk remains negligibly small, but as the diffraction limit is angular in nature [132,133], it becomes more pronounced at long working distances. To avoid blurring at these longer distances, wider apertures may be used to reduce Airy disk size.

However, wider apertures also have a negative effect on the focus of the image, due to reduced depth of field [134]. Thus, existing guidance in DIC measurements generally suggests using as narrow of an aperture as possible while still maintain sufficient lighting, in order to mitigate blurring caused by poor depth of field [135]. As such, blurring can be caused by both defocusing and Airy disks [136], with defocus improving through narrow apertures and Airy disks improving through wider apertures. Due to the relationship between Airy disk and working distance, the optimization of aperture settings is important to improving the resolution of in-situ high magnification DIC.

1.3. Objectives

The central objectives of the dissertation are listed below:

1. Develop high-magnification, high-temperature capability for full-field strain measurement through digital image correlation (DIC) using a custom lens and demonstrate its efficacy.
2. Improve spatial resolution, accuracy, precision, and confidence of strain measurements using super resolution (SR) processing coupled with DIC.
3. Examine the effect of the diffraction limit of light on high-magnification DIC measurements, particularly with longer working distances.
4. Develop Ring Hoop Tensile Test (RHTT) methods for accurate extraction of mechanical behaviors, including plasticity properties.
5. Use full-field measurements of strain during cladding testing through the elasto-plastic regime to failure to understand the effects of hydride microstructure and temperature on cladding behavior, and to provide validation experiments for fuel cladding modelling code.

1.4. Dissertation Outline

This dissertation is organized in a multi-paper format, with seven chapters. This first chapter contains the introduction material, while chapters 2, 3, 4, and 6 contain papers that have been published, submitted, or that are in preparation for publication in peer-reviewed scientific journals. Chapter 5 contains a post-internship report with results critical to the dissertation topic, and chapter 7 provides summarizing discussion and conclusions of the work as a whole. It should be noted that references are included at the end of each chapter. A chapter-by-chapter summary is included below:

- Chapter 1 covers the motivation for the work, relevant background research, and overall research objectives.

- Chapter 2 is a full-length paper which was published in *Review of Scientific Instruments* and discusses the use of high-magnification UV optics for high-temperature DIC measurements.
- Chapter 3 is a full-length paper which was published in *Experimental Mechanics*, discussing the pairing of computer-based super resolution imaging with DIC measurements.
- Chapter 4 is another full-length paper which has been submitted for review to *Measurement*, investigating the tradeoffs between depth of field and diffraction-caused blurring for high magnification DIC at longer working distances.
- Chapter 5 is a report based on work done during an internship at Idaho National Laboratory, discussing the preferred arrangement for obtaining anisotropic mechanical properties from a Ring Hoop Tension Test (RHTT).
- Chapter 6 is a full-length paper, in preparation for submission to a peer-reviewed scientific journal. It covers the use of DIC paired with hydride mapping to better understand material behavior of aged cladding.
- Chapter 7 contains the conclusion, discussing the contributions of the research and laying the groundwork for future work.

1.5. References

[1] Edsinger, K., Stanek, C. R., and Wirth, B. D., 2011, "Light Water Reactor Fuel Performance: Current Status, Challenges, and Future High Fidelity Modeling," JOM, **63**(8), pp. 49–52.

[2] Duan, Z., Yang, H., Satoh, Y., Murakami, K., Kano, S., Zhao, Z., Shen, J., and Abe, H., 2017, "Current Status of Materials Development of Nuclear Fuel Cladding Tubes for Light Water Reactors," Nuclear Engineering and Design, **316**, pp. 131–150.

[3] Rashid, J. Y. R., Yagnik, S. K., and Montgomery, R. O., 2011, "Light Water Reactor Fuel Performance Modeling and Multi-Dimensional Simulation," JOM, **63**(8), p. 81.

[4] Van Uffelen, P., Hales, J., Li, W., Rossiter, G., and Williamson, R., 2019, "A Review of Fuel Performance Modelling," Journal of Nuclear Materials, **516**, pp. 373–412.

[5] Hales, J. D., Tonks, M. R., Gleicher, F. N., Spencer, B. W., Novascone, S. R., Williamson, R. L., Pastore, G., and Perez, D. M., 2015, "Advanced Multiphysics Coupling for LWR Fuel Performance Analysis," Annals of Nuclear Energy, **84**, pp. 98–110.

[6] Wang, K.-Y., Wang, Y., Jin, X., Wei, J., and Deng, Y.-J., 2020, "A New Relocation Recovery Model for LWR Fuel," Annals of Nuclear Energy, **145**, p. 107528.

[7] Marcus, G. H., 2019, "Nuclear Power around the World," Nature Reviews Physics, **1**(3), pp. 172–173.

[8] Ho, M., Obbard, E., Burr, P. A., and Yeoh, G., 2019, "A Review on the Development of Nuclear Power Reactors," Energy Procedia, **160**, pp. 459–466.

[9] Azevedo, C. R. F., 2011, "Selection of Fuel Cladding Material for Nuclear Fission Reactors," Engineering Failure Analysis, **18**(8), pp. 1943–1962.

[10] Lamarsh, J. R., and Baratta, A. J., 2001, *Introduction to Nuclear Engineering*, Prentice Hall, Upper Saddle River, New Jersey.

[11] Tenckhoff, E., 1988, *Deformation Mechanisms, Texture, and Anisotropy in Zirconium and Zircaloy*, ASTM International.

[12] Linga Murty, K., and Charit, I., 2006, "Texture Development and Anisotropic Deformation of Zircaloys," Progress in Nuclear Energy, **48**(4), pp. 325–359.

[13] Murty, K. L., 1999, "Creep Studies for Zircaloy Life Prediction in Water Reactors," JOM, **51**(10), pp. 32–39.

[14] Ballinger, R. G., Lucas, G. E., and Pelloux, R. M., 1984, "The Effect of Plastic Strain on the Evolution of Crystallographic Texture in Zircaloy-2," Journal of Nuclear Materials, **126**(1), pp. 53–69.

[15] Mihara, T., Udagawa, Y., and Amaya, M., 2018, "Deformation Behavior of Recrystallized and Stress-Relieved Zircaloy-4 Fuel Cladding under Biaxial Stress Conditions," Journal of Nuclear Science and Technology, **55**(2), pp. 151–159.

[16] Miyamoto, Y., Komatsu, Y., Kakuma, T., and Nagai, N., 1976, "Mechanical Behavior of Zircaloy-2 Tubing under Biaxial Stresses," Journal of Nuclear Materials, **61**(1), pp. 53–65.

[17] Lustman, B., 1981, "Development of the Zircaloy-Clad UO2 Fuel Element for Shippingport," Journal of Nuclear Materials, **100**(1), pp. 72–77.

[18] Suman, S., Khan, Mohd. K., Pathak, M., Singh, R. N., and Chakravartty, J. K., 2015, "Hydrogen in Zircaloy: Mechanism and Its Impacts," International Journal of Hydrogen Energy, **40**(17), pp. 5976–5994.

[19] Zieliński, A., and Sobieszczyk, S., 2011, "Hydrogen-Enhanced Degradation and Oxide Effects in Zirconium Alloys for Nuclear Applications," International Journal of Hydrogen Energy, **36**(14), pp. 8619–8629.

[20] Zinkle, S. J., Terrani, K. A., Gehin, J. C., Ott, L. J., and Snead, L. L., 2014, "Accident Tolerant Fuels for LWRs: A Perspective," Journal of Nuclear Materials, **448**(1), pp. 374–379.

[21] Couet, A., Motta, A. T., and Comstock, R. J., 2014, "Hydrogen Pickup Measurements in Zirconium Alloys: Relation to Oxidation Kinetics," Journal of Nuclear Materials, **451**(1), pp. 1–13.

[22] Motta, A. T., and Chen, L.-Q., 2012, "Hydride Formation in Zirconium Alloys," JOM, **64**(12), pp. 1403–1408.

[23] Daum, R. S., Chu, Y. S., and Motta, A. T., 2009, "Identification and Quantification of Hydride Phases in Zircaloy-4 Cladding Using Synchrotron X-Ray Diffraction," Journal of Nuclear Materials, **392**(3), pp. 453–463.

[24] Singh, R. N., Lala Mikin, R., Dey, G. K., Sah, D. N., Batra, I. S., and Ståhle, P., 2006, "Influence of Temperature on Threshold Stress for Reorientation of Hydrides and Residual Stress Variation across Thickness of Zr–2.5Nb Alloy Pressure Tube," Journal of Nuclear Materials, **359**(3), pp. 208–219.

[25] Northwood, D. O., and Kosasih, U., 2013, "Hydrides and Delayed Hydrogen Cracking in Zirconium and Its Alloys," International Metals Reviews.

[26] Kammenzind, B. F., Berquist, B. M., Bajaj, R., Kreyns, P. H., and Franklin, D. G., 2000, "The Long-Range Migration of Hydrogen Through Zircaloy in Response to Tensile and Compressive Stress Gradients," Zirconium in the Nuclear Industry: Twelfth International Symposium.

[27] Leger, M., and Donner, A., 1985, "The Effect of Stress on Orientation of Hydrides in Zirconium Alloy Pressure Tube Materials," Canadian Metallurgical Quarterly, **24**(3), pp. 235–243.

[28] Chu, H. C., Wu, S. K., and Kuo, R. C., 2008, "Hydride Reorientation in Zircaloy-4 Cladding," Journal of Nuclear Materials, **373**(1), pp. 319–327.

[29] Cinbiz, M. N., Koss, D. A., and Motta, A. T., 2016, "The Influence of Stress State on the Reorientation of Hydrides in a Zirconium Alloy," Journal of Nuclear Materials, **477**, pp. 157–164.

[30] Billone, M., Yan, Y., Burtseva, T., Daum, R., and Division, N. E., 2008, *Cladding Embrittlement during Postulated Loss-of-Coolant Accidents.*, NUREG/CR-696, Argonne National Lab. (ANL), Argonne, IL (United States).

[31] Motta, A. T., Capolungo, L., Chen, L.-Q., Cinbiz, M. N., Daymond, M. R., Koss, D. A., Lacroix, E., Pastore, G., Simon, P.-C. A., Tonks, M. R., Wirth, B. D., and Zikry, M. A., 2019, "Hydrogen in Zirconium Alloys: A Review," Journal of Nuclear Materials, **518**, pp. 440–460.

[32] Kubo, T., Kobayashi, Y., and Uchikoshi, H., 2013, "Determination of Fracture Strength of δ-Zirconium Hydrides Embedded in Zirconium Matrix at High Temperatures," Journal of Nuclear Materials, **435**(1), pp. 222–230.

[33] Li, J., Wang, Z., Cheng, Y., Xin, Y., Wu, H., Guo, X., and Chen, G., 2019, "Effect of Hydride Precipitation on the Fatigue Cracking Behavior in a Zirconium Alloy Cladding Tube," International Journal of Fatigue, **129**, p. 105230.

[34] Bouffioux, P., and Rupa, N., 2000, "Impact of Hydrogen on Plasticity and Creep of Unirradiated Zircaloy-4 Cladding Tubes," Zirconium in the Nuclear Industry: Twelfth International Symposium.

[35] Lee, K. W., and Hong, S. I., 2002, "Zirconium Hydrides and Their Effect on the Circumferential Mechanical Properties of Zr–Sn–Fe–Nb Tubes," Journal of Alloys and Compounds, **346**(1), pp. 302–307.

[36] Macdonald, V., Le Boulch, D., Menibus, A. H. de, Besson, J., Auzoux, Q., Crépin, J., and Le Jolu, T., 2014, "Fracture of Zircaloy-4 Fuel Cladding Tubes with Hydride Blisters," Procedia Materials Science, **3**, pp. 233–238.

[37] NAGASE, F., and FUKETA, T., 2005, "Investigation of Hydride Rim Effect on Failure of Zircaloy-4 Cladding with Tube Burst Test," Journal of Nuclear Science and Technology, **42**(1), pp. 58–65.

[38] Daum, R. S., Bates, D. W., Koss, D. A., and Motta, A. T., 2002, *The Influence of a Hydride Layer on the Fracture of Zircaloy-4 Cladding Tubes.*, ANL/ET/CP-107400, Argonne National Lab., IL (US).

[39] Hsu, H.-H., and Tsay, L.-W., 2011, "Effect of Hydride Orientation on Fracture Toughness of Zircaloy-4 Cladding," Journal of Nuclear Materials, **408**(1), pp. 67–72.

[40] Denis, A., and Soba, A., 2003, "Simulation of Pellet-Cladding Thermomechanical Interaction and Fission Gas Release," Nuclear Engineering and Design, **223**(2), pp. 211–229.

[41] Viswanathan, U. K., Sah, D. N., Rath, B. N., and Anantharaman, S., 2009, "Measurement of Fission Gas Release, Internal Pressure and Cladding Creep Rate in the Fuel Pins of PHWR Bundle of Normal Discharge Burnup," Journal of Nuclear Materials, **392**(3), pp. 545–551.

[42] Michel, B., Sercombe, J., Thouvenin, G., and Chatelet, R., 2008, "3D Fuel Cracking Modelling in Pellet Cladding Mechanical Interaction," Engineering Fracture Mechanics, **75**(11), pp. 3581–3598.

[43] Le Saux, M., Poussard, C., Averty, X., Sainte Catherine, C., Carassou, S., and Besson, J., 2007, *High Temperature Expansion Due to Compression Test for the Determination of a Cladding Material Failure Criterion under RIA Loading Conditions*, American Nuclear Society - ANS, La Grange Park (United States).

[44] Desquines, J., Koss, D. A., Motta, A. T., Cazalis, B., and Petit, M., 2011, "The Issue of Stress State during Mechanical Tests to Assess Cladding Performance during a Reactivity-Initiated Accident (RIA)," Journal of Nuclear Materials, **412**(2), pp. 250–267.

[45] ISHIJIMA, K., and NAKAMURA, T., 1996, "Transient Elongation of a Fresh Fuel Rod under Reactivity Initiated Accident Conditions," Journal of Nuclear Science and Technology, **33**(3), pp. 229–238.

[46] Udagawa, Y., Sugiyama, T., Suzuki, M., and Nagase, F., 2013, "Stress Biaxiality in High-Burnup PWR Fuel Cladding under Reactivity-Initiated Accident Conditions," Journal of Nuclear Science and Technology, **50**, pp. 645–653.

[47] Dufournaud, O., Varias, A. G., Grigoriev, V., Jakobsson, R., and Schrire, D., 2002, "Elastic-Plastic Deformation of a Nuclear Fuel Cladding Specimen under the Internal Pressure of a Polymer Pellet."

[48] Hellouin de Menibus, A., Auzoux, Q., Mongabure, P., Macdonald, V., Le Jolu, T., Besson, J., and Crepin, J., 2014, "Fracture of Zircaloy-4 Cladding Tubes with or without Hydride Blisters in Uniaxial to Plane Strain Conditions with Standard and Optimized Expansion Due to Compression Tests," Materials Science and Engineering: A, **604**, pp. 57–66.

[49] Sugie, E., Kaji, H., Taira, T., Ohashi, M., and Sumitomo, Y., 1984, "Shear Fracture Arrestability of Controlled Rolled Steel X70 Line Pipe by Full-Scale Burst Test," J. Energy Resour. Technol, **106**(1), pp. 55–62.

[50] Muaoka, R., Ishikawa, N., Endo, S., and Kondo, J., 2009, "Evaluation for Abnormal Fracture Appearance in Drop Weight Tear Test With High Toughness Linepipe," American Society of Mechanical Engineers Digital Collection, pp. 129–136.

[51] Li, M., Liu, Z., Zhou, Y., Zhao, Y., Li, X., and Zhang, D., 2018, "A Small-Scale Experimental Study on the Initial Burst and the Heterogeneous Evolution Process before CO2 BLEVE," Journal of Hazardous Materials, **342**, pp. 634–642.

[52] Qingquan, D., Hong, Z., Feng, Y., and Changyi, D., 2009, "Hydrostatic Burst Test 0F X80 Grade Steel Pipe," Journal of Loss Prevention in the Process Industries, **22**(6), pp. 897–900.

[53] O'Donoghue, P. E., Kanninen, M. F., Leung, C. P., Demofonti, G., and Venzi, S., 1997, "The Development and Validation of a Dynamic Fracture Propagation Model for Gas

Transmission Pipelines," International Journal of Pressure Vessels and Piping, **70**(1), pp. 11–25.

[54] Nakatsuka, M., Aita, M., Sakamoto, K., and Higuchi, T., 2013, "An Open-End Burst Test Method to Obtain Uniaxial Hoop Tensile Properties of Fuel Cladding in a Hot Cell," Journal of Nuclear Materials, **434**(1), pp. 303–310.

[55] Kim, J. H., Lee, M. H., Jeong, Y. H., and Lim, J. G., 2008, "Behavior of Zirconium Fuel Cladding under Fast Pressurization Rates," Nuclear Engineering and Design, **238**(6), pp. 1441–1447.

[56] Mayuzumi, M., and Onchi, T., 1990, "Creep Deformation and Rupture Properties of Unirradiated Zircaloy-4 Nuclear Fuel Cladding Tube at Temperatures of 727 to 857 K," Journal of Nuclear Materials, **175**(1), pp. 135–142.

[57] Seok, C. S., Marple, B., Song, Y. J., Gollapudi, S., Charit, I., and Murty, K. L., 2011, "High Temperature Deformation Characteristics of Zirlo™ Tubing via Ring-Creep and Burst Tests," Nuclear Engineering and Design, **241**(3), pp. 599–602.

[58] Alva, L. H., Huang, X., Jacobsen, G. M., and Back, C. A., 2015, "High Pressure Burst Testing of SiCf-SiCm Composite Nuclear Fuel Cladding," *Advancement of Optical Methods in Experimental Mechanics, Volume 3*, H. Jin, C. Sciammarella, S. Yoshida, and L. Lamberti, eds., Springer International Publishing, Cham, pp. 387–393.

[59] Cinbiz, M. N., Brown, N. R., Terrani, K. A., Lowden, R. R., and Erdman, D., 2017, "A Pulse-Controlled Modified-Burst Test Instrument for Accident-Tolerant Fuel Cladding," Annals of Nuclear Energy, **109**, pp. 396–404.

[60] Cinbiz, M. N., Gussev, M., Linton, K., and Terrani, K. A., 2019, "An Advanced Experimental Design for Modified Burst Testing of Nuclear Fuel Cladding Materials during Transient Loading," Annals of Nuclear Energy, **127**, pp. 30–38.

[61] UNE, K., 1979, "Deformation and Fracture Behavior of Zircaloy-2 Deformed at Constant Strain Rate in Iodine Environment, (I)," Journal of Nuclear Science and Technology, **16**(8), pp. 577–587.

[62] Wang, H., Bouchard, R., Eagleson, R., Martin, P., Tyson, W., Martin, P., and Tyson, W., 2002, "Ring Hoop Tension Test (RHTT): A Test for Transverse Tensile Properties of Tubular Materials," J. Test. Eval., **30**(5), p. 382.

[63] ONCHI, T., and TANAKA, H., 1981, "Iodine Stress Corrosion Cracking of Unirradiated Zircaloy-2 Tubing by Means of Ring Tension Test," Journal of Nuclear Science and Technology, **18**(12), pp. 930–939.

[64] Arsene, S., and Bai, J., 1996, "A New Approach to Measuring Transverse Properties of Structural Tubing by a Ring Test," JTE, **24**(6), pp. 386–391.

[65] El-Bagory, T. M. A. A., Younan, M. Y. A., and Alarifi, I. M., 2018, "Failure Analysis of Ring Hoop Tension Test (RHTT) Specimen Under Different Loading Conditions," American Society of Mechanical Engineers Digital Collection.

[66] Dick, C. P., and Korkolis, Y. P., 2014, "Mechanics and Full-Field Deformation Study of the Ring Hoop Tension Test," International Journal of Solids and Structures, **51**(18), pp. 3042–3057.

[67] Grigoriev, V., Jakobsson, R., Josefsson, B., and Schrire, D., 2002, "Advanced Techniques for Mechanical Testing of Irradiated Cladding Materials."

[68] Kim, J. H., Lee, M. H., Choi, B. K., and Jeong, Y. H., 2006, "Effects of Oxide and Hydrogen on the Circumferential Mechanical Properties of Zircaloy-4 Cladding," Nuclear Engineering and Design, **236**(18), pp. 1867–1873.

[69] Sutton, M. A., Orteu, J. J., and Schreier, H., 2009, *Image Correlation for Shape, Motion and Deformation Measurements: Basic Concepts,Theory and Applications*, Springer Science & Business Media.

[70] Field, K. G., Gussev, M. N., Hu, X., Yamamoto, Y., and Howard, R. H., 2015, *First Annual Progress Report on Radiation Tolerance of Controlled Fusion Welds in High Temperature Oxidation Resistant FeCrAl Alloys*, ORNL/TM-2015/770, Oak Ridge National Lab. (ORNL), Oak Ridge, TN (United States).

[71] Hild F. and Roux S., 2006, "Digital Image Correlation: From Displacement Measurement to Identification of Elastic Properties – a Review," Strain, **42**(2), pp. 69–80.

[72] Thai, T. Q., Hansen, R. S., Smith, A. J., Lambros, J., and Berke, R. B., 2019, "Importance of Exposure Time on DIC Measurement Uncertainty at Extreme Temperatures," Exp Tech, **43**(3), pp. 261–271.

[73] Dong, Y. L., and Pan, B., 2017, "A Review of Speckle Pattern Fabrication and Assessment for Digital Image Correlation," Exp Mech, **57**(8), pp. 1161–1181.

[74] Reu, P., 2014, "All about Speckles: Speckle Size Measurement," Experimental Techniques, **38**(6), pp. 1–2.

[75] Palanca, M., Tozzi, G., and Cristofolini, L., 2016, "The Use of Digital Image Correlation in the Biomechanical Area: A Review," International Biomechanics, **3**(1), pp. 1–21.

[76] Lecompte, D., Smits, A., Bossuyt, S., Sol, H., Vantomme, J., Van Hemelrijck, D., and Habraken, A. M., 2006, "Quality Assessment of Speckle Patterns for Digital Image Correlation," Optics and Lasers in Engineering, **44**(11), pp. 1132–1145.

[77] Hua, T., Xie, H., Wang, S., Hu, Z., Chen, P., and Zhang, Q., 2011, "Evaluation of the Quality of a Speckle Pattern in the Digital Image Correlation Method by Mean Subset Fluctuation," Optics & Laser Technology, **43**(1), pp. 9–13.

[78] Pan, B., Qian, K., Xie, H., and Asundi, A., 2009, "Two-Dimensional Digital Image Correlation for in-Plane Displacement and Strain Measurement: A Review," Meas. Sci. Technol., **20**(6), p. 062001.

[79] Reu Phillip, 2012, "Introduction to Digital Image Correlation: Best Practices and Applications," Experimental Techniques, **36**(1), pp. 3–4.

[80] Cheng, P., Sutton, M. A., Schreier, H. W., and McNeill, S. R., 2002, "Full-Field Speckle Pattern Image Correlation with B-Spline Deformation Function," Experimental Mechanics, **42**(3), pp. 344–352.

[81] Wittevrongel, L., Lava, P., Lomov, S. V., and Debruyne, D., 2015, "A Self Adaptive Global Digital Image Correlation Algorithm," Experimental Mechanics, **55**(2), pp. 361–378.

[82] Wang, B., and Pan, B., 2016, "Subset-Based Local vs. Finite Element-Based Global Digital Image Correlation: A Comparison Study," Theoretical and Applied Mechanics Letters, **6**(5), pp. 200–208.

[83] Correlated Solutions, 2009, "Vic-2D User Manual."

[84] Arun Shukla and James W. Dally, 2014, *Experimental Solid Mechanics*, College House Enterprises, Knoxville, TN.

[85] Giachetti, A., 2000, "Matching Techniques to Compute Image Motion," Image and Vision Computing, **18**(3), pp. 247–260.

[86] Tong, W., 2005, "An Evaluation of Digital Image Correlation Criteria for Strain Mapping Applications," Strain, **41**(4), pp. 167–175.

[87] Pan, B., Wu, D., Wang, Z., and Xia, Y., 2011, "High-Temperature Digital Image Correlation Method for Full-Field Deformation Measurement at 1200 °C," Meas. Sci. Technol., **22**(1), p. 015701.

[88] Le, D. B., Tran, S. D., Torero, J. L., and Dao, V. T. N., 2019, "Application of Digital Image Correlation System for Reliable Deformation Measurement of Concrete Structures at High Temperatures," Engineering Structures, **192**, pp. 181–189.

[89] Bing, P., Hui-min, X., Tao, H., and Asundi, A., 2009, "Measurement of Coefficient of Thermal Expansion of Films Using Digital Image Correlation Method," Polymer Testing, **28**(1), pp. 75–83.

[90] Blaber, J., Adair, B. S., and Antoniou, A., 2015, "A Methodology for High Resolution Digital Image Correlation in High Temperature Experiments," Review of Scientific Instruments, **86**(3), p. 035111.

[91] Novak, M. D., and Zok, F. W., 2011, "High-Temperature Materials Testing with Full-Field Strain Measurement: Experimental Design and Practice," Review of Scientific Instruments, **82**(11), p. 115101.

[92] Grant, B. M. B., Stone, H. J., Withers, P. J., and Preuss, M., 2009, "High-Temperature Strain Field Measurement Using Digital Image Correlation," The Journal of Strain Analysis for Engineering Design, **44**(4), pp. 263–271.

[93] Leplay, P., Lafforgue, O., and Hild, F., 2015, "Analysis of Asymmetrical Creep of a Ceramic at 1350°C by Digital Image Correlation," Journal of the American Ceramic Society, **98**(7), pp. 2240–2247.

[94] Berke, R. B., and Lambros, J., 2014, "Ultraviolet Digital Image Correlation (UV-DIC) for High Temperature Applications," Review of Scientific Instruments, **85**(4), p. 045121.

[95] Hansen, R. S., Bird, T. J., Voie, R., Burn, K. Z., and Berke, R. B., 2019, "A High Magnification UV Lens for High Temperature Optical Strain Measurements," Review of Scientific Instruments, **90**(4), p. 045117.

[96] Thai, T. Q., Smith, A. J., Rowley, R. J., Gradl, P. R., and Berke, R. B., 2020, "Change of Exposure Time Mid-Test in High Temperature DIC Measurement," Meas. Sci. Technol., **31**(7), p. 075402.

[97] Wang, S., Giuliani, F., and Britton, T. B., 2019, "Microstructure and Formation Mechanisms of δ-Hydrides in Variable Grain Size Zircaloy-4 Studied by Electron Backscatter Diffraction," Acta Materialia, **169**, pp. 76–87.

[98] Yuan Lin, and Zhiwen Lan, 2010, "Sub-Pixel Displacement Measurement in Digital Image Correlation Using Particle Swarm Optimization," *2010 International Conference on Information, Networking and Automation (ICINA)*, pp. V2-497-V2-501.

[99] Bing, P., Hui-min, X., Bo-qin, X., and Fu-long, D., 2006, "Performance of Sub-Pixel Registration Algorithms in Digital Image Correlation," Meas. Sci. Technol., **17**(6), pp. 1615–1621.

[100] Yaofeng, S., and Pang, J. H. L., 2007, "Study of Optimal Subset Size in Digital Image Correlation of Speckle Pattern Images," Optics and Lasers in Engineering, **45**(9), pp. 967–974.

[101] Bornert, M., Brémand, F., Doumalin, P., Dupré, J.-C., Fazzini, M., Grédiac, M., Hild, F., Mistou, S., Molimard, J., Orteu, J.-J., Robert, L., Surrel, Y., Vacher, P., and Wattrisse, B., 2009, "Assessment of Digital Image Correlation Measurement Errors: Methodology and Results," Exp Mech, **49**(3), pp. 353–370.

[102] Lu, H., and Cary, P. D., 2000, "Deformation Measurements by Digital Image Correlation: Implementation of a Second-Order Displacement Gradient," Experimental Mechanics, **40**(4), pp. 393–400.

[103] Reu, P., 2015, "Virtual Strain Gage Size Study," Exp Tech, **39**(5), pp. 1–3.

[104] LePage, W. S., Daly, S. H., and Shaw, J. A., 2016, "Cross Polarization for Improved Digital Image Correlation," Exp Mech, **56**(6), pp. 969–985.

[105] Berfield, T. A., Patel, J. K., Shimmin, R. G., Braun, P. V., Lambros, J., and Sottos, N. R., 2007, "Micro- and Nanoscale Deformation Measurement of Surface and Internal Planes via Digital Image Correlation," Exp Mech, **47**(1), pp. 51–62.

[106] Kammers, A. D., and Daly, S., 2013, "Self-Assembled Nanoparticle Surface Patterning for Improved Digital Image Correlation in a Scanning Electron Microscope," Exp Mech, **53**(8), pp. 1333–1341.

[107] Kammers, A. D., and Daly, S., 2013, "Digital Image Correlation under Scanning Electron Microscopy: Methodology and Validation," Exp Mech, **53**(9), pp. 1743–1761.

[108] Maraghechi, S., Hoefnagels, J. P. M., Peerlings, R. H. J., Rokoš, O., and Geers, M. G. D., 2019, "Correction of Scanning Electron Microscope Imaging Artifacts in a Novel Digital Image Correlation Framework," Exp Mech, **59**(4), pp. 489–516.

[109] Tasan, C. C., Hoefnagels, J. P. M., Diehl, M., Yan, D., Roters, F., and Raabe, D., 2014, "Strain Localization and Damage in Dual Phase Steels Investigated by Coupled In-Situ Deformation Experiments and Crystal Plasticity Simulations," International Journal of Plasticity, **63**, pp. 198–210.

[110] Zhao, Z., Ramesh, M., Raabe, D., Cuitiño, A. M., and Radovitzky, R., 2008, "Investigation of Three-Dimensional Aspects of Grain-Scale Plastic Surface Deformation of an Aluminum Oligocrystal," International Journal of Plasticity, **24**(12), pp. 2278–2297.

[111] Merzouki, T., Collard, C., Bourgeois, N., Ben Zineb, T., and Meraghni, F., 2010, "Coupling between Measured Kinematic Fields and Multicrystal SMA Finite Element Calculations," Mechanics of Materials, **42**(1), pp. 72–95.

[112] Pataky, G. J., and Sehitoglu, H., 2015, "Experimental Methodology for Studying Strain Heterogeneity with Microstructural Data from High Temperature Deformation," Exp Mech, **55**(1), pp. 53–63.

[113] Bumgardner, C., Croom, B., and Li, X., 2017, "High-Temperature Delamination Mechanisms of Thermal Barrier Coatings: In-Situ Digital Image Correlation and Finite Element Analyses," Acta Materialia, **128**, pp. 54–63.

[114] Carroll, J., Abuzaid, W., Lambros, J., and Sehitoglu, H., 2010, "An Experimental Methodology to Relate Local Strain to Microstructural Texture," Review of Scientific Instruments, **81**(8), p. 083703.

[115] Abuzaid, W., and Patriarca, L., 2020, "A Study on Slip Activation for a Coarse-Grained and Single Crystalline CoCrNi Medium Entropy Alloy," Intermetallics, **117**, p. 106682.

[116] Chen, Z., Lenthe, W., Stinville, J. C., Echlin, M., Pollock, T. M., and Daly, S., 2018, "High-Resolution Deformation Mapping Across Large Fields of View Using Scanning Electron Microscopy and Digital Image Correlation," Exp Mech, **58**(9), pp. 1407–1421.

[117] Stinville, J. C., Echlin, M. P., Texier, D., Bridier, F., Bocher, P., and Pollock, T. M., 2016, "Sub-Grain Scale Digital Image Correlation by Electron Microscopy for Polycrystalline Materials during Elastic and Plastic Deformation," Exp Mech, **56**(2), pp. 197–216.

[118] Jain, D., 2005, "Superresolution Using Papoulis-Gerchberg Algorithm," EE392J-Digital Video Processing, Stanford University.

[119] Gerchberg, R. W., 1974, "Super-Resolution through Error Energy Reduction," Optica Acta: International Journal of Optics, **21**(9), pp. 709–720.

[120] Vandewalle, P., Süsstrunk, S., and Vetterli, M., 2006, "A Frequency Domain Approach to Registration of Aliased Images with Application to Super-Resolution," EURASIP J. Adv. Signal Process., **2006**(1), p. 071459.

[121] Keren, D., Peleg, S., and Brada, R., 1988, "Image Sequence Enhancement Using Sub-Pixel Displacements," Proceedings CVPR '88: The Computer Society Conference on Computer Vision and Pattern Recognition, pp. 742–746.

[122] Gluckman, J., 2003, "Gradient Field Distributions for the Registration of Images," *Proceedings 2003 International Conference on Image Processing (Cat. No.03CH37429)*, p. II–691.

[123] Irani, M., and Peleg, S., 1990, "Super Resolution from Image Sequences," *10th International Conference on Pattern Recognition [1990] Proceedings*, pp. 115–120 vol.2.

[124] Zomet, A., Rav-Acha, A., and Peleg, S., 2001, "Robust Super-Resolution," *Proceedings of the 2001 IEEE Computer Society Conference on Computer Vision and Pattern Recognition. CVPR 2001*, p. I–I.

[125] Pham, T. Q., van Vliet, L. J., and Schutte, K., 2006, "Robust Fusion of Irregularly Sampled Data Using Adaptive Normalized Convolution," EURASIP J. Adv. Signal Process., **2006**(1), p. 083268.

[126] Agard, D. A., Steinberg, R. A., and Stroud, R. M., 1981, "Quantitative Analysis of Electrophoretograms: A Mathematical Approach to Super-Resolution," Analytical Biochemistry, **111**(2), pp. 257–268.

[127] Zhang, Y., Wu, Y., Zhang, Y., and Ozcan, A., 2016, "Color Calibration and Fusion of Lens-Free and Mobile-Phone Microscopy Images for High-Resolution and Accurate Color Reproduction," Scientific Reports, **6**(1), pp. 1–14.

[128] Wronski, B., Garcia-Dorado, I., Ernst, M., Kelly, D., Krainin, M., Liang, C.-K., Levoy, M., and Milanfar, P., 2019, "Handheld Multi-Frame Super-Resolution," ACM Trans. Graph., **38**(4), p. 28:1-28:18.

[129] Fienup, J. R., 1980, "Iterative Method Applied To Image Reconstruction And To Computer-Generated Holograms," OE, **19**(3), p. 193297.

[130] Stelzer, E. H. K., 2002, “Beyond the Diffraction Limit?,” Nature, **417**(6891), pp. 806–807.

[131] Rivera-Ortega, U., and Pico-Gonzalez, B., 2015, “Wavelength Estimation by Using the Airy Disk from a Diffraction Pattern with Didactic Purposes,” Phys. Educ., **51**(1), p. 015012.

[132] Choi, Y., Yang, T. D., Fang-Yen, C., Kang, P., Lee, K. J., Dasari, R. R., Feld, M. S., and Choi, W., 2011, “Overcoming the Diffraction Limit Using Multiple Light Scattering in a Highly Disordered Medium,” Phys. Rev. Lett., **107**(2), p. 023902.

[133] Chen, S., and Moitra, A., 2021, “Algorithmic Foundations for the Diffraction Limit,” *Proceedings of the 53rd Annual ACM SIGACT Symposium on Theory of Computing*, Association for Computing Machinery, New York, NY, USA, pp. 490–503.

[134] Nagahara, H., Kuthirummal, S., Zhou, C., and Nayar, S. K., 2008, “Flexible Depth of Field Photography,” *Computer Vision – ECCV 2008*, D. Forsyth, P. Torr, and A. Zisserman, eds., Springer, Berlin, Heidelberg, pp. 60–73.

[135] Correlated Solutions, 2018, “Vic-3D 8: Testing Guide.”

[136] Liu, Y.-Q., Du, X., Shen, H.-L., and Chen, S.-J., 2021, “Estimating Generalized Gaussian Blur Kernels for Out-of-Focus Image Deblurring,” IEEE Transactions on Circuits and Systems for Video Technology, **31**(3), pp. 829–843.

CHAPTER 2
A HIGH MAGNIFICATION UV LENS FOR HIGH TEMPERATURE OPTICAL STRAIN MEASUREMENTS

2.1. Prologue

This chapter contains a full-length paper which was published in the peer-reviewed journal *Review of Scientific Instruments* in April 2019, under the title "A High Magnification UV Lens for High Temperature Optical Strain Measurements." The author list is Robert S. Hansen, Trevor J. Bird, Ren Voie, Katharine Z. Burn, and Ryan B. Berke. The experiments were conducted and data collected at Utah State University, Logan, UT. The entire published paper is given below.

2.2. Abstract

Digital Image Correlation (DIC) measures full-field strains by tracking displacements of a specimen using images taken before and after deformation. At high temperatures, materials emit light in the form of blackbody radiation, which can interfere with DIC images. To screen out that light, DIC has been recently adapted by using ultraviolet (UV) range cameras, lenses, and filters. Before now, UV-DIC had been demonstrated at the centimeter scale using commercially available UV lenses and filters. Commercial high-magnification lenses using visible light have also been used for DIC. However, there is currently no commercially available high-magnification lens that will allow images to be taken (a) in the UV range, (b) at a sub-millimeter scale, and (c) from a relatively long working distance separating a specimen inside a test chamber and a camera outside the chamber. In this work, a custom UV high-magnification lens is demonstrated to perform high-magnification, high-temperature DIC measurements.

To demonstrate the capabilities of this lens, a series of thermo-mechanical tests was run on a stainless-steel ring specimen. Two UV cameras performed simultaneous measurements: one at lower magnification using a commercial UV lens, and one with the custom high-magnification UV lens. At room temperature, the custom lens produces sufficiently bright images to perform DIC, while at high temperature (demonstrated to 900°C) the images retained sufficient contrast while avoiding oversaturation. The lens can detect sub-millimeter rigid motion and tensile strains from long working distances and high magnification. These tests show that the custom lens is suitable for use in high-magnification UV-DIC measurements.

2.3. Introduction

Digital Image Correlation (DIC) is a non-contact method used to produce full-field displacement and strain measurements of a specimen surface. It is a popular strain measurement in a variety of experimental applications because it: (i) is a non-contact measurement[1], (ii) is easily adapted to different length scales[2], and (iii) provides strain distributions across an entire surface rather than a single point[3]. These advantages make DIC an ideal candidate for measuring heterogeneous strain in high-temperature and high-magnification situations. DIC has been demonstrated at a wide variety of length scales, ranging from large scale to microscale[4] and even nanoscale[5], with the use of scanning electron microscopes. Small-scale measurements are especially useful in materials characterization[6], when features such as grains or small platelets and precipitates in a specimen are particularly important[7].

To compute displacements and strains using DIC, images must be taken before and after deformation. There are two main approaches to performing DIC; subset-based local, and finite-element-based global digital image correlation. The local DIC algorithm divides a region of interest into subsets surrounding a single pixel, and tracks the motion of each subset using a

correlation algorithm, resulting in a pointwise displacement field[8]. In contrast, global DIC simultaneously tracks the motion of all pixels within the region of interest, resulting in the measurement of motion of a complete mesh[9]. This mesh allows for convenient comparison or coupling with finite element analysis[10] and ensures that continuity constraints are maintained, leading to more accurate measurements[11]. In both local and global DIC, the derivatives of the calculated displacement fields are used to compute the strains. In this paper, local DIC is used because of advantages of ease of use and computational efficiency[12], and it should be assumed that future uses of the phrase "DIC" refer to the local DIC technique.

For the correlation algorithm to capture the motion, DIC requires a high-contrast speckle pattern on the specimen surface[13]. The size of the speckles in the applied pattern must ensure that each subset has a unique array of grayscale values and pixel arrangements[14]. If the speckle is too small for the length scale of a test, the subset will become a collection of similar-valued pixels. If it is too large, there is a greater risk of an entire subset being dominated by a single speckle, rendering different subsets indistinguishable. Thus, the subset size used in the correlation depends on the speckle pattern applied. A smaller subset and smaller spacing between subsets results in more data points compared with a larger subset, but smaller subsets are also more susceptible to noise which affects the uncertainty in the measurement[15]. Choosing an appropriate subset size has a great impact on the accuracy of the calculated displacements, and the proper subset size will depend on the individual speckle pattern[16].

At extreme temperatures, there are additional challenges to perform DIC. Above 600°C, materials emit Planck radiation within the visible spectrum which can saturate the camera sensor[17]. The emitted light is known to be brighter at longer wavelengths, so taking images primarily with shorter-wavelength blue light sources and filters has been shown to effectively raise the

temperature at which images useful for DIC can be recorded[18]. By eliminating longer wavelengths of light using an optical bandpass filter, the light emitted from the heated specimen does not oversaturate the image captured by the camera. This has been well-demonstrated using blue lights, filters and optics up to temperatures ranging from 1000°C for crack-opening displacement measurements[19] to 1500°C for ceramic composites[20], with other notable work in that temperature range made possible with blue light[21,22].

Evidence suggests that the temperature range can be extended further with the use of ultraviolet (UV) light sources and filters, utilizing even shorter wavelengths[23]. At ta given temperature, UV light is emitted from the specimen at a lower intensity than light with longer wavelengths, including blue. However, this method requires that all lenses transmit light with shorter wavelengths which are allowed to pass through the filter, and that the camera sensor is sensitive to those shorter wavelengths. Additional light sources that provide incident light at the desired wavelength are also necessary. UV-DIC has been demonstrated at the centimeter scale up to at least 1600°C using commercial UV lenses, and can potentially be used even higher on materials with higher melting points[24]. However, there is currently no commercially available high-magnification lens that will allow images to be taken (i) in the UV range, (ii) at a sub-millimeter scale, and (iii) at a long enough working distance for a specimen to be placed inside a testing chamber while the camera is placed outside the chamber window.

In this work, a custom high-magnification UV lens is presented to perform DIC. The lens is demonstrated using a series of thermo-mechanical experiments on a steel ring specimen. A high-temperature test, a rigid body motion test, and a mechanical deformation test were conducted. For each of the three tests, a two-camera set-up was used to compare the custom high-magnification UV lens with a commercially available UV lens.

2.4. Materials and Methods

2.4.1. Custom High-Magnification UV Lens

To extend UV-DIC measurements to the sub-millimeter range, a custom high-magnification UV lens was designed to resolve a 2.2 mm horizontal field of view at a 254 mm working distance. Furthermore, the design was restricted to using off-the-shelf components to reduce costs and allow in-house assembly. To meet the above criteria, an infinity-corrected, telephoto lens with a nominal 3.2 paraxial magnification was designed as follows.

The custom UV lens assembly was designed to be paired with a JAI CM-140GE-UV camera with C-mount type threading. The camera features a 6.4mm sensor with a sensor pixel size of 4.65 μm. When paired with a UV lens, the camera produces images which contain 1392 x 1040 pixels. Thus, when the horizontal field of view of 2.2 mm, each pixel represents an area roughly 1.60 μm square. The assembly can be paired with a UV band-pass filter from LDP LLC and a pair of external UV light sources with a peak wavelength of 365 nm. This pairing of equipment has been demonstrated in previous experiments to successfully perform UV-DIC[23].

The lens was designed with the commercial software package OpticStudio, developed by Zemax LLC for designing and characterizing optical assemblies. A ray diagram of the lens is shown in Figure 2.1(a). The entire assembly was built in-house using off-the-shelf components, which were bought primarily from Edmund Optics and ThorLabs Inc., including 13 singlet lenses. The lenses can be separated into three functional groups: a translating focus group, a stationary magnification group, and a stationary master group, seen in the cross section of the assembly, shown in Figure 2.1(b).

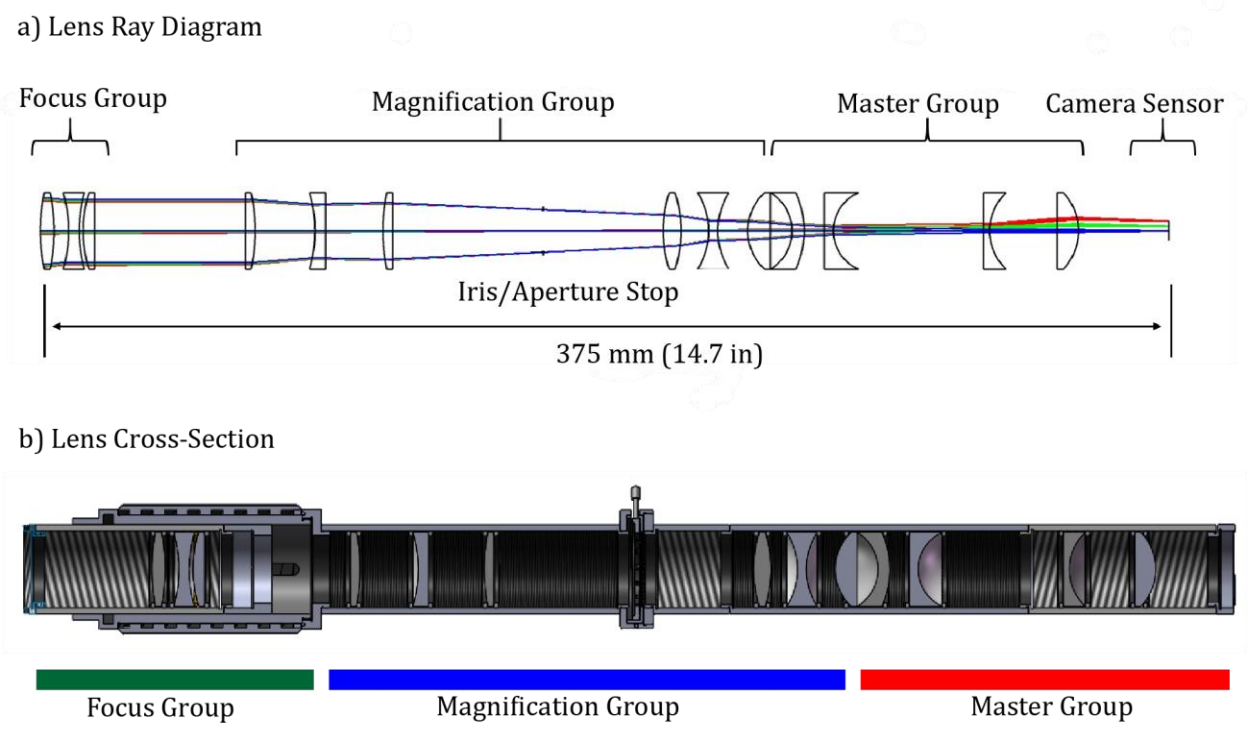

Figure 2.1: ***(a)*** *Ray diagram of the 13 lenses used in the assembly, with the three lens groups indicated.* ***(b)*** *Cross-sectional view of the custom UV lens assembly and group subassemblies*

The focus group consists of three lenses (LB5247-E, LD4293-UV, and LA5817-E, from ThorLabs) having an effective focal length equivalent to the desired working distance, collecting light as it enters the assembly and collimating it to be used by the magnification group[25,26]. These lenses are placed in a telescoping lens tube (SM1NR1, ThorLabs) This technique is used in infinity-corrected microscopes and allows fine focal point adjustments to be made after positioning the camera.

The magnification group receives the collimated light from the focus group and extends the focal point to the master group[27], magnifying the image by a factor of 3.2X. The group of lenses (two of LA5012-E, and one each of LC4888-UV, LB5284-E, LD4931-UV, and LA5370-E from ThorLabs) is placed in a static housing (parts SM1L40 and SM1L10, ThorLabs) resulting in

a fixed magnification power. An adjustable iris (SM1D25, ThorLabs) is used to change the effective f-number of the system, thereby adjusting the diffraction limit, spot size, and depth of field[28]. The diameter of the selected iris ranges from 5-20 mm.

The purpose of the master group is to receive light from the magnification group to correct aberrations[27] and transmit the image to the camera sensor. The group is designed as a telephoto-lens system, shortening the effective focal length of the assembly, and consists of four lenses (LF5895-E, LC4252-UV, LC5269-E, and LA4306-UV, ThorLabs). This allows closer placement of the camera sensor to the lenses. The master group is placed in another static housing (SM1L40 and modified part SM1L25-MOD of depth 58.01 mm), separate from the magnification group, and features a C-mount adapter (SM1A975, ThorLabs) to connect the overall assembly to the camera. Additional information on parts used and assembly are referenced in the supplementary material section.

In order to reduce chromatic aberrations, the lenses used throughout the assembly alternate between calcium fluoride and fused silica, both of which are known to be good transmitters of UV light, with a transmittance between 0.7 and 0.9 through most of the ultraviolet range[29]. The assembly is fully color-corrected for wavelengths between 270 to 400 nm. Due to the relatively large number of lenses in the assembly, the overall transmissivity is 58% at the 365nm wavelength, which corresponds to the peak wavelength of the external light sources.

The entire assembly has an overall working distance of 254 mm, allowing the camera and lens to be placed safely outside an environmental chamber while focusing through a window to a test specimen inside. This is critical for use with the intended high-temperature testing. When focused at such a distance, the camera and lens have a field of view of about 2.2 x 1.7 mm. To evaluate the above design, the camera and lens were aimed at a USAF 1951 test target and a series

of Ronchi rulings. The maximum resolution was found to resolve to between 101.6 and 110 line pairs per mm.

2.4.2. Thermo-Mechanical Experiments

Three thermo-mechanical experiments were performed: (i) a rigid body motion test to compare DIC measurements made with the custom lens with known displacements, (ii) a thermal test to capture high-temperature images, and (iii) a mechanical deformation test to demonstrate the ability for the custom lens to measure strain.

In each demonstration of the designed lens, the specimen used was a T-316 stainless steel ring, approximately 12.7 mm in diameter, 3 mm in width, and with a wall thickness of 1.2 mm, similar to the dimensions of some LWR zirconium fuel cladding testing samples. The high-magnification lens, focused on a single section of the thickness of the ring, was used to capture images at the same time as a camera with a commercially available, low-magnification lens, which captured images of the entire ring. The low-magnification lens used was a UKA Optics UV5035B 50 mm focal-length lens from Universe Kogaku America. This two-camera setup, used in all three phases of testing, allows for direct comparison of the custom high-magnification lens with its commercially available low-magnification counterpart.

A high-contrast pattern was applied to the top surface of the ring with VHT spray-paint, which is rated for temperatures up to 1090 °C and is commonly used to perform high-temperature DIC[30]. The black speckles were applied with an airbrush by making a fine mist of slightly thinned paint above the surface, letting the mist droplets settle onto the white surface. This resulted in a very small, high-contrast, black-speckle pattern on a white background appropriate for both the

larger and the smaller field of view. The speckle size varied, but the smallest speckles were roughly 10-20 µm across as shown in Figure 2.2.

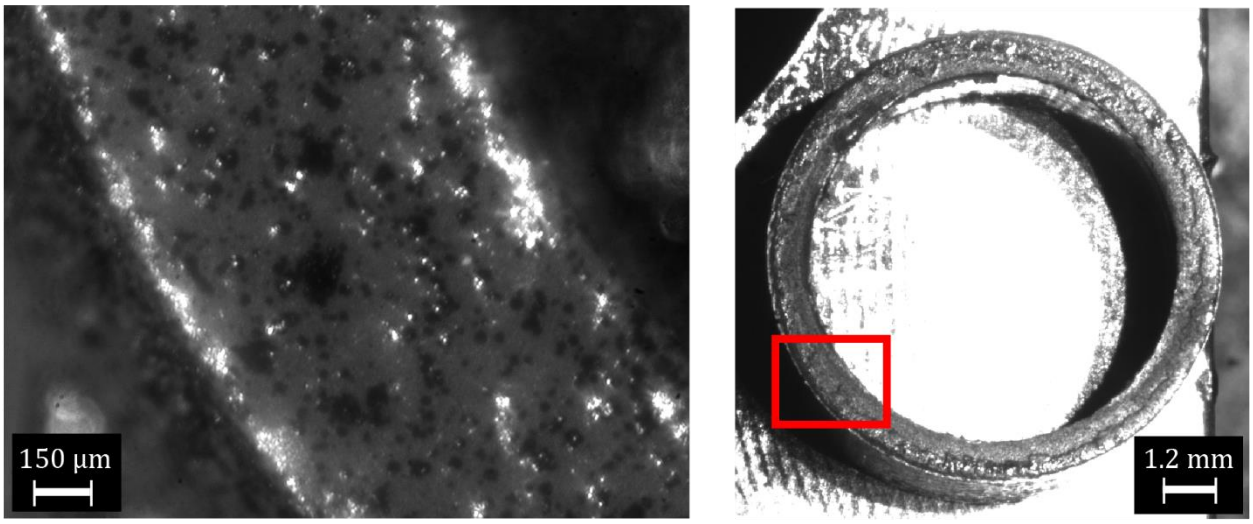

*Figure 2.2: Sample Speckle Pattern, taken with high-magnification lens (**left**) and low-magnification lens (**right**). The high-magnification image has been brightened for legibility by multiplying pixel values by a uniform factor of 2 using MATLAB.*

2.4.2.1. Rigid Body Motion Test

The specimen was mounted to a micrometer-driven stage made by Thor Labs Inc. The stage applied rigid translations in 0.0254 mm intervals in both the vertical and horizontal directions. The stage and camera assembly were rigidly fixed to an optical table, to minimize any relative displacement between the specimen and the cameras, aside from the applied displacements. The cameras were positioned to be perpendicular to the stage so the translations applied to the specimen would result in predominantly in-plane motion. The custom lens was placed 254mm away from the specimen and the 50 mm lens was placed 330 mm away. The rigid body motion experimental setup is shown in Figure 2.3.

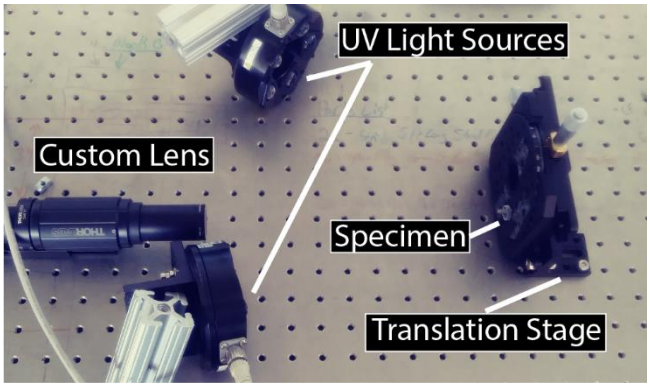

*Figure 2.3: Rigid Body Motion Experimental Setup with lenses (**left**), UV external light sources (top center, bottom center), and translating stage with specimen (**right**)*

Reference images of the specimen surface were collected with the high-magnification lens and camera prior to any motion. Displacements were then applied in both the positive and negative horizontal directions at 8 regular increments, resulting in displacements ranging from -0.203 to 0.203mm, relative to the position of the reference image. Images were taken after each translation. Motion was small to ensure that the region of interest for the custom lens remained in the field of view in all images. The process was then repeated for the vertical direction with the same camera. The low-magnification lens and camera then replaced the other lens and camera at the position perpendicular to the specimen, and the same method was followed to capture the horizontal and then vertical translations.

2.4.2.2. Thermal Test

For the thermal test, the specimen was tested in a temperature-controlled load frame chamber, the Gleeble 1500D, shown in Figure 2.4(a). The system consists of a load frame and resistive heater inside an environmental test chamber, which can support air, vacuum, or inert gas

environments. The chamber features a borosilicate glass window, allowing images to be taken for DIC. Specimens are heated by passing an electrical current through the water-cooled grips to an electrically conductive specimen, reaching the desired temperature via joule heating. Temperatures of at least 1600 °C have been achieved with the Gleeble to demonstrate DIC[24], and the machine is rated for use to 3000 °C. For these thermal and mechanical tests, the ring specimen was placed in custom grips located within the environmental chamber, shown in detail through the chamber window in Figure 2.4(b).

The custom lens had the aperture opened as wide as possible to allow enough light in the image, so the adjustable iris diameter was 20 mm. The UKA 50 mm lens had the aperture opened to give an effective f-number of 16. The front of the custom lens was placed 254 mm away from the specimen and the front of the 50 mm lens was placed 330 mm away from the specimen. Each of the cameras and the UV light source were mounted using aluminum T-slot frames and were arranged so that the cameras were perpendicular to the specimen surface. The optical system, mounted on top of the chamber window, is shown in Figure 2.4(c).

The specimen was supported by a pair of hooked grips, made from T-303 stainless-steel rods with a diameter of 10 mm, shown in Figure 2.4(d). One end of the grip is threaded (labeled A in the figure) to accommodate a backing nut which is pulled to apply tension. The hook features a flat surface (labeled B) on which the specimen rests. At the right end of the grip is a semicircle-shaped hook (labeled C), which goes on the inside of the ring. Each grip is fastened into the Gleeble and the ring is placed over the two semicircles. Once loading begins, the inside face of the ring comes into contact with the curved face of the semicircle hook (C), and the bottom face of the ring remains in contact with the flat face of the grip (B). The radius of curvature of the semicircle hook is slightly smaller than the inner radius of the ring, meaning that initially the two surfaces will

contact only at one line on the circumference of the ring. The ring is then pre-loaded to 1.5 kN, which causes the ring to become non-circular as some deformation occurs and the ring begins to appear oblong. This is necessary for the specimen to fit the shape of the hook, increasing the contact area through which electrical current is applied for heating and preventing electrical arcing.

Before the thermal test, K-type thermocouples were welded to the outside of the ring specimen, centered between both the top and bottom surfaces, to provide temperature feedback to the thermal control system of the Gleeble. The specimen was oriented so the top flat surface of the ring was parallel to the camera. Reference images were taken after pre-loading but prior to heating. A thermal load was then gradually applied, raising the temperature to 900 °C by increments of 50 °C every two minutes. At each increment, each of the cameras took an image. The grips were moved as the specimen was heated to allow for movement due to thermal expansion without losing electrical contact, while keeping the load at or below 1.5 kN to avoid excessive permanent deformation. It should be noted that as temperatures increased, the ring slowly continued to deform and elongate as the load necessary for electrical contact was maintained. Upon completion of the test, the temperature was decreased to room temperature, the load was released, and the specimen was removed.

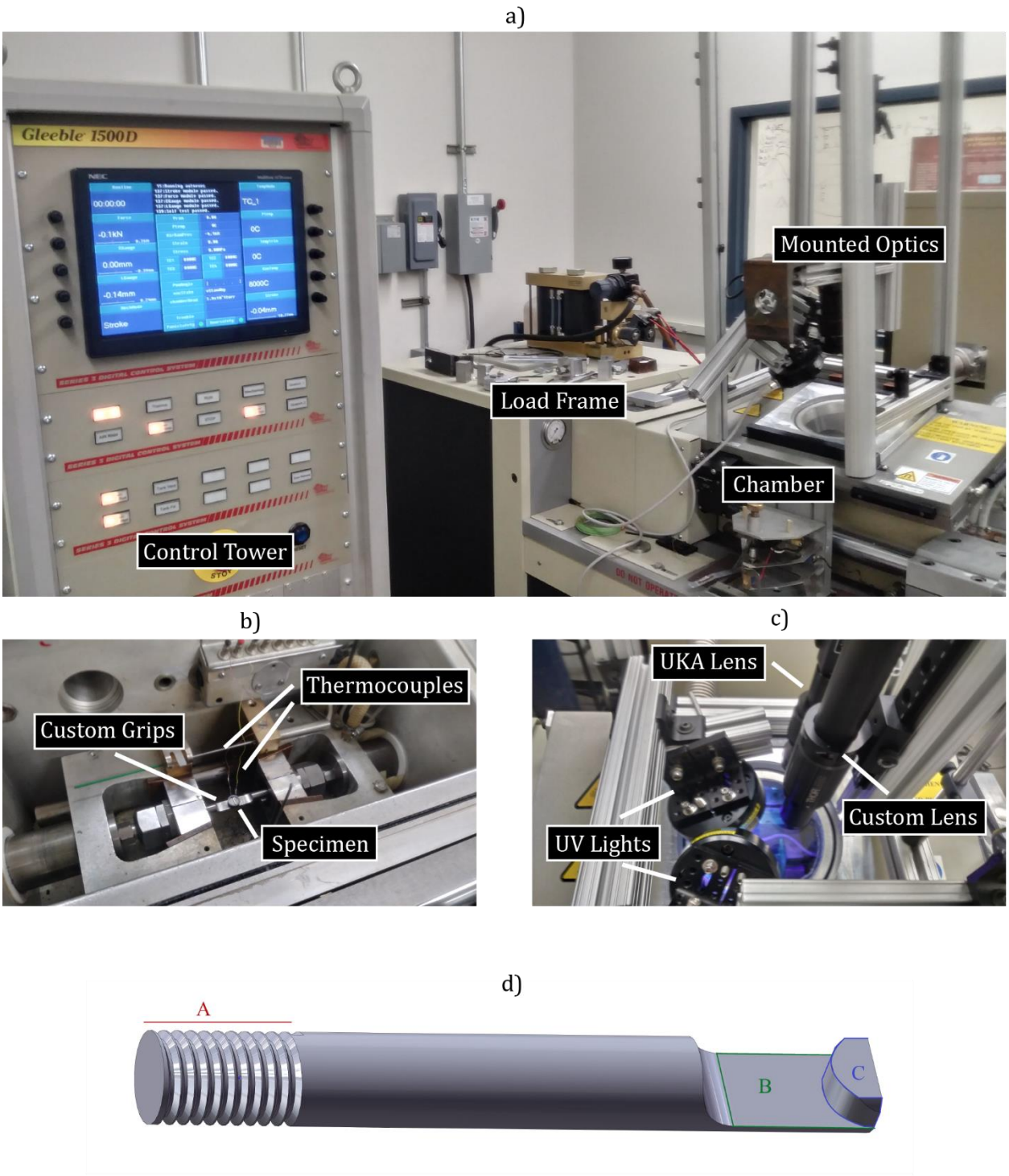

*Figure 2.4: (**a**) Gleeble 1500 D control tower, load frame and testing chamber, and mounted cameras and light source; (**b**) Ring specimen with K-type thermocouples loaded into custom hooked grips in the Gleeble 1500D standard specimen grips; (**c**) Mounted optics, with UKA*

*Optics 50 mm lens and camera, top middle, custom lens, middle right, and UV light source, bottom left, over the environmental chamber viewing window; (**d**) Diagram of custom hooked grip with A) Threaded End, B) Flat Ring Resting Surface, C) Semicircle Grip*

2.4.2.3. Mechanical Deformation Test

The specimen was loaded in the same grips and with the same method as described in the thermal test. The camera arrangements and orientations were also similar, although the aperture was reduced from a diameter of 20 mm to 10 mm to improve depth of field, and a second UV light source was used to compensate for the reduced light transmission through the smaller aperture.

The specimen was deformed in displacement control while monitoring the resulting load reported by the load frame. A preload of 0.9 kN was applied before any images were taken. This preload allowed the ring to become seated on the grips, ensuring contact between the grips and the ring to prevent slipping or translation during further loading. A reference image of the specimen was taken at the initial preloaded position using both the camera with the high-magnification lens, and the camera with the commercial lens. The displacement gauge was then zeroed, and the grips were moved apart under displacement control at increments of 0.02-0.05 mm (smallest increment of displacement between grips) until a maximum displacement of 0.34 mm. Subsequent images were captured with both cameras at each interval as the specimen was deformed. After reaching 0.34 mm grip displacement and capturing both images, the specimen was unloaded. Final images were taken of the unloaded specimen.

For comparison purposes, a finite element analysis was used to model the non-uniform deformation experienced by the ring specimen. The model was performed using FEMAP, a commercial finite element package from Siemens Corporation. Models of the ring and a simplified

grip (a semicircle pin of the same radius as the semicircle grip used in the experiments) were produced, using quarter symmetry to simplify the analysis. The ring and grip were both meshed using solid hex elements. Contact between the ring and grip was modeled using FEMAP's built-in contact algorithms, and the load conditions were set to simulate those present in one of the images. NX Nastran advanced nonlinear static analysis was used and strains in the direction of loading were displayed on the contour of the deformed specimen. These strain contours serve as a coarse validation of strain distributions measured through DIC.

2.4.2.4. Image processing

DIC was performed on the images from the rigid body motion and mechanical deformation tests to determine the full-field displacements. The reference and displaced images were imported in VIC-2D, a commercial DIC software package by Correlated Solutions, LLC and then correlated. Several different subsets and step sizes were explored, ranging from subsets of 25 pixels to 57 pixels for the custom lens and 7 to 25 pixels for the commercial lens. Of the sizes explored, the combinations which produced the best spatial resolution and fewest dropped subsets are summarized in Table 2.1. The VIC-2D software was also used to compute the full-field strains from the resulting displacements, using Lagrangian strain formulations.

Table 2.1: Subset and Step Sizes used in VIC-2D

Lens	Test Type	Subset Size	Step Size
Custom Lens	Rigid Body Motion	31 pixels	12 pixels
	Mechanical Deformation	31 pixels	12 pixels
Commercial Lens	Rigid Body Motion	11 pixels	5 pixels

	Mechanical Deformation	11 pixels	5 pixels

2.5. Results

2.5.1. Rigid Body Motion Test Results

The vertical and horizontal displacement results were compared with the known applied displacements. Figure 2.5(a) shows the horizontal applied displacements and averages of the measured displacements of the subsets in each high-magnification picture and each low-magnification picture. A similar plot for vertical displacements is shown in Figure 2.5(b).

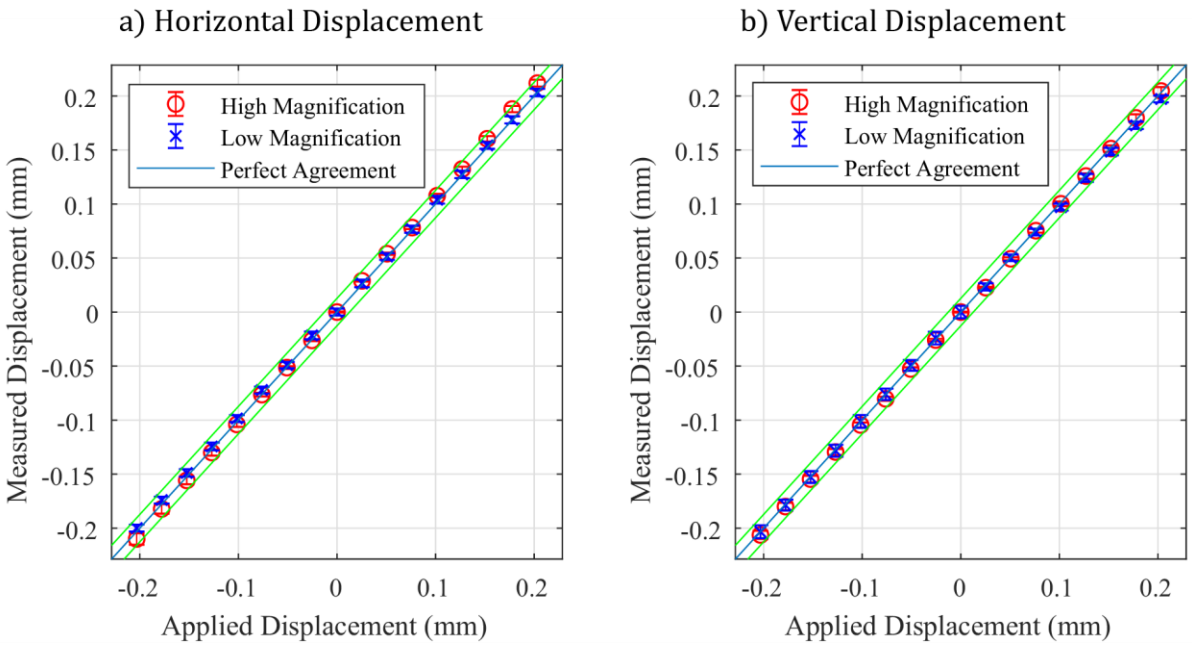

*Figure 2.5: Horizontal (**a**) and Vertical (**b**) Applied Displacement for High- and Low-Magnification Images*

Both plots include a light blue line at a 45-degree angle, representing perfect agreement between applied and measured displacements. Uncertainty bands represent twice the standard

deviation of the measured displacements across all subsets of the image. The noise floor, defined here as the variation between static images due to random noise, is represented by the uncertainty bands at zero displacement, with values of 0.48 µm for high magnification and 3.20 µm for low magnification. The green bounding lines above and below the blue line are the measurement resolution uncertainty of the translation stage, indicating half a tick mark on the physical scale. The low-magnification images gave data comparable to the high-magnification images – for both, the reported displacements are very close to the applied displacements represented by the blue line, and are within the green resolution uncertainty bounding lines.

A contour for the vertical displacement of the low-magnification image is shown in Figure 6(a), while a contour of the high-magnification image at the same displacement is given in Figure 2.6(b). It can be noted from the colored scale bars that both cover similar displacements. This suggests that the commercial lens and custom lens were both able to detect small displacements with similar success.

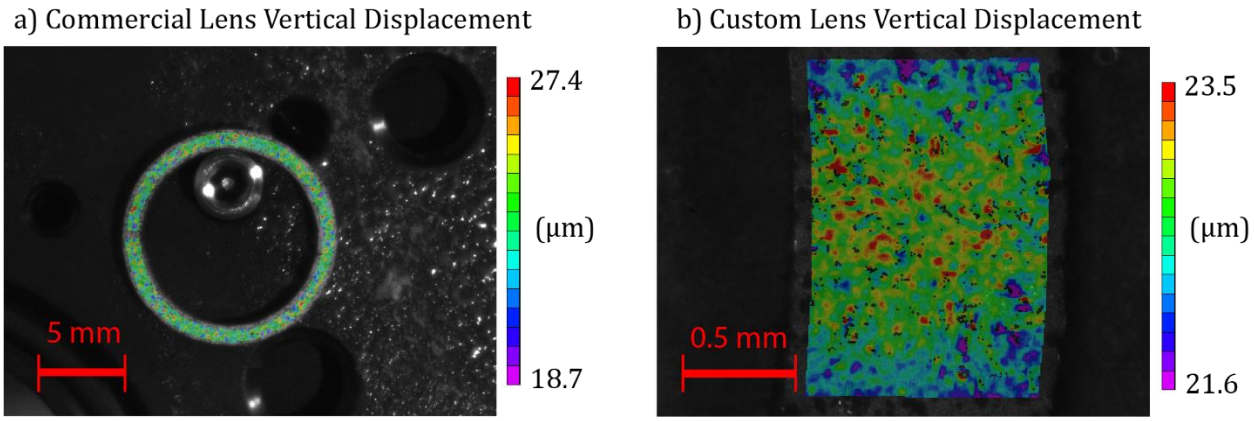

Figure 2.6: Vertical Displacement Contour for (a) Low-Magnification Image, subset of 11 pixels, and (b) High-Magnification Image, subset of 31 pixels

2.5.2. Thermal Test Results

Images were successfully captured at 50 °C increments using 3 cases: a) the commercial 50mm lens without a UV bandpass filter, b) the commercial lens in conjunction with the filter, and c) the custom lens which includes a built-in filter. Figure 2.7 shows the results for 50 °C, 500 °C, 800 °C and 900 °C, respectively, for each of these cases. Note that the custom lens is focused on the region of the ring marked by the red box in both of the commercial lens images at 50°C. For clarity in this paper, the high-magnification images in Figure 2.7(c) have been artificially brightened by multiplying each pixel value by a uniform factor of 2.5 using MATLAB. However, the actual images used for processing in the DIC software were not brightened. As temperatures increase, significant glowing can be seen in the unfiltered, low-magnification images while only slight, uniform changes appear in both of the other sets of images (b and c).

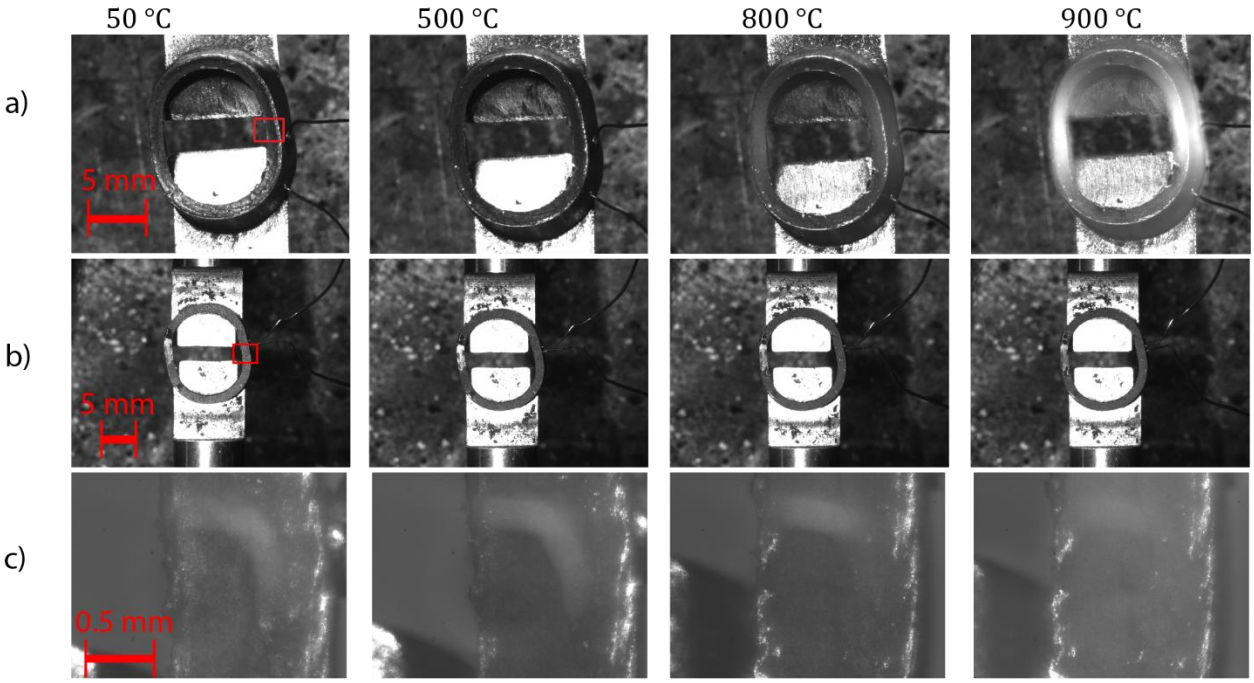

Figure 2.7: Low-Magnification without a UV bandpass filter (a), with a bandpass filter (b), and High-Magnification (c) images at 50 °C to 900 °C. Red box shows placement of high-magnification image.

2.5.3. Mechanical Deformation Test Results

The images of deformed states were produced by both lenses and imported into the DIC software as described previously. Contours showing full-field normal strain in the direction of loading at a representative load about midway through the test are shown in Figure 2.8. Part (a) is the commercial lens contour; part (b) is the portion of the DIC contour in (a), artificially zoomed to be the size of the custom lens image; and part (c) is the custom lens contour. The noise floor for this strain measurement, interpreted as two standard deviations of the strain variation between repeated static images (similar to the noise floor described earlier with the rigid body motion), was 0.00078 for high magnification and 0.00153 for low magnification.

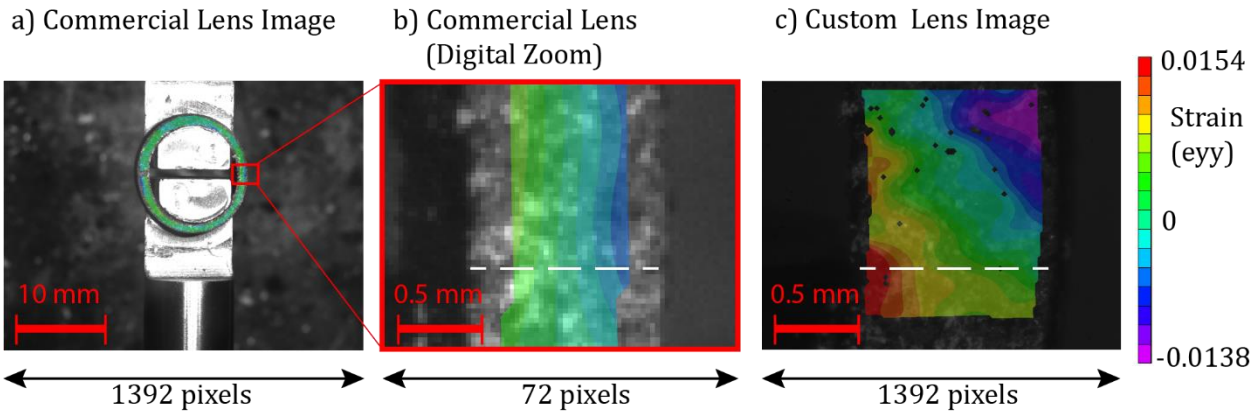

*Figure 2.8: Lagrangian full-field strain at 0.17mm grip displacement (1.2 kN load) for (**a**) commercial lens (subset 11, step size 3), (b) zoomed in perspective of commercial image in (a), and (**c**) custom lens (subset 51, step size 12). A white dotted line shows the location where data in Figure 2.9 is sampled from both images.*

Both the high-magnification and low-magnification contours showed the greatest positive strain values at the inside edge of the ring, and the greatest negative strain values at the outer edge of the ring. This be seen in Figure 2.9, where the strain in the direction of loading is shown as a

function of distance from the inside edge of the ring along a horizontal midline. The midline is placed at the same vertical location on the ring for both the high-magnification and low-magnification images. Note that because VIC-2D contours plot their data at the centers of subsets, each contour in Figure 8 appears to be missing about a half-subset's worth of data along the perimeter of the region of interest. Thus, the data in Figure 2.9 does not appear to span all the way to the inner edge of the ring, though the high magnification data is able to span closer to the edge than the low magnification data. However, they differ in the magnitude of those strains, as shown in Figure 2.10. The High-magnification images produced by the custom lens led to consistently higher measured strains at the inside edge compared to the measurements resulting from the low-magnification images produced by the commercial lens.

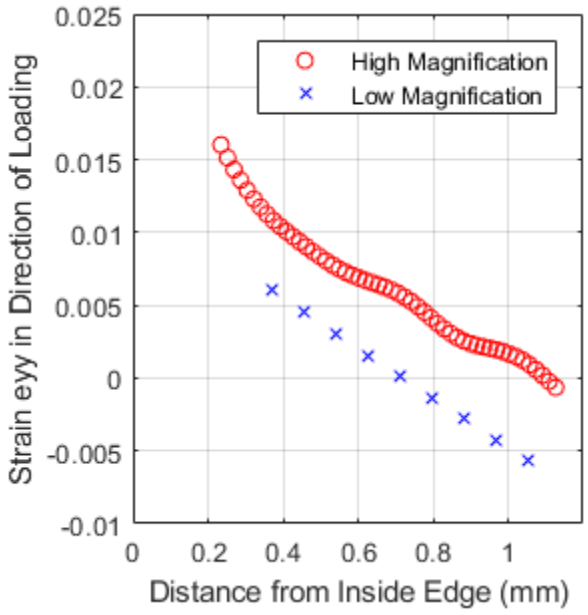

Figure 2.9: Strain eyy through midline of ring as a function of wall thickness position, at grip displacement 0.17 mm

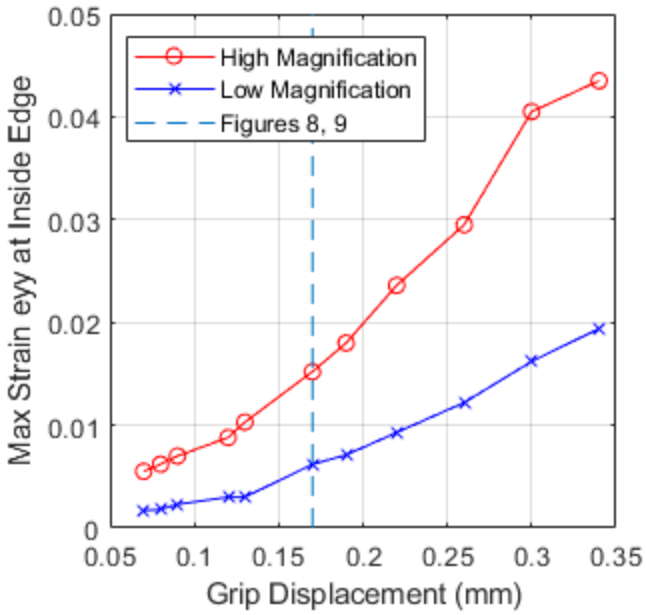

Figure 2.10: Maximum positive strain in direction of loading for high-magnification and low-magnification DIC contours. Dashed line indicates grip dispalcement corresponding with data presented in Figure 2.8 and Figure 2.9.

The FEMAP model of the ring under the same load condition as Figure 2.8 (1.2 kN load, or 0.17 mm grip displacement) is shown in Figure 2.11 in its deformed state, with the contour showing strain in the direction of loading. Both the high-magnification and low-magnification perspectives are shown.

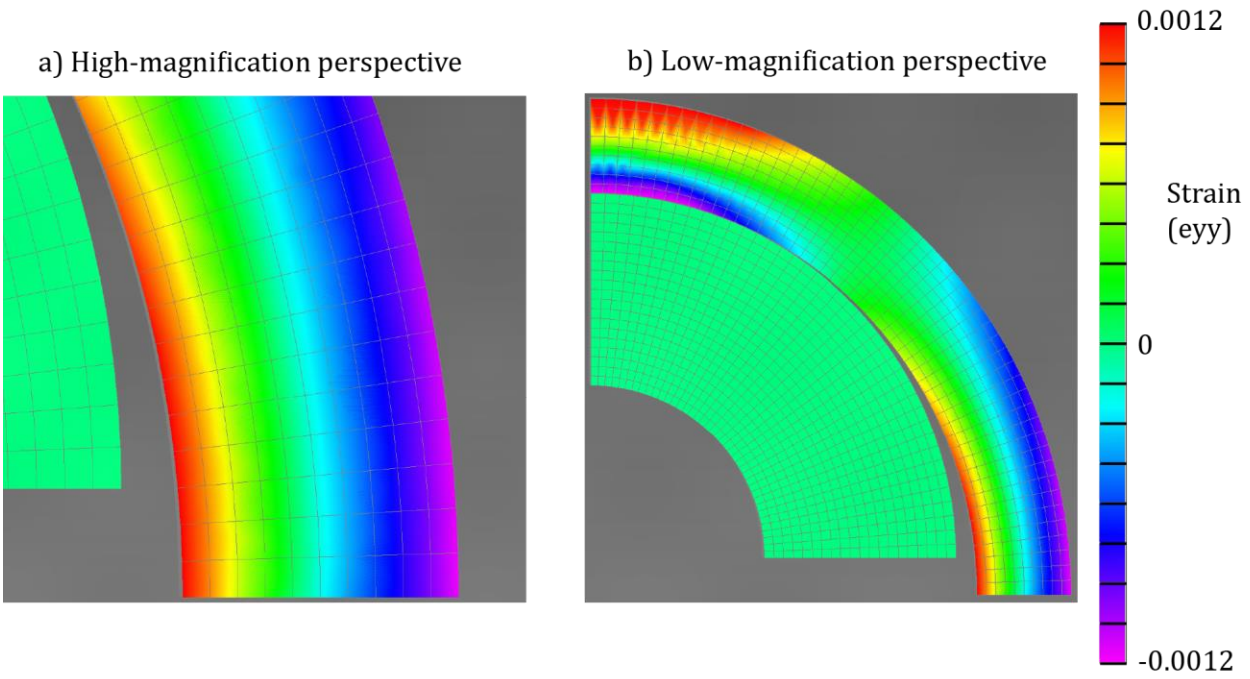

*Figure 2.11: Finite element analysis loading-direction strain (eyy) contours, shown in (**a**) high magnification and (**b**) low magnification perspectives at a load of 1.2 kN (equivalent to 0.17 mm grip displacement). Quarter symmetry has been used to simplify the model.*

2.6. Discussion

The three tests demonstrate three key advantages of the custom lens over commercial UV lenses. First, the rigid body motion test demonstrated the ability to accurately measure a small, known, uniform displacement. Next, the thermal test demonstrated the ability for the custom lens (which includes a built-in UV band-pass filter) to record DIC images at high temperatures, while the unfiltered commercial lens produced saturated images at the same high temperatures. Finally, the deformation test demonstrated the ability to detect heterogeneous strains. Although both lenses agreed generally on the placement of high and low strain, they differ slightly in the degree of symmetry about the midline of the ring, and they differed significantly in terms of magnitude.

The rigid body motion test demonstrates the ability of the custom lens to produce accurate DIC results. Figure 2.5 shows that both lenses closely approach perfect agreement between measured and applied displacements. Inspection of the displacement contours shows that the high-magnification lens produces a smoother contour, that is, the displacement value of a subset is more likely to match its neighbors, when compared with the low-magnification contour. The success of the custom lens is at least partly due to the size and number of subsets that can be correlated. The custom lens allows for an increased number of pixels per mm, which allows for more numerous and larger subsets. Conversely, the commercial lens allows many fewer pixels per mm, which limits both the number of subsets through the ring thickness and their size, leading to potential difficulties in correlation.

The high-temperature test demonstrated the ability of the custom lens to transmit UV light and therefore to avoid oversaturation of the image at temperatures that caused oversaturation in the commercial lens images. Comparing the images in Figure 2.7 shows the difference that the custom lens assembly makes compared to a commercially available lens without a UV filter. At 50°C, the reference images show the speckled surface just above room temperature, where both camera setups produced usable images. At 500°C, the figure shows the specimens at an elevated temperature, but still before glowing occurs. Compared to 50°C, the high-magnification image at 500°C is slightly lighter and the low-magnification image shows some lightening as well. At 800°C, a very faint glow is apparent at the bottom surface of the ring in the low-magnification image. This is where the specimen is beginning to heat up as it approaches a temperature where the visible light will emit with greater intensity. Finally at 900°C, the unfiltered images show very significant saturation in the low-magnification image. The speckle contrast that was previously visible in the image is lost in the glow.

The upper limit of temperatures tested (900°C) was limited by the operating temperatures of the test sample, not the capabilities of the lens. In principle, the lens should be able to record suitable DIC images at much higher temperatures given materials with higher melting points. In fact, UV-DIC has already been demonstrated to at least 1600°C using commercial UV lenses[24], which the custom lens should be equally capable of reaching when paired with sufficiently bright light sources.

The mechanical deformation test showed that the custom lens can be implemented successfully into an experimental setup to detect heterogeneous strain via DIC. The working distance of 254 mm allows tests to be conducted on specimens inside environmental chambers, while the camera sits safely outside of a viewing window.

The mechanical deformation test also demonstrated the usefulness of the custom lens in capturing strain concentrations or features on a smaller scale. The low-magnification strain contour in Figure 2.8 shows that at the inside edge of the ring, there may be a small region of higher positive strain. This is an expected result from the loading of the ring, which would cause a bending moment on the ring, as it acts like a curved beam being straightened. However, this result from the low-magnification is difficult to differentiate from noise in the measurement, and this contour alone may be inconclusive. The high-magnification contour confirms the strain distribution hinted at by the low-magnification measurement and shows a much more detailed strain distribution. Figure 2.8(b) and (c) clearly shows the difference between the low- and high-magnification perspectives of the same area. The high-magnification contour is able to represent the strain field in greater detail, because of the physical size represented by each subset and the increase in number of subsets being used.

The high-magnification strain field also gives a higher value for the maximum strain in the direction of loading in the ring, as seen in Figure 2.10. At each applied displacement where an image was taken, the custom lens produced a peak strain measurement roughly twice that of the measurement produced by the commercial lens. This is expected for two reasons: (i) the higher magnification allows subsets to be used closer to the edge of the ring, and (ii) the higher magnification means each subset covers a smaller area. Because the highest strains occur at the edges of the ring, subsets closer to the edge will better capture the higher strains. In addition, the smaller area of an individual subset results in better spatial resolution. A subset strain value will be 'averaged' across the entire subset, so a larger subset is not able to capture the extreme strain values as well as a smaller subset is able to capture them. These two phenomenon of capturing strains closer to the edge of the ring, and of reducing the spatial averaging of the subset, are clearly shown in Figure 2.9. The high-magnification clearly gets closer to both the inside and outside edges of the ring, and it is able to capture higher strains because of the smaller subset size. This demonstrates the advantage of the high-magnification lens holds in experiments where large spatial strain gradients are expected.

The finite element analysis confirms the strain distribution presented by both the high-magnification and low-magnification DIC results. Simplifying assumptions were made which may contribute to the inaccuracy of the strain magnitudes. However, the location of high positive and negative strains do match the results given by both the low- and high-magnification lens. This provides some confirmation that type of deformation is similar to straightening out a curved beam, resulting in tensile strain on the inside edge and compressive strain on the outside edge. Curved beam theory equations[31] predict a strain in the direction of loading of 0.0098 under the load conditions matching the 0.17mm grip displacement and at the first distance from the edge which

was captured by both high- and low-magnification in Figure 9. This agrees well with the high-magnification measurement at the same location. These combined analyses demonstrate that the custom lens can effectively measure the mechanically induced deformations experienced by the specimen.

One drawback of the custom lens is that it transmits relatively little light. With 13 singlet lenses in the assembly, the transmissivity is low and the resulting images appear less bright. This can be countered in an experiment by opening the aperture, but that can result in a less focused image due to decreased depth of field. Brightness can also be improved by increasing exposure time, but this can also lead to potential blurring of the image if the object is moving[32]. This can be especially difficult in vacuum chambers if the vibration of a vacuum pump imposes relative motion between the camera and a test specimen. Thus, it is important to ensure that sufficient light reaches the specimen when the lens is used, especially in a dark environment such as a testing chamber.

It can be seen in the images taken with the custom lens that a slight ‘ghost ring’ image appears, centered on the middle of the image, as shown against a white paper background in Figure 2.12. Moving the image in and out of focus demonstrated that this aberration is more pronounced when the image is not in focus and is less visible as the focus of the image is improved. The results of the rigid body motion tests show that this does not necessarily interfere with the ability of DIC to measure the deformation. The results of these tests clearly demonstrate that images produced by a camera fitted with the custom lens can accurately measure the displacement of a specimen. When comparing the contour plots with the ghost ring placement in Figure 2.6: Vertical Displacement Contour for (a) Low-Magnification Image, subset of 11 pixels, and (b) High-Magnification Image, subset of 31 pixels, there is no association between the areas where the ring appears and the dropping of subsets in the image due to a poor correlation from the DIC software.

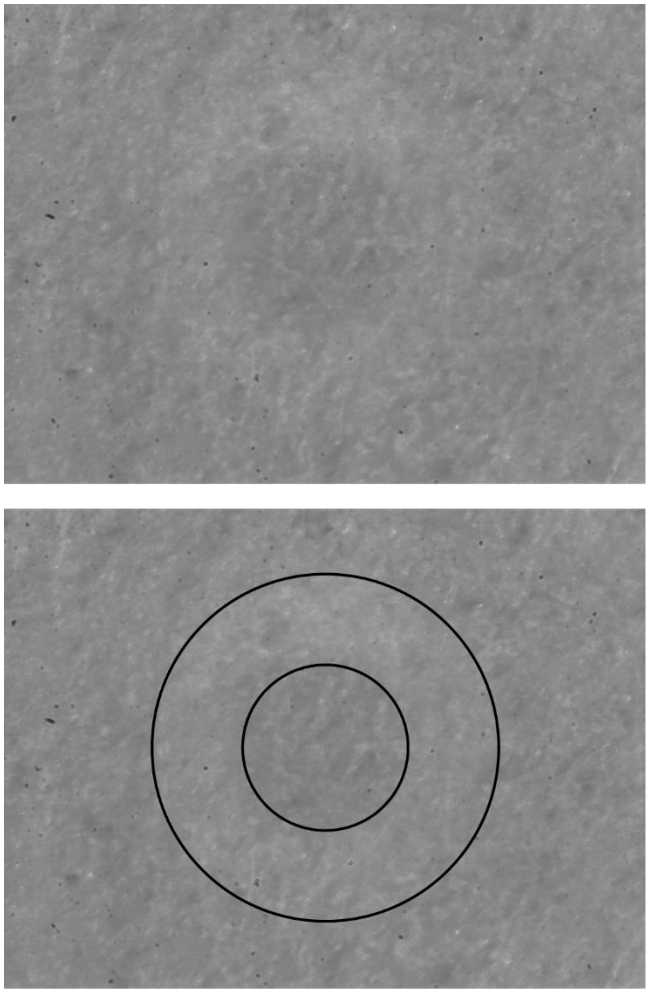

*Figure 2.12: (**top**) Image of a white paper background, obtained using the custom UV lens; (**bottom**) the same image, with dark lines emphasizing the boundary of the ghost ring.*

One of the most impressive capabilities offered by the custom lens is the improvement in the field of view despite a relatively long working distance. This can benefit many potential applications where small features are studied. When a low-magnification lens is used outside the chamber, the entire ring specimen is captured by a field of view 38.7 mm across, yet the majority of the image is not filled by the specimen. The difficulty that arises with this field of view comes from the thickness of the ring being viewed. From a comparable working distance, the field of

view for the camera with the custom lens was 2.2 mm across, allowing the camera to focus on a smaller portion of the ring where higher strain values are present. The result of the custom lens is more displacement data over a smaller region, with each displacement measurement being more reliable when compared with the commercial lens.

Another advantage of the UV lens is that the diffraction limit of light is wavelength-dependent, and thus UV microscopy is known to achieve better resolutions compared to optical microscopy using light with longer wavelengths. Based on a wavelength of 365 nm and a working distance of 254 mm, the Airy disc radius is estimated to be 15.34 μm using software from Zemax. By contrast, blue light has a wavelength closer to 450 nm, and thus its Airy disc is significantly larger. As the new lens has been shown to resolve Ronchi rulings down to 110 line pairs per mm, this means that the new lens can resolve down to the diffraction limit of UV light at its working distance.

More broadly, this lens has potential application in a wide range of fields other than solid mechanics. UV imaging has been used in the analysis of electrical components through detection of corona discharge[33], in-vitro drug release testing[34], and visualization of latent fingerprints in forensic sciences[35]. In addition, the shorter wavelength of UV light allows the detections of small surface features otherwise invisible, such as scratches[36]. The long working distance and high magnification capabilities of this custom lens could easily lend it to use in these or other UV imaging applications, in addition to UV-DIC.

2.7. Conclusions

In summary, a custom UV lens was designed and demonstrated for high-magnification, high-temperature optical strain measurements. The custom lens was shown to meet three criteria: (i) It transmitted light in the UV range while blocking the high-intensity longer wavelengths

through the use of a filter, while a traditional lens and camera without the filter did not; (ii) it was able to produce a field of view that was 2.32 mm across, a significant improvement over commercial UV lenses; and, (iii) it was demonstrated in an experimental setup with a working distance of 254 mm, allowing it to be placed outside an environmental chamber window and to be protected from hazardous conditions.

The custom lens is capable of being used in future work where measurements of strain on a small region of interest, on the order of 2 mm, are desired at high temperatures. This has potential application for material characterization of nuclear materials at accident conditions[37,38], studying microcrack fatigue or stress corrosion cracking[39], or other phenomena on a microscale at high temperatures. It can be beneficially implemented in these conditions to produce accurate, full-field strain and displacement measurements on a small scale.

2.8. Supplementary Material

See supplementary material for complete drawings and bill of materials for the custom lens.

2.9. Acknowledgements

This material is based upon work supported under an Integrated University Program Graduate Fellowship. Any opinions, findings, conclusions or recommendations expressed in this publication are those of the author and do not necessarily reflect the views of the Department of Energy Office of Nuclear Energy.

2.10. References

[1] K.G. Field, M.N. Gussev, X. Hu, Y. Yamamoto, and R.H. Howard, *First Annual Progress Report on Radiation Tolerance of Controlled Fusion Welds in High Temperature Oxidation Resistant FeCrAl Alloys* (Oak Ridge National Lab. (ORNL), Oak Ridge, TN (United States), 2015).

[2] Hild F. and Roux S., Strain **42**, 69 (2006).

[3] M.A. Sutton, J.J. Orteu, and H. Schreier, *Image Correlation for Shape, Motion and Deformation Measurements: Basic Concepts,Theory and Applications* (Springer Science & Business Media, 2009).

[4] T.A. Berfield, J.K. Patel, R.G. Shimmin, P.V. Braun, J. Lambros, and N.R. Sottos, Exp Mech **47**, 51 (2007).

[5] W.A. Scrivens, Y. Luo, M.A. Sutton, S.A. Collette, M.L. Myrick, P. Miney, P.E. Colavita, A.P. Reynolds, and X. Li, Exp Mech **47**, 63 (2007).

[6] F.D. Gioacchino and J.Q. da Fonseca, Exp Mech **53**, 743 (2013).

[7] J.D. Carroll, W. Abuzaid, J. Lambros, and H. Sehitoglu, International Journal of Fatigue **57**, 140 (2013).

[8] Reu Phillip, Experimental Techniques **36**, 3 (2012).

[9] L. Wittevrongel, P. Lava, S.V. Lomov, and D. Debruyne, Experimental Mechanics **55**, 361 (2015).

[10] G. Besnard, F. Hild, and S. Roux, Experimental Mechanics **46**, 789 (2006).

[11] P. Cheng, M.A. Sutton, H.W. Schreier, and S.R. McNeill, 9 (n.d.).

[12] B. Wang and B. Pan, Theoretical and Applied Mechanics Letters **6**, 200 (2016).

[13] T. Hua, H. Xie, S. Wang, Z. Hu, P. Chen, and Q. Zhang, Optics & Laser Technology **43**, 9 (2011).

[14] P. Reu, Experimental Techniques **39**, 1 (2015).

[15] C. Lane, R.L. Burguete, and A. Shterenlikht, 9 (n.d.).

[16] B. Pan, H. Xie, Z. Wang, K. Qian, and Z. Wang, Opt. Express, OE **16**, 7037 (2008).

[17] B. Pan, D. Wu, Z. Wang, and Y. Xia, Meas. Sci. Technol. **22**, 015701 (2011).

[18] P. Bing, X. Hui-min, H. Tao, and A. Asundi, Polymer Testing **28**, 75 (2009).

[19] J. Blaber, B.S. Adair, and A. Antoniou, Review of Scientific Instruments **86**, 035111 (2015).

[20] M.D. Novak and F.W. Zok, Review of Scientific Instruments **82**, 115101 (2011).

[21] B.M.B. Grant, H.J. Stone, P.J. Withers, and M. Preuss, The Journal of Strain Analysis for Engineering Design **44**, 263 (2009).

[22] P. Leplay, O. Lafforgue, and F. Hild, Journal of the American Ceramic Society **98**, 2240 (2015).

[23] R.B. Berke and J. Lambros, Review of Scientific Instruments **85**, 045121 (2014).

[24] T.Q. Thai, R.S. Hansen, A.J. Smith, J. Lambros, and R.B. Berke, Exp Tech (2019).

[25] M. Laikin, *Lens Design* (CRC Press, 2006).

[26] E.B. Burgh, K.H. Nordsieck, H.A. Kobulnicky, T.B. Williams, D. O'Donoghue, M.P. Smith, and J.W. Percival, in *Instrument Design and Performance for Optical/Infrared Ground-Based Telescopes* (International Society for Optics and Photonics, 2003), pp. 1463–1472.

[27] R. Kingslake and R.B. Johnson, *Lens Design Fundamentals* (Academic Press, 2009).

[28] A. Davis and F. Kühnlenz, Optik & Photonik **2**, 52 (2007).

[29] D.C. Harris, Infrared Physics & Technology **39**, 185 (1998).

[30] L. Rossmann, B. Sarley, J. Hernandez, P. Kenesei, J. Almer, J. Wischek, M. Bartsch, A. Köster, V. Maurel, and S. Raghavan, in *2018 AIAA/ASCE/AHS/ASC Structures, Structural Dynamics, and Materials Conference* (American Institute of Aeronautics and Astronautics, n.d.).

[31] A.P. Boresi, *Advanced Mechanics of Materials*, 6 edition (Wiley, New York, 2002).

[32] C. Ma, Z. Liu, L. Tian, Q. Dai, and L. Waller, Optics Letters **40**, 2281 (2015).

[33] E.G. da Costa, T.V. Ferreira, M.G.G. Neri, I.B. Queiroz, and A.D. Germano, IEEE Transactions on Dielectrics and Electrical Insulation **16**, 985 (2009).

[34] J. Østergaard, E. Meng-Lund, S.W. Larsen, C. Larsen, K. Petersson, J. Lenke, and H. Jensen, Pharm Res **27**, 2614 (2010).

[35] A.A. Cantu, in *Optics and Photonics for Counterterrorism and Crime Fighting III* (International Society for Optics and Photonics, 2007), p. 67410D.

[36] M. Hasegawa and T. Shimakura, Journal of Applied Physics **107**, 084107 (2010).

[37] T. Kubo, Y. Kobayashi, and H. Uchikoshi, Journal of Nuclear Materials **435**, 222 (2013).

[38] K.L. Murty and I. Charit, Journal of Nuclear Materials **383**, 189 (2008).

[39] J.A. Duff and T.J. Marrow, Corrosion Science **68**, 34 (2013).

ITEM NO.	QTY.	PART/ASSEMBLY NUMBER	DESCRIPTION
1	1	SM1A39	EXTERNAL C-MOUNT TO SM1 THREAD ADAPTER, THORLABS
2	1	SM1NR1	TELESCOPING LENS TUBE, THORLABS
3	1	SM1D25	SM1 SERIES IRIS DIAPHRAGM, THORLABS
4	1	SM1A975	C-MOUNT TO SM1 ADAPTER, THORLABS
5	1	LB5247-E	CaF2 BI-CONVEX LENS, f = 75.00 mm, DIA = 25.4 mm, BBAR: 3-5 µm, THORLABS
6	1	LD4293-UV	UVFS BI-CONCAVE LENS, UV COATED, DIA = 25.4 mm, f = -50.2 mm, THORLABS
7	1	LA5817-E	CaF2 PLANO-CONVEX LENS, DIA = 25.4 mm, f = 100.0 mm, BBAR: 2-5 µm, THORLABS
8	2	LA5012-E	CaF2 PLANO CONVEX LENS, DIA = 25.4 mm, f = 150.0 mm, BBAR: 3-5 µm, THORLABS
9	1	LC4888-UV	UVFS PLANO-CONCAVE LENS, UV COATED, DIA = 25.4 mm, f = 100.0 mm, THORLABS
10	1	LB5284-E	CaF2 VACUUM UV BI-CONVEX LENS, DIA = 25.4 mm, f = -40.0 mm, BBAR: 3-5 µm, THORLABS
11	1	LD4931-UV	UVFS BI-CONCAVE LENS, UV COATED, DIA = 25.4 mm, f = -25.1 mm, THORLABS
12	1	LA5370-E	CaF2 PLANO-CONVEX LENS, DIA = 25.4 mm, f = 40.0 mm, THORLABS
13	1	LF5895-E	CaF2 BI-CONVEX LENS, DIA = 25.4 mm, f = 75.00 mm, BBAR: 3-5 µm, THORLABS
14	1	LC4252-UV	UVFS PLANO-CONCAVE LENS, UV COATED, DIA = 25.4 mm, f = -30.0 mm, THORLABS
15	1	LC5269-E	CaF2 VACUUM UV PLANO-CONCAVE LENS, DIA = 25.2 mm, f = -40.0 mm, BBAR: 3-5 µm, THORL
16	1	LA4306-UV	UVFS PLANO CONVEX LENS, UV COATED, DIA = 25.4 mm, f = 40.0 mm, THORLABS
17	22	SM1RR	⏱ 1.035-40 RETAINING RING, THORLABS
18	1	SM1S2M-MOD	MODIFIED OPTIC SPACER, 1.21 mm, THORLABS
19	1	SM1L25	SM1 LENS TUBE, 2.500 in DEEP, THORLABS
20	2	SM1L40	SM1 LENS TUBE, 4.00 in DEEP, THORLABS
21	1	SM1L10	SM1 LENS TUBE, 1.00 in DEEP, THORLABS
22	1	SM1L25-MOD	MODIFIED SM1 LENS TUBE, 2.284 in DEEP, THORLABS
23	2	SM1TC	SM1 SERIES TUBE CLAMP, THORLABS
24	2	RC2_M	METRIC EXTENDED RAIL CARRIER, THORLABS
25	1	RLA1200	12 in OPTICAL RAIL, THORLABS

Mechanical & Aerospace ENGINEERING
Utah State University

PROJECT: UV ZOOM LENS

SPECIFICATIONS AND TOLERANCES

UNLESS OTHERWISE NOTED
DRAWING ARE CREATED IN ACCORDANCE TO ASME Y14.5-2009

DEFAULT DIMENSIONAL TOLERANCES:
LINEAR DIMENSIONS (mm) X±.5, X.X±.1, X.XX±.03, X.XXX±.005
ANGULAR DIMENSIONS (degrees) X±.5, X.X±.5, X.XX±.1
MINIMUM SURFACE FINISH: 25 microinches

PART/ASSEM NAME: UV ZOOM LENS	CHECKED BY: TREVOR BIRD
PART/ASSEM NUMBER: UV-A-1	APPROVED BY: RYAN BERKE
MATERIAL: N/A	DATE APPROVED: 4/14/2017
FINISH: N/A	SHEET SCALE: 2:3 SHEET NUMBER: 1 of

DRAFTED BY: BRIAN GRISENTI

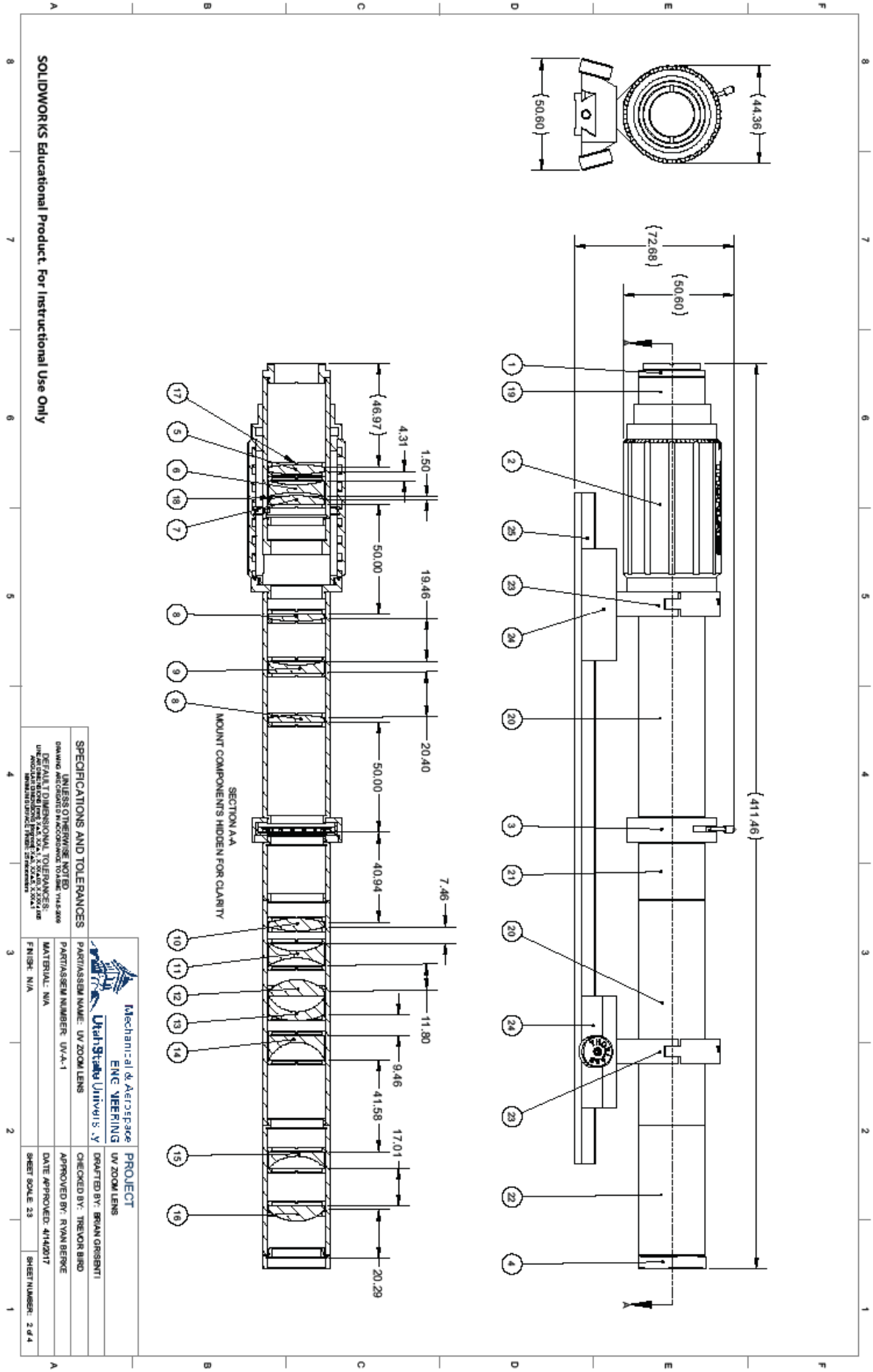
SOLIDWORKS Educational Product. For Instructional Use Only
SECTION A-A
MOUNT COMPONENTS HIDDEN FOR CLARITY
44.36
50.60
72.68
50.60
411.46
46.97
4.31
1.50
50.00
19.46
20.40
50.00
40.94
7.46
11.80
9.46
41.58
17.01
20.29
Mechanical & Aerospace ENGINEERING
Utah State University
PROJECT
UV ZOOM LENS
DRAFTED BY: BRIAN GRISENTI
CHECKED BY: TREVOR BIRD
APPROVED BY: RYAN BERKE
DATE APPROVED: 4/14/2017
SHEET SCALE: 2/3
SHEET NUMBER: 2 of 4
SPECIFICATIONS AND TOLERANCES
UNLESS OTHERWISE NOTED
DRAWING ASSOCIATED IN ACCORDANCE TO ASME Y14.5-2009
DEFAULT DIMENSIONAL TOLERANCES:
PART/ASSEM NAME: UV ZOOM LENS
PART/ASSEM NUMBER: UV-A-1
MATERIAL: N/A
FINISH: N/A

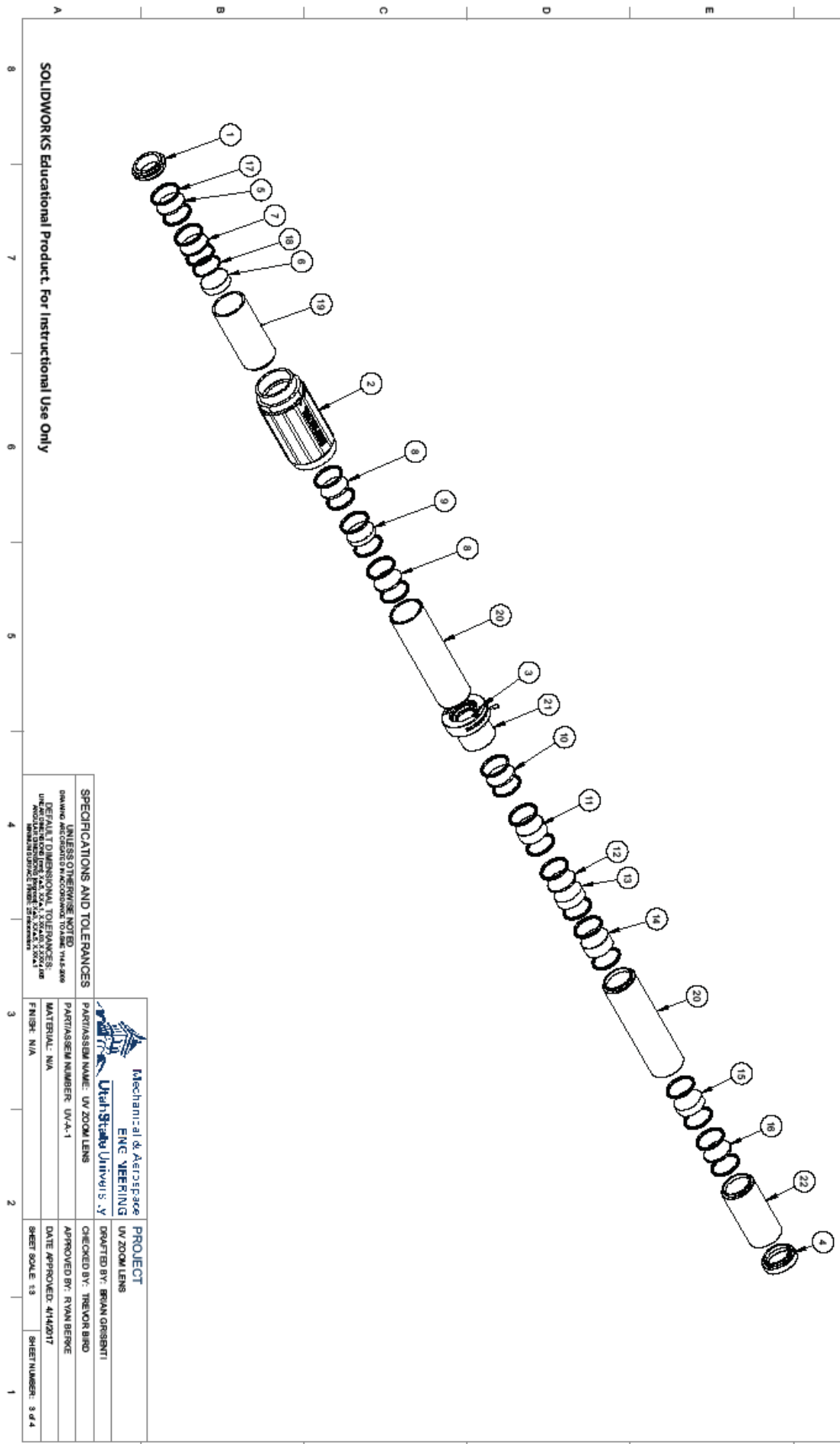

SOLIDWORKS Educational Product. For Instructional Use Only

SPECIFICATIONS AND TOLERANCES	Mechanical & Aerospace ENG. VEERING Utah State University
UNLESS OTHERWISE NOTED DRAWING ARE CREATED IN ACCORDANCE TO ASME Y14.5-2009	PROJECT: UV ZOOM LENS
PART/ASSEM NAME: UV ZOOM LENS	DRAFTED BY: BRIAN GRISENTI
PART/ASSEM NUMBER: UV-A-1	CHECKED BY: TREVOR BIRD
MATERIAL: N/A	APPROVED BY: RYAN BERKE
FINISH: N/A	DATE APPROVED: 4/14/2017
DEFAULT DIMENSIONAL TOLERANCES: LINEAR DIMENSIONS (mm): X.X ±0.1, X.XX ±0.05, X.XXX ±0.025 ANGULAR DIMENSIONS: ±0.5° BREAK EDGES: 0.2 MAXIMUM	SHEET SCALE: 1:3
	SHEET NUMBER: 3 of 4

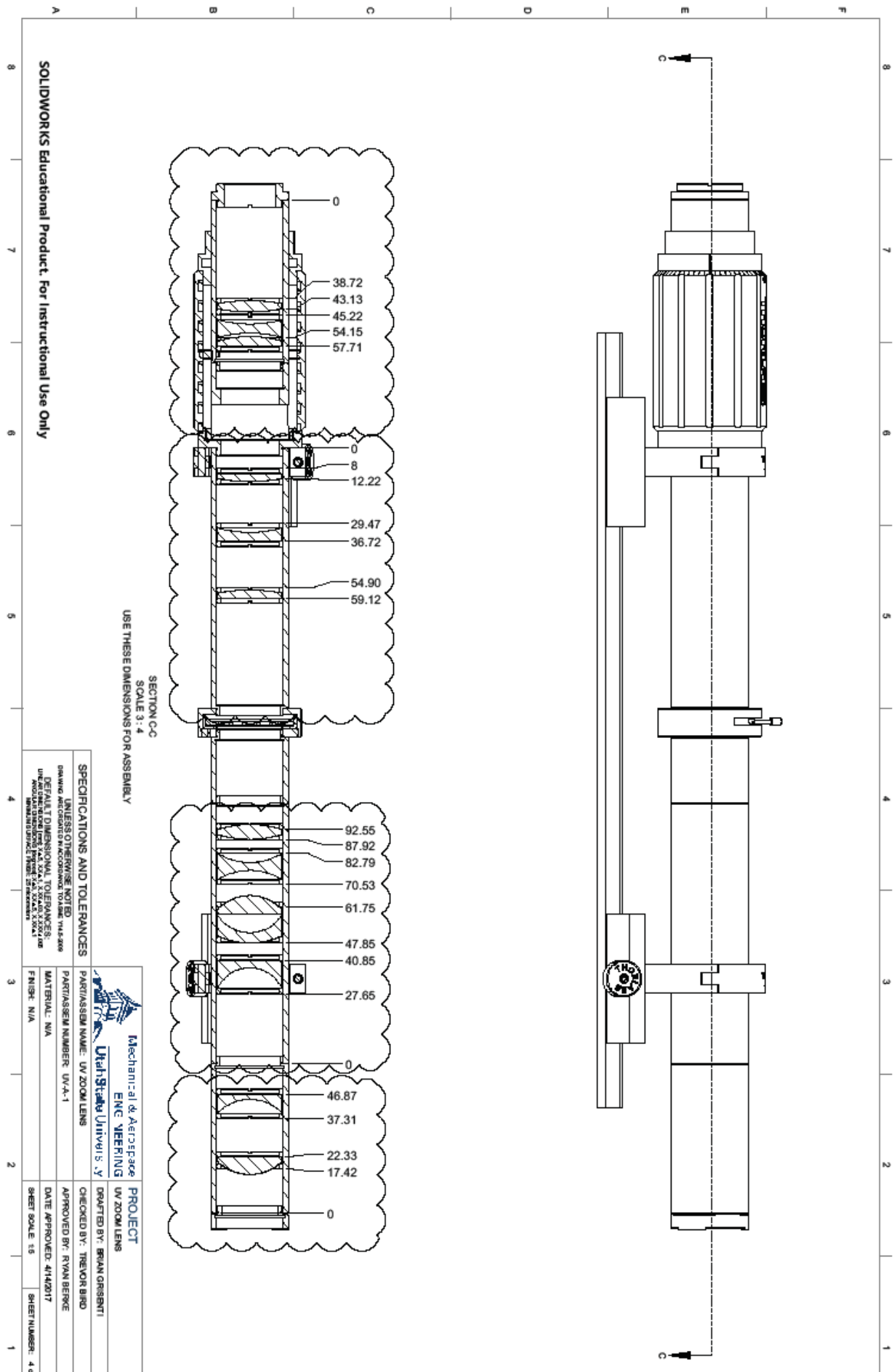
SOLIDWORKS Educational Product. For Instructional Use Only
SECTION C-C
SCALE 3 : 4
USE THESE DIMENSIONS FOR ASSEMBLY
0
38.72
43.13
45.22
54.15
57.71
0
8
12.22
29.47
36.72
54.90
59.12
92.55
87.92
82.79
70.53
61.75
47.85
40.85
27.65
0
46.87
37.31
22.33
17.42
0
SPECIFICATIONS AND TOLERANCES
UNLESS OTHERWISE NOTED
DRAWING ASSOCIATED IN ACCORDANCE TO ASME Y14.5-2009
DEFAULT DIMENSIONAL TOLERANCES:
PART/ASSEM NAME: UV ZOOM LENS
PART/ASSEM NUMBER: UV-A-1
MATERIAL: N/A
FINISH: N/A
Mechanical & Aerospace ENGINEERING
Utah State University
PROJECT
UV ZOOM LENS
DRAFTED BY: BRIAN GRISENTI
CHECKED BY: TREVOR BIRD
APPROVED BY: RYAN BERKE
DATE APPROVED: 4/14/2017
SHEET SCALE: 1:5
SHEET NUMBER: 4 OF

CHAPTER 3

SUPER RESOLUTION DIGITAL IMAGE CORRELATION (SR-DIC): AN ALTERNATIVE TO IMAGE STITCHING AT HIGH MAGNIFICATIONS

3.1. Prologue

This chapter contains a full-text paper which was published in the peer-reviewed journal *Experimental Mechanics* in May 2021, under the title "Super Resolution Digital Image Correlation (SR-DIC): An Alternative to Image Stitching at High Magnification." The author list is Robert S. Hansen, Daniel W. Waldram, Thinh Q. Thai, and Ryan B. Berke. The experiments were conducted and data collected at Utah State University in Logan, UT. The paper in its entirety is given below.

3.2. Abstract

Background: High-resolution Digital Image Correlation (DIC) measurements have previously been produced by stitching of neighboring images, which often requires short working distances. Separately, the image processing community has developed super resolution (SR) imaging techniques, which improve resolution by combining multiple overlapping images. **Objective:** This work investigates the novel pairing of super resolution with digital image correlation, as an alternative method to produce high-resolution full-field strain measurements. **Methods:** First, an image reconstruction test is performed, comparing the ability of three previously published SR algorithms to replicate a high-resolution image. Second, an applied translation is compared against DIC measurement using both low- and super-resolution images. Third, a ring sample is mechanically deformed and DIC strain measurements from low- and super-resolution images are compared. **Results:** SR measurements show improvements compared to low-resolution images, although they do not perfectly replicate the high-resolution image. SR-DIC

demonstrates reduced error and improved confidence in measuring rigid body translation when compared to low resolution alternatives, and it also shows improvement in spatial resolution for strain measurements of ring deformation. **Conclusions:** Super resolution imaging can be effectively paired with Digital Image Correlation, offering improved spatial resolution, reduced error, and increased measurement confidence.

3.3. Introduction

Digital Image Correlation (DIC) is a non-contacting technique used to examine localized strain across a material's surface [1]. By comparing images of a sample before, during, and after load application, DIC can calculate surface deformation and strain at any point which is visible to cameras. This method allows for measurements to be taken at a variety of length scales without a loss of quality in the measurement for different physical scales [2].

Although many physical length scales can be used, the resolution of the images used to compute deformation remains a limiting factor for DIC measurements. DIC can detect sub-pixel magnitudes of displacement [3], but the measurements are computed using subsets of pixels, thus averaging each 'pointwise' displacement measurement over the area of each subset. In addition, strains are computed from multiple subset displacements, averaging the strain measurement over an even larger area [4] and causing undesirable spatial 'smoothing' of measurements [5]. Due to the number of pixels necessary for a single strain data point, the physical size of the subsets used has a direct impact on the spatial smoothing of the measurement. To maximize the benefits of the full-field measurements from DIC compared to single averaged measurements from strain gauges, higher resolution images allow for smaller physical subset sizes which produce each "pointwise" measurement. This is especially true when it is necessary to perform DIC over small regions of interest.

To address the need for improved spatial resolution, some researchers have improved image resolution by removing a sample from an experiment's controlled environment to take DIC images under an optical microscope before and after deformation [6]. Similarly, even higher-resolution DIC images have been captured with a scanning electron microscope (SEM) [7], [8]. Such microscopy techniques enable measurements at the nanometer length scale, improving the spatial resolution. However, this added resolution in a single image often comes with a reduced field of view. To overcome the issue of small fields of view, images with adjacent fields of view can be stitched together to create one single image. At the optical scale, researchers have stitched together multiple images from optical microscopes in order to compare DIC results with grain microstructure [9], [10]. Stitching has also been demonstrated at the SEM scale, [11], [12], allowing even higher resolutions. The result is higher spatial resolution, with DIC subset covering smaller physical areas, while capturing large fields of view.

However, such high-resolution, large field-of-view methods face two key limitations. First, microscopy-based experiments must either be (a) conducted under operating conditions that are survivable by the imaging equipment or (b) performed ex-situ, removing the sample from the experiment's environment. At room temperature, specialized SEM setups have been developed that allow in-situ images [13]–[15], whereas high-temperature applications have traditionally utilized ex-situ measurements [16]. The second limitation stems from the working distance. Previous experiments have been performed using microscopes that have very short working distances, making stitching ill-suited for environmental chambers and long-range optics. High-magnification imaging with low-resolution cameras in specially-fitted has facilitated in-situ DIC of small fields of view at elevated temperatures, but requires a specially fitted optical microscope heating stage [17]. Similarly, long-range optics have allowed for high-resolution DIC

measurements in environmental chambers, but without accommodation for large fields of view [18]. However, the challenge remains that high-magnification in-situ measurements with full fields of view are limited by working distance of the optics.

As an alternate approach, Super Resolution (SR) imaging techniques may produce images of sufficiently high resolution while maintaining larger fields of view and long working distances. Super resolution is a post-processing technique to combine multiple overlapping low resolution (LR) images to produce a high resolution (HR) image in a region common to all images [19]. Image stitching and SR are compared schematically in Figure 1. While both processes are shown to yield similarly increased resolution, image stitching is often done ex situ (or occasionally under an environmental microscope), whereas SR could theoretically improve the process by allowing the LR images to be taken in situ and at longer working distances (although the HR images still require post-processing).

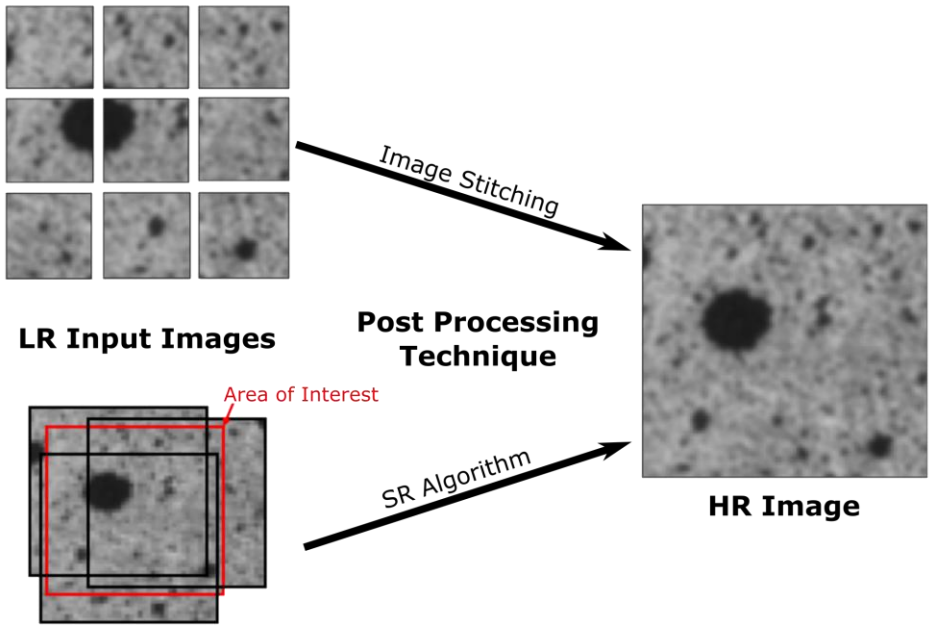

Figure 3.1: The stitching method and SR method are both used to obtain an HR image for a given area of interest.

This super resolution post processing of images has been a growing field over the last several decades. The basic principles were initially studied as early as 1974 as a mathematical method to improve images beyond resolutions otherwise limited by the diffraction limit of light, and reduce effects of blurring in images [20]. In 1984, Tsai and Huang first applied some of these principles for creating higher-resolution images from multiple frames [21]. Early applications ranged from improving resolution of emission spectra images in biochemistry [22] to overcoming the quality-reducing effect of atmospheric turbulence in telescopes [23]. As potential applications for super resolution imaging surfaced, computing ability also improved, leading to several advances in SR taking place in recent years. Emerging applications in other fields include retinal imaging [24], other telepathology [25], and improved smartphone cameras [26]. In the case of smartphones, SR techniques have allowed camera resolution to approach that of traditional cameras such as DSLRs by overcoming current sensor, pixel, aperture, and other hardware limitations. Some variations of super-resolution processes use the techniques to improve a single low-resolution or blurry image [27], compared to traditional applications which use multiple images with overlapping fields of view to improve accuracy [28]. Among the newest advances in super-resolution are the utilization of machine learning, comparing known low- and high-resolution image pairs to train super-resolution algorithms [29], demonstrating the expanding set of potential applications.

While principles of super resolution have been solving a variety of problems for years, SR has yet to be applied in the field of experimental mechanics. This paper demonstrates the potential application of super resolution imaging to improve high-magnification DIC measurements using

open-access SR software. The three techniques featured in this software and examined in this research are Robust Super Resolution [30], the Papoulis Gerchberg method [19], [31], and Structure Adaptive Normalized Convolution [32], the merits of which are discussed in the theory section below. The algorithms are evaluated for their effectiveness to perform DIC: first qualitatively, by reconstructing a sample image and comparing the quality of each visually; then quantitatively, by rigid body displacement and deformation measurements. The quantitative SR tests are then compared with unprocessed LR results to demonstrate the improvements in high-magnification DIC due to the SR resolution.

3.4. Theory

There are two common processes which are essential to all super resolution (SR) algorithms: 1) identifying position of each low resolution (LR) image with respect to one common high resolution (HR) reference grid and 2) projecting LR pixels onto the grid [19]. Figure 2a shows schematically a set of 4 LR pixels on a small section of the HR grid. The LR pixels are numbered 1-4, while the HR pixels are lettered A-D. Because each LR image has some displacement Δx and Δy with respect to the HR grid, the SR algorithm must determine which LR pixels will influence a given HR pixel. In Figure 2a, an HR pixel is shown to be influenced by up to four LR pixels from just a single image. For example, HR pixel A is entirely contained within LR pixel 1; HR pixel B lies partially within LR pixels 1-2; while HR pixel D lies partially within all four LR pixels 1-4. Because there are often several LR images input into a SR algorithm, many LR pixels are used to create a single HR pixel. Figure 2b shows schematically the same 4 HR pixels projected onto a second LR grid with pixels numbered 5-8. For example, pixel A is entirely contained within pixels 1 and 5 and would thus weight both pixels evenly; while pixel B has larger proportions within pixels 2 and 5 than within pixels 1 and 6, and would thus weight pixels 2 and 5 more heavily.

The specific processes of these two steps, as well as a description of the algorithms used to accomplish these steps, are described below.

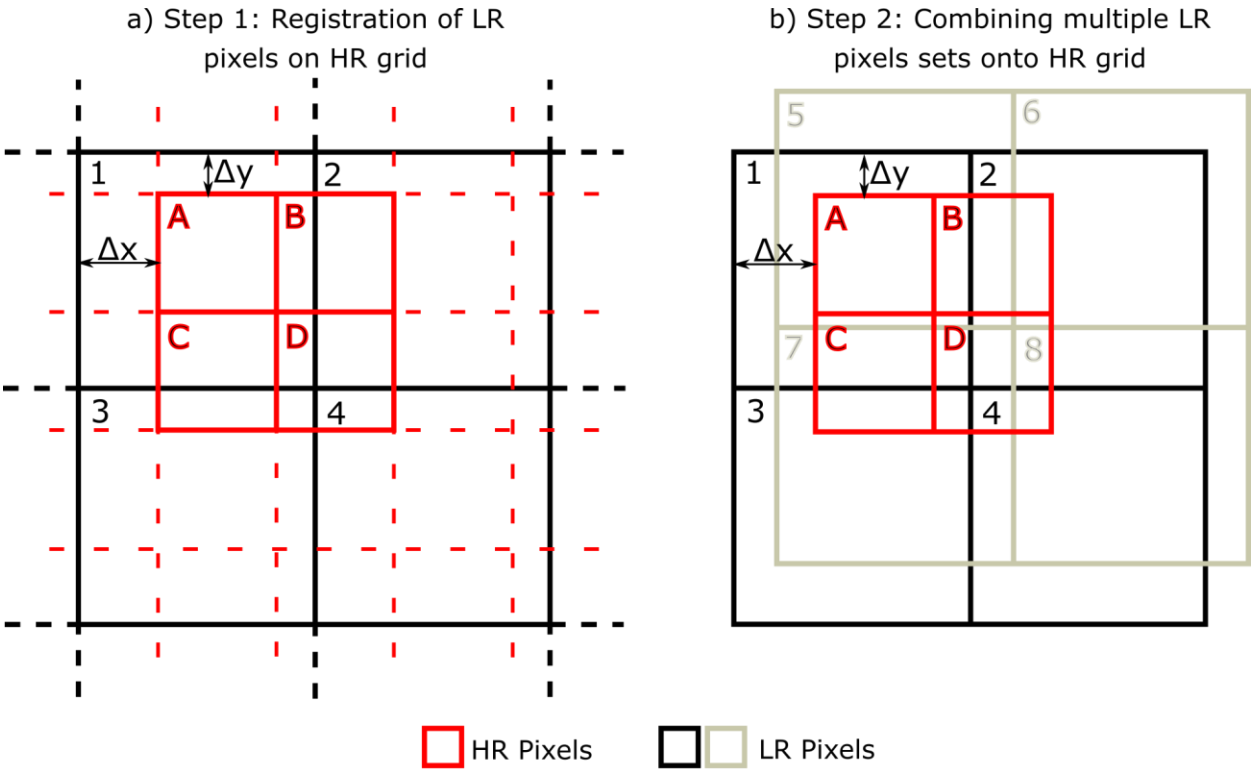

Figure 3.2: a) LR pixels (1, 2, 3, 4) have a displacement of Δx and Δy with respect to the HR grid pixels (A, B, C, D), which allows registration on the common HR grid, and b) Pixels from an LR image (1, 2, 3, 4), overlapping with pixels from another LR image (5, 6, 7, 8) are both used to inform the same HR pixels (A, B, C, D).

3.4.1. Step 1: Position registration between LR and HR

The first challenge in super-resolution computing is placing multiple LR images onto a common grid. To take advantage of information from multiple images, the images must necessarily be unique from each other. This is often due to some small translational displacement between the camera position in the capture of the image [33], but it can also be caused by lens distortion or

other deformations caused by the camera and lens system [34]. To reconcile all images, these camera displacements between a chosen first image and subsequent images must be estimated with sub-pixel accuracy. Those relative displacements then allow the position of each image to be registered on the common grid or framework for the SR image.

There are several algorithms to accomplish this step of position registration. Early efforts used a transformation to the frequency domain, where translations in the horizontal and vertical direction can be estimated by frequency phase shifts [21], [35]. Such methods assume global motion occurs for the entire field of view, which is a potential disadvantage for images whose subjects undergo non-uniform deformation [36]. Several additional techniques have been implemented to improve their performance of such methods. These include extracting rotation information from the phase shifts [35], as well as avoiding aliasing by using low-frequency parts of the image [37]. A more recent algorithm, proposed by Vandewalle et al [38] uses this Fourier transform on the image to identify translation on subsequent images when compared with an initial image. This algorithm combines the robustness against aliasing from frequency filtering with the ability to capture rotations as well as linear displacements from the phase shifts and amplitudes.

Other methods remain in the image spatial domain, rather than the frequency domain [39]. One of the foundational spatial domain algorithms was developed by Keren [40]. It utilizes Taylor expansions to estimate planar motion between images, based on the parameters of rotation and vertical and horizontal shifts. The algorithm then seeks to minimize the error of the approximation, solving a set of linear equations to find the shift and rotation parameters. This is an iterative method, adding the parameter solutions to the system of linear equations and resolving until it converges sufficiently. In order to cut down on computation time, the algorithm uses a ‘Gaussian pyramid’ scheme, which focuses first on a coarse down-sampled image, and then a progressively

finer down-sampled image until the full image is used. Other spatial domain methods have been developed which can account for other motion models such as segmented and temporal motion [41]. Algorithms have also been developed which estimate the rotation first, then correct the rotation before estimating spatial shifts [42].

Both the spatial and frequency-based registration algorithms return rotation and shift parameters. These shifts, with sub-pixel accuracy, allow all LR images to be placed on a common reference grid. Once these shifts have been estimated, the pixel information from the LR images can then be used to construct the SR image [38]. Of the methods discussed, Keren's is used through the rest of this paper.

3.4.2. Step 2: Combining multiple LR images into a single SR image

After positioning all LR images on common coordinates, the overlapping information from the LR pixel sets must be processed and combined into a single SR pixel set. Several algorithms have been developed to accomplish this reconstruction. They have some common features, yet they also vary in complexity. A comparison of the features of four algorithms is included in Table 3.1. They are fairly representative of SR capabilities and provide a framework with which to analyze the application of SR imaging for DIC measurements.

Table 3.1: Comparison of SR reconstruction algorithm features

	Iterated Back Projection (IBP)	**Robust Super Resolution (RSR)**	**Papoulis-Gerchberg (PG)**	**Structure Adaptive Normalized Convolution (SANC)**
Reconstruction Type	Initial pixel guess, down-sample to LR and iterate	Initial pixel guess, down-sample to LR and iterate	Populate known pixels and fill in gaps with interpolation	Predicts original signal by deconvolving pixels and preserves shape influence of pixels on neighbors

Noise Treatment	No significant treatment	Medians and outlier identification	Fourier Transform, Low-pass filtering	Outlier identification, 2nd pass to adapt convolution parameters

One of the earliest SR techniques to create a high-resolution grid from projected low-resolution pixels is Iterated Back Projection (IBP). The goal of IBP is to construct a SR image that, when deconstructed into LR images, best reproduces the original LR set [43]. The SR image is obtained iteratively from an initial guess featuring a grid of SR pixels with the same resolution and placement as the desired SR outcome. After each iteration, the SR image is deconstructed by averaging groups of SR pixels together based on (1) the size of SR pixels with respect to a LR pixel, (2) the diffraction pattern of a single point, transmitted to the image plane on the sensor (the point spread function)[44], and (3) the distance between each SR pixel and the LR pixel being influenced. A simple example, without consideration of the point spread function, is demonstrated in Figure 2b: HR pixel A lies entirely within LR pixel 1 and thus is weighted entirely in the average; whereas HR pixel D is only ¼ within LR pixel 1 and is thus weighted by ¼. Once deconstruction of a HR estimate is complete, the original and deconstructed LR images are compared to update the HR result as informed by considerations (1)-(3). This process is iterated until the simulated LR images converge with the original LR images within an acceptable error.

One of the shortcomings of the IBP method is oversensitivity to noise. In the algorithm, when the normalized average of the LR pixels is taken, there is no significant mechanism to address issues of noise. To respond to this, the Robust Super-Resolution (RSR) algorithm uses a median estimator, rather than an average [30]. This makes the algorithm more robust against noise outliers. The result is an algorithm that builds on IBP by addressing the significant drawback of

high sensitivity to motion blur or high noise. Because RSR is itself a direct improvement upon IBP, only RSR is considered through the rest of this paper.

Similar to IBP and RSR, the Papoulis-Gerchberg (PG) algorithm works through iteration [19]. For its initial guess, any SR pixel which lies entirely within one LR pixel is given the same value as the LR pixel. Any SR pixels which span multiple LR pixels are initially set equal to zero [31]. After known values are assigned, extrapolation between known pixel values is performed using signal processing techniques developed by Papoulis and Gerchberg [45]. This extrapolation is an iterative process of alternate projections and begins by transforming the image signal from the spatial to the frequency domain. The spectral signal goes through a low-pass filter, and the signal is then transformed back to the spatial domain. This new, extrapolated signal is then added to the original known signal, and the transformation and filtering is iterated. Each iteration reduces the mean square error of the extrapolation, and eventually the iterations will converge. The result is a noise-reduced SR image.

Finally, Structure Adaptive Normalized Convolution (SANC) is a response to the need to pick up underlying directional textures in the image, such as lines and curves. SANC works by assuming that LR images are blurred by a Gaussian convolution [32], meaning that a pixel is assumed to be influenced by pixels which lie close to it. Many SR algorithms (including IBP) assume Gaussian blur, which they refer to as a point spread function [4]. SANC is unique, however, because it considers image structure when assuming a Gaussian blur and it accounts for signal certainty. Image structure is considered for every pixel in the use of a gradient structure tensor. The gradient structure tensor determines if a pixel lies along a line in the image. Normalized averaging similar to IBP is performed, but it is improved by using information from the gradient

structure tensor and accounting for signal certainty in a similar way to RSR. SANC uses both methods to limit the effect of noise and accurately predict shape structure when performing SR.

3.5. Methods

To assess the usefulness of SR computing in improving spatial resolution in DIC, three of the algorithms are used in several separate tests: RSR, PG, and SANC. In the first test, a qualitative comparison is performed in which an image is downsampled and then reconstructed using the SR algorithms, to demonstrate the advantages and disadvantages of each algorithm. The second test evaluates the pairing of SR and DIC in comparing applied and DIC-measured rigid body translation of a patterned specimen. The third test consists of a mechanical test which produces a non-uniform strain field, to compare LR and HR images and their effectiveness in DIC strain measurements.

3.5.1. SR Algorithm Initial Comparison

An initial test determined the accuracy with which each SR algorithm could recreate an existing HR image. A test image, shown in Figure 3.3, was chosen which contains 3 important features: a) familiar shapes, b) straight edges, and c) areas of repetitive texture. This highlights the ability of each SR algorithm to reproduce those features. These abilities help to inform the practicability of using these algorithms for DIC-based strain measurements.

Figure 3.3: Test image (representing HR image) used for qualitative comparison by down-sampling and reconstructing using SR

Using super resolution imaging software developed and made publicly available by Vandewalle et al [38], the HR test image is deconstructed into nine overlapping LR images. First, nine copies of the HR image are created, shifting all but the first by random x and y displacements, ranging from -4 to 4 HR pixels in 0.125 HR sub-pixel increments. Next, each of the 9 HR images are converted to LR images, downsampling by averaging each 2x2 group of HR pixels into a single larger LR pixel. In pixels which shift beyond the edge of the initial image, pixels outside the edge of the shifted region of interest retain their original values. Since each LR pixel summarizes data from 4 HR pixels, the overall size of the LR image is reduced to a quarter of the HR image. The 9 LR images are then run through each of the chosen SR algorithms, using the software from Vandewalle, with an interpolation factor of 2, meaning that each dimension of the image is increased by a factor of 2. Thus, each LR pixel covers the same physical area as a 2x2 set of SR pixels. The result of the test is one SR image for each algorithm which could be compared to the HR image of the same resolution and field of view. This process is depicted in Figure 4. Visual inspection rather than numerical interpretation is used for comparison, as is widely done in comparing SR algorithms [46].

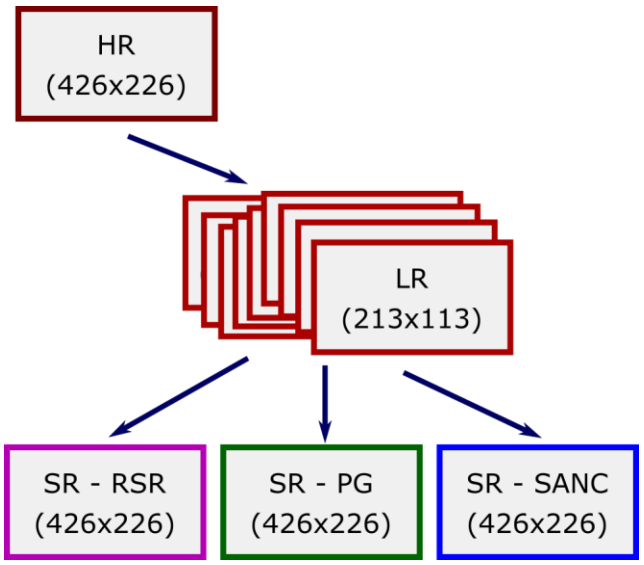

Figure 3.4: Method for visual comparison between super resolution algorithms including down sampling scheme.

3.5.2. Rigid Body Translation Test

As a first introduction of SR imaging in DIC measurements, SR images were used as input images to measure a known translation. First, a micrometer-driven translation stage was positioned vertically as shown in Figure 5, holding a small T-316 stainless steel ring sample, with outer diameter of 12.7 mm and wall thickness of 1.2 mm. A speckle pattern was applied to the ring with black paint on a white background. A Basler 15 MP camera was attached to a second vertically positioned translation stage, allowing controlled offsets of the image to produce overlapping LR fields of view. These stages were separated to allow a 290 mm working distance between the end of a 25mm lens and the ring sample, representative of distance requirements for viewing through an environmental chamber. The specimen was illuminated by Cole-Parmer fiber optic lights. The camera's field of view, including the speckled ring, is shown in the right of the figure.

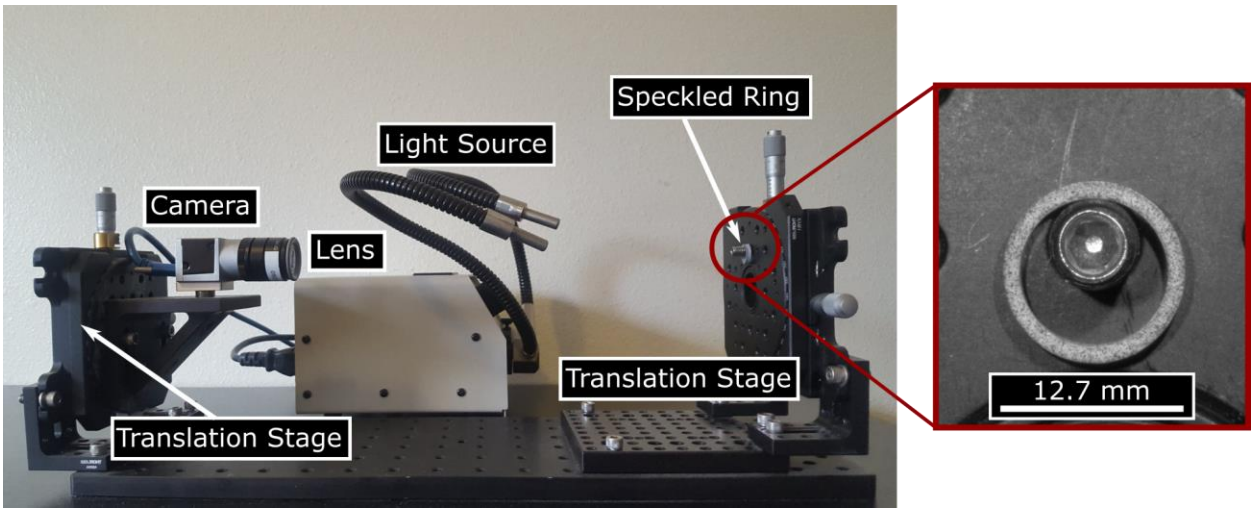

Figure 3.5: Rigid Body Translation test setup. Translation stage with the camera and lens (left) was moved in both vertical and horizontal directions to capture 9 images, while speckled ring translation stage (right) was translated in the vertical direction to produce rigid body motion. Camera field of view, focused on the ring, is shown at the right.

A series of images were then taken of the specimen as summarized in Table 2. After focusing the lens on the ring sample, 9 reference images were taken at differing camera positions, followed by 9 noise images. The camera position varied from ±0.0254 mm in both the vertical and horizontal directions and was centered about zero. The ring sample was then translated 0.127 mm in the vertical direction, and 9 images were taken in the same manner. This process was repeated up to a final ring sample translation of 0.762 mm. Prior to super resolution post-processing, each LR image was cropped to the same size (1500 x 1644 pixels) to still capture the ring along with applied translation, while reducing computation time. The result was a set of images for each algorithm which included a single image at every translation of the ring.

Table 3.2: Image capture scheme for Rigid Body Translation test, showing LR images taken and SR images processed at each displacement.

Image Set	Ring Displacement	LR Images (1500 x 1644)	SR Images (3000 x 3288)
1	0 mm (reference)	9 images	1 RSR, 1 PG, 1 SANC
2	0 mm (noise)	9 images	1 RSR, 1 PG, 1 SANC
3	0.127 mm	9 images	1 RSR, 1 PG, 1 SANC
…	…	9 images	1 RSR, 1 PG, 1 SANC
8	0.762 mm	9 images	1 RSR, 1 PG, 1 SANC

For each set of 9 LR images, the same SR software used in the initial comparison test was used to produce 3 SR images. For all 3 SR images, the step 1 image registration was again performed using the Keren registration algorithm. Step 2 was then performed using the Robust Super Resolution (RSR), Papoulis-Gerchberg (PG), and Structure-Adapted Normalized Convolution (SANC) algorithms, respectively, with an interpolation value of 2. The SR images produced by each of the RSR, PG, and SANC algorithms were then imported into VIC-2D [47], a commercial DIC algorithm which is widely used in the experimental mechanics community. Correlation was performed using a subset size of 49 pixels and a step size of 5 pixels to obtain full field displacements. For comparison, a set of images consisting of one LR image from each displacement was also imported into VIC-2D. A subset size of 25 pixels and step size of 3 pixels was used for the LR measurement, such that a comparable physical area in mm would be represented by each LR and SR subset. The displacements were then plotted against the known applied displacements to assess how closely each of the SR methods can reproduce a known translation, and to compare SR-DIC results to traditional LR-DIC measurements.

As a comparison tool, two additional images sets were produced: One LR image set made by averaging the nine LR images to combat noise (referred to as LR Average), and one HR image set which expands the single LR Average image by a factor of 2 through cubic interpolation (referred to as HR Interpolation). To produce the LR Average image set, the LR images were first shifted by the x and y offsets found with the Step 1 Keren algorithm in order to register on a common grid, then averaged together. Expanding each LR Average image by a factor of 2 through bicubic interpolation, then, provides a benchmark to compare the RSR, PG, and SANC algorithms against. Both the LR Average and HR Interpolation image sets were prepared and imported into VIC-2D for DIC measurement.

After preparing displacement data, further analysis on the accuracy of the measurement was performed, investigating the effect of subset size on the spatial standard deviation of the displacement measurement, as subset size has a significant impact on the correlation accuracy [48]. For each algorithm, the analysis was first performed at the subset sizes described in the methods section (49 for SR, 25 for LR). Smaller subset sizes were investigated, moving down in increments of 4 pixels for SR (45, 41…) and of 2 pixels for LR (23, 21…) to maintain similar physical subset sizes. This reduction in subset size continued until the images no longer correlated, thus exploring the lower limit of subset size for each algorithm. Similarly, subset sizes larger than the sizes of 49 and 25 were investigated in increments of 8 pixels for SR (57, 65…) and 4 pixels for LR (29, 33…) up to a size of 97 or 49 pixels. For every subset size, the same step size was maintained (5 for SR, 3 for LR) to preserve a similar number of total subsets.

3.5.3. Mechanical Deformation Test

To study the full implementation or SR imaging into DIC strain measurements, SR techniques were then used in a mechanical deformation test. The same ring specimen from the

rigid body translation test was placed in a Gleeble 1500D load frame with an environmental chamber. The same camera and lens as before were aimed at the specimen through the chamber viewing window from a working distance of 330 mm. In addition, a Qioptic Optem Fusion zoom lens was used with a second Basler 15 MP camera and focused on a portion of the ring. The variable magnification of the zoom lens was adjusted to produce a field of view roughly 15 times smaller than the LR lens in order to provide a more accurate 'high resolution' image with which to compare the super resolution images. Custom grips were designed to apply a tensile load on the inner surface of the ring, as shown in Figure 3.6.

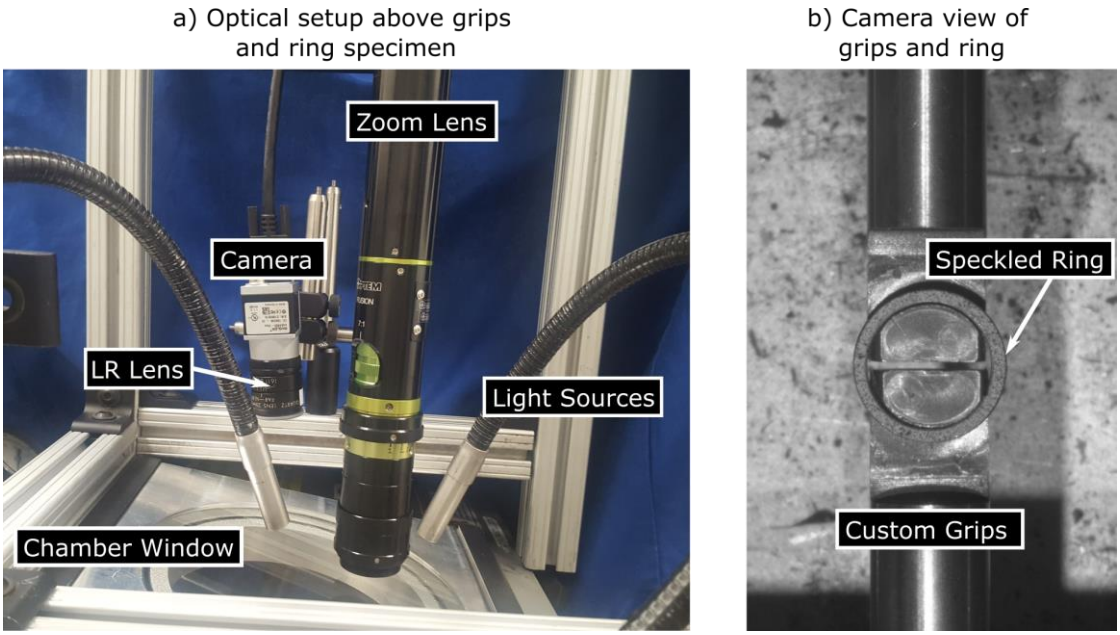

Figure 3.6: Mechanical test setup, showing (a) optical setup, including camera, lens, and light source, pointed through the chamber window at (b) the ring sample on the grips within the Gleeble 1500D load frame.

The grips were slowly moved apart until a small increase of force was registered by the load cell, indicating that both grips had come into contact with the inside face of the ring. From

this zero-displacement location, a set of 9 images was then captured in succession, to be combined later to produce a single SR reference image. Several seconds passed between each of the 9 images to allow for small random offsets of the field of view caused by vibration of the load frame. Another set of 9 images was then captured to provide a noise measurement. The grips were then moved apart under displacement control in increments of 0.1 mm, causing a non-uniform strain distribution in the ring. At each displacement increment, another set of 9 images was captured. This process of grip displacement followed by image capture continued until a final net grip displacement of 1.4 mm was achieved.

Upon completion of the mechanical deformation, each set of 9 LR images was combined using the three SR algorithms. Then, the sets of SR images were imported in VIC-2D and correlated with a subset size of 49 and step size of 5. Similarly, one of the 9 LR images at each displacement was imported and correlated with a subset size of 25 and a step size of 3, allowing similar physical areas to be represented by each subset. The zoom lens images were also imported and correlated with a subset size of 151 and step size of 5. Strain maps were generated and compared for each of the SR methods and for the LR image set. A subset size-match confidence analysis was performed for the mechanical deformation test, following the same process used for the rigid body translation test.

3.6. Results

The comparison of the three chosen SR algorithms to LR imaging techniques is supported by the results of the three tests: The SR algorithm initial comparison, the rigid body translation test, and the mechanical deformation test. These results are summarized below.

3.6.1. SR Algorithm Initial Comparison

Figure 3.7 shows the results of the deconstruction and reconstruction of an image, meant to highlight similarities and differences between the SR algorithms. The original HR image depicting a “one-way” traffic sign in front of a background of trees and sky is shown in part (a); an enlarged section is shown in part (b). The same section of the LR image is shown in part (c), and the three SR versions of the section in parts (d), (e), and (f). A comparison of the HR and LR images shows that the words on the sign are blurred but still readable in the LR image. The straight edges of the sign have also become jagged due to pixel averaging, along with some loss of definition in the leaves in the background.

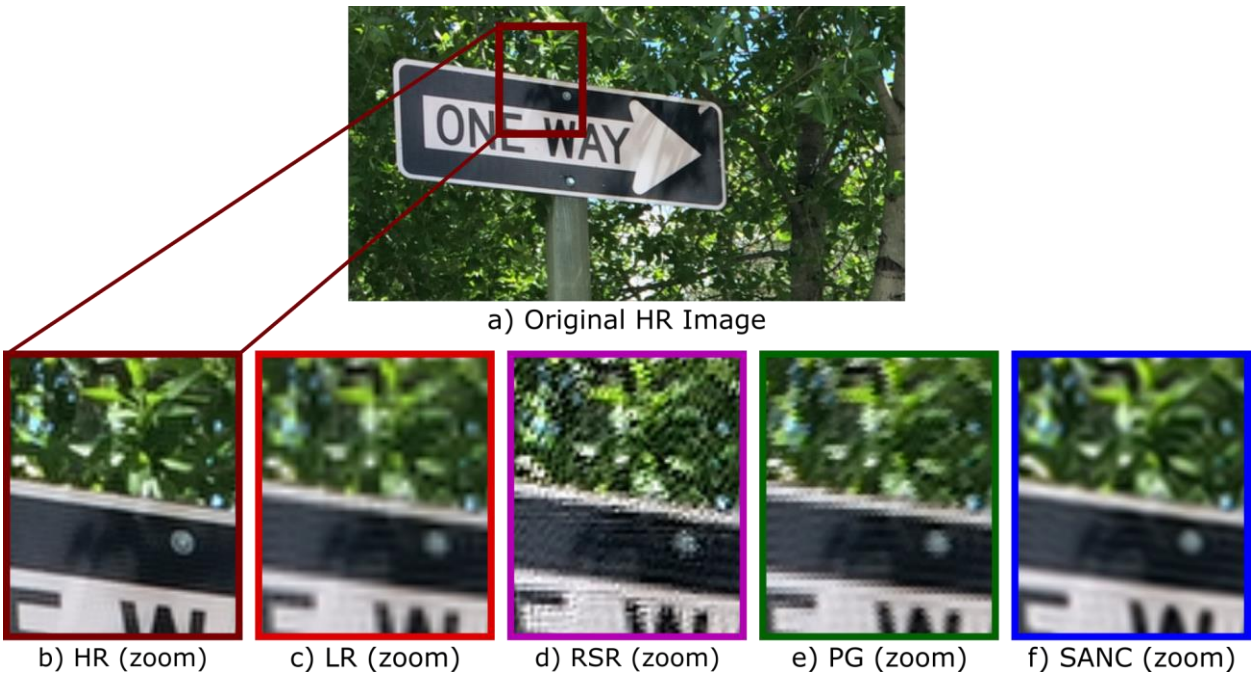

Figure 3.7: The HR and LR images are shown along with the results from all three SR algorithms.

The results of the SR image reconstruction are given in Figure 3.7(d), (e), and (f). The RSR algorithm slightly improves upon the LR image quality in regions of texture, but it also makes some features worse. For example, the leaves recapture some of their sharper colors, but the straight edges of the sign are visibly noisy and grainy. In the PG image, the shape of the letters are clearer than in the RSR and comparable to the LR, with sharper corners. However, the lines still have a more jagged appearance, with the diagonal lines appearing instead as long 'steps'. The opposite is true in the SANC image, where several features are more smoothed over. This improves the quality of some features, such as the straight edges losing some of the jagged 'steps'. However, it also worsens other features, as the corners of letters are less sharp than in PG. Overall, the SR images are generally clearer than the LR image, but they fall short of perfectly replicating the HR image.

The visual similarity between the original HR image and the reconstructed SR images can be compared using a metric developed by Wang et al called structural similarity [49]. The structural similarity (SSIM) index is a quantification of the perceived similarity between two images of the same resolution, scaled between 0 (no similarity) and 1 (perfectly similar). Using a publicly available MATLAB implementation of the SSIM algorithm [49], the grayscale versions of the images were compared against each other. The indices for the super resolution images, compared against the original HR image, were 0.5678 for RSR, 0.6047 for PG, and 0.7663 for SANC. These results show the best score for SANC, with lower scores for PG and RSR.

3.6.2. Rigid Body Translation Test

Figure 8(a-d) shows the average vertical translation measured across all subsets of the ring sample for each LR and SR method as a function of the applied translation. Uncertainty bands of

three standard deviations of the displacement of all subsets at each translation are also plotted. Thus, at the zero displacement, this 3σ uncertainty band represents the noise floor of the measurement, demonstrating the temporal variation when no displacement is applied. At the subsequent displacements, the uncertainty bands represent three times the spatial standard deviation. For many of the data points, the standard deviations are so small that the uncertainty bands overlap with the data markers for the mean displacements. Each plot also features a solid black line indicating the true applied translation of the sample, accompanied by dashed gray lines above and below, indicating the uncertainty of applied translation due to the resolution of the translation stage, defined as half a tick mark (tick marks are every 0.001 in or 0.0254mm). The LR measurements were computed using the center image of each 9-image set, while the SANC, RSR, and PG measurements were computed using the constructed SR images. In all cases, the applied translation is within the applied translation uncertainty associated with the stage resolution, indicating that all 4 measurement methods show sufficient agreement with applied translation. Of note is the fact that the PG images at translation increments of 0.127 mm, 0.254 mm, and 0.381 mm failed to correlate in VIC-2D, and so no measurement data is seen for those measurements.

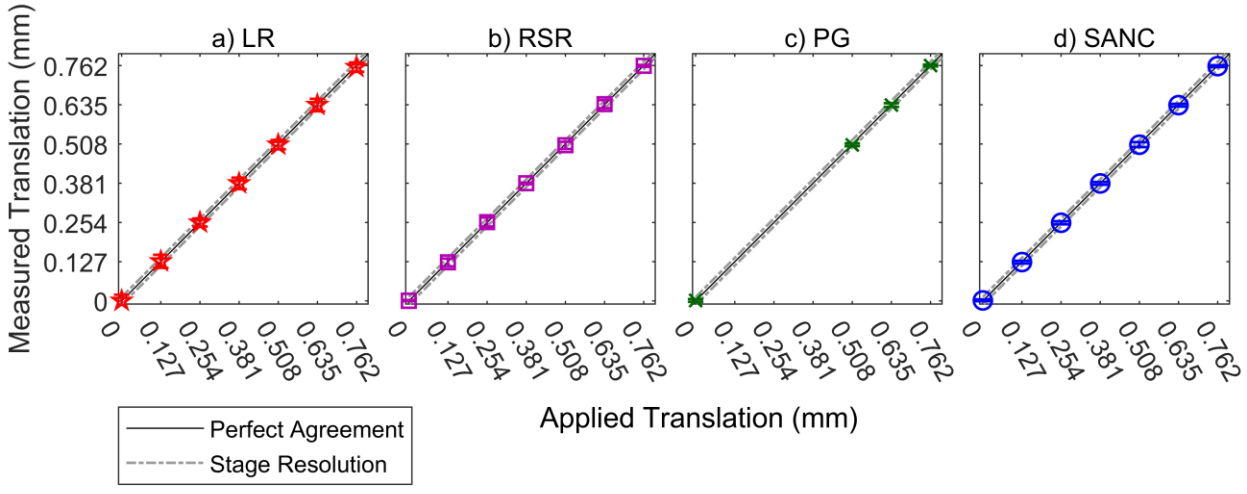

Figure 3.8: Plots showing average measured translation vs. applied translation, with applied resolution uncertainty bands in blue and perfect agreement in brown, for a) LR images, b) RSR images, c) PG images, and d) SANC images. Uncertainty bands on markers represent three standard deviations of the spatial variation in measured translation across all subsets. The solid black line shows perfect agreement between applied and measured translation, and bounding gray lines show uncertainty of applied translation due to stage resolution.

In Figure 3.9, the mean measurement error from all subsets (defined as the applied translation subtracted from the measured translation) of the data displayed in Figure 3.8 is plotted at each translation increment. The uncertainty bands again indicate three standard deviations of the measurement variation. As in Figure 3.8, the solid black line marks zero error, or perfect agreement between applied and measured translation, and the dashed gray bounding lines show uncertainty of the applied translation due to the resolution of tick mark increments on the translation stage. Compared to Figure 8, in which the uncertainty bands were too small to easily see, Figure 9 allows a clearer side-by-side comparison of the error in each SR method. Again, note that due to select images failing to correlate, there is no PG data for the translation increments of 0.127 mm, 0.254 mm, and 0.381 mm. Also included in this figure are the LR Average and HR Interpolation benchmarks described in the methods. The LR Average set is expected to show a reduction in noise from combining all 9 images while maintaining the original resolution, and the HR Interpolation set expands the LR Average by a factor of two to match the size of the SR images without using the SR algorithms.

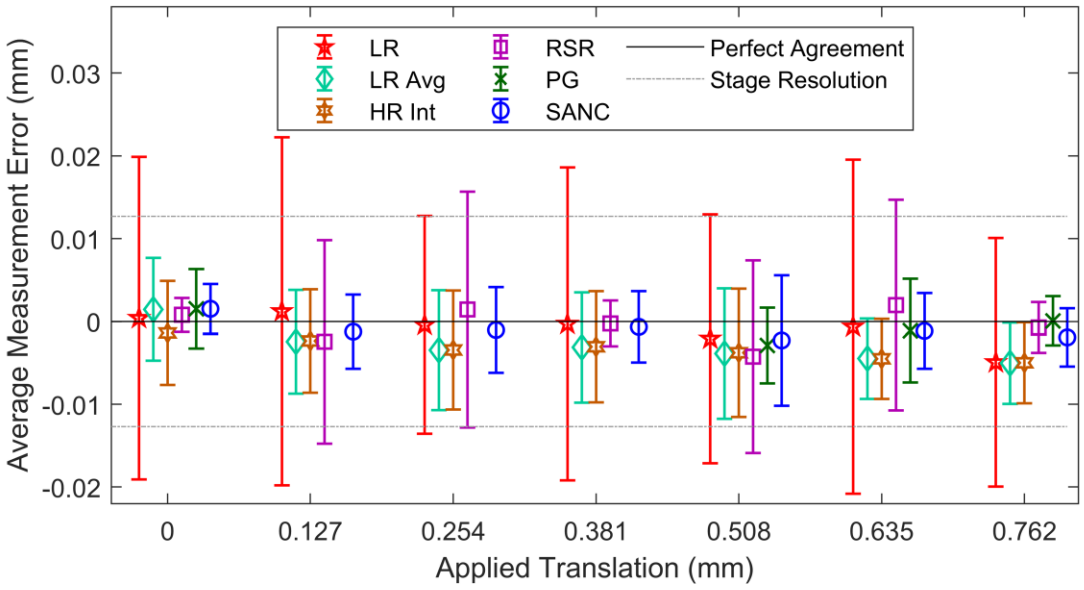

Figure 3.9: The error (measured - applied ring translation) averaged across subsets for DIC results based on LR, LR Average, HR Interpolation, RSR, PG, and SANC images, given at each applied ring translation. Note that markers have been slightly offset for readability, and are grouped around the corresponding applied translation. Uncertainty bands show three standard deviations of spatial variation, and gray bounding lines represent resolution uncertainty of the translation stage.

Figure 3.10 shows further comparison between the SR and LR measurements for the largest applied translation (0.762 mm) in terms of how the spatial standard deviation is affected by subset size. The mean translation measurement for each subset size is shown in the first subplot, along with uncertainty bands (the same 3σ quantities shown in the uncertainty bands of Figure 3.9). The subset size of the LR images is shown (in pixels) on the horizontal axis above the plot, while the subset size of SR images is shown (in pixels) on the horizontal axis below the plot. The second subplot shows the size of the uncertainty bands from the first plot, again as a function of subset size. The common physical subset size is shown on the very bottom horizontal axis. As expected,

the uncertainty band size decreases as subset size increases. It should be noted that this trend holds for all methods, although this decrease is small enough in some cases (such as the LR data) that the spatial noise appears to remain constant on the given y-axis scale of the figure.

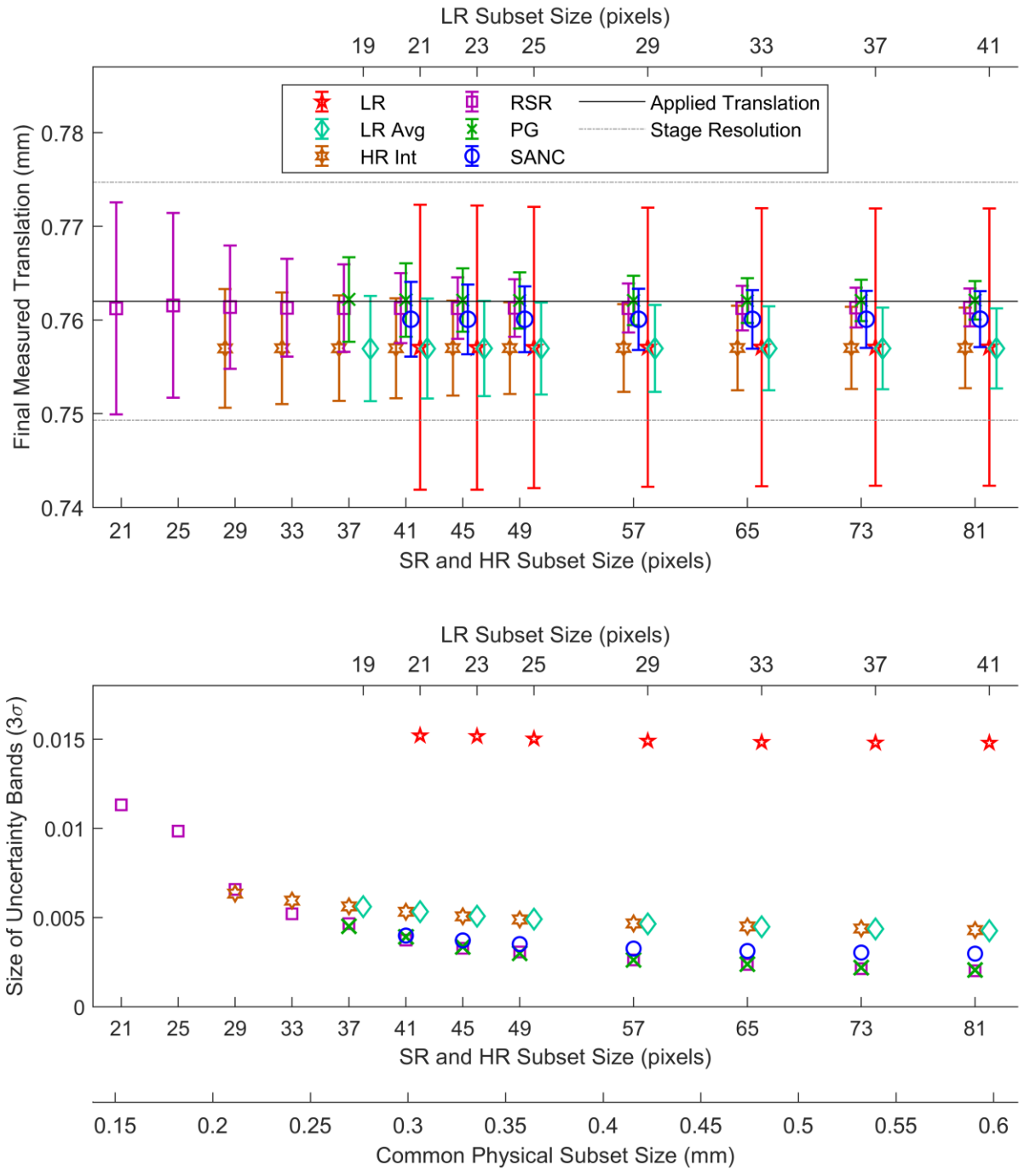

Figure 3.10: Upper subplot: final measured translation plotted with respect to physical subset size, in mm; uncertainty bands indicate the spatial variation across all subsets, represented as three standard deviations. The solid black line shows the applied translation, bounded by dashed gray lines representing uncertainty of applied translation due to stage resolution. Note that SR

data are slightly offset for readability (only sizes indicated by tick marks were used). Lower subplot shows the size of the uncertainty bands from the upper subplot.

3.6.3. Mechanical Deformation Test

The contours of displacements in the direction of loading for the LR, RSR, SANC and zoom lens DIC results are shown in Figure 3.11. Each contour is taken at the same deformation increment and each is plotted on the same scale for the same field of view. The images produced with the PG algorithm failed to correlate, therefore there are no PG contours in Figure 3.11. Also included in the figure are representative subsets of the speckle pattern on the specimen surface. All are taken from the same location on the surface, and the LR, RSR, and SANC cover the same physical area. The zoom lens subset covers a smaller area, located in the upper left corner of the other subsets.

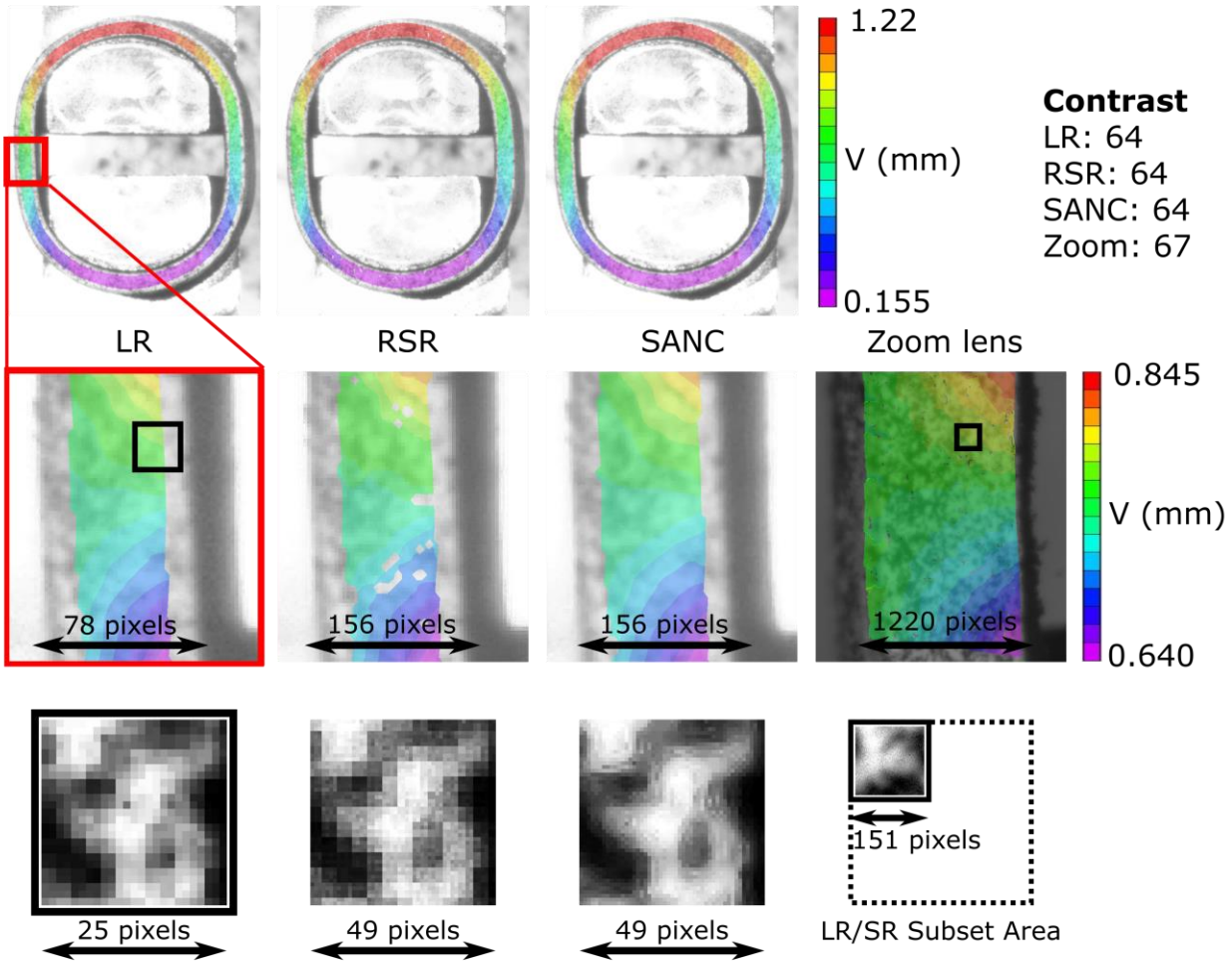

Figure 3.11: DIC contours for displacements in the direction of loading for LR, RSR, SANC, and Zoom lens. Corresponding subsets of the speckle pattern for each method are shown in the bottom row. For visualization of speckles here, the contrast was improved through Matlab's histogram equalization. The original contrast between light and dark speckles from the images used in DIC is also reported, defined as the median 90 percent of pixel gray levels [50].

3.7. Discussion

Based on the results of the three tests just shown, several observations can be made on the strengths and weaknesses of the SR algorithms investigated. In addition, benefits and

disadvantages of using SR imaging instead of traditional LR techniques are also demonstrated. These characteristics shown by the SR initial comparison, rigid body translation, and mechanical deformation tests are discussed below.

3.7.1. SR Initial Comparison Test

The initial comparison effectively shows some of the qualitative differences between the SR algorithm results. Comparing the images in Figure 3.7(b)-(f), all 3 SR algorithms show slight improvements over the LR, but the image quality of each SR image is poor compared to the HR.

In the case of RSR, some features show slight improvement over the LR image, such as recapturing some of the brighter colors on the lighted portions of the leaves. But many of the features become more pixelated than even the LR image, causing a loss of definition. This is evident in the screw at the top of the sign; the circular boundary between screw and sign is more distorted in the RSR image than in the LR image. Although some aspects are visually clearer, the algorithm still adds graininess that is not present in the LR.

In the case of PG, the outline of the blue gaps of sky between leaves is slightly more defined in the PG image. Additionally, the lettering has slightly heavier weight than the LR, making it more comparable to the HR. However, ‘trailing steps’ can be seen leading away to the left from the black-white diagonal border of the sign. This can also be seen in the LR image, but not in the HR image. Rather than smoothing out this boundary to approach the target HR image, the PG amplifies the trailing steps and emphasizes the artificial feature.

In the case of SANC, the appearance seems to fit most closely to the HR image. The lines and boundaries are smooth, and objects are easier to recognize than in either the RSR or the PG

images. However, this strength of the SANC image is also its greatest shortcoming. Some details found in the HR image are lost to the smoothing effect, such as the blurring of letter corners.

This comparison test demonstrates that the most recent innovation of the three SR algorithms (SANC) performs best in visually obvious elements of reconstruction, but also highlights some of the potential downfalls in the new application to DIC. Because the SANC algorithm accounts for shape features, it follows that the features in the SANC-reproduced image more closely resemble those found in the HR image. The algorithm distorts the shape of the convolution kernel to match image geometries based on gradient fields. Thus, the SANC image best replicates the features and objects in an HR image in a qualitative 'eye' test. But this smoothing of feature boundaries could lead to decreased performance in reconstructing speckle patterns. This could be especially true when individual speckles are relatively small compared to the features that the SANC algorithm is built to search for. And while RSR and PG produce more pixelated shapes, they may still work for speckled patterns used in DIC.

3.7.2. Rigid Body Translation Test

In the rigid body translation test, images from all three of the SR algorithms measure an applied translation as well as or better than LR images. In Figure 3.8, the average of all subsets in each image that successfully correlated was within the resolution uncertainty of the translation stage. However, some of the images produced by the PG algorithm failed to correlate, meaning that data was not extractable at all translation increments. Upon inspection of those images which failed to correlate, a checkerboard pattern of black pixels was interspersed in the image. This was also evidenced in the PG images from the mechanical deformation test as seen in Figure 3.12. Three different types of this defect were found: A checkerboard of mostly black pixels, as seen on

the far left of the figure, a series of black pixel vertical stripes, or a checkerboard of mostly non-altered pixels. This conversion of pixels to black did not appear in the LR original, shown in the right of the figure, or in the other SR images, as seen in the subsets of Figure 3.11. This checkerboard pattern also did not appear in the PG images from the initial comparison test with the one-way sign. It may be caused by the PG algorithm, a bug in its implementation in this software [38], or a combination of both, but it can obviously affect the DIC results or make correlation impossible.

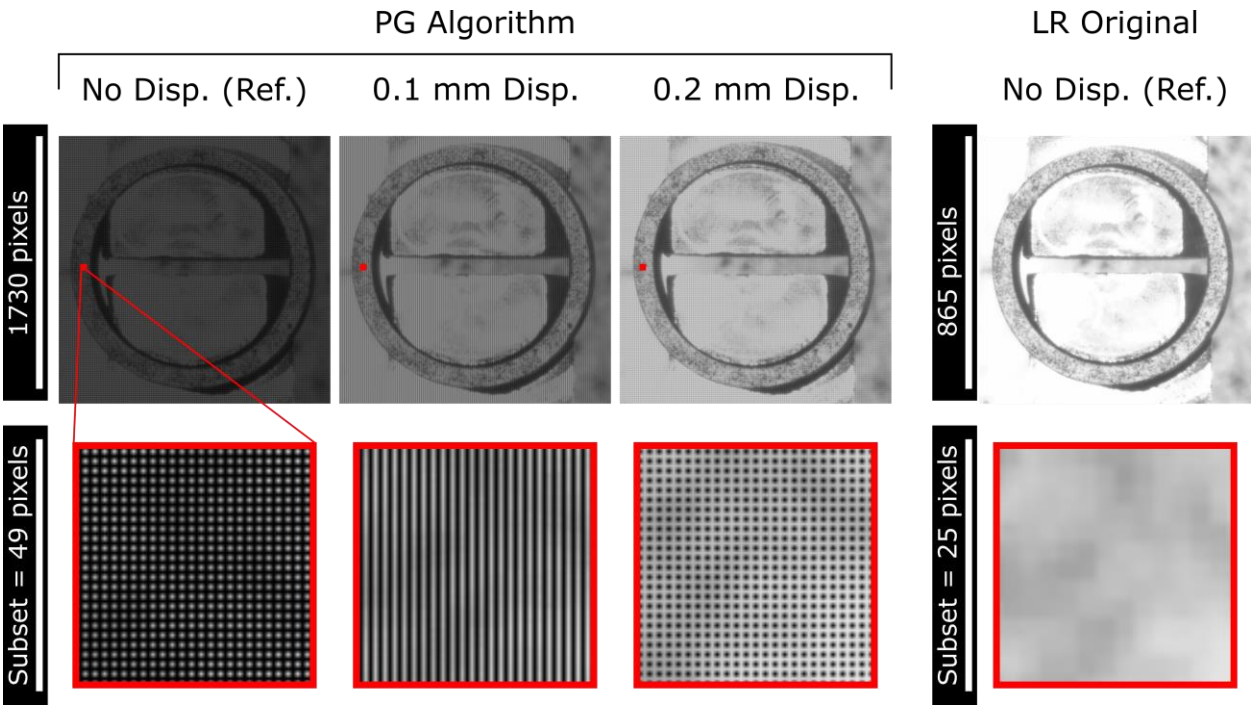

Figure 3.12: PG speckle pattern images from the mechanical deformation test, showing the three types of defects found, from left to right: mostly black pixel checkerboard, vertical stripes of black pixels, and mostly non-altered pixel checkerboard. At the right, the original LR image of the speckle pattern.

Figure 3.9 affords a clearer look at both the accuracy and shortcomings of the different methods, by focusing on the error between the measurement and applied translation. All six image

sets produced averages that lie close to the line of perfect agreement and within the bounding lines marking the uncertainty of applied translation due to stage increment resolution. At each translation increment, the ring translation was the same for all methods, and all images are centered on the same point. Thus, the unknown error in applied translation due to stage resolution uncertainty is the same for each of the three SR methods and the LR method. Therefore, the spread of bias errors shown in the figure between the six methods at each increment reflects on the precision of the methods. Although all six show some variability in these bias errors from increment to increment, they all show acceptable precision well within the stage resolution uncertainty.

Because of this unknown error in the applied measurement, it is difficult to assess the three SR algorithms based solely on the average displacements in Figure 3.9. To provide further clarity, the uncertainty bands can highlight the consistency within each image. Because there is no strain or deformation in this rigid body translation test, the applied motion is nominally uniform and ideal measurement would yield zero variation. At zero translation, the uncertainty bands show the noise floor. As expected, the LR image gives the largest spatial variation, followed by the LR Average and HR Interpolation benchmarks. The three SR algorithms show slight improvement over the benchmarks in their noise floors, with RSR showing the greatest difference.

A significant contribution to this measurement error is the temporal variation from image to image. In particular, the LR image sets are the most prone to temporal variation, or noise. This is because all other methods benefit from combining information from multiple images. To better understand the temporal variation of these inherently noisier LR images, a series of untranslated LR images was correlated, and a specific subset (seen in the left of Figure 3.13) was followed through time. The fluctuation of the measured translation of that subset is shown at the right of

Figure 3.13. This temporal variation helps to quantify the error of the LR measurement associated with the random noise, which is mitigated through averaging in producing the images with the other methods.

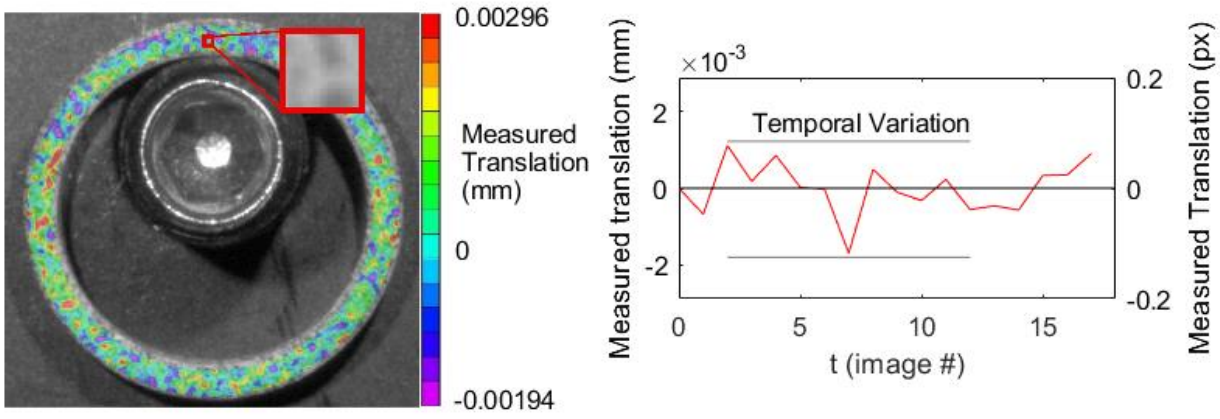

Figure 3.13: Spatial variation of an image with zero translation, at left, and the temporal noise of a specific subset across a series of untranslated images, at right.

At nearly every subsequent translation increment in Figure 3.9, the LR also has the largest bands, demonstrating the greatest spatial variation amongst the subsets. The reduction in spatial variation each method offers over LR is given in Table 3.3. Generally, the size of the uncertainty bands remains uniform from increment to increment for the LR Average and HR Interpolation benchmarks and SR images. However, the RSR varies greatly from increment to increment, showing the best and worst improvement over LR at different increments, as seen in the table. Because the data from the PG image dropped at several increments due to the loss of pixels as shown in Figure 3.12, it also has consistency issues. The SANC and benchmarks demonstrate consistency and seems to show the greatest reliability in the accuracy of the measurement, with the SANC generally having uncertainty bands of a size equal to or smaller than the benchmarks.

Table 3.3: Summary of improvement over LR offered by each method. Values are calculated from the sizes of uncertainty bands reported in Figure 3.9. Note that the average value for PG includes data only from those increments which correlated successfully.

Applied Translation (mm)		**0**	**0.127**	**0.254**	**0.381**	**0.508**	**0.635**	**0.762**	**Avg**
Percent Improvement over LR ($1-\sigma_{method}/\sigma_{LR}$)	LR Avg	68	70	45	65	47	75	67	**63**
	HR Int	68	70	45	64	48	76	67	**63**
	RSR	89	41	-8	85	22	37	80	**50**
	PG	75	N/A	N/A	N/A	70	69	80	**74**
	SANC	85	79	61	77	47	77	77	**72**

The differences in spatial variation are further investigated as a function of subset size in Figure 3.10. These data are taken from the measurements at the final ring translation increment of 0.782 mm, showing uncertainty band size plotted against the common physical subset size for the LR, benchmark, and SR images. At each comparable physical subset size, the SR algorithms all have smaller spatial variation, giving greater confidence in the measurement. Across all subset sizes, the LR Average benchmark showed a reduction in the band size by a factor of about 3, which aligns with the expectation that averaging N images can reduce noise by a factor of $\sqrt{N}$ [51]. Interestingly, the HR Interpolation benchmark data showed nearly identical band size as the LR Average at the same physical subset size, despite having 4 times more pixels per subset. This suggests that the added resolution through single image interpolation provides 'empty magnification' without adding useful information to the LR Average image. In contrast, the SR uncertainty bands are smaller than those of the benchmark data at the same subset sizes. This difference becomes more pronounced as subset size increases, with PG and RSR showing

improvement by a factor of roughly 2 at the largest several subset sizes. This reduction of spatial variation seems to be due to more than just the averaging effect on image noise. As one of the main contributors to spatial variation errors is pattern-induced bias error [52], this may indicate that SR algorithms can improve the quality of the pattern captured.

Also interesting to note in Figure 3.10 is the lower limit to subset size; data is left off the plot once the image no longer correlates. The RSR algorithm has a subset size lower limit of 21 pixels, which is the same as the LR has. However, this 21-pixel RSR subset covers a quarter of the area that the 21-pixel LR subset does, allowing much finer strain resolution. Although the LR Average offers a reduction in noise over the original LR images, the lower limit is only slightly improved from 21 to 19. When considering the actual physical subset size, the lower limit of the HR Interpolation is better than the PG and SANC algorithms but worse than the RSR. This superior range of subset size, combined with superior spatial variation error, clearly demonstrates the advantages the RSR algorithm holds over the other methods.

3.7.3. Mechanical Deformation Test

The mechanical deformation of the ring in this test demonstrated the capabilities of the LR and SR methods to measure heterogeneous strain fields. The results show similar displacement contours between the LR and SR images, as seen in Figure 3.11. In each case, the ring exhibits a greater displacement gradient on the inside edge of the ring compared with the outer edge. This is consistent with higher strains at the inner edge as the curved ring is stretched and straightened, which is the expected behavior in this loading case. This distribution seems to match up well between the LR and SR. There are slight differences between the contours, however, as both the RSR and SANC appear to show slightly greater displacements on the top of the inner edge of the

ring than the LR. The ‘higher resolution’ zoom lens image shows slightly higher displacements than the SR at the same location on the inner edge. However, the fact that the SR contours are slightly closer to the more accurate Zoom contour should not overshadow the reality that all methods produced very similar results.

The subsets shown in the bottom of Figure 3.11 do give some insight into the differences between the various methods. The LR subset shows a typically pixelated speckle pattern. The RSR subset also looks pixelated, although there is a difference in the gray levels the borders of speckles. This seems to indicate a more gradual transition from the dark interior of the speckle to the lighter background. A similar effect is seen in the SANC subset, except that these transition zones are much smoother, leaving speckles that are more ‘bloblike’ than blocky. Neither of the SR methods approached the clarity of speckle offered by the Zoom lens with roughly 15 times the resolution of the LR images, as seen in the Zoom subset.

3.7.4. Pairing of Zoom Lens with Super Resolution

The use of the zoom lens in the mechanical deformation test served as a standard of comparison for the SR algorithms, demonstrating that SR is equally capable in deformation measurements, if not offering slight improvement. It follows that pairing the two methods of higher resolution, a zoom lens and SR techniques, could produce further improvement. That possibility was evaluated by combining multiple zoom lens images at each grip displacement increment using the RSR and SANC algorithms, and then using Vic-2D to produce DIC strain contours. The RSR contour failed to correlate, but the SANC contour is shown in Figure 3.14.

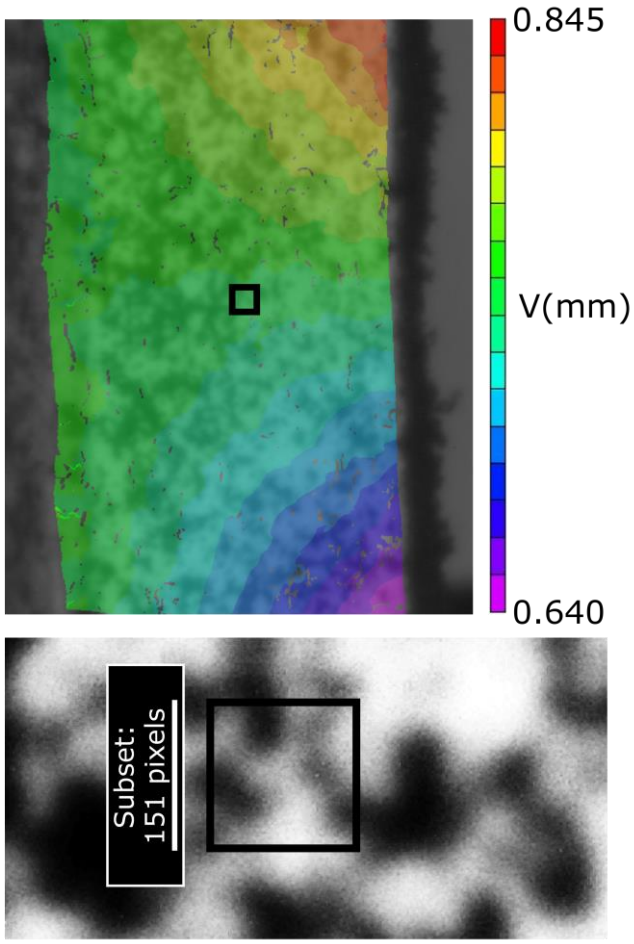

Figure 3.14: DIC displacement field in the direction of loading at final grip displacement increment for the combination of the zoom lens and SR. The SANC algorithm with an interpolation factor of 1.5 was used. A representative subset is overlaid on the portion of the speckle pattern shown below the contour. As with Figure 3.11, the contrast was improved through Matlab's histogram equalization for visualization of speckles. Actual contrast of correlated images is the same as original Zoom images.

The contour shows good agreement with the LR zoom lens results of Figure 3.11, with similar distributions of displacements at comparable locations. However, it should be noted that the same speckle pattern is on the ring for the original LR images and these SR zoom images,

meaning that the speckle size and length scale of the pattern is ill-suited for such an increase in resolution, as can be seen in the subset of Figure 3.14. Because the zoom lens' field of view is roughly 15 times smaller than the lower magnification lens, and because an interpolation factor of 1.5 was used for the SR zoom images, the pixel size of speckles in Figure 3.14 is approximately 23 times larger than in the LR contours of Figure 3.11. As such, the results of the SR zoom images are limited by the speckle pattern. This is expected to be the reason that the RSR zoom images failed to correlate in the DIC software. However, this does highlight that SR can be paired with lenses of varying magnification, as long as the length scale of the speckle pattern is appropriate for the image resolution.

3.7.5. Summary of Algorithm Performance

Through the three tests, differences in performance between traditional LR images and the 3 distinct SR alternatives became apparent. The initial comparison with the one-way sign showed clear improvement from the LR images for SANC, and to a lesser degree the PG and RSR also showed some improvement. However, none perfectly replicated the original HR image. Rigid body translation began to show problems with pairing PG with a DIC speckle pattern, dropping some of the translations. The minimal error in both RSR and SANC measurements showed good accuracy, although the uncertainty bands of SANC showed better consistency than was offered by the RSR algorithm. Conversely, RSR showed the smallest physical subset size, offering the best spatial resolution of the displacement measurement and the lowest spatial variation error. In the mechanical deformation, the issues with PG and DIC became very clear, causing all images to fail to correlate. In pairing SR with the zoom lens, the SANC image set was the only one of the three which was able to successfully correlate to the final deformation.

Table 3.4: Summary of advantages and disadvantages of LR, RSR, PG, and SANC measurements across the three tests.

	Baseline/Low Resolution (LR)	**Robust Super Resolution (RSR)**	**Papoulis-Gerchberg (PG)**	**Structure Adaptive Normalized Convolution (SANC)**
Initial Comparison (One-Way Sign)	Pixelated and blurry	Slightly sharper, but more pixelated lines and region transitions	Visually better than LR and RSR, but still has 'steps' in transition regions	Appears the smoothest; it offers the best reproduction of original HR image
Rigid Body Translation	Worst precision and confidence, but fairly consistent across images.	Less consistent in its precision. Lowest spatial variation error and best spatial resolution (allowed smallest subset size of any).	Good precision, confidence, and spatial resolution when it correlates. However, significant problems with failing to correlate several images.	Good precision, consistent across all images. Performed better than LR and benchmarks but worse than RSR, PG in spatial variation error and spatial resolution.
Mechanical Deformation	Similar displacement fields and lowest confidence.	Displacement fields matched zoom lens well, slightly better than LR	Failed to correlate.	Displacement fields matched 'high resolution' zoom lens contours. Performed very similarly to RSR.

3.8. Conclusion

In summary, the application of super resolution (SR) algorithms was investigated as a method of increasing the resolution of DIC strain measurements for samples at long working distances. Comparisons between Robust Super Resolution (RSR), Papoulis Gerchberg (PG), and Structure Adaptive Normalized Convolution (SANC) were evaluated through three tests: visual inspection, rigid body translation, and mechanical deformation experiments. The first test demonstrated that all three algorithms produce images which have some improvement visually over the LR images they are constructed from, with SANC performing best. The second test showed significant improvement offered by all three algorithms in measurement accuracy, precision, and spatial variation error, with RSR performing the best and PG failing to correlate in some cases. The final test again showed improvement in spatial resolution when using SR methods, and RSR and SANC performed equally well. With all three tests considered, SANC seems the algorithm best suited for SR-DIC among those investigated in this work, although RSR performs nearly as well and computes much more quickly.

When increasing resolution through SR methods, SR-DIC measurements show improvement over the original LR images, although they do not show the same improvement that would be expected from increasing to the same resolution through improved optics. There is some increase in computational time when taking these measurements, and the time required to capture multiple images makes it better suited for quasi-static in-situ experiments. Tests which most benefit from the use of SR techniques are those in which long working distances and small sample size prevent DIC from providing high resolution strain information across an entire region of interest.

3.9. Acknowledgments

This material is based upon work supported under an Integrated University Program Graduate Fellowship. Any opinions, findings, conclusions or recommendations expressed in this publication are those of the author and do not necessarily reflect the views of the Department of Energy Office of Nuclear Energy.

3.10. References

[1] M. A. Sutton, J. J. Orteu, and H. Schreier, *Image Correlation for Shape, Motion and Deformation Measurements: Basic Concepts,Theory and Applications*. Springer Science & Business Media, 2009.

[2] Hild F. and Roux S., "Digital Image Correlation: from Displacement Measurement to Identification of Elastic Properties – a Review," *Strain*, vol. 42, no. 2, pp. 69–80, Apr. 2006, doi: 10.1111/j.1475-1305.2006.00258.x.

[3] Yuan Lin and Zhiwen Lan, "Sub-pixel displacement measurement in Digital Image Correlation using Particle Swarm Optimization," in *2010 International Conference on Information, Networking and Automation (ICINA)*, Oct. 2010, vol. 2, pp. V2-497-V2-501, doi: 10.1109/ICINA.2010.5636461.

[4] P. Reu, "Virtual strain gage size study," *Exp. Tech.*, vol. 39, no. 5, pp. 1–3, Sep. 2015, doi: 10.1111/ext.12172.

[5] W. S. LePage, S. H. Daly, and J. A. Shaw, "Cross Polarization for Improved Digital Image Correlation," *Exp. Mech.*, vol. 56, no. 6, pp. 969–985, Jul. 2016, doi: 10.1007/s11340-016-0129-2.

[6] T. A. Berfield, J. K. Patel, R. G. Shimmin, P. V. Braun, J. Lambros, and N. R. Sottos, "Micro- and Nanoscale Deformation Measurement of Surface and Internal Planes via Digital Image Correlation," *Exp. Mech.*, vol. 47, no. 1, pp. 51–62, Feb. 2007, doi: 10.1007/s11340-006-0531-2.

[7] A. D. Kammers and S. Daly, "Self-Assembled Nanoparticle Surface Patterning for Improved Digital Image Correlation in a Scanning Electron Microscope," *Exp. Mech.*, vol. 53, no. 8, pp. 1333–1341, Oct. 2013, doi: 10.1007/s11340-013-9734-5.

[8] S. Maraghechi, J. P. M. Hoefnagels, R. H. J. Peerlings, O. Rokoš, and M. G. D. Geers, "Correction of Scanning Electron Microscope Imaging Artifacts in a Novel Digital Image

Correlation Framework," *Exp. Mech.*, vol. 59, no. 4, pp. 489–516, 2019, doi: 10.1007/s11340-018-00469-w.

[9] J. Carroll, W. Abuzaid, J. Lambros, and H. Sehitoglu, "An experimental methodology to relate local strain to microstructural texture," *Rev. Sci. Instrum.*, vol. 81, no. 8, p. 083703, Aug. 2010, doi: 10.1063/1.3474902.

[10] W. Abuzaid and L. Patriarca, "A study on slip activation for a coarse-grained and single crystalline CoCrNi medium entropy alloy," *Intermetallics*, vol. 117, p. 106682, Feb. 2020, doi: 10.1016/j.intermet.2019.106682.

[11] Z. Chen, W. Lenthe, J. C. Stinville, M. Echlin, T. M. Pollock, and S. Daly, "High-Resolution Deformation Mapping Across Large Fields of View Using Scanning Electron Microscopy and Digital Image Correlation," *Exp. Mech.*, vol. 58, no. 9, pp. 1407–1421, Nov. 2018, doi: 10.1007/s11340-018-0419-y.

[12] J. C. Stinville, M. P. Echlin, D. Texier, F. Bridier, P. Bocher, and T. M. Pollock, "Sub-Grain Scale Digital Image Correlation by Electron Microscopy for Polycrystalline Materials during Elastic and Plastic Deformation," *Exp. Mech.*, vol. 56, no. 2, pp. 197–216, Feb. 2016, doi: 10.1007/s11340-015-0083-4.

[13] C. C. Tasan, J. P. M. Hoefnagels, M. Diehl, D. Yan, F. Roters, and D. Raabe, "Strain localization and damage in dual phase steels investigated by coupled in-situ deformation experiments and crystal plasticity simulations," *Int. J. Plast.*, vol. 63, pp. 198–210, Dec. 2014, doi: 10.1016/j.ijplas.2014.06.004.

[14] Z. Zhao, M. Ramesh, D. Raabe, A. M. Cuitiño, and R. Radovitzky, "Investigation of three-dimensional aspects of grain-scale plastic surface deformation of an aluminum oligocrystal," *Int. J. Plast.*, vol. 24, no. 12, pp. 2278–2297, Dec. 2008, doi: 10.1016/j.ijplas.2008.01.002.

[15] T. Merzouki, C. Collard, N. Bourgeois, T. Ben Zineb, and F. Meraghni, "Coupling between measured kinematic fields and multicrystal SMA finite element calculations," *Mech. Mater.*, vol. 42, no. 1, pp. 72–95, Jan. 2010, doi: 10.1016/j.mechmat.2009.09.003.

[16] G. J. Pataky and H. Sehitoglu, "Experimental Methodology for Studying Strain Heterogeneity with Microstructural Data from High Temperature Deformation," *Exp. Mech.*, vol. 55, no. 1, pp. 53–63, Jan. 2015, doi: 10.1007/s11340-014-9926-7.

[17] C. Bumgardner, B. Croom, and X. Li, "High-temperature delamination mechanisms of thermal barrier coatings: In-situ digital image correlation and finite element analyses," *Acta Mater.*, vol. 128, pp. 54–63, Apr. 2017, doi: 10.1016/j.actamat.2017.01.061.

[18] R. S. Hansen, T. J. Bird, R. Voie, K. Z. Burn, and R. B. Berke, "A high magnification UV lens for high temperature optical strain measurements," *Rev. Sci. Instrum.*, vol. 90, no. 4, p. 045117, Apr. 2019, doi: 10.1063/1.5081899.

[19] D. Jain, “Superresolution using Papoulis-Gerchberg algorithm,” EE392J-Digital Video Processing, Stanford University, CA, 2005.

[20] R. W. Gerchberg, “Super-resolution through Error Energy Reduction,” *Opt. Acta Int. J. Opt.*, vol. 21, no. 9, pp. 709–720, Sep. 1974, doi: 10.1080/713818946.

[21] R. Y. Tsai and T. S. Huang, “Advances in Computer Vision and Image Processing,” *Proc. Inst Elect Eng*, vol. 1, pp. 317–339, 1984.

[22] D. A. Agard, R. A. Steinberg, and R. M. Stroud, “Quantitative analysis of electrophoretograms: A mathematical approach to super-resolution,” *Anal. Biochem.*, vol. 111, no. 2, pp. 257–268, Mar. 1981, doi: 10.1016/0003-2697(81)90562-5.

[23] J. R. Fienup, “Iterative Method Applied To Image Reconstruction And To Computer-Generated Holograms,” *Opt. Eng.*, vol. 19, no. 3, p. 193297, Jun. 1980, doi: 10.1117/12.7972513.

[24] D. Mahapatra, B. Bozorgtabar, S. Hewavitharanage, and R. Garnavi, “Image Super Resolution Using Generative Adversarial Networks and Local Saliency Maps for Retinal Image Analysis,” in *Medical Image Computing and Computer Assisted Intervention − MICCAI 2017*, Cham, 2017, pp. 382–390, doi: 10.1007/978-3-319-66179-7_44.

[25] Y. Zhang, Y. Wu, Y. Zhang, and A. Ozcan, “Color calibration and fusion of lens-free and mobile-phone microscopy images for high-resolution and accurate color reproduction,” *Sci. Rep.*, vol. 6, no. 1, pp. 1–14, Jun. 2016, doi: 10.1038/srep27811.

[26] B. Wronski *et al.*, “Handheld multi-frame super-resolution,” *ACM Trans. Graph. TOG*, vol. 38, no. 4, p. 28:1-28:18, Jul. 2019, doi: 10.1145/3306346.3323024.

[27] C. Ledig *et al.*, “Photo-Realistic Single Image Super-Resolution Using a Generative Adversarial Network,” in *2017 IEEE Conference on Computer Vision and Pattern Recognition (CVPR)*, Jul. 2017, pp. 105–114, doi: 10.1109/CVPR.2017.19.

[28] L. Zhang, H. Zhang, H. Shen, and P. Li, “A super-resolution reconstruction algorithm for surveillance images,” *Signal Process.*, vol. 90, no. 3, pp. 848–859, Mar. 2010, doi: 10.1016/j.sigpro.2009.09.002.

[29] M. Kawulok *et al.*, “Deep learning for fast super-resolution reconstruction from multiple images,” in *Real-Time Image Processing and Deep Learning 2019*, May 2019, vol. 10996, p. 109960B, doi: 10.1117/12.2519579.

[30] A. Zomet, A. Rav-Acha, and S. Peleg, “Robust super-resolution,” in *Proceedings of the 2001 IEEE Computer Society Conference on Computer Vision and Pattern Recognition. CVPR 2001*, Dec. 2001, vol. 1, p. I–I, doi: 10.1109/CVPR.2001.990535.

[31] A. Papoulis, “A new algorithm in spectral analysis and band-limited extrapolation,” *IEEE Trans. Circuits Syst.*, vol. 22, no. 9, pp. 735–742, Sep. 1975, doi: 10.1109/TCS.1975.1084118.

[32] T. Q. Pham, L. J. van Vliet, and K. Schutte, “Robust Fusion of Irregularly Sampled Data Using Adaptive Normalized Convolution,” *EURASIP J. Adv. Signal Process.*, vol. 2006, no. 1, p. 083268, Dec. 2006, doi: 10.1155/ASP/2006/83268.

[33] R. R. Schultz, L. Meng, and R. L. Stevenson, “Subpixel Motion Estimation for Super-Resolution Image Sequence Enhancement,” *J. Vis. Commun. Image Represent.*, vol. 9, no. 1, pp. 38–50, Mar. 1998, doi: 10.1006/jvci.1997.0370.

[34] D. Capel and A. Zisserman, “Computer vision applied to super resolution,” *IEEE Signal Process. Mag.*, vol. 20, no. 3, pp. 75–86, May 2003, doi: 10.1109/MSP.2003.1203211.

[35] B. S. Reddy and B. N. Chatterji, “An FFT-based technique for translation, rotation, and scale-invariant image registration,” *IEEE Trans. Image Process.*, vol. 5, no. 8, pp. 1266–1271, Aug. 1996, doi: 10.1109/83.506761.

[36] P. Vandewalle, S. E. Susstrunk, and M. Vetterli, “Superresolution images reconstructed from aliased images,” in *Visual Communications and Image Processing 2003*, Jun. 2003, vol. 5150, pp. 1398–1405, doi: 10.1117/12.506874.

[37] H. Foroosh, J. B. Zerubia, and M. Berthod, “Extension of phase correlation to subpixel registration,” *IEEE Trans. Image Process.*, vol. 11, no. 3, pp. 188–200, Mar. 2002, doi: 10.1109/83.988953.

[38] P. Vandewalle, S. Süsstrunk, and M. Vetterli, “A Frequency Domain Approach to Registration of Aliased Images with Application to Super-resolution,” *EURASIP J. Adv. Signal Process.*, vol. 2006, no. 1, p. 071459, Dec. 2006, doi: 10.1155/ASP/2006/71459.

[39] M. A. Fischler and R. C. Bolles, “Random sample consensus: a paradigm for model fitting with applications to image analysis and automated cartography,” *Commun. ACM*, vol. 24, no. 6, pp. 381–395, Jun. 1981, doi: 10.1145/358669.358692.

[40] D. Keren, S. Peleg, and R. Brada, “Image sequence enhancement using sub-pixel displacements,” *Proc. CVPR 88 Comput. Soc. Conf. Comput. Vis. Pattern Recognit.*, pp. 742–746, 1988, doi: 10.1109/CVPR.1988.196317.

[41] M. Irani, B. Rousso, and S. Peleg, “Computing occluding and transparent motions,” *Int. J. Comput. Vis.*, vol. 12, no. 1, pp. 5–16, Feb. 1994, doi: 10.1007/BF01420982.

[42] J. Gluckman, “Gradient field distributions for the registration of images,” in *Proceedings 2003 International Conference on Image Processing (Cat. No.03CH37429)*, Sep. 2003, vol. 2, p. II–691, doi: 10.1109/ICIP.2003.1246774.

[43] M. Irani and S. Peleg, “Super resolution from image sequences,” in *10th International Conference on Pattern Recognition [1990] Proceedings*, Jun. 1990, vol. ii, pp. 115–120 vol.2, doi: 10.1109/ICPR.1990.119340.

[44] Y. Shechtman, L. E. Weiss, A. S. Backer, M. Y. Lee, and W. E. Moerner, “Multicolour localization microscopy by point-spread-function engineering,” *Nat. Photonics*, vol. 10, no. 9, Art. no. 9, Sep. 2016, doi: 10.1038/nphoton.2016.137.

[45] P. Chatterjee, S. Mukherjee, and G. Seetharaman, “Application of Papoulis-Gerchberg Method in Image Super-resolution and Inpainting.”

[46] M. Giansiracusa, S. Ezekiel, J. Raquepas, E. Blasch, and M. Thomas, “A comparative study of multi-scale image super-resolution techniques,” in *2016 IEEE Applied Imagery Pattern Recognition Workshop (AIPR)*, Oct. 2016, pp. 1–7, doi: 10.1109/AIPR.2016.8010598.

[47] Correlated Solutions, “Vic-2D User Manual.” Irmo, South Carolina, 2009.

[48] B. Pan, H. Xie, Z. Wang, K. Qian, and Z. Wang, “Study on subset size selection in digital image correlation for speckle patterns,” *Opt. Express*, vol. 16, no. 10, pp. 7037–7048, May 2008, doi: 10.1364/OE.16.007037.

[49] Zhou Wang, A. C. Bovik, H. R. Sheikh, and E. P. Simoncelli, “Image quality assessment: from error visibility to structural similarity,” *IEEE Trans. Image Process.*, vol. 13, no. 4, pp. 600–612, Apr. 2004, doi: 10.1109/TIP.2003.819861.

[50] T. Q. Thai, R. S. Hansen, A. J. Smith, J. Lambros, and R. B. Berke, “Importance of Exposure Time on DIC Measurement Uncertainty at Extreme Temperatures,” *Exp. Tech.*, vol. 43, no. 3, pp. 261–271, Jun. 2019, doi: 10.1007/s40799-019-00313-3.

[51] Z. Gao, X. Xu, Y. Su, and Q. Zhang, “Experimental analysis of image noise and interpolation bias in digital image correlation,” *Opt. Lasers Eng.*, vol. 81, pp. 46–53, Jun. 2016, doi: 10.1016/j.optlaseng.2016.01.002.

[52] S. S. Fayad, D. T. Seidl, and P. L. Reu, “Spatial DIC Errors due to Pattern-Induced Bias and Grey Level Discretization,” *Exp. Mech.*, vol. 60, no. 2, pp. 249–263, Feb. 2020, doi: 10.1007/s11340-019-00553-9.

CHAPTER 4

DIGITAL IMAGE CORRELATION AT LONG WORKING DISTANCES: THE INFLUENCE OF DIFFRACTION LIMITS

4.1. Prologue

This chapter includes a full-text paper which is in review at the journal *Measurement*, under the title "Digital Image Correlation at Long Working Distances: The Influence of Diffraction Limits.". The author list consists of Robert S. Hansen, Katharine Z. Burn, Cynthia M. Rigby, Emma K. Ashby, Ethan K. Nickerson, and Ryan B. Berke. The experiments were conducted and the data collected at Utah State University, Logan, UT. The full paper is given below.

4.2. Abstract

Digital Image Correlation (DIC) is an optical measurement technique that can easily be adapted for high magnification applications. These high magnifications involve competing phenomena which must be balanced to produce the highest quality measurements. When out-of-plane displacements cause the specimen under investigation to move out of the depth of field, worsened focus negatively affects the measurement. As a result, it is often recommended to reduce aperture size to improve the depth of field. However, smaller aperture sizes can also cause worsened focus as the diffraction limit of light causes larger Airy disks, particularly at longer working distances. This work investigates the competing effects of both depth of field and Airy disk size in three test cases: higher magnification and shorter working distance, lower magnification and shorter working distance, and lower magnification and longer working distance. Different aperture sizes are found to change which effect dominates, and a recommendation for selecting the aperture setting to minimize measurement error from both phenomena is made.

Keywords: Digital Image Correlation, Diffraction Limit, Long Working Distance, High Magnification, Aperture, Depth of Field, Airy Disk.

4.3. Introduction

Digital Image Correlation (DIC) is a non-contact, optical measurement technique to measure full field displacements and strains. The technique works by applying a high contrast pattern to the surface of a deforming object and recording images with a high-resolution camera before and after deformation. An algorithm then correlates the images to compute full-field displacements, the derivatives of which can then be used to compute strain [1]. Compared to strain gauges, DIC is favorable because (i) it is non-contacting aside from a thin layer of paint, and thus does not greatly influence deformation [2]; (ii) it records full-field data in all directions, as opposed to normal strain at one direction and at one point [3]; and (iii) it can be performed at any time scale (determined by cameras) or length scale (determined by lenses). DIC has been demonstrated at lengths ranging from sub-micrometer [4], [5] to tens of meters [6], speeds ranging from quasi-static to high speed impact [7], and temperatures of up to 3000°C [8].

To study fundamental material phenomena, it is often desirable to map high magnification DIC strains against the unique microstructures of test specimens. Such approaches have been widely demonstrated via scanning electronic microscopy (SEM) by Daly et al. [4], [9], Hoefnagels et al. [10], [11], and others [12]–[14]. However, generating a speckle pattern is especially challenging [15], and high temperature SEM have historically been limited to about 800°C [16], although recent advancements have allowed in-SEM measurements up to 1150°C [17]. Similar microstructural strain mapping has been demonstrated optically by Carroll et al. [18] and Pataky et al. [19], but required very short working distances in order to achieve high magnifications, from

which high resolution images were then constructed via image stitching. In both optical studies, specimens had to be moved to a microscope to perform high magnification imaging, which limited the techniques to *ex situ* measurements of permanent deformation such as plastic yielding and creep deformation, respectively. More recently, Hansen et al. have demonstrated that high magnification measurements can be recorded at longer working distances using super-resolution imaging (SR-DIC) which constructs high resolution images from multiple overlapping images [20]. By enabling longer working distances, SR-DIC potentially enables a wider range of in situ measurements at longer working distances.

In harsh environments, a specimen may need to be loaded into an environmental chamber while the camera views the specimen from outside the chamber through a window. This imposes a long working distance between the camera and the specimen, which limits magnification. High magnifications can still be achieved using specialized zoom lenses [21], but the image resolution may be limited by the diffraction limit of the light [22]. Diffraction limits are angular in nature, so image blurring increases in proportion to the working distance [23]. The radius of blurring is defined as the Airy disk [24]. The Airy disk is additionally proportional to the wavelength of light, and inversely proportional to the diameter of the aperture of the lens [25].

When performing DIC using a lens with an adjustable aperture, it is common practice to adopt as small an aperture as possible while maintaining sufficient lighting [26]. Small apertures produce better depth of field, allowing the image to remain in focus over a limited range of out-of-plane motion [27]. However, small apertures also produce larger Airy disks, which defocus the image at long working distances [28], [29]. Thus, when combining DIC at high magnifications and long working distances, there is an inherent trade-off between the depth of field and the diffraction limit of the light, both of which impact the focus of the image. This trade-off has been well-

explored in the field of photography [30], [31], but its effect has yet to be demonstrated on DIC at long working distances.

The purpose of this research is to quantify the effects of decreased aperture on both depth of field and Airy disk diameter when images are taken at high magnification and long working distance. Static DIC measurements are taken using two lenses with different working distances: roughly 8 inches and 8 feet. The amount of noise present in the measurements is quantified for various aperture sizes, which assists in determining the optimal range of aperture sizes for performing long range DIC measurements. The recommendations produced in this paper will improve high magnification DIC at long working distances, thus enabling in situ measurement of deformation in harsh environments.

4.4. Methods

Long range DIC was explored over a series of three rigid-body motion experiments, as summarized in Table 4.1. The experiments were performed using the test setups in Figure 4.1(a) for Tests A and B and Figure 4.1(b) for Test C. In each test, the specimen was mounted vertically on top of two 2-axis micrometer-driven translation stages to apply either in-plane or out-of-plane rigid-body displacements, as seen in Figure 4.1(c). Each stage translates over a maximum range of ±0.5 in increments of 0.001 in, representing the smallest tick mark of translation, allowing a combined motion of ±1.0 in. All three tests were performed using a JAI CM-140-GE-UV digital camera which has a resolution of 1392 x 1040 pixels. Tests A and B were performed at a working distance of 7.5 in (190 mm) and 5.5 in (140 mm), respectively, between the lens and the test specimen using a Qioptic Optem FUSION Zoom Lens. Test C was extended to a working distance of 100 in (2.54 m) using a K2 Distamax Long Range microscope. All the tests used a ring

specimen, shown in Figure 4.1(d), machined from stainless steel tubing with an outer diameter of 12.68 mm and a wall thickness of 1.23 mm. The specimen was illuminated with a LDR2-90BL2 blue ring light from CCS, Inc., which has a peak wavelength of 470 nm. Test A produced a field of view on the order of 0.12 x 0.09 in (3.05 x 2.29 mm), capturing the wall thickness of the specimen. Tests B and C produced a larger field of view, on the order of 0.8 x 0.6 in (20.3 x 15.2 mm) and 0.95 x 0.71 in (24.1 x 18.1 mm) respectively, capturing the full ring. Accordingly, Test A had a magnification of 2.7x, while Tests B and C had only a magnification of 0.32x and 0.27x. Test A achieved a higher magnification than Test B by using a 3x extension tube in the Optem lens, while Test B utilized a 1x tube. To achieve the magnification necessary at the longer working distance, in Test C the Distamax was paired with one 2x extension ring purchased from the manufacturer.

Table 4.1: Summary of the three rigid-body motion experiments.

	Working Distance	Lens	Magnification	Field of View	In-plane Applied Motion	Portion Imaged
Test A	190 mm (7.5 in)	Optem Zoom	2.6x	2.5 x 1.9 mm (0.10 x 0.07 in)	0.076 mm (0.003 in)	Wall Thickness
Test B	140 mm (5.5 in)	Optem Zoom	0.33x	19.7 x 14.7 mm (0.78 x 0.58 in)	0.76 mm (0.03 in)	Full Ring
Test C	2.54 m (100 in)	Distamax	0.26x	25.1 x 18.8 mm (0.99 x 0.74 in)	0.76 mm (0.03 in)	Full Ring

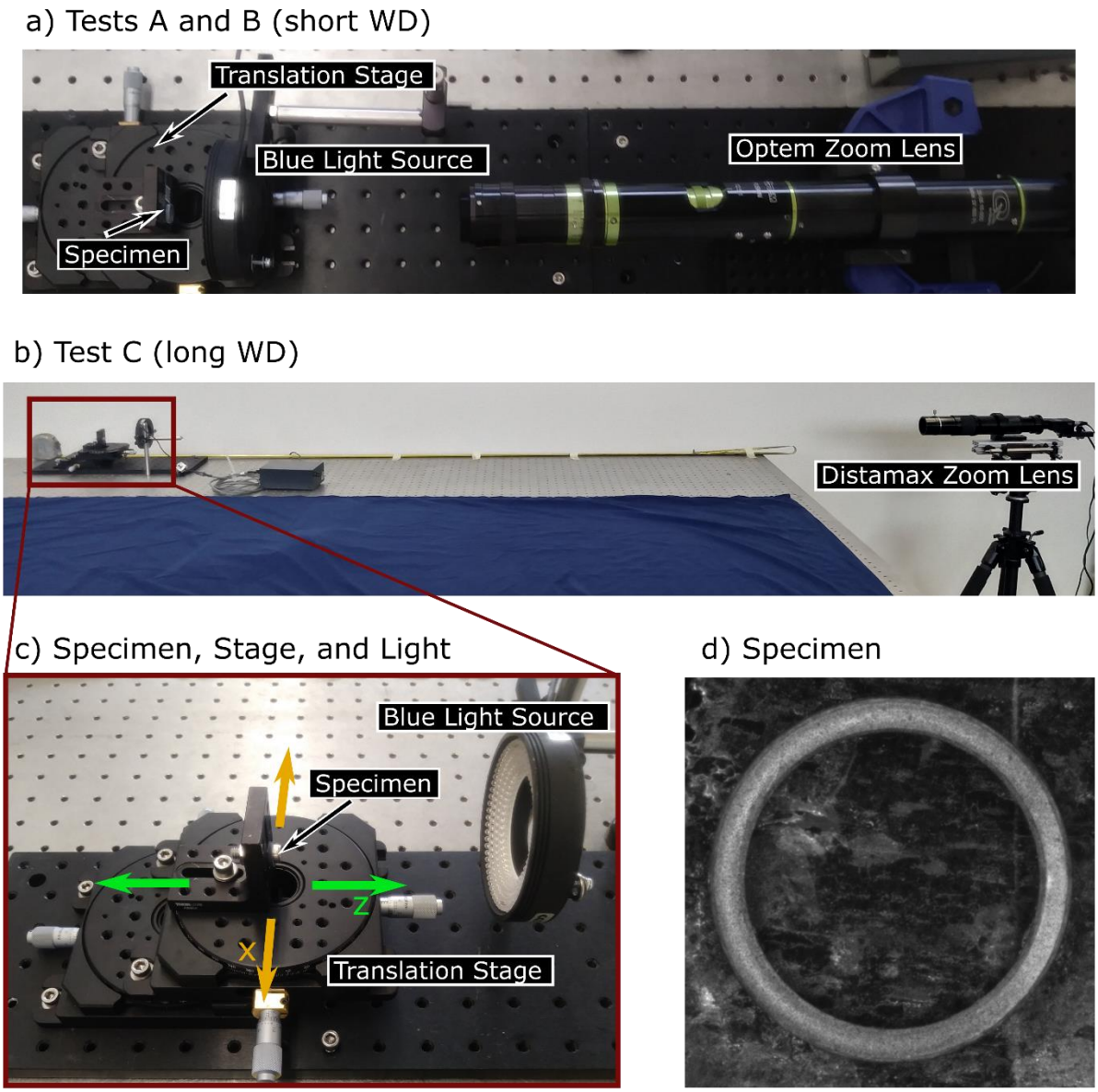

Figure 4.1: Test setups for (a) the Optem Zoom Lens used in Tests A and B (190 mm and 140 mm working distance, respectively); and (b) the Distamax Zoom Lens used in Test C (2540 mm working distance). In (c), the specimen, precision translation stages, and blue light source are shown, with the yellow arrows showing the direction of in-plane (measured) displacement, and green arrows showing the direction of out-of-plane displacement (changing working distance). In (d), the speckled ring specimen used is shown.

The experiments were performed using the small ring specimen with the same speckle pattern for all three tests. The speckle pattern was fine enough for the higher magnification in Test A, and coarse enough for the lower magnification in Tests B and C. To produce the pattern, the specimen was sprayed with a uniform coat of white VHT Flameproof spray paint to create a background for the DIC speckle patterns. The fine speckle was then created immediately afterwards by depositing graphite powder particles on the still-wet white paint. To avoid overly large speckles, powder clumps were broken up and particles were filtered to be under 25 microns in size using compressed air to force the powder through a particle-filtering wire cloth (200 x 600 mesh size, McMaster-Carr), in a procedure similar to that used by Jonnalagadda et al. [32]. Some initial images were then collected using the setup for each of the three tests to assess the typical speckle size measured in pixels, as seen in Figure 4.2.

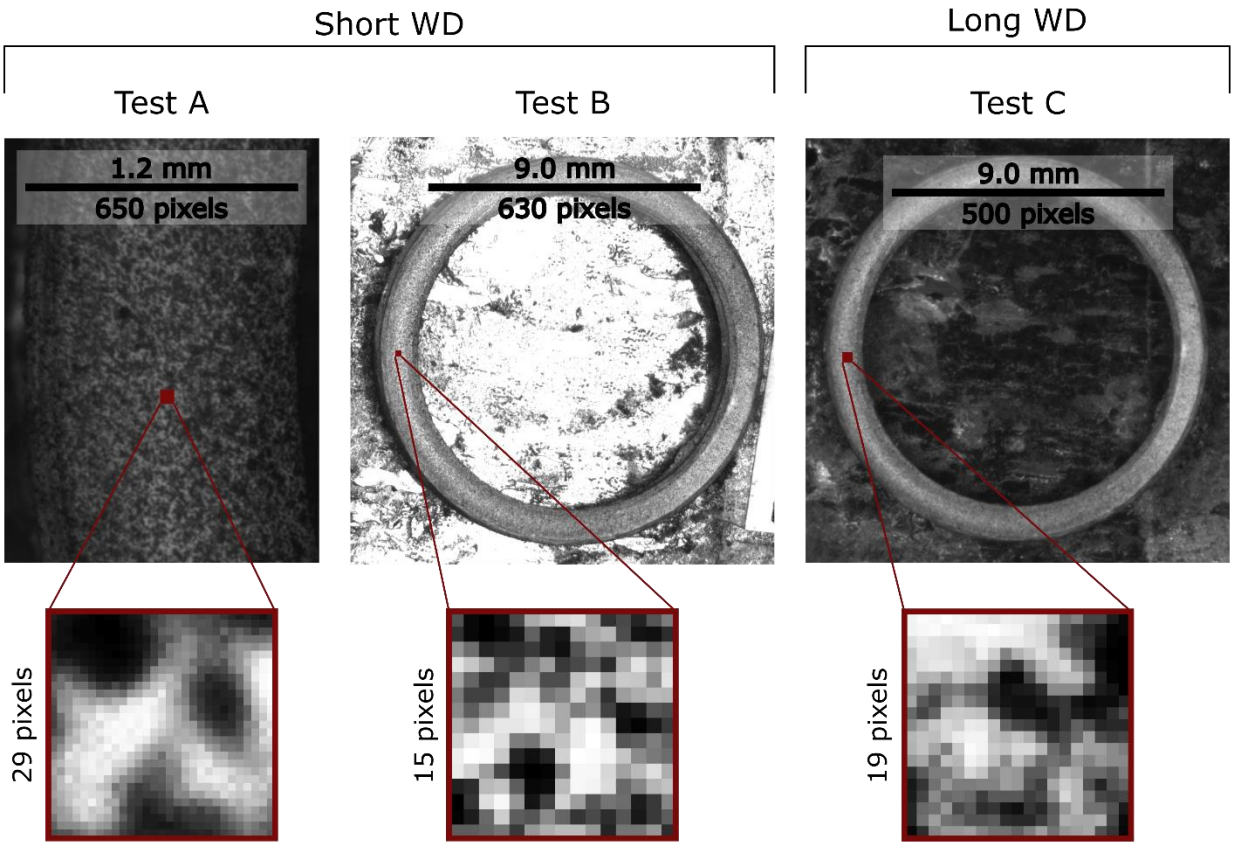

Figure 4.2: Sample speckle images and DIC subsets obtained at the start of tests A, B, and C, respectively. Note that Tests B and C show the same region of interest as recorded by two different lenses. For better visualization of speckles, the contrast of the subsets in the figure was improved through Matlab's histogram equalization. The original contrast can be found in Table 4.2.

Each lens was initially set to its largest aperture size, as summarized in Table 4.2, and then brought into focus to obtain the speckle images in Figure 4.2 to be used as reference images. The specimen was then translated in-plane (in the x direction indicated by the yellow arrow in Figure 4.1(c)) in known increments of 0.0005 inches in Test A and 0.005 inches in Tests B and C, with a new "deformed" image being captured at each increment. This was continued for a total of 6 increments, bringing the final displacement to 0.003 inches in Test A and 0.030 inches in Tests B and C. Once the in-plane x-displacement and image capture were complete, the specimen was then returned to its initial in-plane position and translated forward out of plane (in the z direction indicated by the green arrow in Figure 4.1(c)) by a percentage of the initial working distance. A new reference image was collected, followed by a new in-plane translation the same distances as before, and the subsequent "deformed" images were also collected. The procedure is repeated, moving in-plane then out-of-plane, until the out-of-plane displacements have covered the entire depth of field for that test. Because the depth of field is different for each of the lens arrangements, the increments of out-of-plane (z direction) displacements varied from test to test. Test A featured out-of-plane displacement increments of ±0.1% of the working distance up to ±0.6%, Test B had increments of ±0.4% up to ±3.6%, and Test C moved in increments of ±0.2% up to ±1.0%. Upon completion of both in-plane and out-of-plane displacement at the largest aperture, the procedure was then further repeated for the progressively smaller aperture sizes listed in Table 4.1. This

resulted in a total of 52 image pairs of reference and final deformed images in Test A (4 apertures x 13 working distances), 76 image pairs in Test B (4 x 19), and 44 pairs in Test C (4 x 11). Critically, aside from reducing the aperture, the lens is otherwise untouched to retain its initial focus through all of the image pairs for each test.

Table 4.2: Summary of aperture sizes and resulting Airy disk diameters explored in each of the three tests.

Test A Subset size: 29 pixels	Aperture diameter, a (mm)	10.2	8.3	6.3	4.4
	Exposure time (μs)	9601	12958	22677	61966
	Speckle contrast, Δ (counts)	59	59	59	58
	Airy disk size, d (μm)	21.5	26.5	34.4	49.1
	Airy disk size, d (pix)	11.6	14.3	18.6	26.6
	Aspect ratio, d/subset (%)	40	49	64	91
Test B Subset size: 15 pixels	Aperture diameter, a (mm)	10.2	8.3	6.3	4.4
	Exposure time (μs)	5478	6008	7068	7539
	Speckle contrast, Δ (counts)	64	57	63	54
	Airy disk size, d (μm)	15.8	19.4	25.2	36.0
	Airy disk size, d (pix)	1.1	1.4	1.8	2.5
	Aspect ratio, d/subset (%)	7	9	12	17
Test C Subset size: 19 pixels	Aperture diameter, a (mm)	22.9	19.0	15.2	11.4
	Exposure time (μs)	6715	7068	11545	26801
	Speckle contrast, Δ (counts)	61	61	61	61
	Airy disk size, d (μm)	127.4	152.9	191.1	254.8
	Airy disk size, d (pix)	7.0	8.4	10.6	14.1
	Aspect ratio, d/subset (%)	37	44	56	74

Changes in aperture not only affect the depth of field and the size of the Airy disk, but smaller apertures also produce darker images by reducing how much light reaches the camera sensor. Thus, to eliminate variable brightness as a potential source of measurement error, each

time the aperture is reduced there is an accompanying change of lighting to offset the light lost due to aperture. Light is increased in two ways: first by increasing the intensity of the light sources themselves, and then by increasing the exposure time on the camera sensor as listed in Table 2. The amount by which the lighting is increased is determined by (1) plotting a histogram of how frequently each greyscale value (0-255 for an 8-bit camera) occurs in each speckle image; (2) computing Delta, defined as the span of greyscale values which include the central 90% of all pixels in the region of interest [33]; and (3) adjusting the exposure time until each Delta agrees with its counterpart image in Figure 4.2 as closely as possible. A sample calculation of Delta for the largest and smallest apertures in Test A is illustrated in Figure 4.3. For all apertures across the three tests, Delta is greater than the recommended minimum value of 50 counts [34]. These values are also given in Table 4.2.

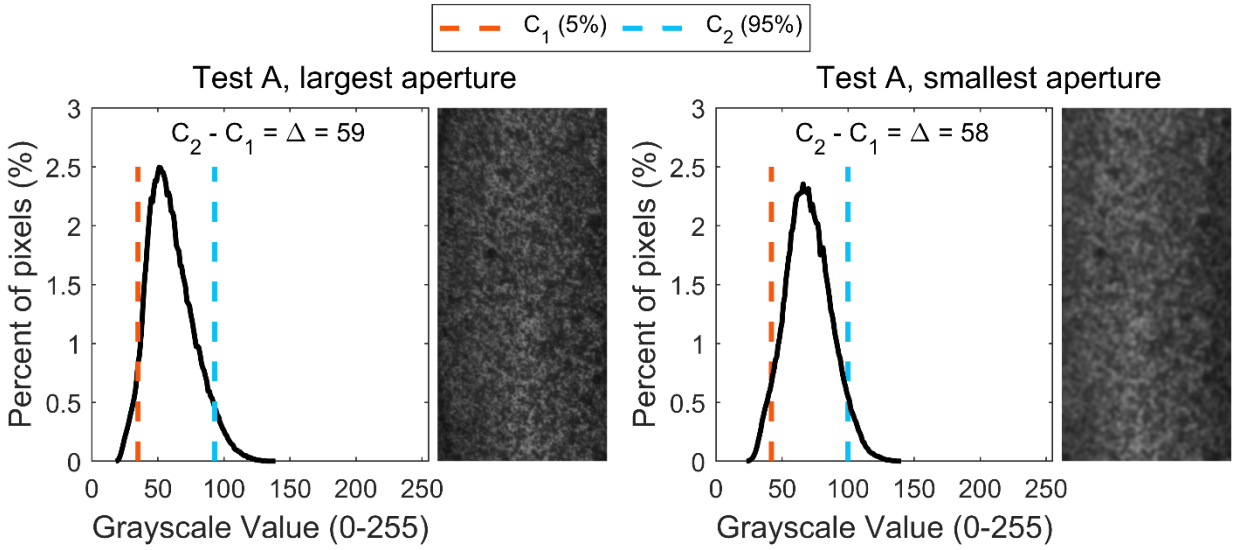

Figure 4.3: Sample calculation of Delta for Test A, showing the largest and smallest apertures.

Once all 172 reference-final image pairs were obtained, the image pairs were post-processed in Vic-2D, a commercial DIC algorithm which is widely used in the experimental mechanics community [35]. The correlation was performed using a subset size of 29 pixels for

Test A, 15 pixels for Test B, and 19 pixels for Test C, and a step size of 4 pixels for all three tests. As seen in the representative subsets in Figure 4.2, the subsets used in each test capture roughly 3 speckles per subset. The subset sizes were chosen to be as small as possible while still allowing images from the smallest aperture (and largest depth of field) to correlate in Vic-2D. Thus, while subset size varies between tests, it remains consistent across aperture sizes within each test.

The size of the Airy disk for each aperture in each test was then calculated using Equation 4.1 [36]:

$$d = \frac{2.44 * \lambda * R}{a} \qquad (Eq. 4.1)$$

where d is the diameter of the Airy disk (in m), λ is the wavelength of the light source (470 x 10^{-9} m), R is the distance between the aperture and the specimen, and a is the aperture diameter.

This calculated Airy disk diameter was also converted into units of pixels, and then the aspect ratio of the Airy disk diameter to the size of the subset was calculated (d/subset size). The values of Airy disk diameter in both mm and pixels, as well as the aspect ratio of Airy disk to subset width, are all given in Table 4.2.

4.5. Results

The DIC-measured in-plane displacement generally showed good agreement with the applied displacement, although there is spatial variation between subsets, as demonstrated in Figure 4.4. The figure shows the maximum applied displacement of 0.0762 mm at the neutral working distance in Test A, with a measured mean translation of 0.0702 mm and a standard deviation of 0.108 μm. These values are well within the resolution of the translation stage, for which the smallest tick mark is 0.0254 mm. This spatial variation is an indication of the noise of

the measurement, as the actual displacement field of a specimen undergoing rigid body translation would nominally be spatially uniform.

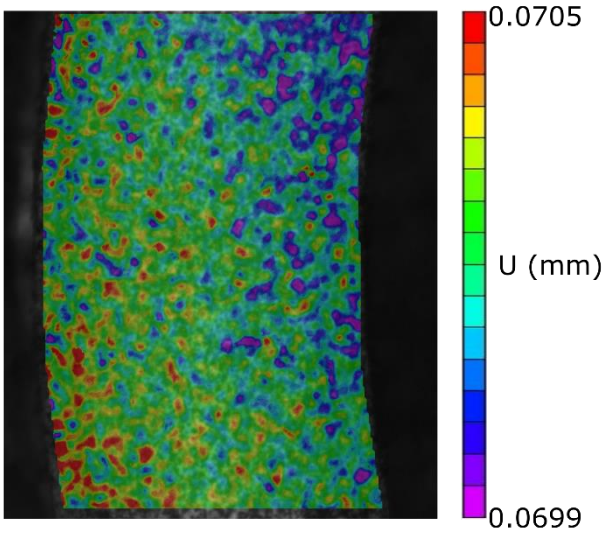

Figure 4.4: DIC contour showing the maximum U displacement (translation in-plane or in the x direction) for the neutral working distance of Test A using the largest aperture size.

The DIC measured in-plane displacements of Test A are plotted as a function of the out-of-plane displacements in the upper portion of Figure 4.5. For ease of comparison between all three tests, the out-of-plane displacements are reported as a percentage of the working distance. The plot includes a horizontal solid line, representing the applied displacement of 0.0762 mm. To capture the spatial variation of the displacement due to measurement noise, each measurement is plotted as a mean and three standard deviations. Each of the four aperture diameters used in Test A are plotted in different colors and markers, showing the effect of the aperture size on the noise of the measurement. It should be noted that the smallest tick mark on the translation stage is 0.0254 mm, which means that the uncertainty of the applied translation due to stage resolution is ± 0.0127

mm. This stage resolution confidence interval is represented in the plot by the dashed lines above and below the solid horizontal line.

The bottom portion of Figure 4.5 shows the size of the uncertainty bands from the upper portion of the figure, still as a function of the out-of-plane displacements. The uncertainty bands are given in units of mm, and the markers showing uncertainty band size are connected by a solid line for each aperture. It should be noted that, for the larger aperture diameters, the size of the uncertainty bands is greater at the furthest out-of-plane displacements (the far left and right of the plot) than at the center of the plot where the image is in the best focus.

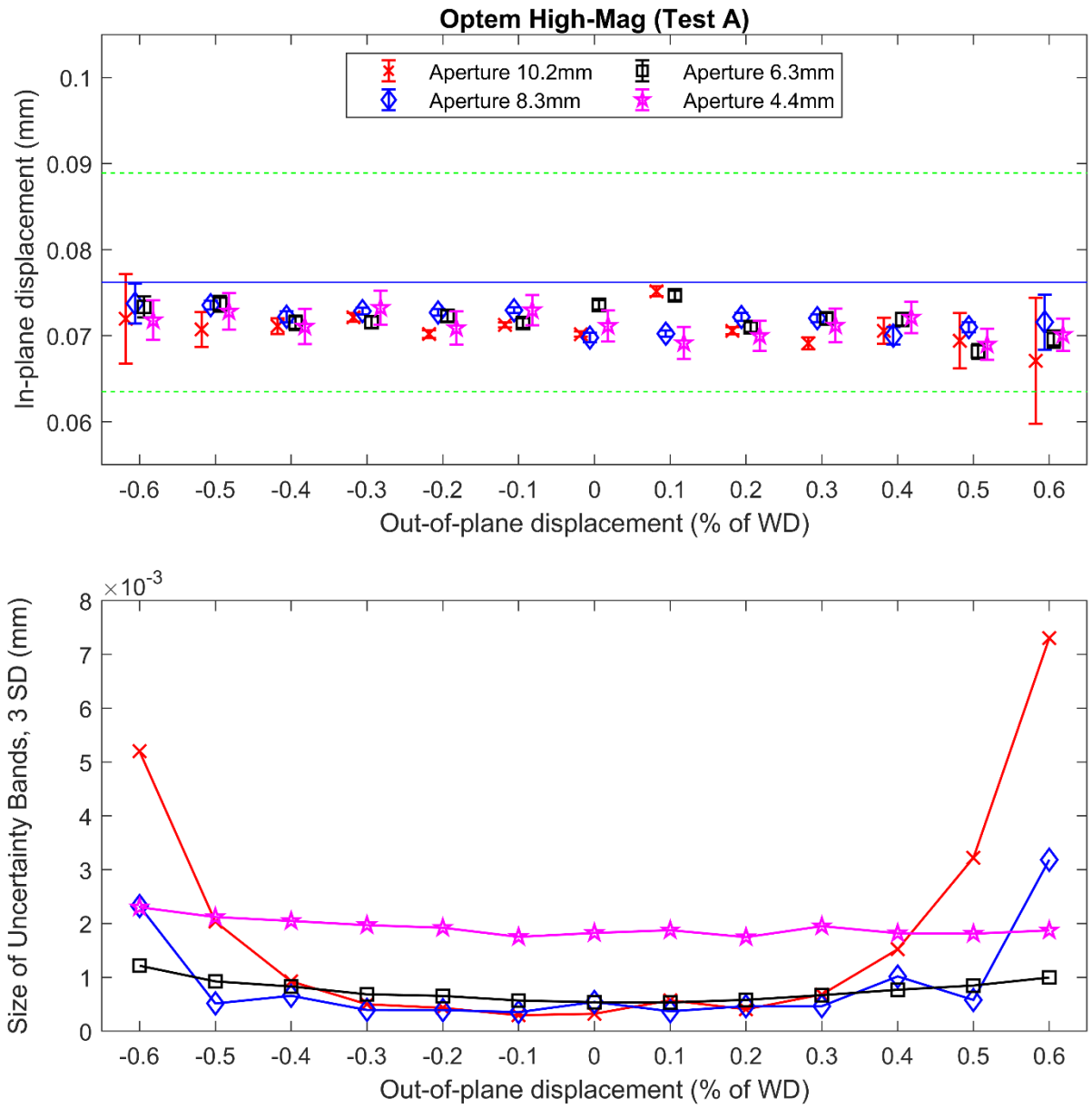

Figure 4.5: Optem High-Magnification (Test A) measured in-plane translation reported in mm (above), and the size of the uncertainty bands, representing 3 standard deviations of spatial variation and reported in mm (below), as a function of out-of-plane motion, reported as a percentage of the working distance.

The displacements measured in Test B are plotted in the upper portion Figure 4.6. The plots are very similar to those from Test A, but the uncertainty bands are more consistently large across

all out-of-plane displacements, as can be seen in the lower portion of the figure. Note that the vertical axes of the first plot in Figure 4.6 are at the same scale as in Figure 4.5, although the magnitude of the measurement is 10 times larger so the y-axis is centered on a different value (0.762 mm as opposed to 0.0762 mm). The bottom portions of Figure 4.5 and Figure 4.6, however, have the same y-axis values.

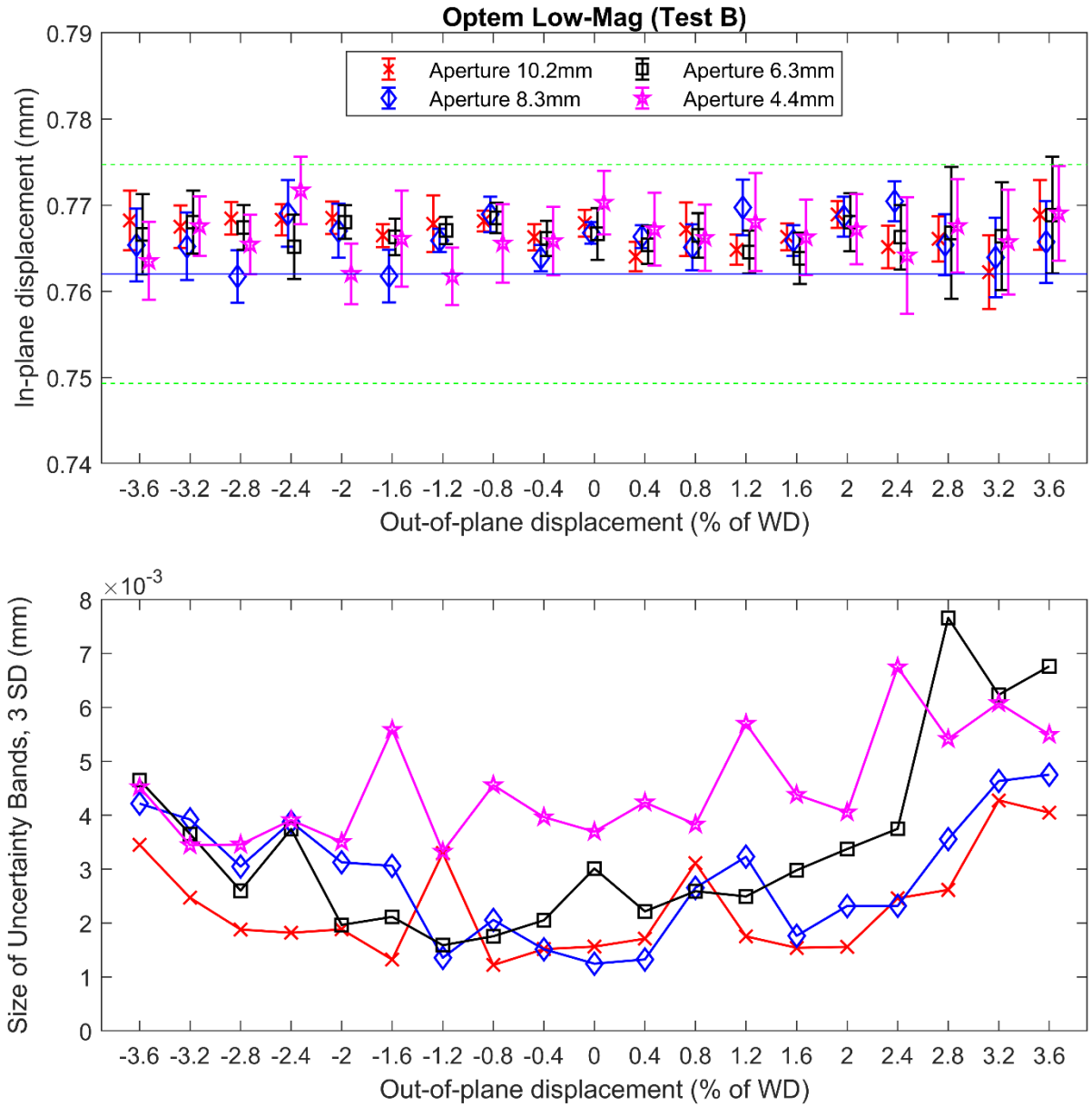

Figure 4.6: Optem Low-Magnification (Test B) measured in-plane translation reported in mm (above), and the size of the uncertainty bands, representing 3 standard deviations of spatial variation and reported in mm (below), as a function of out-of-plane motion, reported as a percentage of the working distance.

The displacements measured and accompanying uncertainty band sizes in Test C are plotted in Figure 4.7. The plots have features similar to those from Tests A and B. The magnitude of applied displacement is the same as Test B (as seen in the y-axis of the upper portion of the figures). The uncertainty bands are more comparable to those seen in Test A than Test B. However, the uncertainty band sizes are roughly 2-3 times larger than in either Test A or Test B and they exceed the uncertainty of the applied displacement at the furthest out-of-plane displacements for some aperture sizes.

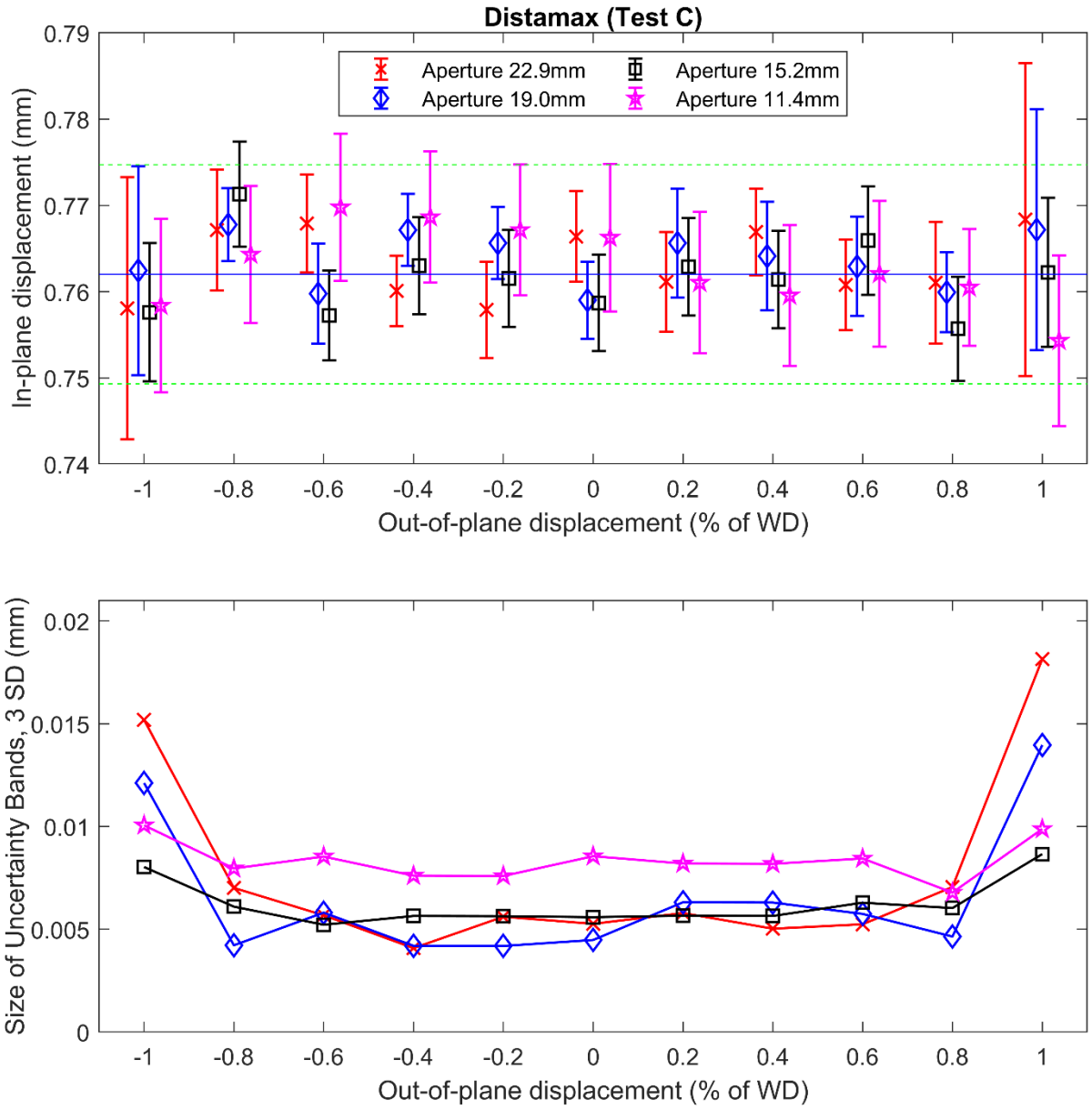

Figure 4.7: Distamax (Test C) measured in-plane translation reported in mm (above), and the size of the uncertainty bands, representing 3 standard deviations of spatial variation and reported in mm (below), as a function of out-of-plane motion, reported as a percentage of the working distance.

4.6. Discussion

For the largest aperture sizes in each of the three tests, the spatial variation of the displacement increased as the specimen was moved further away from the center of the depth of field. This is manifested in the growing size of uncertainty bands as the out-of-plane displacement increases in Figure 4.5 and Figure 4.7, and causes the ‘U’ shape for the red line in the bottom of each figure. This behavior is consistent with poor depth of field due to the large apertures. For larger apertures, moving closer to or further away from the camera after achieving ideal focus would be expected to cause blurring and consequently focus would decrease. This is clearly the case for these larger apertures, as the worsening focus increases the noise of the measurement at the far left and right of the plots. This is demonstrated visually in the top row of Figure 4.8, which presents an excerpt of the same speckle from test A through the different combinations of aperture sizes and working distances. The figure also includes a white square which indicates the subset size. This top row shows the speckle blurring as the specimen is brought forward towards the camera, demonstrating the poor depth of field at this largest aperture.

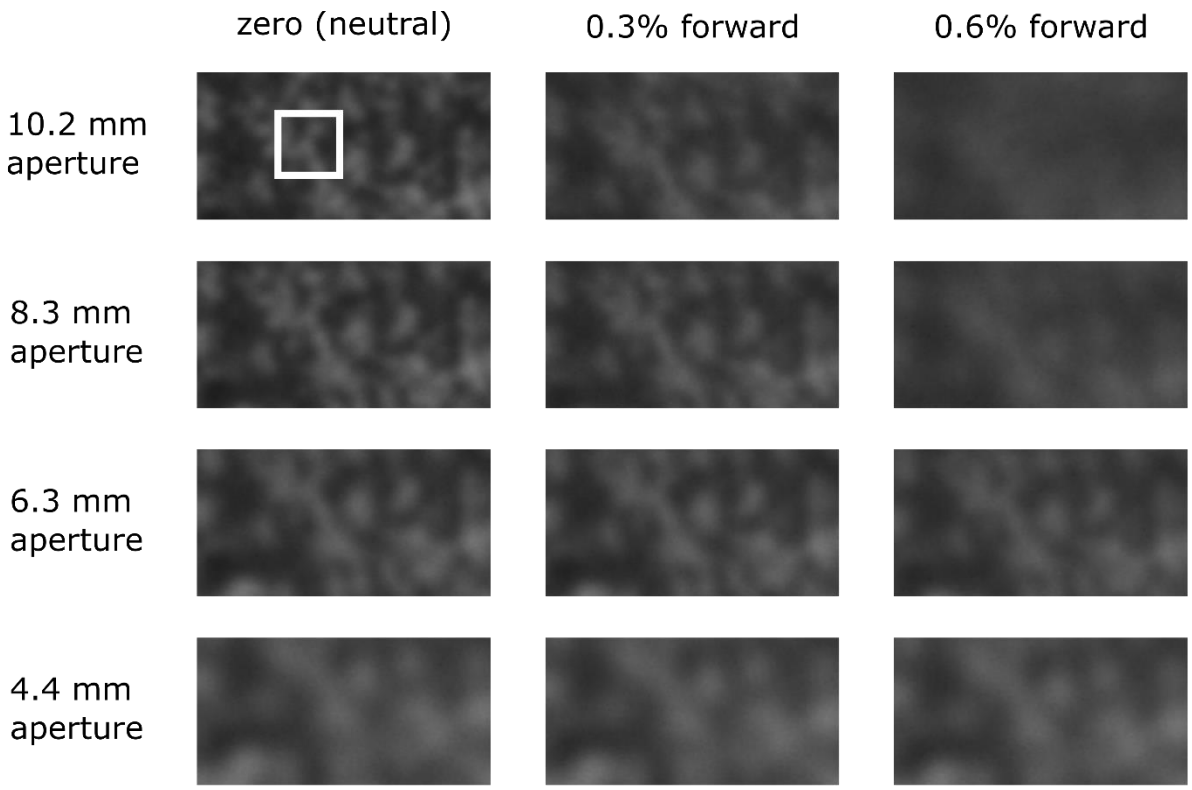

Figure 4.8: Comparison of the same speckled region from Test A through changes in aperture and working distance. The columns show different out-of-plane displacements, demonstrating the depth of field, and the rows show different aperture sizes, demonstrating the effect of Airy disk size. The subset size is shown by the white box.

4.6.1. Effect of Working Distance

For smaller apertures, the depth of field is expected to improve at larger out of plane displacements, leaving less image blurring and less measurement noise than what is experienced with larger apertures. This can also be seen clearly in Figure 4.5 and Figure 4.7, as uncertainty band size at the greatest out-of-plane displacements becomes smaller as the aperture diameter decreases. Looking at the bottom portion of the figures, this improved depth of field results in the

‘U’ shape of the larger apertures being flattened, as the smaller apertures resemble more of a horizontal line. This can also be confirmed by looking at the right column of Figure 4.8; as the aperture size decreases, the blurring at this furthest out-of-plane displacement also visibly decreases. This trend holds for the three larger apertures, but in the smallest one the blurring increases as poor depth of field dominates.

Adjusting aperture size changes not only the depth of field, but also the Airy disk size. As smaller apertures are used, the uncertainty in Figure 4.5 through Figure 4.7 becomes less sensitive to the depth of field, but is uniformly larger across all the working distances. This behavior is consistent with noise caused by increasingly larger Airy disks. Thus, although smaller apertures tend to improve measurement error at the extremes of the depth of field, they can also worsen measurement error even at the neutral working distance which offers the best focus. This can be seen in the left column of Figure 4.8, which shows the speckle pattern at this optimal focus where depth of field has little to no effect. As the aperture size decreases in this left column, the blurring increases, especially for the smallest aperture. Clearly, care must be taken to not reduce the aperture size so much that blurring occurs.

Although the three tests show similarities in these trends of depth of field and Airy disk, the magnitude of these impacts varies between the tests. To better compare the three different tests, the data from the bottom portions of Figure 4.5 through Figure 4.7 is plotted on common axes in Figure 4.9. It quickly becomes apparent that Test B is the most forgiving in regards to the effect of both depth of field and Airy disk on the uncertainty band size. This is not surprising, as the depth of field is greater with shorter working distances [37] and with lower magnification factors [38]. Test B has a much lower magnification than Test A at a similar working distance, and a much shorter working distance than Test C at a similar magnification, resulting in the best depth of field

of all three tests. This is easily seen in the less-pronounced ‘U’ shapes in Figure 4.6, and the contrast to the deeper ‘U’ shapes of Tests A and C is more obvious in Figure 4.9.

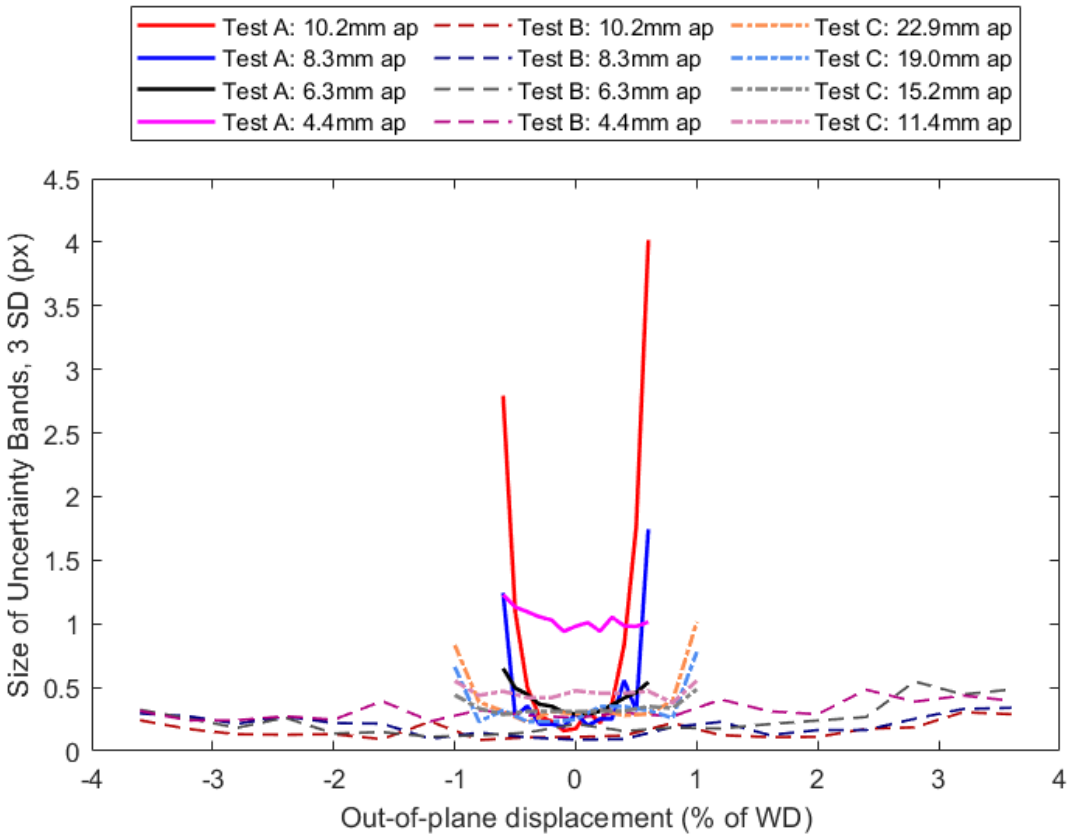

Figure 4.9: Comparison of size of uncertainty bands across all three tests reported in Figure 4.5 through Figure 4.7; Test A data is shown with solid lines, one for each aperture, Test B with darker dashed lines, and Test C with lighter dotted lines. All uncertainty band sizes are reported in units of pixels, and the out-of-plane displacements are reported as a percentage of the working distance.

Test B is similarly insulated from the effects of Airy disk, as the short working distance compared to Test C leads to smaller Airy disks, and the lower magnification compared to Test A means that those Airy disks make up a smaller portion of the subset, as seen in Table 4.2. Thus,

Airy disks are not nearly as impactful to the correlation and to the noise of the resulting measurement for Test B as for Tests A and C. The limited impact of Airy disks on Test B explains why the smallest aperture only minimally raises the uncertainty band size at all working distances in Figure 4.6. Because Test B is less sensitive to error from depth of field or Airy disks, the other error sources dominate. This is apparent in the random fluctuations in uncertainty band size at different working distances in Figure 4.6, making Test B appear nosier than Tests A and C. However, the side-by-side plots in Figure 4.9 show that this random variation between working distances is comparable for all three tests.

The side-by-side comparison of all three tests in Figure 4.9 highlights other important differences between the tests. Test A had roughly 10 times the magnification of the other tests, and Test C had roughly 10 times the working distance of the others, meaning that Test A and C included factors that made each of them more prone to both depth of field and Airy disk issues. However, as far as uncertainty band size in pixels, Test A showed the greatest increase (the worst noise) when using the smallest aperture allowed. This seems to show that higher magnifications (like Test A) are more sensitive to the effects of both depth of field and Airy disk than longer working distances (like Test C), and both are more sensitive than the low magnification and short working distances in Test B.

4.6.2. Effect of Airy Disk Size

These tests have demonstrated that in addition to the effect of aperture size on depth of field, its effect on Airy disk size should also be considered, particularly when looking at high magnifications and/or long working distances. Because the long range DIC tests spans two working distances (Tests A & B vs Test C) and two length scales (Test A vs Tests B & C), it is

beneficial to observe the data in a way that directly compares the Airy disk size between the three tests. In part (a) of Figure 4.10, the data from Figure 4.9 is plotted as a function of the Airy disk size, calculated from Equation 4.1, and normalized for the different test parameters by reporting it as an aspect ratio of Airy disk diameter to subset width as shown in Table 4.2.

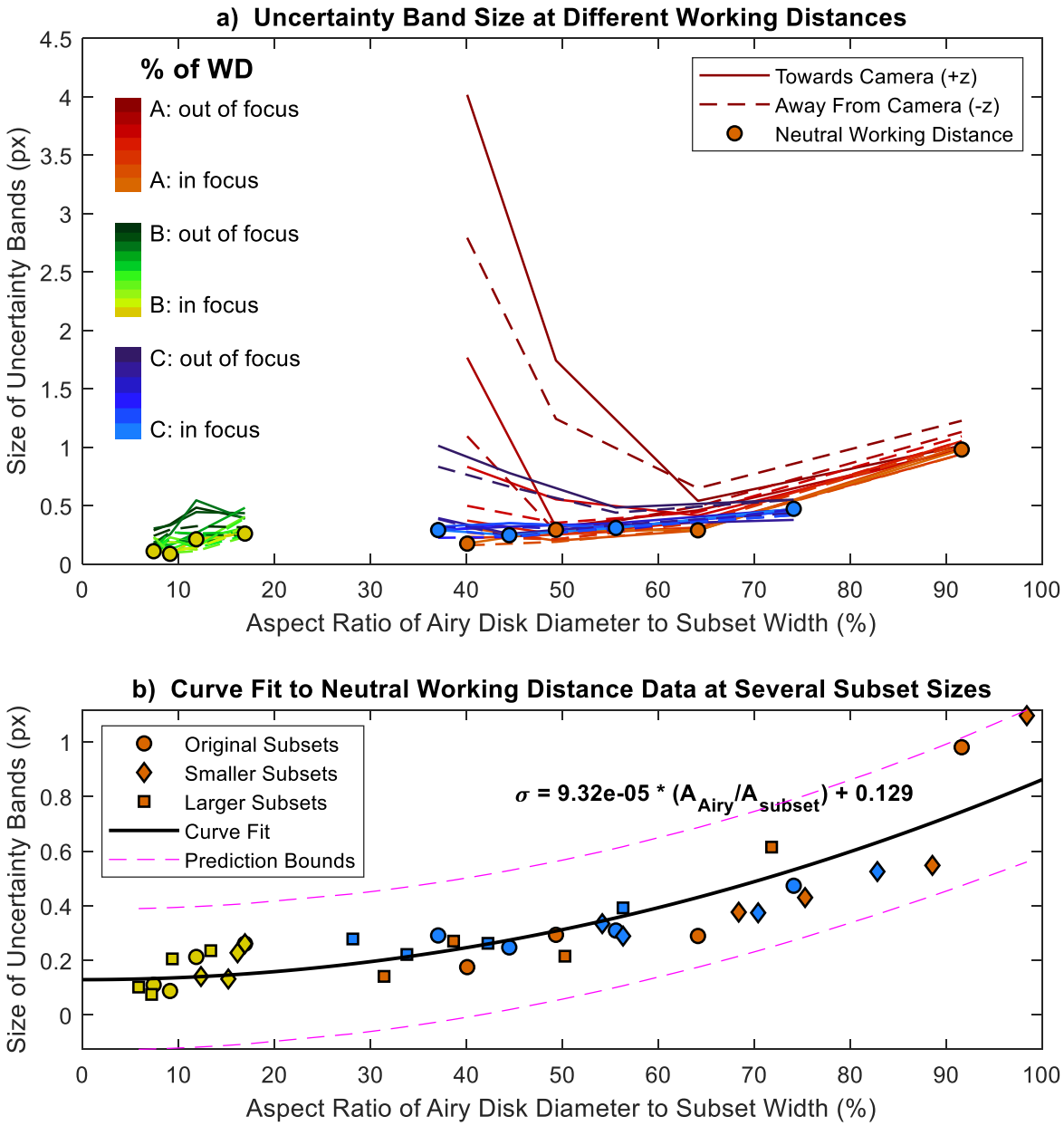

Figure 4.10: Comparison of the effect of Airy disk size on the three tests. In a) the size of uncertainty bands in pixels as a function of the aspect ratio of Airy disk diameter to subset width.

Each test is color coded, with lighter colors being closer to the neutral working distance of best focus and darker colors showing data from further out-of-plane displacement. In b) the results at the neutral working distances from part a) are plotted, with additional data from smaller and larger subsets. The black line shows the second-order polynomial curve fit.

Figure 4.10(a) again shows the similarities between Tests A and C. Due to the angular nature of the diffraction of light, the Airy disks at the longer working distance (Test C) were calculated to be roughly an order of magnitude larger than those at the shorter distances (Tests A & B). However, because the magnification in Tests B & C was much smaller than in Test A, the proportion of the images filled by each Airy Disk in Test C was more comparable to the proportions in Test A than Test B, as can be seen in the figure.

The lines representing the different working distances for Tests A and C highlight a key feature in the tradeoff between depth of field and Airy disk. For the smallest Airy disk aspect ratios, the uncertainty band size drops significantly as the out-of-plane displacement is reduced, showing the sensitivity associated with poor depth of field. As the aperture size decreases (and consequently the Airy disk grows larger, moving towards the right of Figure 4.10), the spread between the lines showing different working distances predictably shrinks as the further out-of-plane displacement produces lower uncertainty. However, this decrease in measurement noise is not unbounded, as virtually all of the lines from Tests A and C eventually begin to rise, showing increasing noise with larger Airy disk size. This demonstrates that at a certain point, the gains in depth of field made by smaller apertures are overcome by the losses in focus resulting from growing Airy disks.

To demonstrate the effect that Airy disk size has on uncertainty band size independent of depth of field effects, the 12 data points (3 tests x 4 apertures) from the neutral working distance

are indicated by circles in Figure 4.10(a). These show a definite trend of increasing uncertainty as the airy disk diameter increases. To demonstrate that this holds for other subset sizes, the image sets were correlated again in Vic-2D, but with varying subset sizes. One set of 12 data points was generated using the smallest subset size that would correlate at each aperture, and another set of 12 with larger subset sizes than the original. These subset sizes are given in Table 4.3. A second order polynomial was fitted to these 36 data points, shown by the black line in the figure. The equation of the fitted polynomial is also shown in Figure 4.10(b), where σ is the size of the uncertainty bands in pixels (three standard deviations) written in terms of the circular area of the Airy disk, A_{Airy}, and the square area of the subset, A_{subset}. Please note that the plot x-axis is in units of the dimension aspect ratio (diameter/width), while the equation is given in units of area ratio (area/area).

Table 4.3: Summary of subset sizes used in Figure 4.10(b)

		Test A				Test B				Test C			
Aperture size (mm)		10.2	8.3	6.3	4.4	10.2	8.3	6.3	4.4	22.9	19.0	15.2	11.4
Subset Size (px)	Smaller	17	19	21	27	9	9	11	15	13	15	15	17
	Original	29	29	29	29	15	15	15	15	19	19	19	19
	Larger	37	37	37	37	19	19	19	19	25	25	25	25

Although the exact numbers of this equation are not necessarily applicable to all possible high magnification and long working distance DIC setups, the equation still demonstrates the physical relationship. Even if an Airy disk were to be so small as to approach zero on the horizontal axis and there was no loss of focus due to out-of-plane motion, there would still be some spatial variation due to other sources of noise. This is represented by the y-intercept of the equation, in this case 0.129 pixels. However, as the area obscured by the Airy disk grows, the uncertainty of the measurement grows as well. Somewhat surprisingly, the aspect ratio at which this contribution

becomes significant is quite large. By looking at the convergence of the downward curves in Figure 4.10(a), it can be seen the Airy disk begins causing uncertainty band size to increase again. This is where the depth of field effects (seen in those individual lines of part (a)) begin to meet the Airy disk effects (seen in the curve fit of part (b)), which corresponds to an aspect ratio of roughly 60-70%. Even though the Airy disk diameter at that point is roughly two-thirds of the span of the subset, this seems to be the 'sweet spot' at which the Airy disk and depth of field effects are best balanced. Thus, aperture can be reduced up until this point, improving depth of field without significantly compromising focus due to the Airy disk. Alternatively, one can increase the subset size used in the DIC calculation, but this comes at the expense of spatial resolution.

4.6.3. Additional Considerations

As previously noted in the methods section, the aperture on the lens not only affects Airy disks and depth of field, but it also affects lighting. There are five main ways to control lighting, each with its own tradeoffs. When performing DIC, it is generally advised (1) to use as bright a light source as is safely available, and to select (2) the exposure time on the camera and (3) the aperture on the lens based on the needs of the experiment [39]. For example, high speed tests require short exposure times to avoid motion blur [40], [41] while large out-of-plane displacements demand small apertures to improve depth of field [37]. Lighting can also be increased (4) by increasing the gain on the camera amplifier, but this results in a noisy measurement and should generally be avoided at all costs [42]. Lastly, lighting can be artificially controlled (5) through post-processing of images [43] but this also carries a risk of corrupting the measurement. Because the tests in this paper were all quasi-static and thus carried no risk of motion blur, we chose to offset changes in lighting due to aperture by changing exposure time. As seen in the delta contrast values of Table 4.2, varying the exposure time successfully led to consistent lighting and contrast

conditions. For Tests A and C, those contrast values stayed within one count of each other across the different apertures for their respective tests. Test B stayed within an acceptable ten count range; the consistency across apertures in this test was limited by the size of exposure time increments for the camera (note in Table 4.2 that the range of exposure times is much smaller for Test B than for Tests A and C).

It is worth noting that diffraction limits also depend on the wavelength of light, as seen in Equation 4.1. Blue lights were used throughout these tests, but in principle one could reduce the Airy disks by switching to ultraviolet (UV), which has a shorter wavelength [44]. There are currently no known commercially available lenses which can perform at (i) high magnification, (ii) long working distances, and (iii) transmit in UV. There exists a custom-built UV lens that can be used at a working distance of 10 inches, comparable to tests A and B [21], but there isn't a UV high-magnification lens that can be used at the 8 foot working distance featured in Test C.

Ultimately, long range DIC enables users to study more challenging environments *in situ* without sacrificing the camera. However, such measurements often involve environmental chambers which place a window between the camera and specimen, so additional consideration should be given to thick-glass distortions in these cases [45], [46]. For example, the Hot Fuel Examination Facility at Idaho National Laboratory is uniquely positioned to take in-situ measurements of irradiated materials within the environmental chamber, with the specimen visible through thick leaded glass windows [47]. The principles of high magnifications and long working distances discussed in this work can greatly benefit DIC measurements in hot cells such as these, as long as thick glass distortions are considered.

4.7. Conclusion

In DIC, it is often recommended to perform tests using lenses with as small of an aperture as possible while maintaining sufficient lighting in order to maximize depth of field. However, when performing DIC at long ranges and high magnifications, the aperture of the lens introduces competing phenomena. Larger apertures admit more light and are less sensitive to the diffraction limit of light but have poor depth of field. Conversely, smaller apertures admit less light (thus producing significantly darker images) and have better depth of field but are more sensitive to diffraction limits. The intensity of light can be controlled by other means which include using brighter light sources or increasing exposure time on the camera sensor. The remaining considerations -- diffraction limits and depth of field -- must be weighed when selecting an aperture in the experimental design. In seeking to improve focus of the image by reducing aperture, care must be taken to not cause large Airy disks, which also lead to blurring of the image. It is recommended that aperture size not be reduced such that the Airy disk diameter exceeds two-thirds of the width of the DIC subset.

4.8. Acknowledgements

The authors would like to thank the US Nuclear Regulatory Commission for supporting this work under award number NRC-HQ-84-15-G0033. RSH would also like to thank the US Department of Energy Office of Nuclear Energy for his fellowship from the Integrated University Program. This material is based upon work supported under an Integrated University Program Graduate Fellowship. Any opinions, findings, conclusions, or recommendations expressed in this publication are those of the author and do not necessarily reflect the views of the Department of Energy Office of Nuclear Energy.

4.9. References

[1] M. A. Sutton, J. J. Orteu, and H. Schreier, *Image Correlation for Shape, Motion and Deformation Measurements: Basic Concepts,Theory and Applications*. Springer Science & Business Media, 2009.

[2] K. G. Field, M. N. Gussev, X. Hu, Y. Yamamoto, and R. H. Howard, "First Annual Progress Report on Radiation Tolerance of Controlled Fusion Welds in High Temperature Oxidation Resistant FeCrAl Alloys," Oak Ridge National Lab. (ORNL), Oak Ridge, TN (United States), ORNL/TM-2015/770, Dec. 2015. doi: 10.2172/1235007.

[3] B. Pan, K. Qian, H. Xie, and A. Asundi, "Two-dimensional digital image correlation for in-plane displacement and strain measurement: a review," *Meas. Sci. Technol.*, vol. 20, no. 6, p. 062001, Apr. 2009, doi: 10.1088/0957-0233/20/6/062001.

[4] Z. Chen, W. Lenthe, J. C. Stinville, M. Echlin, T. M. Pollock, and S. Daly, "High-Resolution Deformation Mapping Across Large Fields of View Using Scanning Electron Microscopy and Digital Image Correlation," *Exp. Mech.*, vol. 58, no. 9, pp. 1407–1421, Nov. 2018, doi: 10.1007/s11340-018-0419-y.

[5] A. D. Kammers and S. Daly, "Digital Image Correlation under Scanning Electron Microscopy: Methodology and Validation," *Exp. Mech.*, vol. 53, no. 9, pp. 1743–1761, Nov. 2013, doi: 10.1007/s11340-013-9782-x.

[6] P. R. Gradl, "Digital Image Correlation Techniques Applied to Large Scale Rocket Engine Testing," presented at the AIAA Propulsion and Power 2016 Conference, Salt Lake City, UT, United States, Jul. 2016, Accessed: Feb. 26, 2020. [Online]. Available: https://ntrs.nasa.gov/search.jsp?R=20160009712.

[7] B. Koohbor, A. Kidane, M. A. Sutton, X. Zhao, and S. Mallon, "Analysis of dynamic bending test using ultra high speed DIC and the virtual fields method," *Int. J. Impact Eng.*, vol. 110, pp. 299–310, Dec. 2017, doi: 10.1016/j.ijimpeng.2016.12.021.

[8] Z. Pan, S. Huang, Y. Su, M. Qiao, and Q. Zhang, "Strain field measurements over 3000 ℃ using 3D-Digital image correlation," *Opt. Lasers Eng.*, vol. 127, p. 105942, Apr. 2020, doi: 10.1016/j.optlaseng.2019.105942.

[9] Z. Chen and S. H. Daly, "Active Slip System Identification in Polycrystalline Metals by Digital Image Correlation (DIC)," *Exp. Mech.*, vol. 57, no. 1, pp. 115–127, Jan. 2017, doi: 10.1007/s11340-016-0217-3.

[10] S. Maraghechi, J. P. M. Hoefnagels, R. H. J. Peerlings, O. Rokoš, and M. G. D. Geers, "Correction of Scanning Electron Microscope Imaging Artifacts in a Novel Digital Image Correlation Framework," *Exp. Mech.*, vol. 59, no. 4, pp. 489–516, 2019, doi: 10.1007/s11340-018-00469-w.

[11] C. C. Tasan, J. P. M. Hoefnagels, M. Diehl, D. Yan, F. Roters, and D. Raabe, "Strain localization and damage in dual phase steels investigated by coupled in-situ deformation

experiments and crystal plasticity simulations," *Int. J. Plast.*, vol. 63, pp. 198–210, Dec. 2014, doi: 10.1016/j.ijplas.2014.06.004.

[12] J. C. Stinville, M. P. Echlin, D. Texier, F. Bridier, P. Bocher, and T. M. Pollock, "Sub-Grain Scale Digital Image Correlation by Electron Microscopy for Polycrystalline Materials during Elastic and Plastic Deformation," *Exp. Mech.*, vol. 56, no. 2, pp. 197–216, Feb. 2016, doi: 10.1007/s11340-015-0083-4.

[13] Z. Zhao, M. Ramesh, D. Raabe, A. M. Cuitiño, and R. Radovitzky, "Investigation of three-dimensional aspects of grain-scale plastic surface deformation of an aluminum oligocrystal," *Int. J. Plast.*, vol. 24, no. 12, pp. 2278–2297, Dec. 2008, doi: 10.1016/j.ijplas.2008.01.002.

[14] T. Merzouki, C. Collard, N. Bourgeois, T. Ben Zineb, and F. Meraghni, "Coupling between measured kinematic fields and multicrystal SMA finite element calculations," *Mech. Mater.*, vol. 42, no. 1, pp. 72–95, Jan. 2010, doi: 10.1016/j.mechmat.2009.09.003.

[15] A. D. Kammers and S. Daly, "Self-Assembled Nanoparticle Surface Patterning for Improved Digital Image Correlation in a Scanning Electron Microscope," *Exp. Mech.*, vol. 53, no. 8, pp. 1333–1341, Oct. 2013, doi: 10.1007/s11340-013-9734-5.

[16] J. Liang, Z. Wang, H. Xie, and X. Li, "In situ scanning electron microscopy-based high-temperature deformation measurement of nickel-based single crystal superalloy up to 800 °C," *Opt. Lasers Eng.*, vol. 108, pp. 1–14, Sep. 2018, doi: 10.1016/j.optlaseng.2018.04.016.

[17] J. Ma *et al.*, "A novel instrument for investigating the dynamic microstructure evolution of high temperature service materials up to 1150 °C in scanning electron microscope," *Rev. Sci. Instrum.*, vol. 91, no. 4, p. 043704, Apr. 2020, doi: 10.1063/1.5142807.

[18] J. Carroll, W. Abuzaid, J. Lambros, and H. Sehitoglu, "An experimental methodology to relate local strain to microstructural texture," *Rev. Sci. Instrum.*, vol. 81, no. 8, p. 083703, Aug. 2010, doi: 10.1063/1.3474902.

[19] G. J. Pataky and H. Sehitoglu, "Experimental Methodology for Studying Strain Heterogeneity with Microstructural Data from High Temperature Deformation," *Exp. Mech.*, vol. 55, no. 1, pp. 53–63, Jan. 2015, doi: 10.1007/s11340-014-9926-7.

[20] R. S. Hansen, D. W. Waldram, T. Q. Thai, and R. B. Berke, "Super Resolution Digital Image Correlation (SR-DIC): An Alternative to Image Stitching at High Magnifications," *Exp. Mech.*, vol. Recently Accepted, Apr. 2021.

[21] R. S. Hansen, T. J. Bird, R. Voie, K. Z. Burn, and R. B. Berke, "A high magnification UV lens for high temperature optical strain measurements," *Rev. Sci. Instrum.*, vol. 90, no. 4, p. 045117, Apr. 2019, doi: 10.1063/1.5081899.

[22] E. H. K. Stelzer, "Beyond the diffraction limit?," *Nature*, vol. 417, no. 6891, Art. no. 6891, Jun. 2002, doi: 10.1038/417806a.

[23] A. M. H. Wong and G. V. Eleftheriades, “Sub-Wavelength Focusing at the Multi-Wavelength Range Using Superoscillations: An Experimental Demonstration,” *IEEE Trans. Antennas Propag.*, vol. 59, no. 12, pp. 4766–4776, Dec. 2011, doi: 10.1109/TAP.2011.2165518.

[24] V. Tychinsky, “Wavefront dislocations and registering images inside the Airy disk,” *Opt. Commun.*, vol. 81, no. 1, pp. 131–137, Feb. 1991, doi: 10.1016/0030-4018(91)90307-Y.

[25] A. M. H. Wong and G. V. Eleftheriades, “An Optical Super-Microscope for Far-field, Real-time Imaging Beyond the Diffraction Limit,” *Sci. Rep.*, vol. 3, no. 1, Art. no. 1, Apr. 2013, doi: 10.1038/srep01715.

[26] Correlated Solutions, “Vic-3D 8: Testing Guide.” Irmo, South Carolina, 2018.

[27] H. Nagahara, S. Kuthirummal, C. Zhou, and S. K. Nayar, “Flexible Depth of Field Photography,” in *Computer Vision – ECCV 2008*, Berlin, Heidelberg, 2008, pp. 60–73, doi: 10.1007/978-3-540-88693-8_5.

[28] B. Reedlunn, S. Daly, L. Hector, P. Zavattieri, and J. Shaw, “Tips and Tricks for Characterizing Shape Memory Wire Part 5: Full-Field Strain Measurement by Digital Image Correlation,” *Exp. Tech.*, vol. 37, no. 3, pp. 62–78, 2013, doi: 10.1111/j.1747-1567.2011.00717.x.

[29] K. Trantham and T. J. Reece, “Demonstration of the Airy disk using photography and simple light sources,” *Am. J. Phys.*, vol. 83, no. 11, pp. 928–934, Oct. 2015, doi: 10.1119/1.4927525.

[30] M. Martinello *et al.*, “Dual Aperture Photography: Image and Depth from a Mobile Camera,” in *2015 IEEE International Conference on Computational Photography (ICCP)*, Apr. 2015, pp. 1–10, doi: 10.1109/ICCPHOT.2015.7168366.

[31] P. Green, W. Sun, W. Matusik, and F. Durand, “Multi-aperture photography,” in *ACM SIGGRAPH 2007 papers*, San Diego, California, Jul. 2007, pp. 68-es, doi: 10.1145/1275808.1276462.

[32] K. N. Jonnalagadda *et al.*, “Experimental Investigation of Strain Rate Dependence of Nanocrystalline Pt Films,” *Exp. Mech.*, vol. 50, no. 1, pp. 25–35, Jan. 2010, doi: 10.1007/s11340-008-9212-7.

[33] T. Q. Thai, R. S. Hansen, A. J. Smith, J. Lambros, and R. B. Berke, “Importance of Exposure Time on DIC Measurement Uncertainty at Extreme Temperatures,” *Exp. Tech.*, vol. 43, no. 3, pp. 261–271, Jun. 2019, doi: 10.1007/s40799-019-00313-3.

[34] P. Reu, “Stereo-rig Design: Lighting—Part 5,” *Exp. Tech.*, vol. 37, no. 3, pp. 1–2, 2013, doi: https://doi.org/10.1111/ext.12020.

[35] Correlated Solutions, “Vic-2D User Manual.” Irmo, South Carolina, 2009.

[36] U. Rivera-Ortega and B. Pico-Gonzalez, “Wavelength estimation by using the Airy disk from a diffraction pattern with didactic purposes,” *Phys. Educ.*, vol. 51, no. 1, p. 015012, Dec. 2015, doi: 10.1088/0031-9120/51/1/015012.

[37] B. Van Mieghem, J. Ivens, and A. Van Bael, “Benchmarking of depth of field for large out-of-plane deformations with single camera digital image correlation,” *Opt. Lasers Eng.*, vol. 91, pp. 134–143, Apr. 2017, doi: 10.1016/j.optlaseng.2016.11.019.

[38] G. N. Fokoua, A. Durand, and P. Cuvelier, “Ombroscopic imaging and PTV to reduce the depth of field in a flow with strong curvature effects,” *Opt. Lasers Eng.*, vol. 137, p. 106386, Feb. 2021, doi: 10.1016/j.optlaseng.2020.106386.

[39] T. Thai, “Improvement of Ultraviolet Digital Image Correlation (UV-DIC) at Extreme Temperatures,” PhD Dissertation, Utah State University, Logan, UT, 2020.

[40] T. Q. Thai, A. J. Smith, R. J. Rowley, P. R. Gradl, and R. B. Berke, “Change of exposure time mid-test in high temperature DIC measurement,” *Meas. Sci. Technol.*, vol. 31, no. 7, p. 075402, Apr. 2020, doi: 10.1088/1361-6501/ab7bbf.

[41] E. Zappa, P. Mazzoleni, and A. Matinmanesh, “Uncertainty assessment of digital image correlation method in dynamic applications,” *Opt. Lasers Eng.*, vol. 56, pp. 140–151, May 2014, doi: 10.1016/j.optlaseng.2013.12.016.

[42] International Digital Image Correlation Society *et al.*, “A Good Practices Guide for Digital Image Correlation,” International Digital Image Correlation Society, Oct. 2018. doi: 10.32720/idics/gpg.ed1.

[43] T. Archer, P. Beauchêne, C. Huchette, and F. Hild, “Global digital image correlation up to very high temperatures with grey level corrections,” *Meas. Sci. Technol.*, vol. 31, no. 2, p. 024003, Nov. 2019, doi: 10.1088/1361-6501/ab461e.

[44] R. B. Berke and J. Lambros, “Ultraviolet digital image correlation (UV-DIC) for high temperature applications,” *Rev. Sci. Instrum.*, vol. 85, no. 4, p. 045121, Apr. 2014, doi: 10.1063/1.4871991.

[45] W. A. Take, “Thirty-Sixth Canadian Geotechnical Colloquium: Advances in visualization of geotechnical processes through digital image correlation1,” *Can. Geotech. J.*, Jan. 2015, doi: 10.1139/cgj-2014-0080.

[46] A. Shukla, S. Gupta, H. Matos, and J. M. LeBlanc, “Dynamic Collapse of Underwater Metallic Structures – Recent Investigations: Contributions after the 2011 Murray Lecture,” *Exp. Mech.*, vol. 58, no. 3, pp. 387–405, Mar. 2018, doi: 10.1007/s11340-017-0364-1.

[47] J. L. Schulthess, W. R. Lloyd, B. Rabin, K. Wheeler, and T. W. Walters, “Mechanical properties of irradiated UMo alloy fuel,” *J. Nucl. Mater.*, vol. 515, pp. 91–106, Mar. 2019, doi: 10.1016/j.jnucmat.2018.12.025.

CHAPTER 5
OPTIMIZING THE ARRANGEMENT OF A RING HOOP TENSION TEST FOR NUCLEAR FUEL CLADDING

5.1. Prologue

This work is a concluding report for a summer internship at Idaho National Laboratory. As such, it is not in the format of a full-length paper for submission to a journal, although it has been formatted similarly for readability. Although it is not a full-length paper, the findings presented here are a crucial part of the dissertation, determining the arrangement needed for accurate ring hoop tension testing in subsequent work. The work was performed during the internship as part of the NEUP fellowship program, in collaboration with David Kamerman and Nedim Cinbiz.

5.2. Motivation and Goals

The Ring Hoop Tension Test (RHTT) is a commonly-used testing method for determining hoop direction behavior and material properties. It consists of a ring-shaped specimen cut from a tubular sample, often with a narrowed gauge region, which is placed on two hemicylindrical mandrels. The mandrels are pulled apart, causing tension in the hoop direction of the ring [1]. However, the placement of the gauge region has a great impact on the stress state experienced during the test, and several arrangements and modifications have been proposed. To better understand which of these optimizes performance for obtaining hoop direction properties in the plastic deformation regime, four arrangements have been chosen from literature for finite element modelling. The arrangements were then compared based on their performance according to five different criteria: (1) stress uniaxiality in the hoop direction, (2) strain uniformity throughout the gauge region, (3) concentration of deformation in gauge region, (4) friction sensitivity, and (5)

stress-strain curve extraction. It is anticipated that these results will help inform testing of accident-tolerant fuel cladding or other nuclear fuel cladding, particularly in determining plastic deformation behavior in the hoop direction.

5.3. Description of Test Setups

Four test arrangements from the literature with different orientations of the gauge region and/or grip types were investigated, shown in Figure 5.1. Arrangement A is in the 'top' orientation, where the gauge region is placed on the top of the hemispherical grip. Arrangement B uses the same hemispherical grips, but with the ring rotated 90 degrees so that the gauge region is centered around the gap between the two grips, as in [2]. Arrangement C has the ring rotated 45 degrees [3,4], so it is centered between the locations in A and B. It also uses only one gauge region, rather than the two gauge regions which are used in every other arrangement. Arrangement D uses a dog bone shaped insert to prevent the ring from contracting inwards, and the gauge region is located at the end of the dog bone (where the gap between the two grips would be, at the same location as Arrangement B) [5,6]. The finite element models used in each arrangement took advantage of eighth-symmetry (symmetry across x-y, y-z, and x-z planes), except arrangement C which used half-symmetry (symmetry across the x-y plane, assuming z is out-of-plane in Figure 5.1).

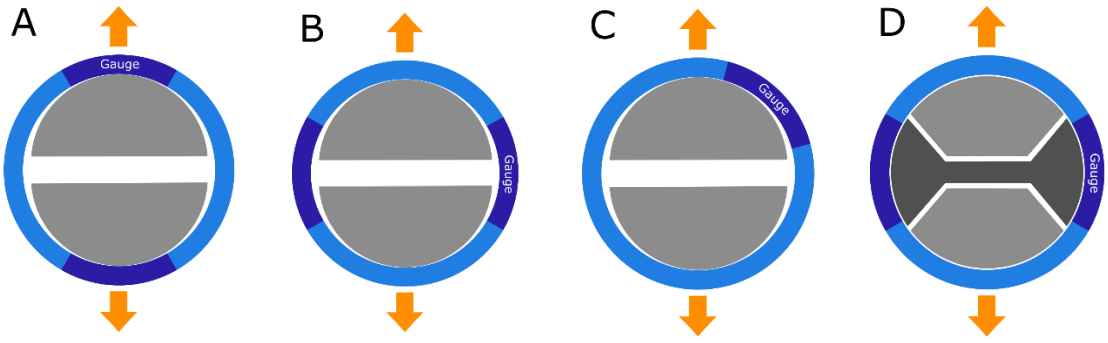

Figure 5.1: Diagram of test arrangements, showing grip type and gauge orientation. Gauge region is shown in dark blue, and direction of loading is shown with the yellow arrows.

The rings were modeled with an outer diameter of 9.5 mm, a wall thickness of 0.57 mm, and a sectioning width of 5 mm. Two different ring specimen models were tested with arrangement A, in order to compare the effects of different gauge sizes. The first, test 1, has a gauge region with length-to-width ratio of 1:1 (2 mm:2 mm). Test 2 is the same 'top' orientation, but with the gauge region having a length-to-width ratio of 4:1 (4 mm:1 mm). A comparison of these gauge sizes is shown in Figure 5.2. For each gauge size, a fillet of 1 mm was used in the transition from the gauge width to the full width of the ring. These gauge dimensions from test 2 were used in tests 3, 4, and 5, in the arrangements B, C, and D, respectively. The tests are summarized in Table 1 below.

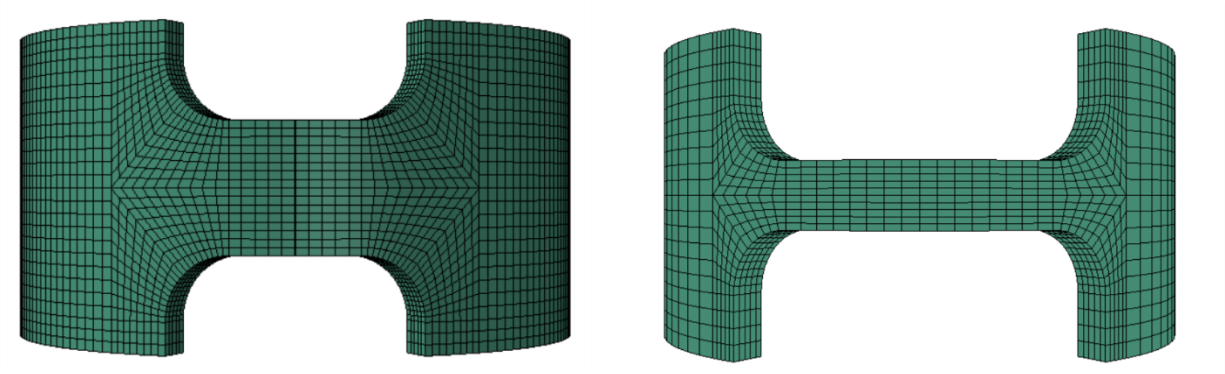

Figure 5.2: Comparison of both gauge sizes. Left, the gauge with 1:1 length-to-width ratio used in test 1. Right, the gauge with 4:1 length-to-width ratio used in tests 2-5.

	Gauge L/W Ratio	Grips Used	Gauge Angle from Loading Direction	Gauges per Ring	Test Arrangement
Test 1	1:1	Hemispherical	0°	2	A
Test 2	4:1	Hemispherical	0°	2	A
Test 3	4:1	Hemispherical	90°	2	B
Test 4	4:1	Hemispherical	45°	1	C

Test 5	4:1	Dogbone Insert	90°	2	D

Table 5.1: Summary of test arrangement parameters

The finite element modelling was done with Abaqus Standard, which uses implicit analysis. The ring model was meshed with linear 8-node reduced integration (C3D8R) elements, seen in Figure 5.1, with roughly 10 elements/mm through the wall thickness. Finer meshing was used along the curved edge (~8 elements/mm) and along the edge of the gauge region (~ 4 elements/mm), as well as through the width of the gauge region (~10 elements/mm). In order to accommodate plastic deformation and contact, nonlinear analysis was also used. Material behavior, including isotropic strain hardening, was based on Zircaloy-4 [7].

The hemicylinder grips were modeled as 3D analytical rigid surfaces, deformation was applied to the ring through grip displacement. Surface-to-surface contact modeling was used with finite sliding and a contact stabilization factor of 0.001. In each of the tests, the results presented assume a friction coefficient of 0.05, closely modelling the expected friction state for a lubricated test insert surface (either from using graphite powder, Teflon tape, or some other method). The sensitivity of this assumption is explored via a friction analysis in which the friction coefficient is varied between this friction coefficient, a conservative expected unlubricated coefficient value of 0.3, and an idealized frictionless case.

5.4. Criterion 1: Uniaxiality of Stress State in the Gauge

5.4.1. Methods

The purpose of this criterion is to ensure that the stress in the gauge region is experienced chiefly in the hoop direction. This ensures that the material properties extracted from the test are truly representative of the behavior experienced in the correct direction. This criterion, like all the

following criteria, was evaluated at several plastic deformations ranging from 1% to 20%. The equivalent plastic strain listed is roughly the maximum strain experienced anywhere in the model, not the average strain in the gauge region. The first metric, α, is a comparison between the hoop direction stress, σ_θ, and the stresses in the other direction (σ_r and σ_z). It is calculated at each integration point in the gauge region, as the larger of σ_r and σ_z divided by σ_θ, as seen in Equation 5.1 below. Thus, if stress is perfectly uniaxial, the ratio would be 0%, and therefore a lower value of metric α is preferable.

$$\alpha = \frac{max(|\sigma_r|, |\sigma_z|)}{|\sigma_\theta|} \qquad (5.1)$$

The metric β is a comparison of the hoop stress σ_θ to the maximum principal stress σ_1, as a secondary measurement of stress uniaxiality. Again, it is calculated at each integration point in the gauge region, as shown in Equation 5.2. This should be given less importance than α in comparing between arrangements. However, it does offer an idea of how well RHTTs in general are able to create a uniaxial stress state, as it is a quantitative indication that the hoop stress is oriented well compared to the major principal stress.

$$\beta = {\sigma_\theta}/{\sigma_1} \qquad (5.2)$$

5.4.2. Results

The values of α in the gauge region is plotted in Figure 5.3 below for each of the test setups. The solid lines indicate the mean value of α across all elements in the gauge region. The dotted lines are upper and lower bounds, defined as the mean plus or minus the standard deviation, again for all gauge elements of the specific test.

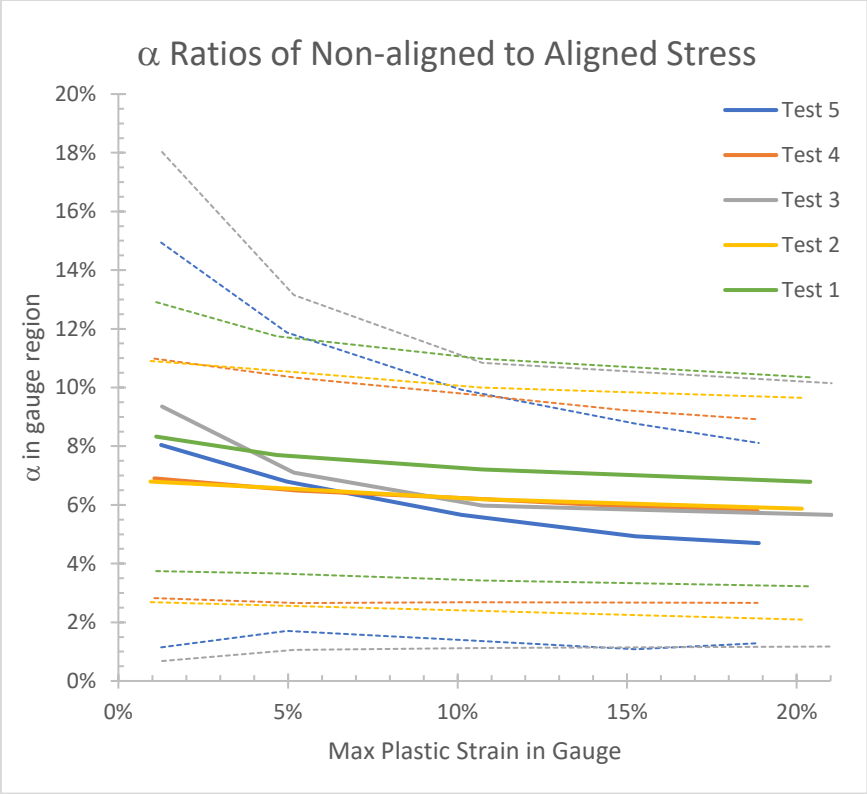

Figure 5.3: The α values in the gauge region for each test, plotted as a function of maximum equivalent plastic strain found in the gauge region. Dashed bounding lines indicate ± one standard deviation.

There are some clear trends in the means from Figure 5.3. Notice that the curves for test 1, test 2, and test 4 are all nearly parallel, with 2 and 4 being nearly the same and 1 being worse by about 1.5%. The curves for tests 3 and 5 also show similarities in their shape, beginning at a worse α and improving as the plastic strain increases. Test 1 shows a worse α than test 5 by 0.5-1.5% for all plastic deformations. Based on these direct comparisons, test 1 and test 3 are the least desirable. Comparing tests 2,4, and 5, shows that test 5 has worse stress alignment at low plastic strains, but between 5 and 10% PEEQ it dips below and outperforms the others through the rest of the plastic strain range evaluated.

Additional information can be gained from the upper and lower bounds, which indicate how uniform the stress state is within the gauge region. It can be seen that test 3 had the widest range of bounds, confirming that this is most likely a poor choice for maintaining uniaxiality. The bounds for tests 2 and 4 are again very similar to one another, except that the standard deviation drops with test 4 as the plastic strain increases, causing the bounds to shrink. Test 5 has a significantly larger standard deviation at low plastic strain, but at larger strains it improves, approaching the level of tests 2 and 4. The variability in the gauge for test 1 is similar to tests 2 and 4.

One can also see the maximum value of α experienced in the gauge region plotted in Figure 5.4, again as a function of plastic strain. The very high values for test 3 are unsurprising after seeing the spread between the upper and lower bounds in Figure 5.3. At the initial onset of plastic strain, tests 2 and 4 are again the lowest, followed by test 1, test 5, and then test 3. Tests 2 and 4 remain the lowest through nearly the entire range of plastic deformation, with 4 generally being the lower of the two.

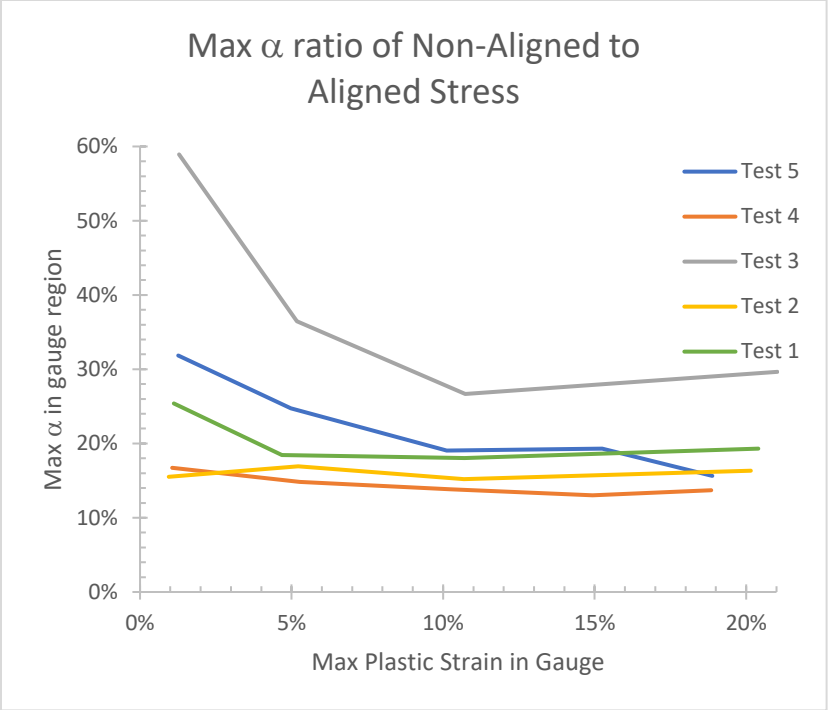

Figure 5.4: Maximum value of α in the gauge region, plotted as a function of maximum equivalent plastic strain found in the gauge region.

The results of the analysis of the β metric are plotted in Figure 5.5. In this metric, a higher value is preferable, as it means a closer agreement between the maximum principal stress and the stress in the hoop direction. Through the entire deformation range, tests 2 and 4 have the highest β values. Values for tests 1, 3, and 5 are effectively the same beyond 10% plastic strain, and at the initial strain it can be sees that test 3 performs the worst, followed by test 5 and then test 1. However, it should be noted that all have values above 99% for the entirety of the tests, indicating that in general, RHTTs ensure that hoop stress is the main contributor to the principal stress state.

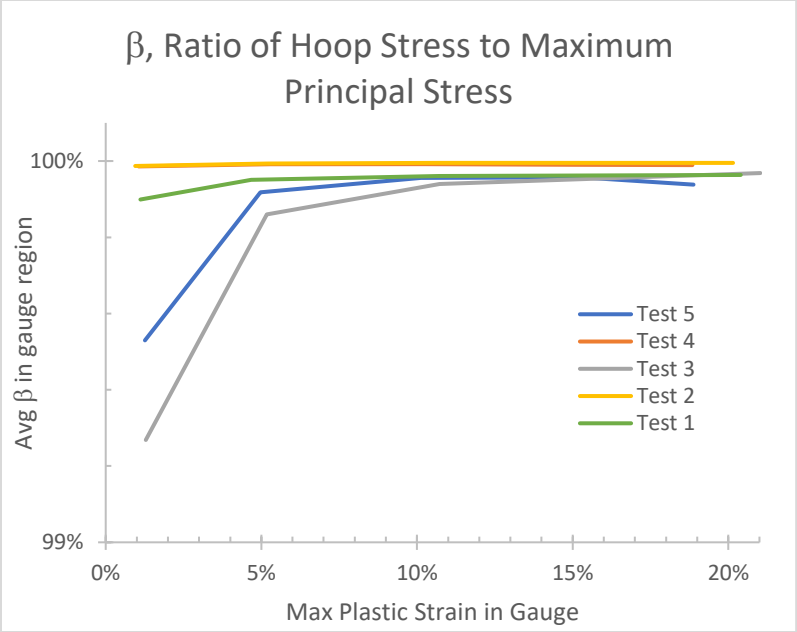

Figure 5.5: Average value of β in the gauge region, plotted as a function of maximum equivalent plastic strain found in the gauge region.

5.4.3. Discussion

Tests 2 and 4 performed very well in all the measures reported above, and tests 1, 2, and 4 are very similar in several characteristics. Because 1 and 2 both use grip/gauge arrangement A, their similarity is not surprising. However, with different gauge dimensions also come differences in performance. Of the two, test 2 performs better than test 1 in every case. This suggests that the length-to-width gauge ratio of 4:1 is more ideal, confirming the recommendation of Zircaloy gauge dimensions in previous studies [8]. Test 4 is also very similar to 1 and 2 because it also prevents the gauge from being located near the corner of the grips or in the gap between the grips, which limits the bending moment being placed on the gauge. The fact that tests 2 and 4 are so similar may indicate that the exact location of the gauge region may not have much of an impact, provided it is still entirely on the face of the insert. If this is the case, then an inadvertent eccentricity of the

load due to misalignment of the specimen on the fixtures will likely not have as significant of an impact on the validity of the results as other arrangements, yielding greater confidence in the results obtained.

Tests 3 and 5 also showed some similarities in performance. This can likely be explained again by the location of the gauge region perpendicular to the direction of loading (centered around the horizontal or 0-180 degree axis, assuming the load is oriented along the 90-270 degree axis). In this location, the ring will experience a combined bending moment and a tensile load at the beginning of the test. This is due to the closing of the gap between the ring and the grips (the dog bone insert in the case of test 5, and the edge of the semicircular grips in test 3). This bending results in a non-uniaxial stress state. It is interesting to note that the introduction of the dog bone insert is meant to directly address this bending moment [9], and while it offers improvement over test 3, bending moment is still present. In order to fit the ring over the grips, there must be some clearance between the ring and the dog bone insert, and this gap still leads to a bending moment in the gauge region.

Overall, tests 2 and 4 performed best in demonstrating uniaxiality. Although test 5 provides a performs slightly better at high plasticity, it is less consistent within the gauge region and throughout the range of plastic deformations. It is expected that in a setting where plastic material behavior is being extracted from the test, the consistency of the uniaxiality offered by tests 2 and 4 is highly valuable. This is especially true if the expected plastic deformation of the test is smaller, such as the 5 and 10% plastic strain range where tests 2 and 4 perform better. Test 4 showed slightly better results than test 2, although the difference between the two in nearly negligible and should be a consideration only as a last resort if the other criteria fail to differentiate between the two tests.

5.5. Criterion 2: Uniformity of Plastic Strain in the Gauge Region

5.5.1. Methods

This criterion was used to determine how uniform the deformation in the gauge region was for each of the tests. The equivalent plastic strain (PEEQ) of all elements in the gauge region was found for each test through the same plastic deformation range of 1% to 20%. The ratio γ of average to maximum PEEQ experienced in the gauge region was calculated, as shown in Equation 5.3.

$$\gamma = {\varepsilon_{PEEQ\ Avg}}/{\varepsilon_{PEEQ\ Max}} \qquad (5.3)$$

If the average and maximum values are very different, the gauge region lacks strain uniformity and there is either a large gradient through the gauge or there is a region of strain concentration. A visual inspection of the plastic strain contours was used to determine if and where these concentrations occur. This qualitative analysis of strain distribution can help identify issues with uniformity in the radial, hoop, and axial directions.

5.5.2. Results

This γ ratio of average to maximum plastic strain in the gauge region as a function of the maximum plastic strain is shown in Figure 5.6. The ratio is the average divided by the maximum, and a higher value indicates a greater degree of uniformity in the gauge region. It can be seen that the ratio remains fairly constant throughout the plastic deformation range for tests 2 and 4, and to a slightly lesser degree for test 1. Test 4 remains the highest and therefore has the best strain uniformity, followed closely by test 2, and then the next highest is test 1.

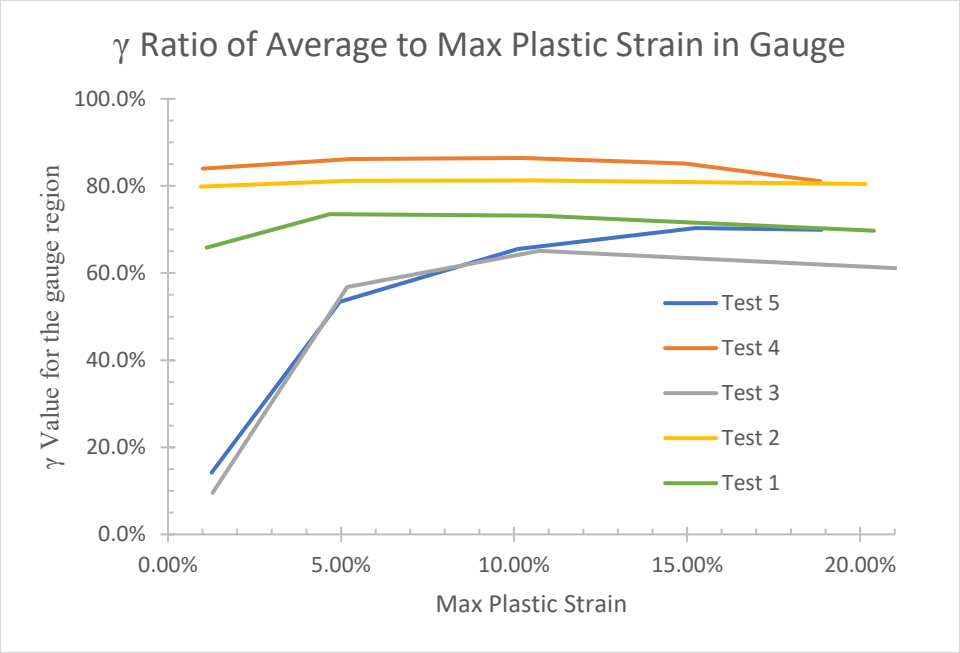

Figure 5.6: The γ ratio of average plastic strain compared to maximum plastic strain experienced in the gauge region is plotted as a function of the maximum plastic strain. A higher ratio value indicates better uniformity.

As with criterion 1, there are clear similarities between tests 3 and 5. Both start with a poor ratio at the onset of plastic deformation, which improves as the strain magnitudes increase. However, both tests 3 and 5 fail to surpass the uniformity of tests 2 and 4, although test 5 reaches the same level of uniformity as test 1 by the end of the test.

Select contours of the different tests are shown in the series of figures below. Figure 5.7 shows the progression from the deformation corresponding to a peak equivalent plastic strain of roughly 1% to 20%. The geometry is shown utilizing symmetry across the y-z plane, and the x-y plane. One can see the strain distribution change from two peak regions in the gauge at the beginning to one single region at the center of the inside edge of the gauge.

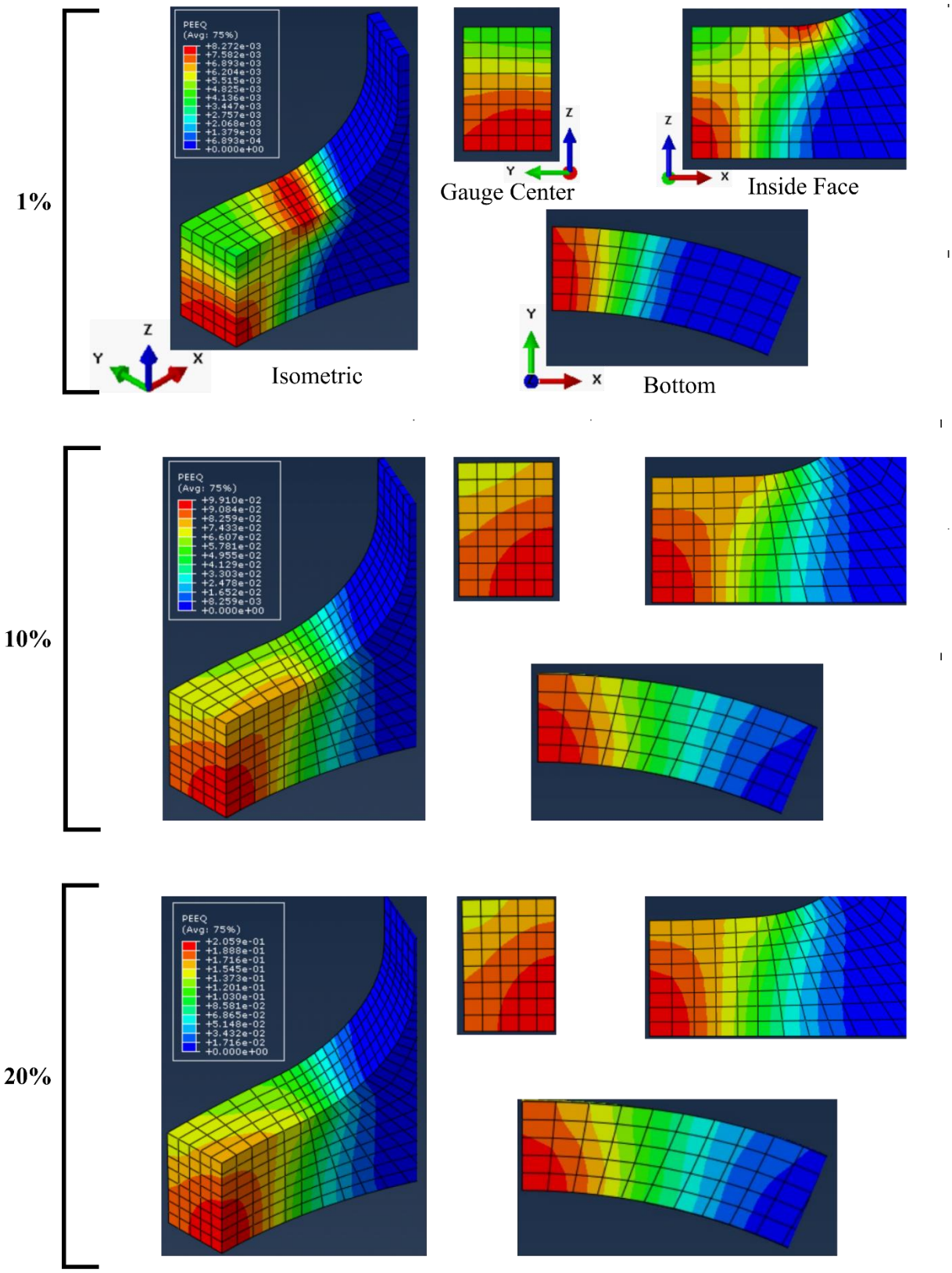

Figure 5.7: Test 1 strain contours, plotted for the gauge and fillet regions.

Figure 5.8 similarly shows the progression through the range of plastic strain from 1% to 20%. The strain remains concentrated between the gauge center and the fillet region throughout the deformation, meaning that in the actual ring there will be two separate peaks per gauge. However, this peak does move closer to the gauge center, and the uniformity improves as compared with the previous arrangement, in test 1.

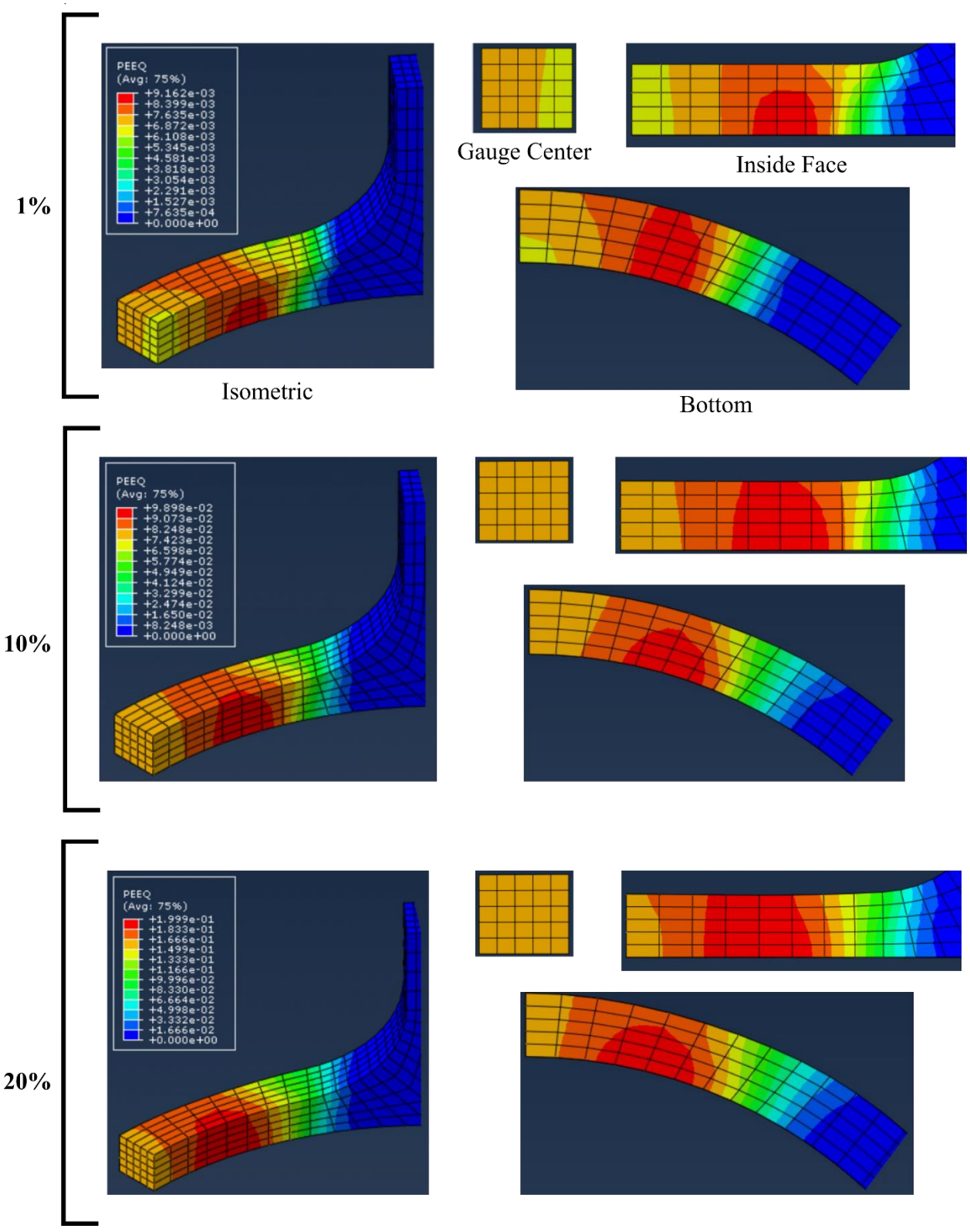

Figure 5.8: Test 2 strain contours, plotted for the gauge and fillet regions.

The strain distributions for test 3 are shown in Figure 5.9. It can be seen that at 1%, the strain is very much concentrated on the inside face of the ring, at the center line of the gauge region. As the deformation progresses, the peak strain region moves from the center of the gauge outwards, in the direction of the fillet. This peak strain region remains highest along the inside edge, although it also becomes deeper in the radial direction as deformation increases. It can also be noted that some locations on the inside edge of the ring experiences some reduction in area.

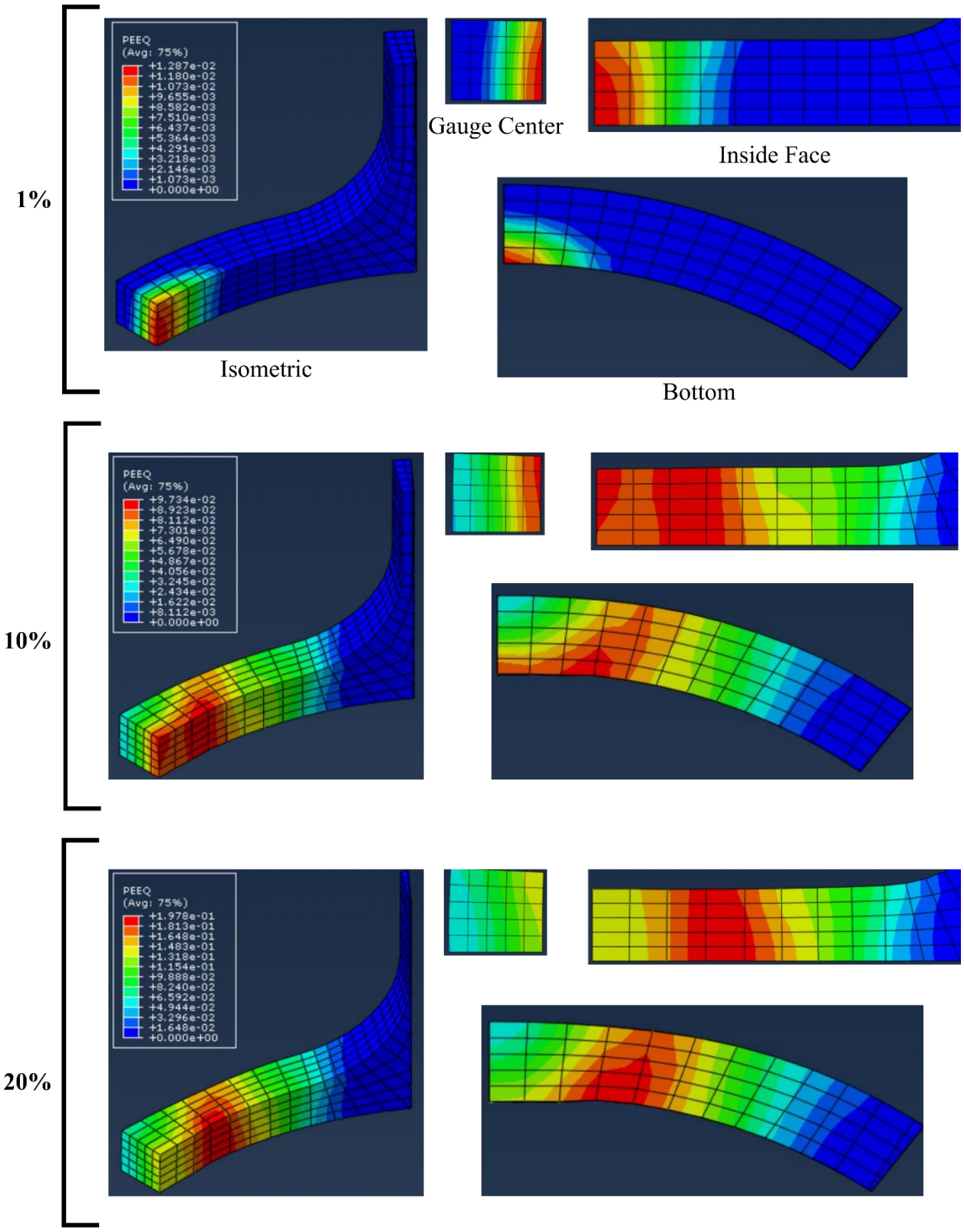

Figure 5.9: Test 3 strain contours, plotted for the gauge and fillet regions.

Test 4 strain distributions are shown in Figure 5.10. Note that because half symmetry was used in this analysis, a greater portion of the ring is shown than for the other eight-symmetry analyses. As in the previous tests, the peak strain regions are found at the inside face; however, there is a greater level of uniformity from 5% strain onward.

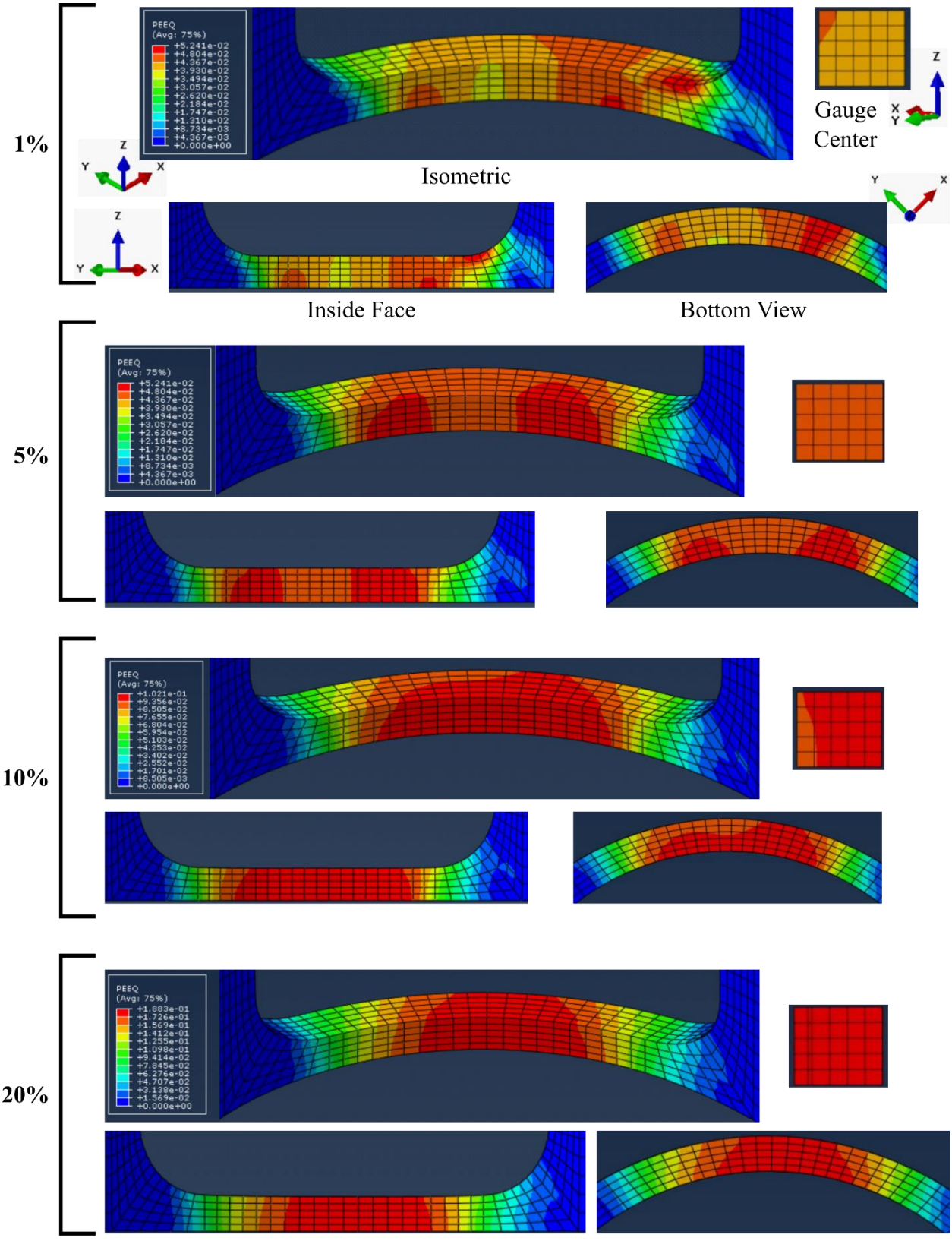
1%
PEEQ
(Avg: 75%)
+5.241e-02
+4.804e-02
+4.367e-02
+3.930e-02
+3.494e-02
+3.057e-02
+2.620e-02
+2.184e-02
+1.747e-02
+1.310e-02
+8.734e-03
+4.367e-03
+0.000e+00
Gauge
Center
Isometric
Inside Face
Bottom View
5%
10%
+1.021e-01
+9.356e-02
+8.505e-02
+7.655e-02
+6.804e-02
+5.954e-02
+5.103e-02
+4.253e-02
+3.402e-02
+2.552e-02
+1.701e-02
+8.505e-03
20%
+1.883e-01
+1.726e-01
+1.569e-01
+1.412e-01
+1.255e-01
+1.098e-01
+9.414e-02
+7.845e-02
+6.276e-02
+4.707e-02
+3.138e-02
+1.569e-02

Figure 5.10: Test 4 strain contours, plotted for the gauge and fillet regions.

The plastic strain contours from the dog bone arrangement, test 5, are shown in Figure 5.11. In the early deformations, the peak strain region is on the inside face, in between the gauge center and the fillet region. But from 15% to 20%, the peak becomes located at the center of the gauge region.

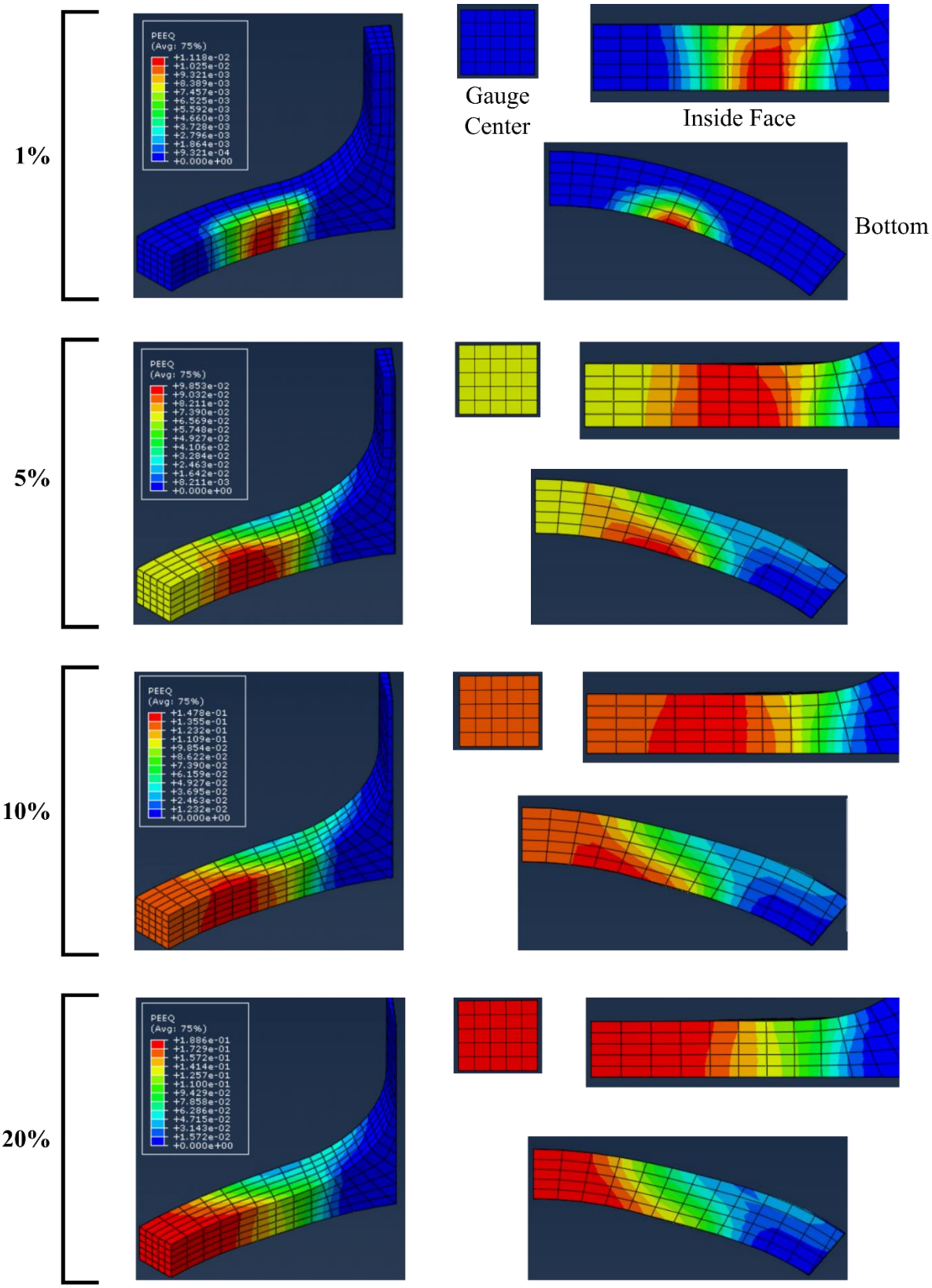

Figure 5.11: Test 5 strain contours, plotted for the gauge and fillet regions.

5.5.3. Discussion

The quantitative results seen in Figure 5.6 are reflected in the strain contours shown in Figure 5.7 through Figure 5.11. The large discrepancies between average and maximum strain apparent in the γ values of Figure 5.6 in the beginning deformation stages of tests 3 and 5 are explained by the small spatial regions where plastic deformation first happens. Observing the 1% set from test 3 shown in Figure 5.9, the initial plastic strain region is located at the center of the gauge region, where the gap between the two grips is located, and on the inside face. In the case of test 5 in Figure 5.11, this concentrated region is located between the gauge center and the fillet region, again at the inside face of the ring. This behavior, as well as the similar orientation of the gauge relative to the direction of loading, may indicate that the same mechanism is at work.

This is most likely due to the combined bending and tension effect at these locations. The bending moment caused as the curved ring is straightened out against the smaller grip would cause tension at the inside face, and compression at the outside face. The unintentional bending load being applied combines with the desired tension load to cause a localization of plastic strain, rather than allowing a more uniform distribution. As the deformation progresses in the test 3 arrangement, the peak strain concentration moves away from the center of the gauge and towards the fillet region. This most likely occurs as the gap between the two grips grows, meaning the corner of the grip moves along the inside of the ring towards this fillet region, translating the location of the bending and therefore the highest plastic strain. In test 5, the dog bone insert is intended to mitigate this bending concentration by preventing the drawing inward of the gauge region. This appears to move the concentration location closer to the fillet regions at the beginning of plastic deformation, rather than prevent the strain localization. As the test progresses, however, this concentration becomes less noticeable, and it approaches more preferable uniformity.

Test 1 contours show a continuous strain concentration at the point located on the inside face and the center of the gauge region throughout the deformation (see Figure 5.7). This is not ideal, although the fact that the gauge region is shorter than the rest means that the concentration makes up a large portion of the gauge region and ensures the maximum strain is relatively close to the average (see Figure 5.6).

Tests 2 and 4 have improved uniformity throughout the deformation range, compared to tests 1, 3, and 5. Figure 5.8 and Figure 5.10 show that for much of the gauge region, strain does not vary significantly. These two arrangements still have strain concentration regions, but the difference between the concentrations and the rest of the gauge is not as severe as in the other arrangements. In tests 2 and 4, this region of concentration is located between the gauge center and the fillet regions, and in both tests the concentration begins to expand towards the gauge center. In test 4, this widening reaches the center of the gauge region at 20% plastic strain, showing the greatest expansion of the high-strain region in the circumferential direction of any of the test arrangements. The only other test arrangement that approaches a similar size of peak strain region is test 5.

The combination of these qualitative and quantitative evaluations would seem to indicate that test 4 offers the best strain uniformity criterion, followed by test 2 and then test 5. However, it is worth noting that uniformity of strain in specific directions may also be an important consideration in some cases. The finite element models used in this analysis are based on a ring that is made solely of zircaloy. But if the RHTT was to be used for a sample made from an accident tolerant fuel cladding tube with a lining on the inside or a treatment/coating on the outside, a strain gradient in the radial direction (through the wall thickness) could be a more serious problem. While a RHTT may be used to test and treat this cladding as a composite, the presence of strain non-

uniformity in the radial direction seen in some of these arrangements would seriously compromise the validity of test results. This may also be true in the case of hydrided cladding, where there is often a gradient of hydrogen concentration in the radial direction as well. Although there could conceivably be property variation in any material direction of a ring specimen, it is expected that such variation in the radial direction is likely to have the most severe consequences.

Taking into consideration those potential repercussions, some of the arrangements separate from the others. Radial variation is fairly small at all strains for test 1, as seen by the gauge center and bottom views of Figure 5.7. Test 2 (Figure 5.8) shows a similar degree of radial uniformity. Test 3 (Figure 5.9) shows very poor uniformity, although the gradients become improved as the degree of plastic deformation increases. Test 4 (Figure 5.10) shows radial gradients like those found in test 2, with only small variations from the inside face to the outside face. Test 5 (Figure 5.11) initially shows poor radial uniformity, although it does improve as the test progresses, almost reaching the degree exhibited by test 2 and 4. Thus, test 4 seems to be the recommended arrangement for optimal strain uniformity, followed by test 2.

5.6. Criterion 3: Highest Stresses and Strains Located in Gauge

5.6.1. Methods

The purpose of this criterion is to confirm that there are no concentrations of stress or strain occurring outside the gauge region. This ensures that the deformation of the ring will be experienced solely by the gauge region. The maximum, minimum, and average values of both equivalent plastic strains (PEEQ) and major principal stresses (σ_1) were found for each region (the gauge region, the curved region, and the full-width region). This was done for each test through the same range of plastic deformations as the previous criteria.

It should be noted that due to geometry differences, the definition of curved region is different between test 1 and tests 2-5, as seen in Figure 5.12. Test 1 has a wider gauge region, and thus the curved region is wider as well, and the curve extends to the top of the ring as pictured. However, the rest of the tests have the smaller gauge region to fit the 4:1 length-to width ratio, meaning that the curved region is smaller. This means that the ratios of averages presented with the criterion may not be directly comparable between test 1 and the other tests. It should also be noted that for test 4, symmetry on either side of the gauge cannot be assumed, and so both curved regions were used in the calculation.

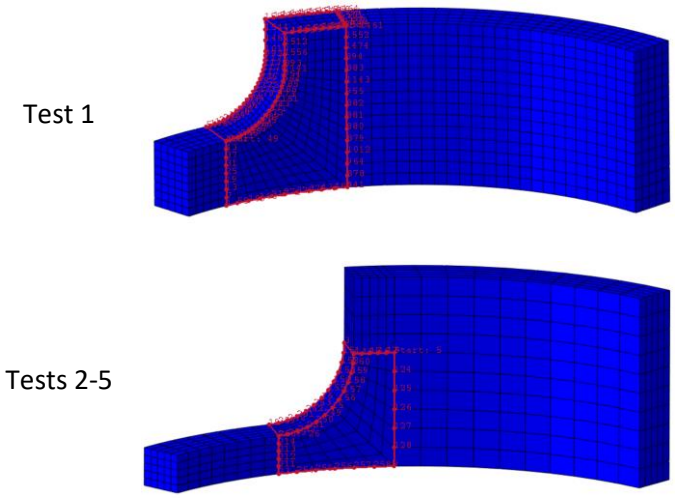

Figure 5.12: Curved region definitions for test 1 and the subsequent tests

To compare average deformation outside and inside the gauge region, the average equivalent plastic strain in all the curved region elements was divided by the plastic strain in the gauge region to give a comparative ratio δ_{curved} as seen in Equation 5.4a. This was repeated with full-width region elements and gauge region elements, producing δ_{full}, seen in Equation 5.4b.

$$\delta_{curved} = {\varepsilon_{PEEQ\ Avg,curved}}/{\varepsilon_{PEEQ\ Avg,gauge}} \quad (5.4a)$$

$$\delta_{full} = {\varepsilon_{PEEQ\ Avg,full}}/{\varepsilon_{PEEQ\ Avg,gauge}} \quad (5.4b)$$

Higher δ ratios mean that significant deformation is occurring outside the gauge region. This directly impacts the ability to determine elongation in the gauge region based on the grip or crosshead displacement; if too much plastic strain is occurring outside the gauge region, then the grip displacement will lead to overcalculation of the actual gauge strain.

The other main consideration in processing these region-specific plastic strains is the maximum strain experienced in the gauge region. As an experiment nears failure, it is important that the peak strain in the gauge region is significantly higher than the strain anywhere else in the ring sample. Otherwise, failure outside the gauge region becomes a possibility. To monitor this, the ratio ζ of the maximum strain outside the gauge region (either in the curved region, or in the full-width region) to the maximum strain found within the gauge region was calculated, as seen in Equation 5.5. A low ζ value is ideal.

$$\zeta = \frac{max\left(\varepsilon_{PEEQ\ Max,curved}, \varepsilon_{PEEQ\ Max,full}\right)}{\varepsilon_{PEEQ\ Max,gauge}} \quad (5.5)$$

5.6.2. Results

The δ ratios, a measure of the average strains in the gauge region and outside the gauge region, are plotted in Figure 5.13. One can see that δ_{curved}, shown with the solid lines, is much higher than ratio δ_{full}, shown with the dashed lines. This behavior is expected because of the smaller width of the curved region and the stress concentrations that the fillet produces. Test 3 shows the lowest values for both δ_{curved} and δ_{full}, but the order of the other tests is not the same for the two

regions. One can also see that test 5 has the highest (worst) ratio in the curved region for most of the deformation range, but that test 1 has the highest ratio for the full-width region. In the full-width region, tests 3, 4, and 5 have a ratio nearly zero, but all five tests are at or below a ratio of 1%. Also in the curved region, all the tests except test 4 follow the same curve shape or trend, increasing in ratio value initially and then slowly tapering off for the rest of the deformation range.

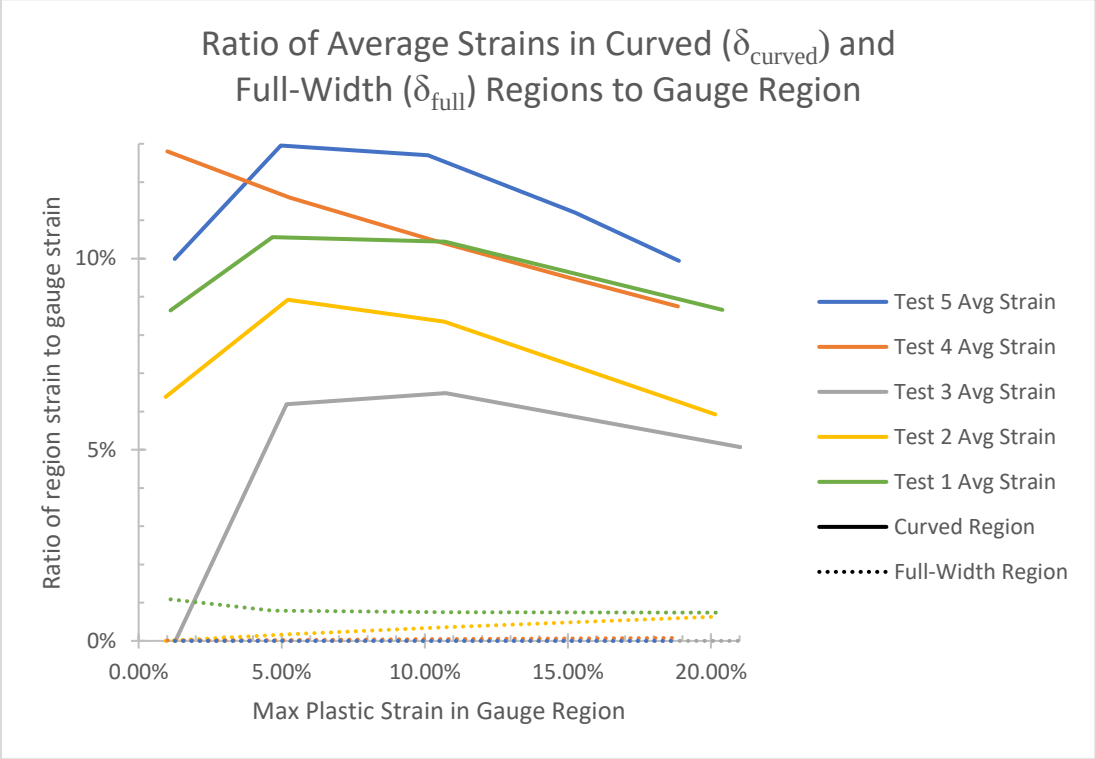

Figure 5.13: Plot of the ratio of average plastic strain in the curved region (solid line) or full-width region (dotted line) to the average plastic strain in the gauge region as a function of the degree of the plastic deformation in the gauge.

The plot of ζ, which compares the maximum out-of-gauge strain to the maximum in-gauge strain, is shown in Figure 5.14. Again, it is evident that test 3 resulted in the lowest (best) ratio. Test 1 has the highest (worst) ratio for most of the deformation range, and the other three tests are similar from 5% plastic strain through the rest of the deformation. The ratio for test 1 and test 4 is

initially above 100%, meaning that the strain somewhere outside of the gauge region is higher than any strain inside the gauge region. At greater plastic strains, however, the performance of test 4 approaches that of tests 2 and 5.

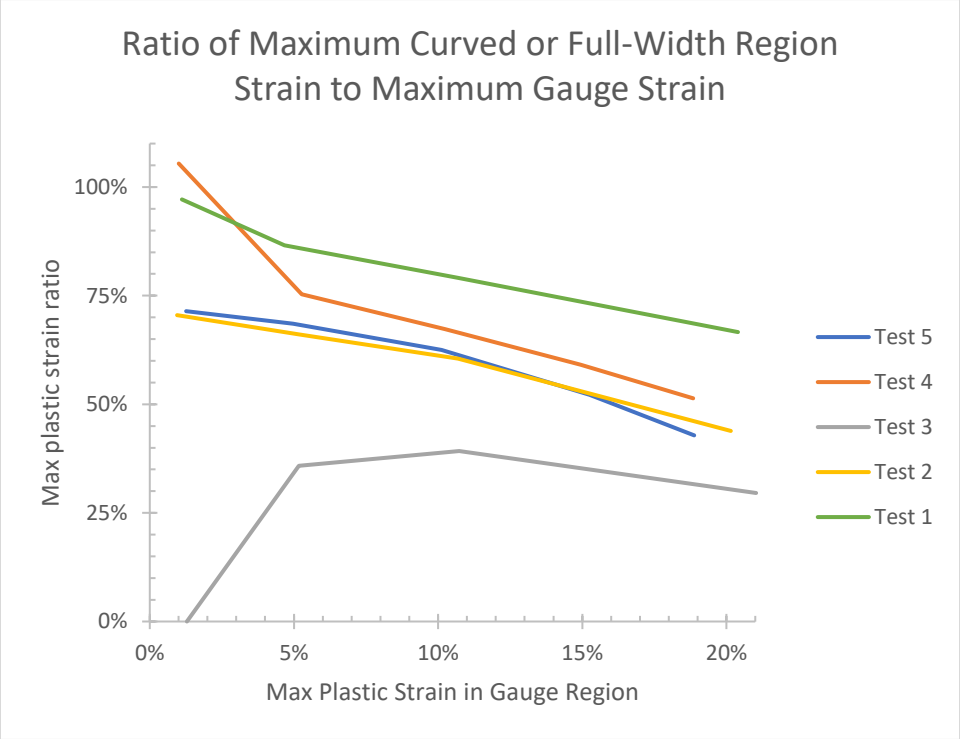

Figure 5.14: Plot of the ratio of maximum strain outside the gauge region to maximum strain in the gauge region, as a function of the maximum plastic strain in the gauge region.

5.6.3. Discussion

The results of the δ ratios, comparing average strains inside and outside the gauge region, seem to counteract the benefits of the previous criterion by saying tests 4 and 5 are among the worst and test 3 performs the best. However, it is important to note that in the curved region (solid lines in Figure 5.13), all test arrangements yield δ_{curved} values below 13%. This is an indicator that all tests have average gauge strains roughly 7-8 times higher than curved region strains. In tests 2-

5, the curved region is much shorter than the gauge region, meaning the resultant elongation will be even less impactful. The average plastic strain in the full-width region is much smaller, so the average strain in the gauge region is at least 100 times larger than the strain in the full-width region. However, the full-width region is about the same length as the gauge region in most of the tests, and longer in the case of test 1 and test 4. Thus, although there is some strain present outside the gauge region, the grip or crosshead displacement can be used to satisfactorily estimate the gauge elongation. However, the accuracy of such a measurement can be improved with the formulation of correction factors to account for slight elongation in the other regions.

It is worth noting that, although counterintuitive, high ζ ratios may be a sign of a good test, as they can be product of good strain uniformity throughout the gauge region. The curved region is essentially a buffer between the high-strain gauge region and the low-strain full-width region. An ideal test would include a uniform relatively high strain throughout the gauge region, a uniform low or zero strain in the full-width region, and thus a significant gradient through the curved region. By this reasoning, the ideal test should have a low but nonzero δ_{curved} value, paired with a potentially higher ζ value. However, a δ_{full} value much higher than zero could be a sign of problems with the test.

Following this logic, Figure 5.13 shows that although tests 4 and 5 have some of the highest δ_{curved} values, they have δ_{full} values that are essentially zero. This finding addresses concerns about inaccuracy of elongation calculations from the grip displacement, suggesting that higher δ_{curved} and ζ values are likely due to high strains at the border between the gauge and curve regions followed by a steep strain gradient in the circumferential direction. This is confirmed by looking at the strain contours in Figure 5.10 and Figure 5.11. When all three metrics of criterion 3 are considered, tests 4 and 5 appear to offer the best performance.

Additionally, more can be inferred about the ultimate failure and necking behavior by observing the trends in Figure 5.14. This ζ ratio helps to determine if the failure and necking will occur outside the gauge region; if the ratio is near or above 100% at a deformation state where failure is expected, then it is very possible that failure will occur outside the gauge region. At the earliest stages of plastic deformation (less than 5% PEEQ), tests 1 and 4 may be susceptible to non-gauge failure. However, if failure is ductile and doesn't occur until at least 5% plastic strain, then it is unlikely that any of the tests will experience failure outside the gauge region.

5.7. Criterion 4: Friction Effects

5.7.1. Methods

The previous criteria were all evaluated with a coefficient of friction of μ=0.05 to represent a low-friction state resulting from a lubricated grip surface. However, the ring arrangements are likely to behave very differently with different friction states, and so this criterion investigates the sensitivity of the models to changing coefficients of friction. The same tests were modeled with a coefficient value of μ=0.3 to simulate a possible unlubricated surface condition of metal-to-metal contact, and then again with a value of μ=0 to simulate the frictionless case. The overall behavior was compared by qualitatively observing strain distribution in the ring.

5.7.2. Results

The test 1 plastic strain contours in and near the gauge region for each of the three friction cases are shown in Figure 5.15. At both the onset of plastic deformation and at the final deformation of 20% plastic strain, the behavior of the lubricated case is similar to the frictionless case. In the full-friction, unlubricated case, the strain concentrates solely at the transition between

the gauge and fillet region. This trend continues throughout the deformation and ends with the same strain magnitude in that transition region as in the center of the gauge region.

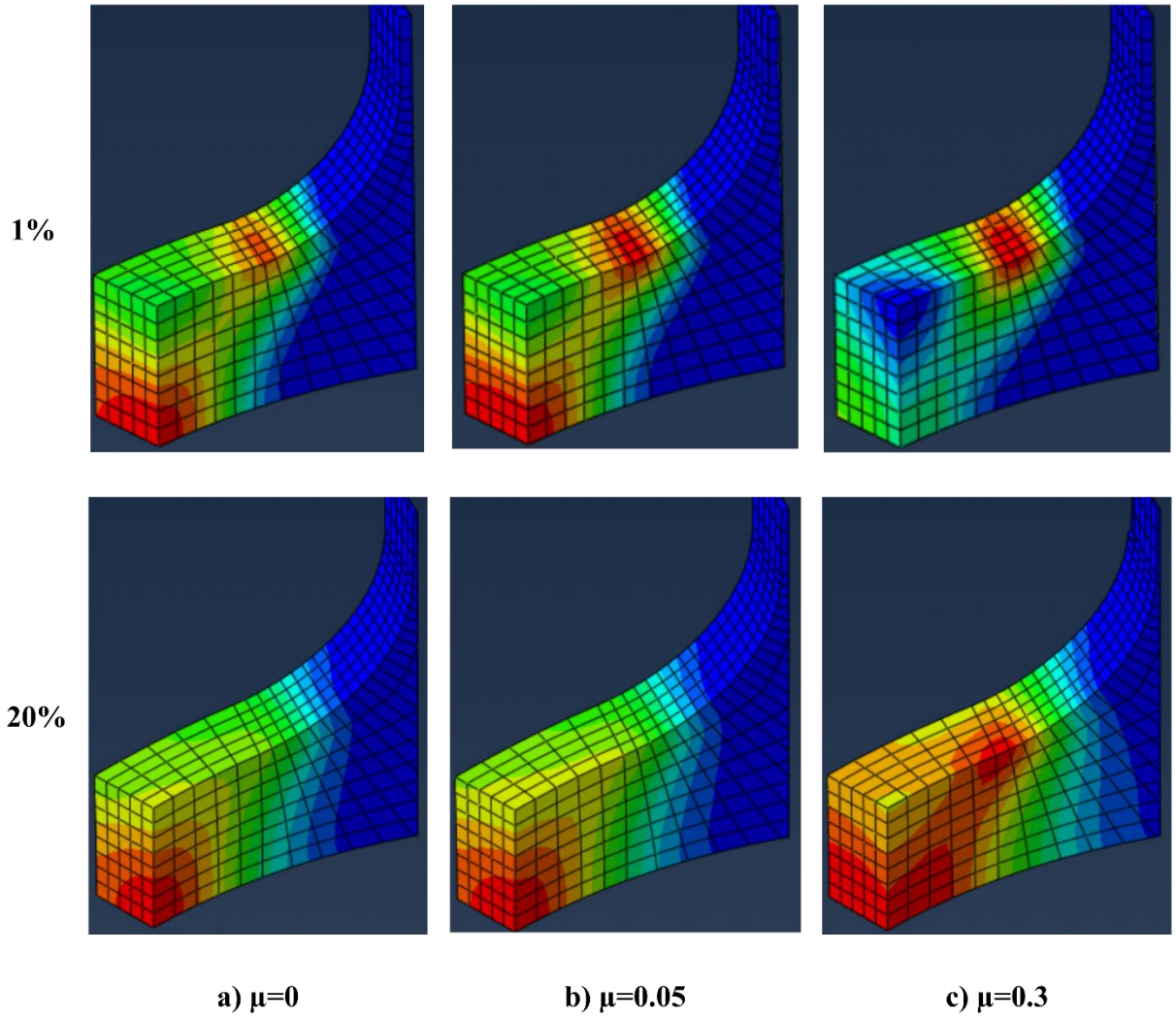

Figure 5.15: Test 1 plastic strain contours at a peak strain of 1% (top row) and of 20% (bottom row), for a) frictionless, b) lubricated, and c) unlubricated cases.

Figure 5.16 shows the test 2 strain contours for the three friction cases at the end of deformation (peak plastic strain of 20%). At plastic onset, all three cases showed strain concentration at the same location. However, the unlubricated case shows that the concentration

did not move, the lubricated case shows some movement, and the frictionless case shows the concentration moving fully to the center of the gauge.

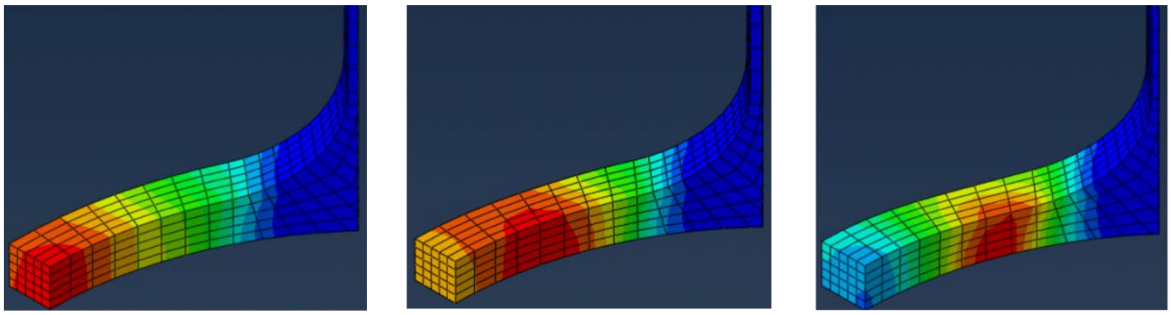

a) μ=0 **b) μ=0.05** **c) μ=0.3**

Figure 5.16: Test 2 plastic strain contours, peak strain of 20%, for a) frictionless, b) lubricated, and c) unlubricated cases.

The contours in Figure 5.17 show that for test 3, there is little difference between the frictionless and the lubricated cases, with almost identical distributions. The unlubricated case in part c) shows that at 20% peak plastic strain, the high strain region is distributed further along the inside face but does not penetrate as deeply in the radial direction. The strain does not stretch as far towards the curved region in the unlubricated case. This means that at the end of the gauge region, the unlubricated case has lower strains and therefore less strain uniformity within the gauge region.

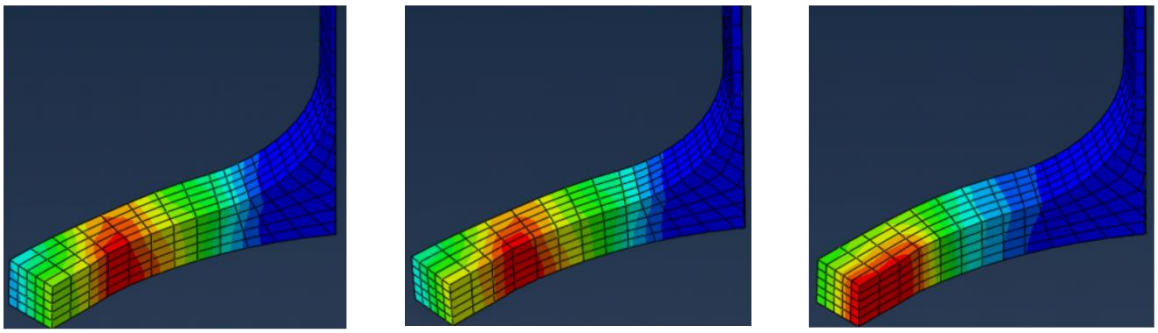

a) μ=0 **b) μ=0.05** **c) μ=0.3**

Figure 5.17: Test 3 plastic strain contours, peak strain of 20%, for a) frictionless, b) lubricated, and c) unlubricated cases.

Contour comparisons in Figure 5.18 show that different friction states have a clear effect on the symmetry of the gauge in test 4. At peak plastic strain of 1%, the frictionless and lubricated cases both show similar distributions with strain distributed across the gauge. In contrast, the unlubricated case shows that only one side of the gauge experiences any significant plastic strain. At peak strain of 20%, the unlubricated case approaches symmetry, but the peak strains are not located at the center of the gauge, and uniformity has worsened in comparison with the lubricated case. The frictionless case shows a greater degree of asymmetry about the gauge center than the lubricated case does, with a slightly smaller high-strain region compared to the lubricated case.

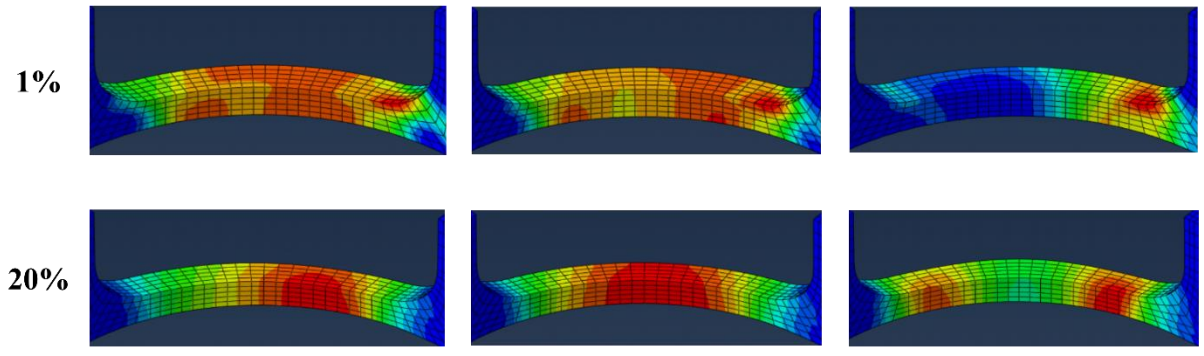

a) μ=0 **b) μ=0.05** **c) μ=0.3**

Figure 5.18: Test 4 plastic strain contours at a peak strain of 1% (top row) and of 20% (bottom row), for a) frictionless, b) lubricated, and c) unlubricated cases.

The contours in Figure 5.19 show the effects of friction on the test 5 at the final stage of deformation. Both the frictionless and the lubricated cases feature a maximum strain located at the gauge center, and both follow a similar distribution shape. The primary difference is that the high-strain region stretches further in the circumferential direction for the lubricated case, compared to the frictionless case. For the unlubricated case, the peak strain region is located in between the gauge center and the fillet region and is smaller than for the lubricated case.

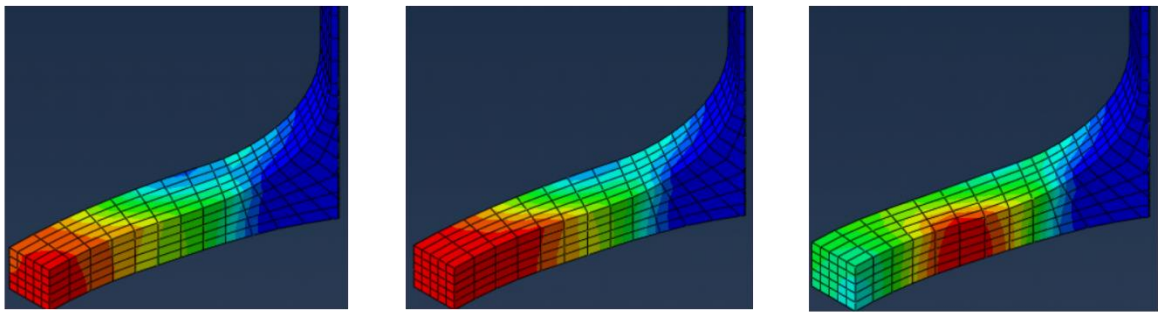

a) μ=0 **b) μ=0.05** **c) μ=0.3**

Figure 5.19: Test 5 plastic strain contours, peak strain of 20%, for a) frictionless, b) lubricated, and c) unlubricated cases.

5.7.3. Discussion

For all 5 tests, the higher or unlubricated friction state results in negative strain behavior. In many of the tests, higher friction means that the peak strain region is not located at the center of the gauge region, even at greater deformations. This can be problematic because as the strain to uniform elongation is reached and necking begins, a peak strain not located at the center of the gauge means that there will be two regions with high strain, and potentially necking at two different

locations. This is the case with tests 2, 4, and 5. For test 1, the higher friction keeps a high strain location at the transition region between the gauge and the fillet, on the inside face, which may have the same double-necking effect. The exception to this trend is test 3, where the friction causes the peak strain location to reach the center of the gauge (see Figure 5.17). However, in test 3 the uniformity is still negatively impacted by higher friction, as less of the gauge region experiences a similar magnitude of strain, with lower strains shown at the fillet end of the gauge region. These results indicate that for all tests, higher friction results in worse strain conditions.

The effects of decreasing the friction from a lubricated (μ=0.05) condition to a frictionless (μ=0) condition seems to have minimal effect in most cases. The differences in strain distribution between the two conditions are nearly indistinguishable for test 1 and test 3. In test 2 (Figure 5.16), reducing friction to zero caused strain to be better centered in the gauge region, but it also caused a smaller portion of the gauge to have the same range of strain. Thus, for test 2, the consequence of zero friction is a tradeoff between peak strain location and strain uniformity.

Although somewhat counterintuitive, the performance worsens with a decrease in friction for some tests. For example, in test 4 (Figure 5.18), the uniform high strain region shrinks and moves away from the center of the gauge. Test 5 (Figure 5.19) also shows the high strain regions shrinking. Thus, for test configurations 4 and 5, the ideal case for strain distribution is with lubrication rather than zero friction.

Unsurprisingly, all the tests are somewhat susceptible to worsened strain distribution quality due to higher friction in the non-lubricated case. However, tests 1 and 3 are likely the least affected by higher friction. Test 2 is likely to improve slightly by even more substantial lubrication. Tests 4 and 5 are likely near their greatest performance potential in the lubricated condition.

It should be noted that if an experiment is conducted to uniform elongation, the location of the high strain region becomes less important, and the uniformity of the strain distribution is likely the most important factor. This would make tests 2, 4, and 5 better-suited for use even at a friction coefficient higher than μ=0.05. It is also possible that if the deformation is intended to go past uniform elongation to ultimate failure, the strain distribution could be improved by narrowing the gauge slightly at its center. This narrowing is often done to encourage necking in a certain location, and in this case it could also improve the strain uniformity throughout the gauge region. If the lubrication is not possible, then tapering should be strongly considered for tests 2, 4 and 5.

5.8. Criterion 5: Extraction of Stress-Strain from Load-Displacement Data

5.8.1. Methods

The purpose of this criteria is to ensure that the stress-strain relationship can be determined from the information that would be available in an actual experiment. This can be broken into 2 subtasks: determining the stress and determining the strain. The only available data source for determining stress is the load detected by the test frame. The strain calculation, however, can potentially be determined using crosshead displacement in the test frame, with a physical strain gauge fixed to the specimen, or through a non-contact imaging method such as digital image correlation (DIC). Finding a way to obtain reliable data for both stress and strain through only the test frame outputs (crosshead load and displacement) would be ideal, but there are multiple strain measurement methods that could be used. As such, the primary focus here will be finding stress in the gauge region resulting from the grip force load, the only method for determining the stress from experimental data where the plastic constitutive stress-strain relations are being determined.

For the purposes of accurately modelling an experimental setup, the “experimental” crosshead load and displacement were defined as the reaction force and displacement in the direction of loading on the grips reported in the Abaqus model. These are the forces and displacements that the actual grips would experience, and presumably the forces reported by the load cell. The displacement is more likely to be overestimated than underestimated by using crosshead displacement because of compliance in the load train. However, it can be assumed that the compliance of the gauge region in the specimen, with its small cross-section, is the dominating factor in the compliance of the system.

As previously stated, the goal of this criteria is to determine the “experimental” stress calculated from the load cell and compare it with the “standard” of the actual stress expected over the range of plastic deformation based on the material input data. This material input is defined by a series of yield stresses and their corresponding plastic strains [7], and is therefore independent of the actual analysis. Thus, an ideal test configuration would return experimentally derived stresses which match up with these material inputs at corresponding strains.

Implementation of two correction factors was found to better transform the crosshead data into an accurate stress-strain curve which matches material inputs. These corrections will be outlined below with some explanation of their purpose; however, the accuracy of these steps will be shown in the results section, and the reasons for their use will be further reviewed in the discussion section. As a proof of concept, the information presented is all obtained from the finite element analysis (except the material inputs, on which the analysis was based), but the procedure is designed to work with experimentally obtained data. This is done so that in an actual ring hoop tensile test, the plastic stress-strain behavior could be obtained without any additional finite element modelling.

The first two values that need to be determined are the grip force and grip displacement. In an actual experiment, these are test frame outputs; in this analysis, they are the resultant force and displacement in the direction of loading of the grip analytical rigid surface. An estimated value for strain in the gauge region, ε_{est}, is calculated using the well-known Equation 5.6, where δ_{grip} is the displacement of the grip and l_0 is the original length of the gauge. It should be noted that for test 4, the original gauge length is the full length of 4 mm, while for the others since symmetry is employed across the gauge, the original gauge is taken as half of the length (2 mm for tests 2, 3, and 5, and 1 mm for test 1).

$$\varepsilon_{est} = ln\left(\frac{\delta_{grip}+l_0}{l_0}\right) \qquad (5.6)$$

In order to find an accurate estimate of the stress in the gauge region, a series of correction factors were applied to the reported force. The first correction factor is intended to adjust for the force needed to bring the ring specimen and grips into good contact with each other. First, the grip load is plotted against the strain estimate, and a line is fitted to the straight elastic portion of the curve. This line is then offset by 0.2% strain to the left, and the intersection between the offset and the load-strain curve is measured, as seen in Figure 5.20. The determination of this gap closure force is procedurally similar to the method for finding the yield stress from a stress-strain curve, and a more detailed justification of this method can be found in the discussion section. This force to gap closure offset value is then subtracted from the force data obtained from the test frame, correcting the force to better reflect the load causing deformation in the gauge region.

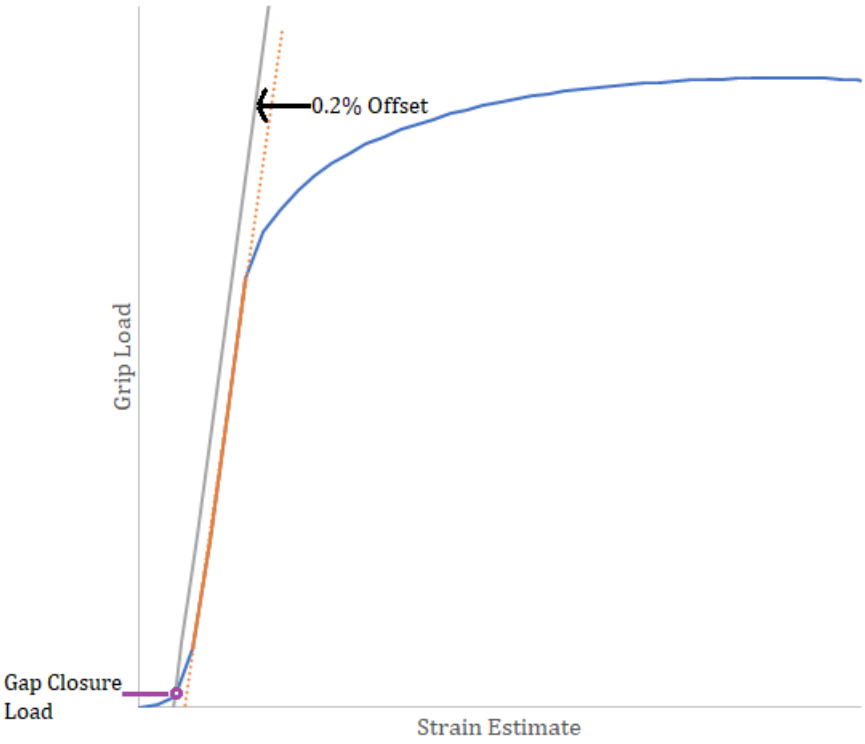

Figure 5.20: Diagram of the procedure for finding the required load to close the gap between the ring and grips.

The other correction applied to the force calculation is a friction factor. Friction between the grips and the inside edge of the ring must be accounted for, as the resultant force will act in a direction opposite the force exerted on the ring in the hoop direction. This means that the force experienced in the ring will be less than the force exerted by the grip and will vary in the hoop direction as a function of the angle around the grip. This angular variation is described by the belt or capstan equation, given in Equation 5.7, which shows the ratio of tensile load at an angle (N_θ) to the load exerted at the grip gap (N_0) as a function of the angle (θ) and the friction coefficient (μ).

$$\frac{N_\theta}{N_0} = e^{-\mu\theta} \qquad (5.7)$$

This ratio can be multiplied by the force from the crosshead to find the load experienced at any position on the ring. Using this relationship, the friction correction factor (f), or the average ratio over the gauge region (from positions θ_1 to θ_2), can be found using Equation 5.8. This friction factor is calculated based on geometry of the test arrangement and the coefficient of friction, meaning that it is found by the same method for both the finite element model and for an experimental setup.

$$f = \int_{\theta_1}^{\theta_2} \frac{e^{-\mu\theta}}{\theta_2 - \theta_1}\, d\theta \qquad (5.8)$$

The resulting adjusted force can then be used to calculate the apparent engineering hoop stress of the gauge region, using the force divided by the gauge cross-section. In the case of test 4, the force must also be divided by two, because half-symmetry was used and thus two sides of the ring are present in the model, meaning the gauge region is experiencing only half of the force exerted on the ring. This is true in the finite element simulations of test 4 as well as in experimental cases. For tests 1, 2, 3, and 5, when the procedure is being used for experimental results rather than computational results, the full cross-sectional area of both gauge regions should be used with the full force reported by the crosshead (for example, 2 x 1.0 mm x 0.57 mm).

The apparent true stress can be found from the apparent engineering stress by using Equation 5.9, where the ratio of initial area to instantaneous area can be rewritten in terms of elasticity. This holds for plastic deformation, where the volume is constant (Poisson ratio is 0.5). In an experimental setup, this strain would be determined either through a strain gauge or a non-contact method like DIC. In the finite element analysis, this ‘measured strain’ was calculated as the average equivalent plastic strain from the gauge region elements (described in criterion 2)

summed with the elastic strain (found by dividing the engineering stress by the modulus of elasticity).

$$\sigma_{true} = \sigma_{eng}\left(\frac{A_0}{A}\right) = \sigma_{eng}(1+\varepsilon) \qquad (5.9)$$

This true stress, based on force adjusted with the correction factors, can then be plotted against the equivalent plastic strain (PEEQ) to produce the final plastic strain vs yield stress plot and compared with the input parameters.

5.8.2. Results

The friction correction factor and gap closure load correction, applied to each of the 5 test arrangements, is shown below in Figure 5.21. Tests 2 and 4 most closely replicated the input plasticity parameters which were used in the model, demonstrating good agreement.

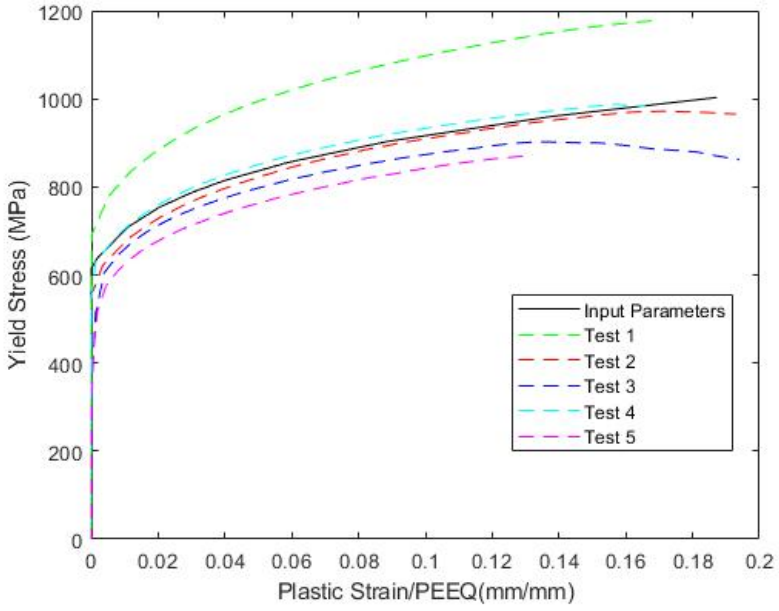

Figure 5.21: Plot of yield stress-plastic strain curves for all test arrangements, with friction correction factor and gap closure loads, compared against the target input parameters.

5.8.3. Discussion

The importance of using the strain estimate rather than the strain reported in the gauge region can be seen by looking at the shape of the curve in Figure 5.20; rather than the linear elastic region beginning at zero load and zero strain, the stress-strain curve shows a ‘ramp-up’ region which is curved, eventually transitioning into the elastic region. This is an artifact of the test method, and clearly doesn’t represent actual material behavior. Subsequent application of the gap closure load correction, along with the friction correction factor, brings the simulated stress-strain extraction curves closest to the original ‘target’ input parameters, shown in Figure 5.21.

Of all the tests, test 2 and test 4 performed the best according to this criterion, as they are the tests directly above and below the input parameter curve. Test 4 begins closer to the input, following very closely through the yield point, and eventually diverging slightly above. Test 2, however, starts slightly further below, and approaches closer to the input as plastic deformation increases. Test 3 is even further below, and appears to be next best, followed by test 5 which is significantly below. Test 1 is much higher, making it the worst-performing arrangement in its ability to replicate the actual stress-strain behavior.

It is worth noting that test 5, which uses the dogbone insert meant to prevent the bending moment which causes the beginning ‘ramp-up’ curve prior to elastic loading seen in Figure 5.20, still exhibits less-than ideal behavior in the stress-strain extraction. However, this is not due to a misapplication of the gap closure load correction; if there was no ‘ramp-up’ curve behavior at the beginning of loading, then there would be no offset load to subtract, and therefore the correction would have no effect. This demonstrates that the intended effect of the dogbone insert is either not realized, by not preventing the ramp-up, or worsens the stress state, by introducing new grip-gauge interference behavior.

5.9. Conclusions

This study focused on the comparison of five different test methods for the ring hoop tension test (RHTT). The methods were evaluated based on five criteria: (1) stress uniaxiality in the hoop direction, (2) strain uniformity throughout the gauge region, (3) concentration of deformation in gauge region, (4) friction sensitivity, and (5) stress-strain curve extraction. Comparing tests 1 and 2, which used the same arrangement but with different gauge dimensions, showed that the 4:1 length-to-width ratio for the gauge region of tests 2-5 performed best. Of those, tests 2 and 4 were consistently the top performers, with test 4 slightly outperforming test 2 in a few metrics. Based on this study, test 4 is recommended for future experimental testing.

5.10. References

[1] Wang, H., Bouchard, R., Eagleson, R., Martin, P., Tyson, W., Martin, P., and Tyson, W., 2002, "Ring Hoop Tension Test (RHTT): A Test for Transverse Tensile Properties of Tubular Materials," J. Test. Eval., **30**(5), p. 382.

[2] El-Bagory, T. M. A. A., Younan, M. Y. A., and Alarifi, I. M., 2018, "Failure Analysis of Ring Hoop Tension Test (RHTT) Specimen Under Different Loading Conditions," American Society of Mechanical Engineers Digital Collection.

[3] Dick, C. P., and Korkolis, Y. P., 2014, "Mechanics and Full-Field Deformation Study of the Ring Hoop Tension Test," Int. J. Solids Struct., **51**(18), pp. 3042–3057.

[4] Kubo, T., Kobayashi, Y., and Uchikoshi, H., 2013, "Determination of Fracture Strength of δ-Zirconium Hydrides Embedded in Zirconium Matrix at High Temperatures," J. Nucl. Mater., **435**(1), pp. 222–230.

[5] Kim, J. H., Lee, M. H., Choi, B. K., and Jeong, Y. H., 2006, "Effects of Oxide and Hydrogen on the Circumferential Mechanical Properties of Zircaloy-4 Cladding," Nucl. Eng. Des., **236**(18), pp. 1867–1873.

[6] Grigoriev, V., Jakobsson, R., Josefsson, B., and Schrire, D., 2002, "Advanced Techniques for Mechanical Testing of Irradiated Cladding Materials."

[7] Geelhood, K. J., Beyer, C. E., and Luscher, W. G., 2008, *PNNL Stress/Strain Correlation for Zircaloy*, PNNL-17700, 969740.

[8] Pierron, O. N., Koss, D. A., and Motta, A. T., 2003, “Tensile Specimen Geometry and the Constitutive Behavior of Zircaloy-4,” J. Nucl. Mater., **312**(2), pp. 257–261.

[9] Josefsson, B., and Grigoriev, V., 1996, “Modified Ring Tensile Testing and a New Method for Fracture Toughness Testing of Irradiated Cladding.”

CHAPTER 6

IN-SITU HIGH MAGNIFICATION DIGITAL IMAGE CORRELATION OF AGED NUCLEAR FUEL CLADDING IN RING HOOP TENSION TESTS

6.1. Prologue

This chapter consists of a paper which is currently in preparation for submission to a peer-reviewed journal. Hydrided zircaloy ring specimens were procured from Idaho National Laboratory, and all testing was performed at Utah State University in Logan, Utah.

6.2. Abstract

Zirconium alloys are commonly the material of choice for nuclear fuel cladding in light water reactors, acting as a barrier between the uranium fuel and the water coolant. During the course of operation, however, the cladding can become embrittled with zirconium hydride precipitates, thereby altering the mechanical behavior of the cladding. In this work, ring samples from artificially-aged Zircaloy-4 cladding with circumferential hydrides are investigated. The rings, which have varying concentrations of hydrogen, are inspected to produce full-field hydride maps. The specimens are then tested at room temperature with a ring hoop tensile test (RHTT), and high magnification digital image correlation (DIC) measurement techniques are used to produce full-field displacement maps. The hydride microstructural maps are then compared with displacement maps to investigate the effect of hydrides on plastic deformation and failure. Post-mortem analysis of fracture surfaces and comparison between mechanical behavior of rings with different hydride concentrations are also included.

Keywords: High magnification, hydrides, zirconium alloy cladding, in-situ, digital image correlation, ring hoop tension test

6.3. Introduction

Light Water Reactors (LWRs) are an important part of the current nuclear power fleet, accounting for roughly 80% of commercial nuclear power reactors [1]. For these reactors, zirconium alloys are often the material of choice for fuel cladding, due to desirable mechanical properties and neutron cross section [2]. However, zirconium alloys are susceptible to hydrogen pickup from the water coolant, and when hydrogen concentrations exceed the solubility limit of the zirconium alloy matrix, a second phase of zirconium hydride precipitates forms [3]. These hydrides often form in a circumferential orientation [4], although stress cycling at higher temperatures can cause them to reorient in the radial direction [5]. The inclusion of these hydrides causes the cladding to become more brittle [6], and further altering the behavior of already anisotropic non-hydrided zircaloy cladding [7].

Understanding exactly how these hydrides affect the behavior of cladding therefore becomes important to ensuring the safe operation of light water reactors. This is particularly true when considering accident conditions, such as when expanding fuel pellets interact with the cladding, greatly increasing hoop stresses [8–10]. Consequently, several studies have investigated the impact of hydrides on hoop direction mechanical behavior, including expansion due to compression (EDC) tests [11,12] and more traditional burst tests [13,14]. Due to the ease of testing and the ability to perform in-situ optical measurements, this work focuses on another testing method, the ring hoop tension test (RHTT). In these tests, a ring specimen is cut from the cladding and placed over hemicylindrical grips, which are pulled apart to create tension in the circumferential direction [15]. This work uses an arrangement which optimizes the stress and strain profiles by orienting the gauge at a 45 degree angle to the direction of loading [16,17] to best produce uniaxial hoop stress and uniform gauge strain.

To make the most of these hoop directional tests, it is beneficial to take in-situ measurements of the deformation of the ring. Digital Image Correlation (DIC) is a non-contact optical measurement technique in which a high-contrast speckle pattern is applied to a surface of interest and images are captured before and during deformation, then correlated to produce full-field displacement maps [18]. It is capable of being used at a variety of length scales, from meters [19] to micrometers [20]. As such, it is well suited to the in-situ deformation measurements of a RHTT, and has been implemented by previous researchers for a different gauge arrangement [21].

One key advantage of DIC is the ability to pair full-field displacement maps with the underlying microstructure. This has been done previously with grain boundaries and strain fields to determine the effect of grains on the deformation fields [22,23], and similar methods could be used with hydride microstructure and strain maps. Many studies have utilized hydride maps paired with mechanical experiments, but these have mostly been ex-situ [24–26]. Previous in-situ measurements of hydrided zircaloy have mostly been limited to small non-ring specimens that can fit in a specially-fitted SEM [27] or have not utilized DIC to measure strain [28], and those that feature in-situ DIC have been of lower magnifications and have not compared strain and hydride maps [21]. However, development of super resolution DIC techniques [29], combined with other high magnification DIC techniques, allow in-situ high-magnification DIC measurements of hydrided cladding and compare directly with hydride maps. The resulting hydride-deformation map pairs enable further investigation of the interaction between hydrides and the zircaloy matrix through plastic deformation to fracture. This also shows potential for use in validation of Multiphysics predictive modelling tools for hydrided cladding.

In this paper, ring test specimens of artificially hydrided (non-irradiated) Zircaloy-4 cladding with a variety of hydrogen concentrations that are imaged to create hydride maps. The

rings are then loaded in the circumferential direction using a ring hoop tension test, and in-situ DIC measurements of the cladding are taken during the deformation. Then, the displacement fields are overlaid on the hydride maps to produce full-field hydride-displacement map pairs. Finally, stress-strain behaviors of the rings with different hydride concentrations are compared, and failure location and behavior are discussed.

6.4. Methods

Artificially hydrided cold worked stress relieved (CWSR) Zircaloy-4 cladding that had been machined into ring test specimens was provided by Idaho National Laboratory for imaging and testing. Each ring had an outer diameter (OD) of 9.5 mm, width (W) of 5 mm, and wall thickness (T) of 0.57 mm, with a gauge region of length (L_{gauge}) 4 mm and of width (W_{gauge}) 1 mm, as seen in Figure 6.1. The dimensions of the gauge region result in a 4:1 length-to-width ratio, which has been recommended by other researchers [30], and a fillet radius of 1 mm was used to transition from the gauge region to mitigate stress concentrations.

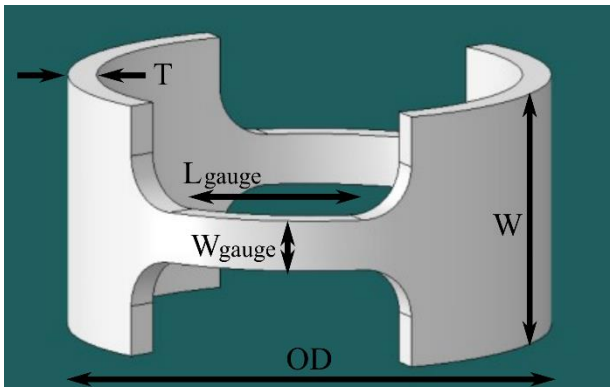

Figure 6.1: Diagram of ring specimen with dimensions as follows: OD=9.5mm, W=5mm, T=0.57mm, L_{gauge}=4mm, W_{gauge}=1mm.

Hydrogen concentrations of the specimens varied from ring to ring, as seen in Table 6.1. The variety of concentrations in the cladding was achieved by introducing different pressures of H_2 in a furnace, then sealing and heating to 400°C. Concentrations were found to vary depending on the axial location in the cladding where the specimen was taken from, and therefore reported concentrations are found by sampling the cladding on either side of the specimen location in a hydrogen analyzer, using the inert gas fusion method, similar to [31,32]. A diagram of the sectioning profile for aged cladding tubes can be seen in Figure 6.2. The uncertainty of the concentrations due to sampling near the specimen location is reflected in the ranges reported for each ring.

Table 6.1: Hydrogen concentrations in each of the ring specimens

Specimen	Ring #1	Ring #2	Ring #3	Ring #4
H_2 concentration (ppm)	150 ± 10	370 ± 20	570 ± 30	1025 ± 75

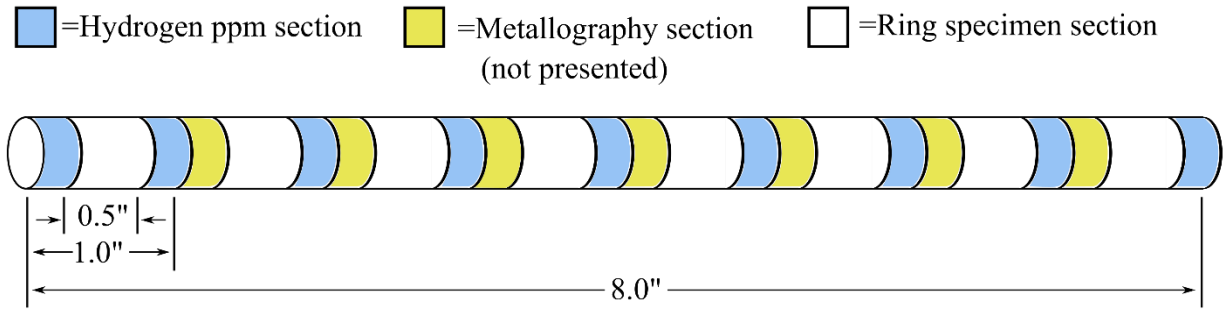

Figure 6.2: Section diagram for aged cladding. Hydrogen concentrations determined from select blue sections, and ring specimen cut from select white sections.

In order to map the hydride locations within each ring, the rings were ground, polished and then etched. The surface of interest for each ring was the cross-sectional surface of the gauge region surface, which is recessed below the rest of the cross-sectional surface of the ring. Thus,

traditional mechanical polishing methods which utilized a disk grinder/polisher could not be utilized, and the specimens were prepared by hand grinding and polishing. The appropriate grinding paper or polishing cloth was placed over a fixed metal plate with a thickness of ~3mm, and the specimen was moved back and forth in all directions while gently pressing down by hand on the paper or cloth, as seen in Figure 6.3. Grinding and polishing steps were based on parameters and methods used in previous work for metallography of CWSR Zircaloy-4 cladding tubes [33].

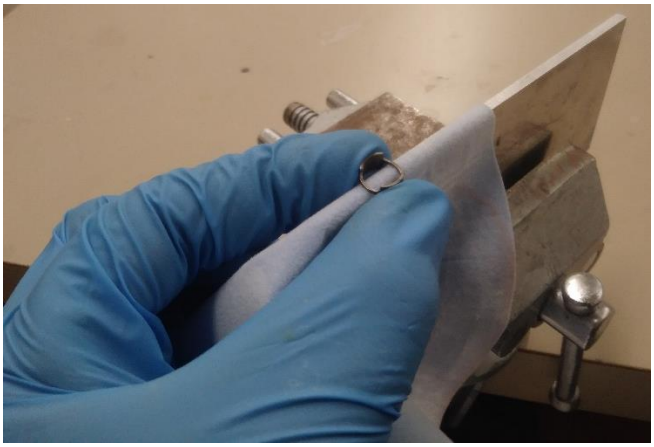

Figure 6.3: Hand polishing method for ring specimen. The recessed gauge region is reached by placing polishing cloth over a thin clamped sheet of metal.

Each grinding step was done until scratches and marks from the previous step were removed, roughly 10 minutes for each step. The grinding was done using waterproof SiC papers with grits of 400, 600, and 1200, sequentially, using medium hand pressure. During the grinding steps, water was periodically applied to the SiC paper to ensure water cooling for improved grinding performance. Polishing was then performed, first with a 3 μm polishing slurry on a silk cloth, then with a 1 μm diamond paste with diamond extender on a medium nap felt polishing cloth, and finally with a 0.05 μm colloidal silica solution on a medium nap felt polishing cloth.

Each of the polishing steps was performed by hand with medium-light pressure for roughly 10 minutes. Upon completion of all the grinding and polishing steps, some width material had been removed from the surface, resulting in a new gauge width W_{gauge} of 0.93 mm at the center of the gauge region.

After polishing until specimens exhibited a mirror finish on the gauge region, etching was performed with an acid solution to reveal where hydride precipitates are located in the specimen [34]. Based on previous etching work for optical microscopy [33,35,36], which recommend an etchant with HF and a higher concentration of HNO3, Kroll's reagent was selected. Both gauge regions on each ring were etched by vigorously rubbing a cotton swab with the etchant across the surface for approximately ten seconds.

Once etching was completed, the surfaces were imaged using a Qioptic Optem FUSION Zoom Lens with variable magnification. The lens was paired with a Point Grey GS3-U3-50S5M-C digital camera, with a resolution of 2448 x 2048 pixels. A series of images were taken of the gauge region, ensuring some overlap between images, and then stitched together using Adobe Lightroom Classic software. Then, the contrast of the images was improved through image postprocessing in Adobe Photoshop software so that hydrides would be more easily visible in strain-hydride image overlays. An example of both a single hydride image and the stitched and contrasted hydride map are shown in Figure 6.4. The hydrides appear as long dark line-like features, as seen in the yellow circle in the figure. Dark regions which serve as fiducial markers to line up future layers are shown by the green arrows.

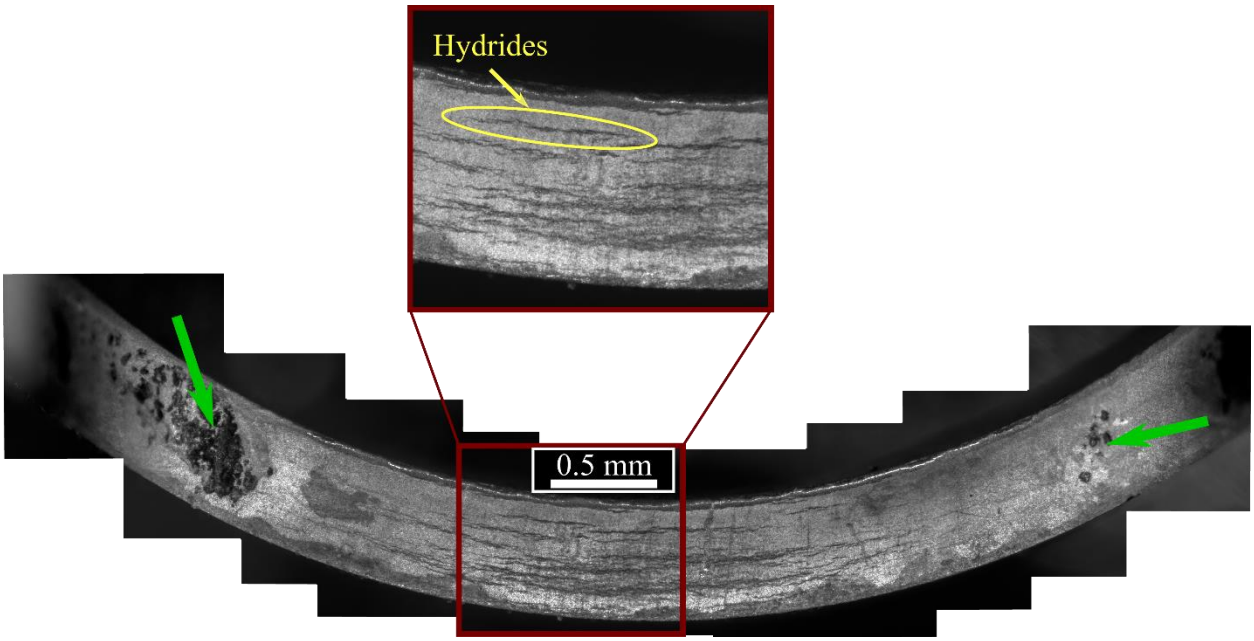

Figure 6.4: Diagram showing hydride map image stitching for ring #4 (1025 ppm). Above, a single image captured with zoom lens of the gauge region; below, the entire gauge region hydride map, made of several images stitched together. Sample hydride is circled in yellow. Naturally occurring fiducial markers are indicated by the green arrows.

Polishing and imaging were done such that regions of pitting occurred at the edges of the gauge region, where the gauge begins to curve in the fillet and join the full-width ring. These dark patterns, which are indicated by the green arrows at the edges of Figure 6.4, serve as fiducial markers, which are important to the overlaying of microstructural maps with the deformation maps produced with DIC [22,23]. It is worth noting that these are very shallow, and as they are located in the wider fillet region, are not expected to cause premature failure during mechanical testing.

Once hydride mapping has been completed, the specimens are then prepared for DIC by applying a fine speckle pattern to the surface of the gauge regions. First, the fiducial markers and fillet regions are covered with tape to prevent the speckle pattern from obscuring the markers,

ensuring that they will be visible in both the hydride maps and DIC images. Next, a coat of white VHT Flameproof spray paint was deposited on the surface. While the paint was still wet, graphite powder particles were deposited, mixing compressed air and the powder in a chamber, similar to the method employed by Jonnalagadda et al. [37]. This forces the particles through a fine wire mesh (200 x 600 mesh size, purchased from McMaster-Carr) at the bottom of the chamber, breaking up clumps and evenly distributing the particles on the wet paint surface, resulting in a fine speckle pattern with most speckle sizes of roughly 10-15 microns across. A sample of the speckle pattern on the ring can be seen in Figure 6.5.

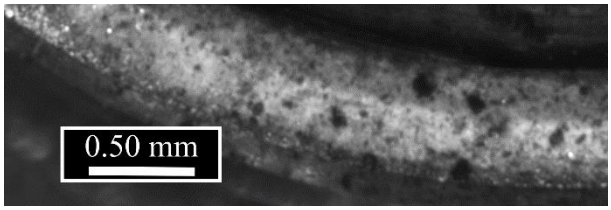

Figure 6.5: Sample speckle pattern of graphite powder on white paint, for the ring specimen.

After speckling the ring, excess paint and any other material on the inside of the ring or over the fiducial markers was removed with gentle application of acetone. It is important that the inside surface of the ring be clean to reduce friction between the ring and grips during mechanical testing. Extra care was taken to ensure that removal with acetone did not remove any of the speckle pattern on the gauge region surface. The inside of the ring was then lightly brushed with graphite powder lubricant to further reduce friction with the grip.

The specimens were then loaded into a Gleeble 1500D, a load frame fitted with an environmental chamber and viewing window. Special grips were designed with hemicylinders to fit inside the ring, as seen in Figure 6.6. Thus, when the grips are pulled apart by the load frame, the ring is pulled in tension. The orientation of the gauge region at a 45-degree angle with the

direction of loading ensures that it is not located by the corner of the hemicylinder, preventing both inward bending at the gap between the grips and stress concentrations from the corner. This orientation also helps reduce the friction experienced by the gauge, and that friction is lessened by applying graphite powder lubricant to the grip surface.

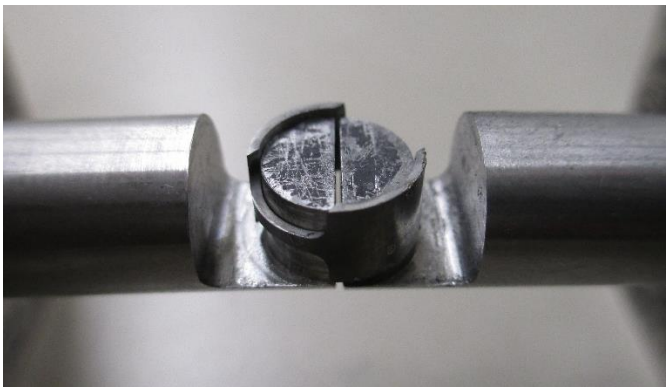

Figure 6.6: Ring specimen over custom grips. The center of the gauge region is located at an angle of 45 degrees with the direction of loading.

Cameras with zoom lenses and light sources were pointed through the viewing window of the environmental chamber, as seen in Figure 6.7. Two Optem zoom lenses of the same type used in hydride imaging were again paired with the Point Grey digital cameras, although a different lower lens was used to accommodate the longer working distance needed with the environmental chamber. In addition, a UKA Optics UV5035B 50 mm focal-length lens was paired with a JAI CM-140GE-UV digital camera to provide a lower magnification view of the grips, and black VHT Flameproof spray paint was applied to the top surface of the grips so that DIC could confirm the relative displacement between the grips during mechanical testing. A pair of Cole-Parmer fiber optic lights were used to illuminate the gauge regions of the specimen, one focused on each gauge.

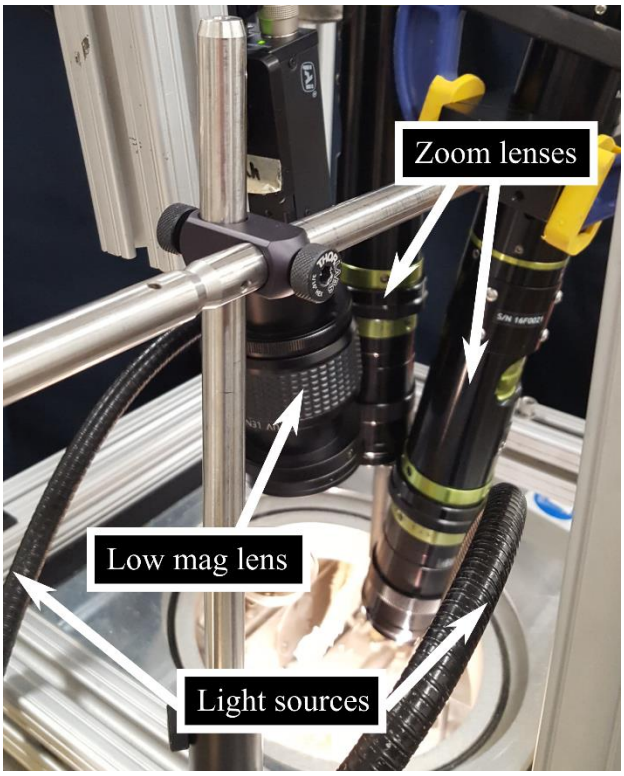

Figure 6.7: Lenses and light sources pointing through observation window of Gleeble during mechanical testing.

Prior to mechanical deformation, the grips were moved apart until the ring had seated and adjusted on the grips. A series of 9 images was captured with each of the zoom lenses, and a single image was captured with the low magnification lens, to produce reference images. Then before any deformation, the same number of images were captured with the lenses to produce noise images. After reference and noise images were captured, the grips were moved apart under load frame displacement control in increments of 0.05 mm until the ring experienced failure. At each increment, a series of 9 images was captured with each zoom lens and a single image with the low magnification lens. Each series of 9 images from the zoom lenses was then combined into a single higher resolution image using the Keren and Robust Super Resolution algorithms, with an

interpolation factor of 2, recommended for improving image resolution in DIC [29]. Load frame force and displacement data were sampled at each increment as well.

The images were then correlated using Vic-2D to produce the displacement and strain fields. The zoom lens images used a subset size of 151 and a step size of 5, while the low magnification lens images used a subset size of 51 and a step size of 5. Lagrangian strains were calculated with a strain window of 33. The relative displacement data between the grips as measured by DIC with the low magnification images were then combined with the load frame data and corrected to produce load-displacement curves, from which macroscale stress-strain curves were calculated.

The hydride maps of each gauge region were then overlaid on the corresponding reference image of the speckled ring specimen using Adobe photoshop. The dark regions shown by the green arrows in Figure 6.4, which appear in both hydride maps and speckle images, were used to align the two images. This hybrid image was then used as the background for the DIC contours. In addition to these deformation contours and hydride maps, fracture surfaces for each of the tests were also imaged with the Optem zoom lens in the same configuration that was used for hydride mapping.

6.5. Results

The results for the four rings are given below. First, the engineering stress-displacement curves are given for each of the ring tests. Next, DIC contours are given for a variety of deformations and variables. Finally, select images of the fracture surface are shown for fractographic analysis.

6.5.1. Stress-Strain Data

The force was measured by the Gleeble at the beginning of each displacement increment. The displacement data for each test were calculated using the relative displacements between the two grips, as measured by DIC. However, as each test may begin with a slightly different gap between the grips and the ring, this raw relative grip displacement is underreported. To correct this, linear regression was used to fit a line to the linear elastic region and extrapolated to the displacement axis, as seen by the dotted lines in Figure 6.8. Displacements were then shifted so that the x-intercept occurs at the zero, meaning that all curves register zero displacement when zero force is applied. Using these shifted displacements, global engineering strains are calculated using the original gauge length L_{gauge} of 4 mm, assuming that all significant deformation occurs in the gauge region. Engineering stresses are also calculated using the initial gauge cross section. The resulting stress-strain curves are shown in Figure 6.8.

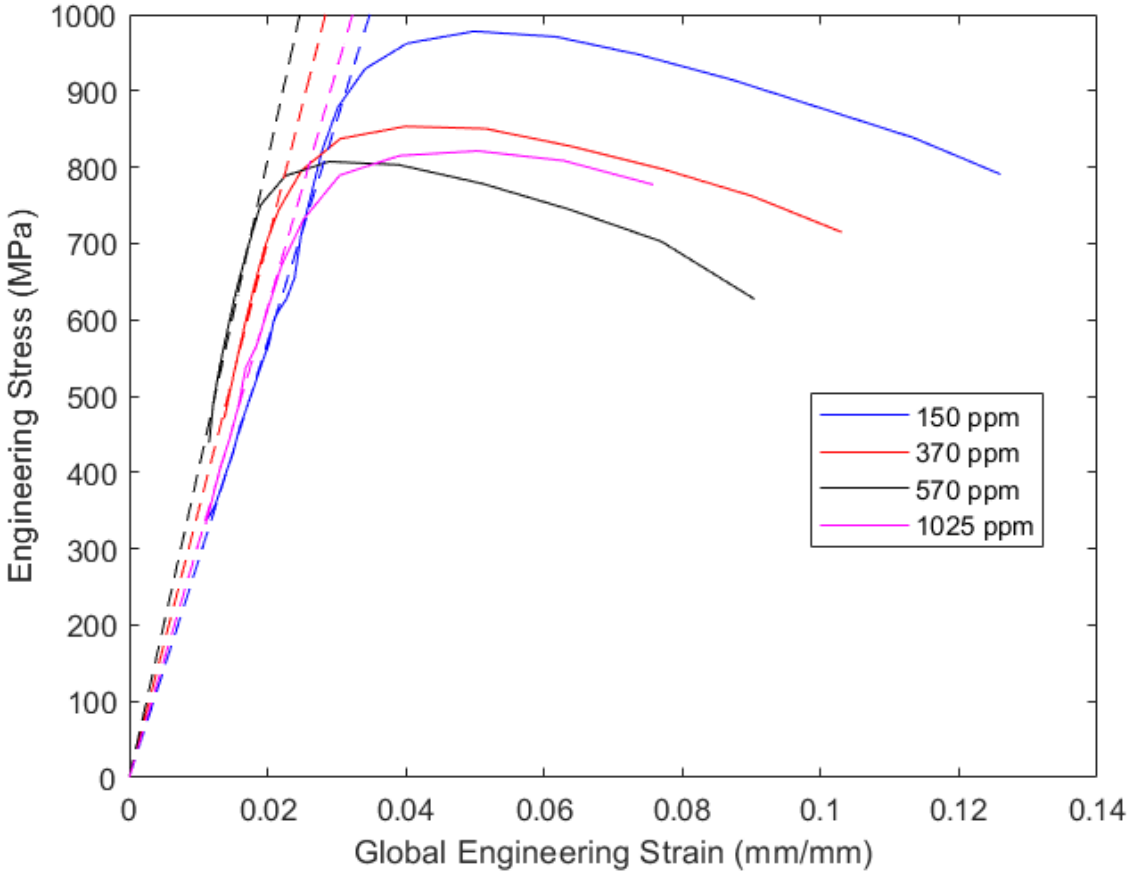

Figure 6.8: Engineering stress as a function of global engineering strain for each of the four rings.

6.5.2. Strain Contours

The DIC results for each of the tests were obtained using the parameters listed previously in the methods section. Due to variations in speckle patterns, some test results yielded stronger correlations than others, although nearly all eight of the gauge regions from the tests correlated without dropping many subsets. A sample noise contour paired with a contour at the final deformation increment prior to fracture for the 1025 ppm ring test is shown in Figure 6.9. Both contours are overlaid on the superimposed image of the hydride map and reference image, produced by the method described previously in the methods section.

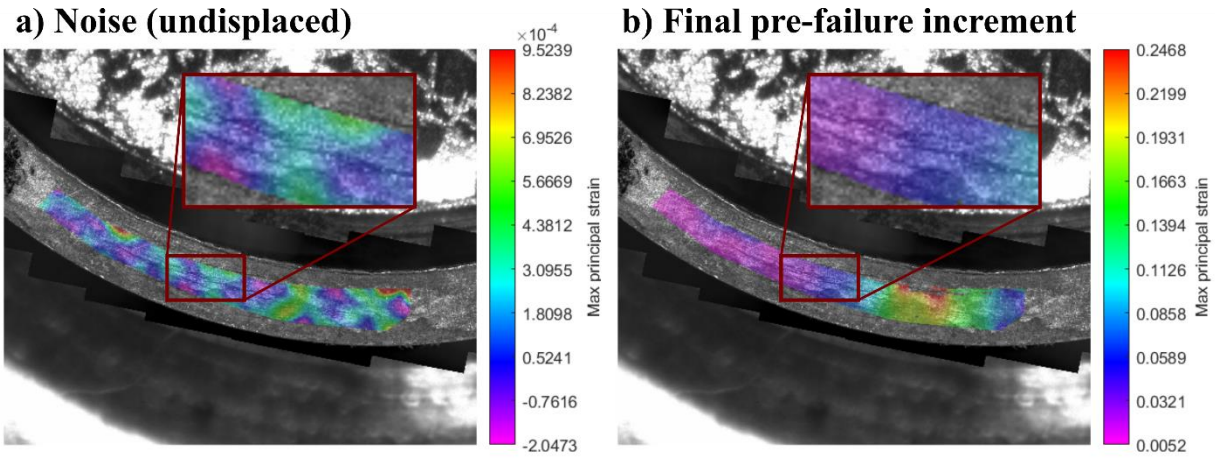

Figure 6.9: Maximum principal strain contours for a) the noise image and b) image at increment prior to failure (right) for a gauge region on 1025 ppm ring test.

The maximum principal strain contours for the final images captured prior to failure in each of the tests are shown in Figure 6.10. Both gauge regions are shown for each test, and it is easily seen that the quality of the correlation varies from gauge to gauge. Because these images are immediately prior to failure, they feature extreme deformation, and therefore some gauge regions exhibit a corresponding loss of subsets. This is especially apparent in the second gauge region for the 370 ppm tests and in the first gauge region for the 1025 ppm test. However, contours from earlier increments (not shown here) the correlation quality is still high, with minimal dropped subsets. Except for those cases where significant portions of the region of interest were dropped, all of the DIC contours tend to be similar in strain distribution across the gauge. Additionally, the magnitude of strains tends to match up well between both gauge regions from each ring test.

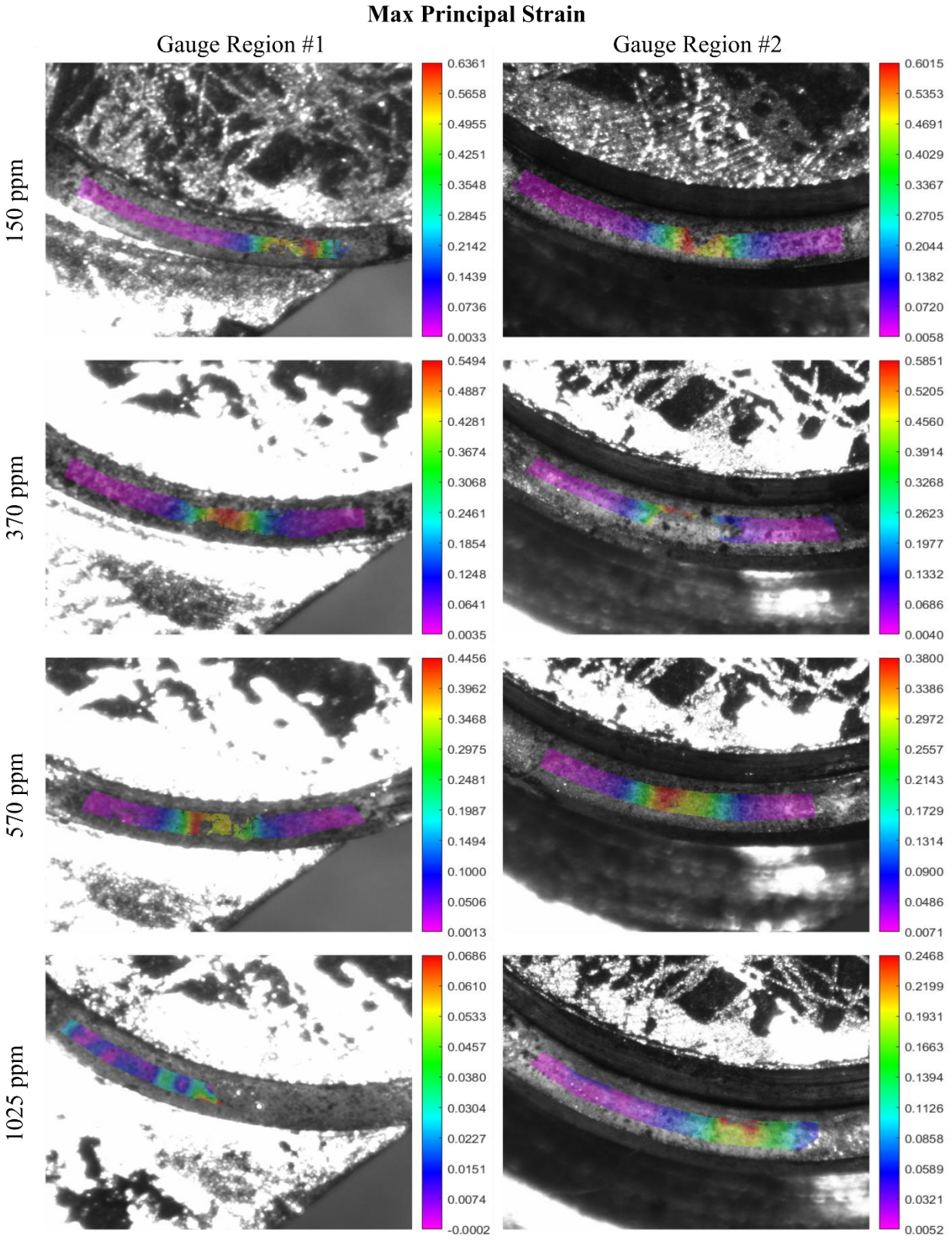

Figure 6.10:Max principal strain contour pairs on reference images for both gauge regions.

6.5.3. Fractographic Analysis

Greater understanding of how failure varies through different concentrations can be gained through considering the fracture surface. The fracture surfaces for the 370 ppm, 570 ppm, and 1025 ppm rings are shown in Figure 6.11. The 150 ppm ring was not included for the fractographic analysis. The surfaces are viewed from both the cross-sectional surface that was unspeckled (the backside from the DIC images) and the side profile, as specified in the ring diagram to the left of the figure. For each profile, the top and bottom images have been paired together. Each of the rings showed significant reduction in area, particularly visible in the side profile images. This is consistent with the necking indicated by the strain concentrations in the DIC results shown in Figure 6.10.

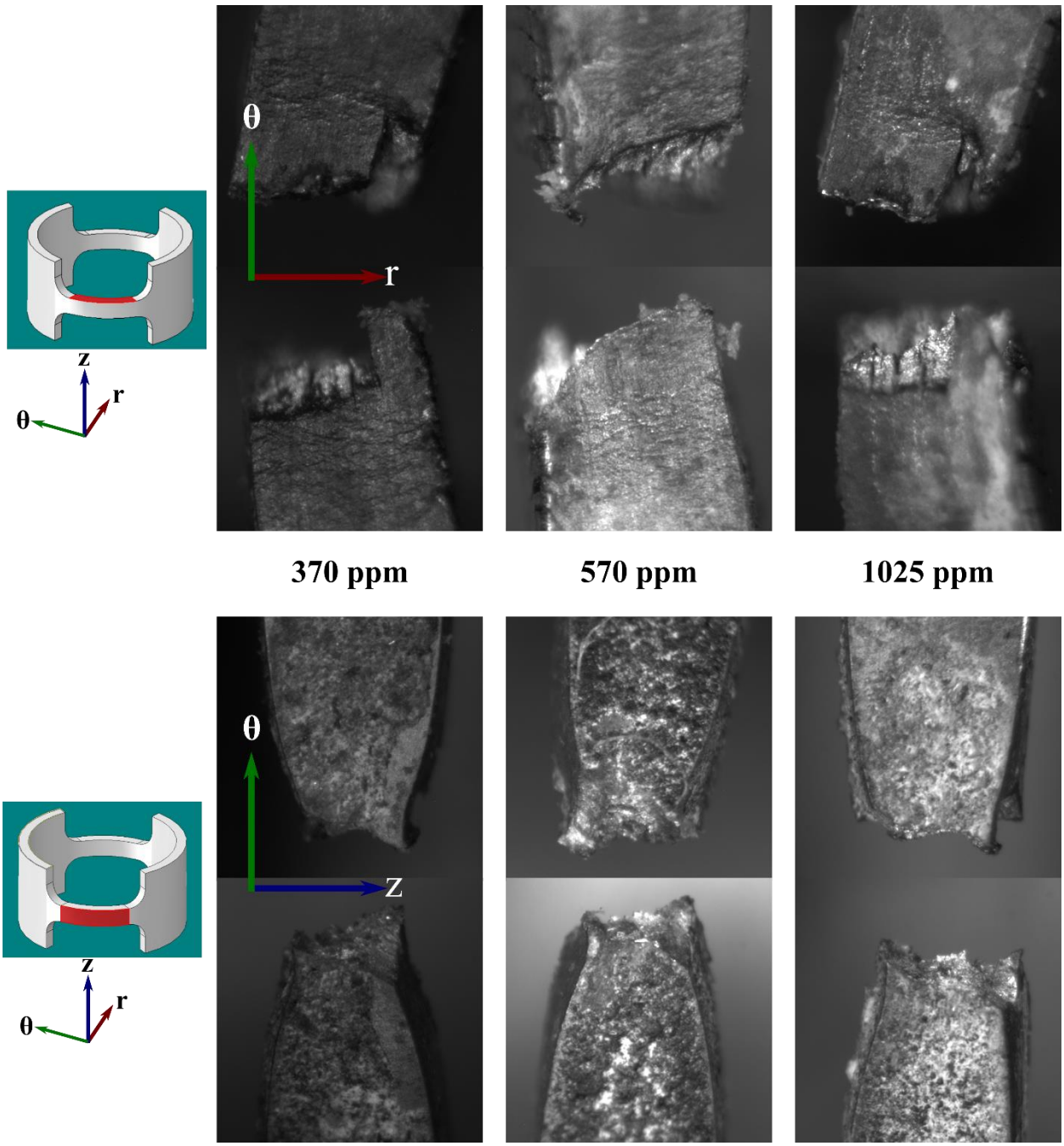

Figure 6.11: Cross-sectional profiles (above) and side profiles (below) of fracture in the gauge region for the 370 ppm (left), 570 ppm (middle), and 1025 ppm (right) ring tests.

The through-thickness fracture surfaces for the same three rings are shown in Figure 6.12. In each case, the radial direction is horizontal, and the axial direction is vertical. The top and bottom rows correspond respectively to the top and bottom images in the pairs of Figure 6.11.

These fracture surfaces highlight the out-of-page height difference between regions of the cross section. Due to depth of field, portions of the image that are at different working distances relative to the camera cannot be in focus at the same time (i.e. parts of the fracture surface that lay closer to or further from the camera will be out of focus). It is apparent that the darker hydrides often form the boundary between regions of different focus, indicating that abrupt changes in depth often occur as cracks grow out of plane along hydride locations.

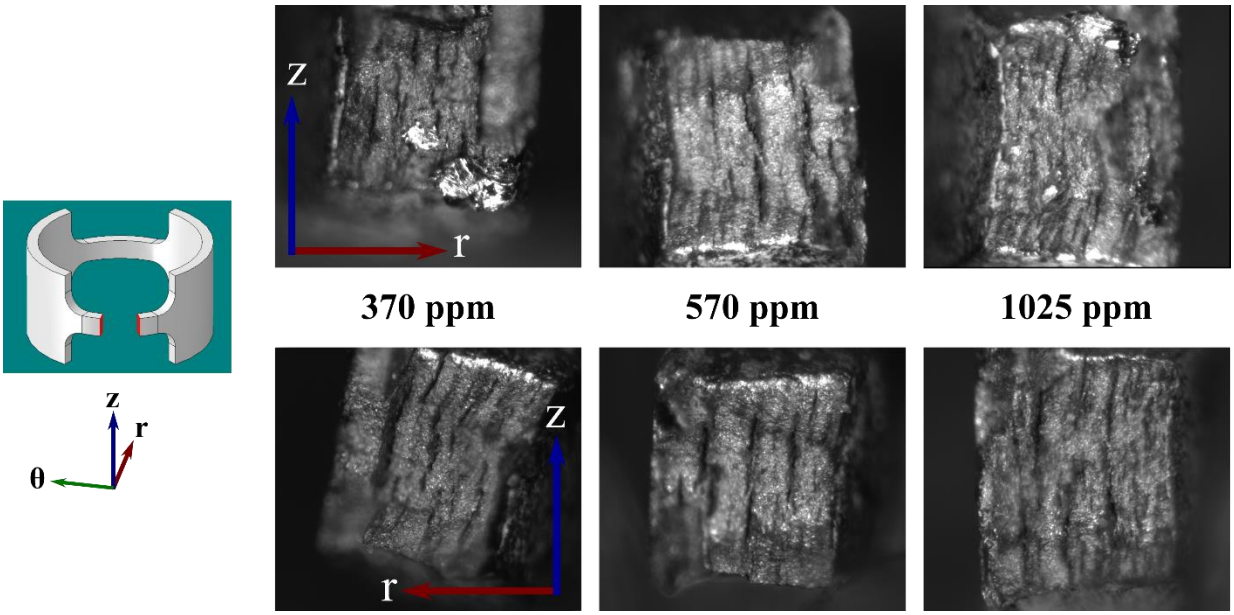

Figure 6.12: Fracture surfaces for the 370 ppm (left), 570 ppm (middle), and 1025 ppm (right) rings. The red lines along the edges of the images indicate the surfaces of the side and cross section profiles in Figure 6.11. The top row of this figure corresponds to the top row in Figure 6.11.

6.6. Discussion

The results of the ring hoop tension tests highlight some key features of the general mechanical behavior of hydrided Zircaloy-4 cladding in optimized hoop-direction loading. They also emphasize the effect or non-effect of variation in hydrogen concentration. These results are

discussed in further depth, focusing on the stress-strain curves, DIC strain contours, and fractographic analysis.

6.6.1. Stress-Strain Data

Upon initial observation of the stress-strain curves in Figure 6.8, some key trends immediately stand out. First, at higher hydrogen concentrations, behavior is more brittle, as evidenced by failure at lower strains. Thus, the 1025 ppm specimen failed at the lowest apparent strain (just under 0.08), while the 150 ppm specimen failed at the highest apparent strain (just under 0.13). This aligns with the general understanding of the embrittling effect of zirconium hydrides, as hydrides have a lower ductility than the zirconium matrix [38], as well as results of other researchers [25]. Also interesting to note is the effect of the hydride concentration on the yield strength. Observation of Figure 6.8 gives a yield strength of roughly 900 MPa for the 150 ppm ring, roughly 750 MPa for the 370 ppm and 570 ppm rings, and roughly 700 MPa for the 1025 ppm ring.

The tensile strength also varies for hydride concentration. Again, the highest engineering hoop tensile strength is for the specimen with the lowest hydride concentration. The two highest hydride concentrations also have the lowest tensile strength, although all but the 150 ppm ring are very similar, within 50 MPa. Results of previous work by other researchers has shown an increase in yield and ultimate tensile strength with increasing hydride concentration [21], while the opposite trend is shown in the current work. It is possible that random variation of specimens may be great enough that it dwarfs the effect of hydride concentration. This may explain the differences between the higher concentration rings in particular.

6.6.2. Strain Contours

The DIC strain contour results in Figure 6.9(a) show that the highest strain noise is on the order of 0.001. Compared to the strains measured through the hoop tension test to failure, this noise is less significant, as can be seen by the lack of strain noise patterns in the strain contour in part (b) of the figure just prior to failure. Based on the subset size, step size, and strain window, the virtual strain gauge size is roughly 310 pixels, or 450 μm, meaning that the strain measurement is effectively averaged over that physical distance [39]. The virtual strain gauge size is limited greatly by the subset size, and while some of the rings were able to correlate with smaller subsets, the larger subset size was chosen to maintain uniformity for better comparison between tests. While this virtual strain gauge size limits the effectiveness of mapping strain against specific hydrides, the pairing of hydride maps with DIC strains still allows additional insights into how the hydrides affect the overall behavior of the specimen. It also provides the potential for future validation of computer modelling efforts based on hydride maps.

The strain contours of Figure 6.10 confirm the embrittlement effect that increasing hydride concentrations have on strain behavior. Comparing the maximum strains in each of the specimens prior to failure shows the same trend of lower failure strains for higher hydride concentrations as the stress-strain curves. However, the magnitudes of the strains in the DIC contours are much greater than the apparent strains taken from load frame data. This is caused by the higher strain regions in the center of the gauge region seen in Figure 6.10, where necking occurs. After the onset of necking, the apparent strain is not expected to match the localized strain displayed in the DIC results, hence the discrepancy.

The strain contour at the increment just before uniform elongation is shown in part a) of Figure 6.13, while the contour at the increment of ultimate stress is shown in part b). This

demonstrates that before this point, higher strains are located in the middle of the gauge region, but it is relatively uniform and spread over a wider area with the expected noise of Figure 6.9. At this ultimate stress increment, however, higher strains begin to accumulate in the exact center of the gauge region, particularly at the inside edge. It is easy to see how this changing strain distribution naturally leads to the necking behavior seen in Figure 6.10. This evolution of strain helps demonstrate the typical behavior of this arrangement of ring hoop tension testing, allowing more accurate measurement of anisotropic material behavior.

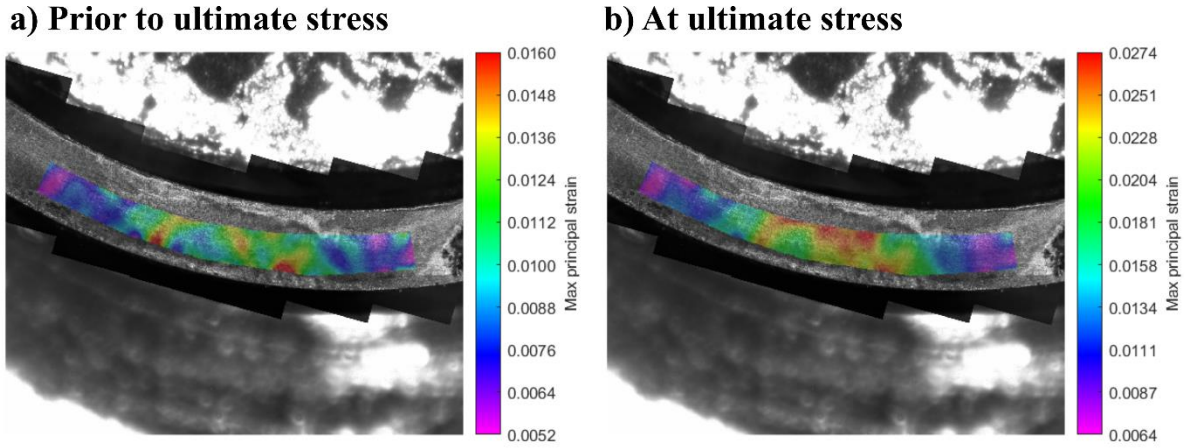

Figure 6.13: Principal strain contours a) immediately before and b) at the increment of ultimate stress. Note that at ultimate stress, strain begins to concentrate at necking location.

6.6.3. Fractographic Analysis

Comparison of the profiles in Figure 6.11 shows key similarities in the manner of failure for the three ring specimens shown. Each of the rings demonstrated something of a combination between the cup-and-cone like fracture and the flat fracture that have been previously documented by Le Saux et al. for uniformly hydrided zircaloy-4 cladding in ring hoop tension tests [21]. The cross-sectional profiles tend to show a more flat failure mode (with some slight modifications) found more often in higher hydride concentrations. On the other hand, the side profiles tend to

show the cup-and-cone like mode with a somewhat flat center section with 45-degree slants to the left and right typical of lower hydride concentrations.

One of the unique differences seen in this work is the ‘tower’ feature, easily seen in the right part of the cross-sectional profile of the 370 ppm ring, and to a lesser extent, the 1025 ppm ring, in Figure 6.11. Here, the failure mode deviates from the otherwise flat profile, as the break occurs at a different circumferential location for a small portion of the ring, but still with a flat profile. This is also seen in the 370 ppm images of Figure 6.12, where the defocusing of the region at the left of the image indicates a significantly different depth of the fracture surface profile. This view of the fracture surface shows that the right edge of the region aligns with a hydride, which shows up as a dark vertical line in the image. The upper part of the defocused image ends where this hydride also ends, which seems to indicate that this region is solely due to the location of the hydride.

The dark regions in Figure 6.12 mark the location of hydride locations, where cracks form aligned with the hydrides and the direction of loading along the circumferential-axial plane. It has been noted that the hydrides fail before the rest of the zirconium matrix, causing the secondary cracks and cleavage facets (also visible in the 370 ppm and 1025 ppm rings of Figure 6.12) typical of brittle failure [24]. This, combined with the tower features, seems to show that after failure of the hydrides, damage accumulation occurs at several locations in the ring, growing cracks in the radial-axial plane which are perpendicular to the direction of loading. These cracks then grow until they meet the perpendicular hydride cracks, which accounts for the depth variation between regions divided by the macrohydrides. Close inspection of the cross-sectional profile of the 370 ppm ring in Figure 6.11 shows several microcracks forming in this radial-axial direction, which

supports this explanation. It is expected that the concentration of hydrogen in these macrohydrides which are spaced further apart causes this type of failure behavior.

6.7. Conclusions

Using DIC strain measurement methods in conjunction with hydride location mapping offers increased capability for understanding the anisotropic behavior of hydrided cladding. This work demonstrates its efficacy with the ring hoop tension test (RHTT), featuring two gauge regions oriented at a 45-degree angle with the line of loading. A series of these hoop tests with specimens of different hydride concentrations highlighted differences in mechanical behavior. Resulting stress-strain curves showed lower failure strains for rings with higher hydride concentrations. The DIC contours confirmed this trend of lower failure strains, although local strains exceeded the global engineering strains available from load frame data. Additional insight into the influence of hydride morphology on failure mechanisms was added by observing fracture surfaces and hydride location. The pairing of high magnification DIC with ring tests and hydride maps paves the way for more accurate understanding of failure strain and hoop direction mechanical behavior.

6.8. References

[1] Ho, M., Obbard, E., Burr, P. A., and Yeoh, G., 2019, “A Review on the Development of Nuclear Power Reactors,” Energy Procedia, **160**, pp. 459–466.

[2] Azevedo, C. R. F., 2011, “Selection of Fuel Cladding Material for Nuclear Fission Reactors,” Eng. Fail. Anal., **18**(8), pp. 1943–1962.

[3] Motta, A. T., and Chen, L.-Q., 2012, “Hydride Formation in Zirconium Alloys,” JOM, **64**(12), pp. 1403–1408.

[4] Northwood, D. O., and Kosasih, U., 2013, “Hydrides and Delayed Hydrogen Cracking in Zirconium and Its Alloys,” Int. Met. Rev.

[5] Leger, M., and Donner, A., 1985, “The Effect of Stress on Orientation of Hydrides in Zirconium Alloy Pressure Tube Materials,” Can. Metall. Q., **24**(3), pp. 235–243.

[6] Motta, A. T., Capolungo, L., Chen, L.-Q., Cinbiz, M. N., Daymond, M. R., Koss, D. A., Lacroix, E., Pastore, G., Simon, P.-C. A., Tonks, M. R., Wirth, B. D., and Zikry, M. A., 2019, "Hydrogen in Zirconium Alloys: A Review," J. Nucl. Mater., **518**, pp. 440–460.

[7] Linga Murty, K., and Charit, I., 2006, "Texture Development and Anisotropic Deformation of Zircaloys," Prog. Nucl. Energy, **48**(4), pp. 325–359.

[8] Michel, B., Sercombe, J., Thouvenin, G., and Chatelet, R., 2008, "3D Fuel Cracking Modelling in Pellet Cladding Mechanical Interaction," Eng. Fract. Mech., **75**(11), pp. 3581–3598.

[9] Le Saux, M., Poussard, C., Averty, X., Sainte Catherine, C., Carassou, S., and Besson, J., 2007, *High Temperature Expansion Due to Compression Test for the Determination of a Cladding Material Failure Criterion under RIA Loading Conditions*, American Nuclear Society - ANS, La Grange Park (United States).

[10] Desquines, J., Koss, D. A., Motta, A. T., Cazalis, B., and Petit, M., 2011, "The Issue of Stress State during Mechanical Tests to Assess Cladding Performance during a Reactivity-Initiated Accident (RIA)," J. Nucl. Mater., **412**(2), pp. 250–267.

[11] Hellouin de Menibus, A., Auzoux, Q., Mongabure, P., Macdonald, V., Le Jolu, T., Besson, J., and Crepin, J., 2014, "Fracture of Zircaloy-4 Cladding Tubes with or without Hydride Blisters in Uniaxial to Plane Strain Conditions with Standard and Optimized Expansion Due to Compression Tests," Mater. Sci. Eng. A, **604**, pp. 57–66.

[12] Dufournaud, O., Varias, A. G., Grigoriev, V., Jakobsson, R., and Schrire, D., 2002, "Elastic-Plastic Deformation of a Nuclear Fuel Cladding Specimen under the Internal Pressure of a Polymer Pellet."

[13] Nakatsuka, M., Aita, M., Sakamoto, K., and Higuchi, T., 2013, "An Open-End Burst Test Method to Obtain Uniaxial Hoop Tensile Properties of Fuel Cladding in a Hot Cell," J. Nucl. Mater., **434**(1), pp. 303–310.

[14] Kim, J. H., Lee, M. H., Jeong, Y. H., and Lim, J. G., 2008, "Behavior of Zirconium Fuel Cladding under Fast Pressurization Rates," Nucl. Eng. Des., **238**(6), pp. 1441–1447.

[15] Wang, H., Bouchard, R., Eagleson, R., Martin, P., Tyson, W., Martin, P., and Tyson, W., 2002, "Ring Hoop Tension Test (RHTT): A Test for Transverse Tensile Properties of Tubular Materials," J. Test. Eval., **30**(5), p. 382.

[16] Kubo, T., Kobayashi, Y., and Uchikoshi, H., 2013, "Determination of Fracture Strength of δ-Zirconium Hydrides Embedded in Zirconium Matrix at High Temperatures," J. Nucl. Mater., **435**(1), pp. 222–230.

[17] Dick, C. P., and Korkolis, Y. P., 2014, "Mechanics and Full-Field Deformation Study of the Ring Hoop Tension Test," Int. J. Solids Struct., **51**(18), pp. 3042–3057.

[18] Sutton, M. A., Orteu, J. J., and Schreier, H., 2009, *Image Correlation for Shape, Motion and Deformation Measurements: Basic Concepts,Theory and Applications*, Springer Science & Business Media.

[19] Forquin, P., Rota, L., Charles, Y., and Hild, F., 2004, "A Method to Determine the Macroscopic Toughness Scatter of Brittle Materials," Int. J. Fract., **125**(1), pp. 171–187.

[20] Kammers, A. D., and Daly, S., 2013, "Self-Assembled Nanoparticle Surface Patterning for Improved Digital Image Correlation in a Scanning Electron Microscope," Exp. Mech., **53**(8), pp. 1333–1341.

[21] Le Saux, M., Besson, J., Carassou, S., Poussard, C., and Averty, X., 2010, "Behavior and Failure of Uniformly Hydrided Zircaloy-4 Fuel Claddings between 25°C and 480°C under Various Stress States, Including RIA Loading Conditions," Eng. Fail. Anal., **17**(3), pp. 683–700.

[22] Pataky, G. J., and Sehitoglu, H., 2015, "Experimental Methodology for Studying Strain Heterogeneity with Microstructural Data from High Temperature Deformation," Exp. Mech., **55**(1), pp. 53–63.

[23] Carroll, J., Abuzaid, W., Lambros, J., and Sehitoglu, H., 2010, "An Experimental Methodology to Relate Local Strain to Microstructural Texture," Rev. Sci. Instrum., **81**(8), p. 083703.

[24] Ruiz-Hervias, J., Simbruner, K., Cristobal-Beneyto, M., Perez-Gallego, D., and Zencker, U., 2021, "Failure Mechanisms in Unirradiated ZIRLO® Cladding with Radial Hydrides," J. Nucl. Mater., **544**, p. 152668.

[25] Arsene, S., Bai, J. B., and Bompard, P., 2003, "Hydride Embrittlement and Irradiation Effects on the Hoop Mechanical Properties of Pressurized Water Reactor (PWR) and Boiling-Water Reactor (BWR) ZIRCALOY Cladding Tubes: Part I. Hydride Embrittlement in Stress-Relieved, Annealed, and Recrystallized ZIRCALOYs at 20 °C and 300 °C," Metall. Mater. Trans. A, **34**(3), pp. 553–566.

[26] Li, J., Wang, Z., Cheng, Y., Xin, Y., Wu, H., Guo, X., and Chen, G., 2019, "Effect of Hydride Precipitation on the Fatigue Cracking Behavior in a Zirconium Alloy Cladding Tube," Int. J. Fatigue, **129**, p. 105230.

[27] Wang, S., Giuliani, F., and Ben Britton, T., 2020, "Slip–Hydride Interactions in Zircaloy-4: Multiscale Mechanical Testing and Characterisation," Acta Mater., **200**, pp. 537–550.

[28] Colas, K. B., Motta, A. T., Almer, J. D., Daymond, M. R., Kerr, M., Banchik, A. D., Vizcaino, P., and Santisteban, J. R., 2010, "In Situ Study of Hydride Precipitation Kinetics and Re-Orientation in Zircaloy Using Synchrotron Radiation," Acta Mater., **58**(20), pp. 6575–6583.

[29] Hansen, R. S., Waldram, D. W., Thai, T. Q., and Berke, R. B., 2021, “Super Resolution Digital Image Correlation (SR-DIC): An Alternative to Image Stitching at High Magnifications,” Exp. Mech.

[30] Pierron, O. N., Koss, D. A., and Motta, A. T., 2003, “Tensile Specimen Geometry and the Constitutive Behavior of Zircaloy-4,” J. Nucl. Mater., **312**(2), pp. 257–261.

[31] Daum, R. S., Chu, Y. S., and Motta, A. T., 2009, “Identification and Quantification of Hydride Phases in Zircaloy-4 Cladding Using Synchrotron X-Ray Diffraction,” J. Nucl. Mater., **392**(3), pp. 453–463.

[32] Kim, J.-S., Kim, T.-H., Kook, D.-H., and Kim, Y.-S., 2015, “Effects of Hydride Morphology on the Embrittlement of Zircaloy-4 Cladding,” J. Nucl. Mater., **456**, pp. 235–245.

[33] Lan, K.-C., Zhong, W., Mouche, P. A., Tung, H.-M., Lee, H., Heuser, B. J., and Stubbins, J. F., 2018, “The Challenge of Acquiring a Satisfactory EBSD Result of CWSR Zircaloy-4 Cladding Tube,” J. Microsc., **272**(1), pp. 25–34.

[34] Valance, S., Bertsch, J., Bruetsch, R., Martin, M., Namburi, H., Portier, S., Proff, C., Mine, N., and Abolhassani, S., 2013, “Hydrides in Zirconium Alloys - A Characterization Methods Comparison,” LWR Fuel Perform. Meet. Top Fuel 2013, **1**, pp. 359–366.

[35] DAUM, R. S., MAJUMDAR, S., LIU, Y., and BILLONE, M. C., 2006, “Radial-Hydride Embrittlement of High-Burnup Zircaloy-4 Fuel Cladding,” J. Nucl. Sci. Technol., **43**(9), pp. 1054–1067.

[36] Kaufmann, P. D., Danielson, P., and Baroch, E. F., 1974, “Improved Metallography of Zirconium Alloys,” Zircon. Nucl. Appl.

[37] Jonnalagadda, K. N., Chasiotis, I., Yagnamurthy, S., Lambros, J., Pulskamp, J., Polcawich, R., and Dubey, M., 2010, “Experimental Investigation of Strain Rate Dependence of Nanocrystalline Pt Films,” Exp. Mech., **50**(1), pp. 25–35.

[38] Qin, W., Szpunar, J. A., and Kozinski, J., 2012, “Hydride-Induced Degradation of Hoop Ductility in Textured Zirconium-Alloy Tubes: A Theoretical Analysis,” Acta Mater., **60**(12), pp. 4845–4855.

[39] Reu, P., 2015, “Virtual Strain Gage Size Study,” Exp. Tech., **39**(5), pp. 1–3.

CHAPTER 7

SUMMARY AND CONCLUSIONS

This dissertation introduced and explored several novel methods and techniques for high-magnification, in-situ digital image correlation (DIC) measurements, which culminated with their application in deformation measurements of hydrided nuclear fuel cladding. The first chapter included an extensive review of cladding behavior, mechanical testing methods, DIC, and high-magnification DIC modifications. The next three chapters (2-4) featured papers on high magnification DIC topics that have been published or are in review. Chapter 5 covered the optimization of ring tests for determining hoop direction cladding behavior. The next chapter then presented a manuscript in preparation for publication on the use of high-magnification DIC combined with hydride mapping for those optimized ring tests. Together, they provide a comprehensive treatment of a more accurate measurement of anisotropic behavior in cladding, with results that also apply more broadly to in-situ DIC measurements for high-magnification or extreme environment situations.

My first paper (chapter 2) presented a custom high-magnification UV lens, and investigated its use with DIC measurements. A steel ring specimen was used and speckled and observed through a series of tests using both the custom lens and a commercial alternative. Rigid translation experiments showed that the lens provided DIC measurements at least as good as the alternate lens, but with much better spatial resolution. The lens also performed well at high temperatures, showing the improved measurement capability of the UV optics. In the hoop tension test, the custom lens produced DIC contours that better matched the behavior predicted by finite element.

The next paper (chapter 3) expanded on the high magnification capability by implementing previously developed super resolution imaging techniques, applying them for the first time to DIC. Super resolution DIC (SR-DIC) relies on post-processing a series of overlapping images taken at the same deformation increment, then combining them to create a single image of higher resolution. Again, a ring specimen of similar size to fuel cladding was used to demonstrate SR-DIC with a rigid translation test and a hoop tension test. SR-DIC improved the quality of the measurement, reducing uncertainties and increasing spatial resolution, preparing the way for its use in actual cladding tests. The problematic nonuniformity of strain shown in the contours from the hoop tension test, however, highlighted the need for better arrangements in future experiments.

The subsequent paper (chapter 4) investigated one of the key drawbacks and limitations in high-magnification DIC, the diffraction limit of light. When longer working distances are required for in-situ measurements such as in extreme environments, the diffraction of light causes a disk of blurring or airy disk. This blurring can be lessened by increasing aperture size, but that comes at the expense of worsened depth of field and its resultant defocusing. I conducted a series of rigid translation tests on the ring specimen, using different combinations of working distances and magnifications. For each combination, the effect the tradeoff between depth of field and airy disk has on DIC measurements was studied. At low magnification, the diffraction limit effect was negligible, but at high magnifications and especially long working distances it became dominant. The optimal point at which both negative effects are minimized was found to occur at the aperture setting where the disk diameter was roughly two thirds of the correlation subset width (a DIC calculation parameter). The direct relationship between airy disk size and measurement uncertainty was also demonstrated. This paper showed the challenges of high-magnification optical DIC, but also demonstrated that accurate measurements can still be obtained with significant blurring.

As was made evident by non-uniform tension in the ring hoop tension tests (RHTT) of the first two papers, it was necessary to determine a better arrangement for future testing. The RHTT is designed to provide tensile properties in the hoop direction for anisotropic materials such as nuclear fuel cladding. Several gauge locations and grip designs had been proposed by previous researchers, and so the purpose of this work was to evaluate the most promising designs. Finite element models of a variety of ring and grip arrangements were produced and RHTTs were simulated. The arrangements were evaluated based on several criteria, including hoop stress uniaxiality, uniform strain distribution, and replication of expected stress-strain curve behavior. The optimal arrangement was found to be a ring with a 4:1 length-to-width ratio of the gauge, with two gauges oriented at a 45-degree angle to the load line. Using this arrangement offered the best balance of desired qualities, promising the best behavior for future RHTTs.

Chapter 6, a paper on testing hydrided cladding currently in preparation for journal submission, built on each of the previous chapters. The expanded understanding of high-magnification DIC techniques and tradeoffs, as well as the optimal RHTT arrangement, were used to test hydrided cladding with different hydrogen concentrations. New methods and innovations were developed to allow direct comparison of hydride maps with strain contours. Those contours in turn gave additional information about the anisotropic behavior through plastic deformation, specimen necking, and fracture. This directly enables the goal of the dissertation, to allow high-fidelity strain measurements at high magnification for validation of multiphysics models of hydrided cladding.

In addition to explicitly meeting this goal of measuring hydrided cladding tests with DIC, the work contained in this dissertation also greatly expands the existing knowledge base. Many aspects of high magnification in-situ DIC measurements have been treated here, allowing

researchers to expand past previous limitations. It also offers potential applicability to many other experiments in the fields of solid mechanics, micromechanics, and material science. As such, this work has been shared through numerous oral presentations at conferences for the American Society of Mechanical Engineers (ASME) and the Society for Experimental Mechanics (SEM). Based on the results of this dissertation, I see several opportunities for continued exploration:

First, our understanding of ideal RHTTs would greatly benefit from experimental validation of the finite element analysis in chapter 5 with unhydrided cladding samples. This would confirm the findings of that chapter, while assessing the compatibility of the test arrangements with DIC. Obtaining zircaloy cladding samples for chapter 6 was especially challenging and time consuming, thus limiting the number and type of cladding specimens. Thus, this type of testing would be ideal in a setting where cladding specimens are more readily available. As a postdoctoral researcher, I plan to continue this non-hydrided cladding validation effort in conjunction with researchers at Idaho National Laboratory.

Second, these results would translate very well to testing in extreme environments. This could include high temperature tests of hydrided cladding, as well as tests of cladding that has been both hydrided and irradiated. Experiments such as these are precisely the type that benefit from the work on understanding diffraction limit effects in high-magnification DIC at long working distances. Experiments through windows of hot cells that contain irradiated material would draw on this and other topics of the dissertation while offering further information about anisotropic behavior of used cladding. This research can also be done in coordination with Idaho National Laboratory.

Third, these high-magnification in-situ techniques can also be used for axial direction tests. The work of this dissertation focused primarily on hoop tension testing; however, to understand the anisotropic behavior of cladding, axial tension tests are also necessary. To this end, specimens of hydrided cladding have been produced for use in bend testing, both at room temperature and operating temperatures. These specimens can therefore be tested by future labmates at Utah State University. The techniques described in this dissertation will be vital for performing these high magnification, in-situ room temperature and high temperature tests.

CURRICULUM VITAE

Robert S. Hansen
Utah State University

EDUCATION

Utah State University, USA

- Ph.D., Mechanical Engineering (GPA: 4.00) 2018-2021 (Expected)
  Anisotropic Fracture of Aged Nuclear Cladding after Hydrogen Embrittlement
  Advisor: Dr. Ryan Berke

- M.S., Mechanical Engineering (GPA: 3.92) 2017-2018
  A High Magnification UV Lens for High Temperature Optical Strain Measurements
  Advisor: Dr. Ryan Berke

- B.S., Mechanical Engineering, Minors in Mathematics and Chemistry (GPA: 3.91) 2011-2016

AWARDS AND ACHIEVEMENTS

- MAE Outstanding Doctoral Scholar of the Year, USU Mechanical and Aerospace Engineering, 2021
- Third Place, Student Paper Competition, ASME Technical Committee for Experimental Mechanics, 2019
- Finalist, Michael Sutton International Student Paper Competition, Society for Experimental Mechanics, 2019
- IUP-NEUP Graduate Fellowship, $155k, Department of Energy, 2017
- Graduated Magna Cum Laude, Utah State University, 2017
- Nominated Outstanding Junior, Dept. of Mechanical and Aerospace Engineering, 2016
- A-Pin Recipient, Utah State University (4.00 GPA for two consecutive semesters), 2015
- Presidential Scholar, Utah State University, 2011-2016

RESEARCH INTERESTS AND SKILLS

- **Solid Mechanics:** Micromechanics, material science, fracture mechanics, conduction heat transfer, nuclear materials and hydrogen embrittlement, finite element analysis
- **Experimental Methods:** High-temperature strain measurements, UV optics, high-magnification optics, in-situ measurement techniques, digital image correlation (DIC), super-resolution imaging, statistical design of experiments
- **Math and Chemistry:** statistical thermodynamics and molecular dynamics, partial differential equations and applied mathematics, physical and organic chemistry, statistical design of experiments

RESEARCH AND RELATED EXPERIENCE

Fuel Development and Design Group, Idaho National Laboratory Mentor: David Kamerman
Co-mentor: Nedim Cinbiz
NEUP Intern (extended 1 year) 2019-2020

- **Project:** Evaluate testing methodologies for anisotropic plastic properties in nuclear fuel cladding in the hoop direction, using finite element analysis and validation with experimental results.
- **Responsibilities**: Perform robust finite element analysis of ring samples to inform future testing methods. Conduct sensitivity analysis and create finite model for future pairing with experiments to determine constitutive properties. Develop method to extract material properties from experimental test results. Contribute to hydride development and reorientation subgroup. Design experimental tests for validation of computer models.

Mechanics at Extreme Temperatures Lab, Utah State University Advisor: Ryan Berke, Ph.D.
Graduate Research Fellow 2017-Present

- **Project:** Investigate techniques to optically measure displacement and strain fields at the microscale, including employing a custom UV high-magnification lens for use at high temperatures, and super-resolution image processing.
- **Responsibilities:** Develop and conduct demonstrative experiments to test limits and capabilities of novel magnification lens and to compare with current capabilities. Design test fixtures to apply various mechanical and thermal load states. Perform basic finite element analysis and other mechanics calculations to validate experimental results. Assist undergraduate researchers as senior researcher in High Magnification Optics group within the lab.

Undergraduate Research Fellow 2015-2016

- **Project:** Prepare high-temperature tensile tests of ceramics
- **Responsibilities:** Designing test specimens and equipment fixtures for high-strength alloys. Working in team environment with project-oriented focus, communicating progress in weekly report meetings

TTM Technologies, Logan, UT
Operations Intern 2016

- **Project:** Design and program an Excel-based throughput and manufacturing capacity predictor tool for a printed circuit board manufacturer. Comprehensive program breaks down plant into 25 departments and accounts for variable inputs of equipment downtime, staffing levels, product type, and workflow from previous departments.
- **Responsibilities:** Calculate process times based on observation of operators and equipment, process large data sets, write code, validate program with subsequent throughput data. Provide progress update to Director of Operations, CEO, and other senior-level management. Train manufacturing management staff on use of tool to implement lean manufacturing principles and match scheduled workload.

Department of Mechanical and Aerospace Engineering, Utah State University
Systems Engineer, Senior Capstone Design 2016

- **Project:** Develop an active dehumidification system for remote data acquisition enclosures produced by Campbell Scientific. Investigate multiple dehumidification methods and quantitatively compare through experimentation. Design improved system.
- **Responsibilities:** Perform conceptual design and integration of system components. Network with customer to design a valuable product to fit their needs. Develop and code instrumentation programs. Assemble prototypes and test in varying humidity and temperature environments.

Teaching Assistant, Engineering Dynamics 2015

- **Responsibilities:** Tutor students and enable their development of problem solving, critical thinking, and practical application of theory

Multiscale Thermophysics Lab, Utah State University Advisor: Heng Ban, Ph.D.
Undergraduate Research Fellow 2014

- **Responsibilities:** Assembling and operating laser systems for testing thermal properties of thin fibers. Drafting and machining basic parts for lab projects

PUBLICATIONS AND CONFERENCE PRESENTATIONS

Papers Submitted and Published

[1] **R.S. Hansen**, K.Z. Burn, C. Rigby, E.K. Nickerson, E. Ashby, R.B. Berke, "DIC at Long Working Distances: The Influence of Diffraction Limits," *Measurement* (submitted July 2021).

[2] **R.S. Hansen**, D.W. Waldram, T.Q. Thai, R.B. Berke (2021). "Super Resolution Digital Image Correlation (SR-DIC): An Alternative to Image Stitching at High Magnifications," *Experimental Mechanics*.

[3] T.Q. Thai, R.J. Rowley, **R.S. Hansen**, R.B. Berke, "On the Nature of Emitted Light versus Camera Sensitivity in High Temperature Optical Strain Measurements," *Measurement Science & Technology* (submitted April 2021).

[4] W.D. Craig, F.B. Van Leeuwen, S.R. Jarrett, **R.S. Hansen**, R.B. Berke, "Using Text as a Native Speckle Pattern in Digital Image Correlation," *Journal of Strain Analysis in Engineering Design* (submitted April 2021).

[5] **R.S. Hansen,** T.J. Bird, R. Voie, K. Burn, R.B. Berke (2019). "A High Magnification UV Lens for High Temperature Optical Strain Measurements." *Review of Scientific Instruments*, *90*(4), 045117.

[6] T.Q. Thai, **R.S. Hansen**, A.J. Smith, J. Lambros, R.B. Berke (2019). "The Importance of Exposure Time on DIC Measurement Uncertainty at Extreme Measurements." *Experimental Techniques*, *43*(3), 261.

Manuscripts in Progress

[1] **R.S. Hansen**, D. Kamerman, R.B. Berke, "In-situ High Magnification Digital Image Correlation of Aged Nuclear Fuel Cladding in Ring Hoop Tension Tests, Summer 2021.

[2] F.B. Van Leeuwen, W.D. Craig, **R.S. Hansen**, R.B. Berke, "Stereo Digital Image Correlation with Scheimpflug Adjustment," to be submitted to *Measurement Science & Technology*, Summer 2021.

Oral Presentations

[1] **R.S. Hansen**, M.G. Estrada, R.B. Berke "High Magnification DIC in Hoop Direction Tension Testing of Hydrided Nuclear Fuel Cladding," Annual Meeting of the Society for Experimental Mechanics, Virtual Conference, June 2021.

[2] **R.S. Hansen**, D. Waldram, T. Thai, R.B. Berke "Improving Small-Scale Displacement Measurements Using Super Resolution Digital Image Correlation (SR-DIC)." ASME International Mechanical Engineering Congress & Exposition, Virtual Conference, Nov. 2020.

[3] **R.S. Hansen**, D. Kamerman, R.B. Berke "Finite Element Modeling to Inform Anisotropic Testing of Nuclear Fuel Cladding." SEM XIV International Congress, Virtual Conference, Sept. 2020.

[4] **R.S. Hansen**, D. Waldram, R.B. Berke "Super Resolution Imaging for In-Situ Digital Image Correlation." SEM XIV International Congress, Virtual Conference, Sept. 2020.

[5] **R.S. Hansen**, D. Kamerman, R.B. Berke "Testing Methodologies for Anisotropic Circumferential Properties of Nuclear Fuel Cladding." ASME International Mechanical Engineering Congress & Exposition, Salt Lake City, UT, Nov. 2019.

[6] **R.S. Hansen**, D. Waldram, R.B. Berke, "Digital Image Correlation Using Super Resolution Imaging Techniques." ASME International Mechanical Engineering Congress & Exposition, Salt Lake City, UT, Nov. 2019

[7] **R.S. Hansen**, "High-Magnification Ultraviolet DIC Techniques for High Temperature Strain Measurements." International Student Paper Competition, SEM Annual Conference and Exposition on Experimental and Applied Mechanics, Reno, NV, June 2019.

[8] **R.S. Hansen**, T.J. Bird, R. Voie, K. Burn, D. Waldram, R.B. Berke, "High Magnification In-Situ Optical Strain Measurements at Elevated Temperatures." SEM Annual Conference and Exposition on Experimental and Applied Mechanics, Reno, NV, June 2019.

[9] **R.S. Hansen**, T.J. Bird, R. Voie, R.B. Berke, "A Customized UV Lens for In-Situ Measurements at High Temperatures and High Magnifications," ASME International Mechanical Engineering Congress & Exposition, Pittsburgh, PA, Nov. 2018.

[10] R.B. Berke, T.Q. Thai, R.J. Rowley, S.R. Jarrett, **R.S. Hansen**, "Always use the ZNSSD Correlation Function when Performing DIC at Extreme Temperatures," Annual Meeting of the Society for Experimental Mechanics, Virtual Conference, June 2021.

[11] W.D. Craig, **R.S. Hansen**, F.B. Van Leeuwen, S.R. Jarrett, R.B. Berke, "Using Text as a Native Speckle Pattern in Digital Image Correlation," ASME International Mechanical Engineering Congress & Exposition, Virtual Conference, Nov. 2020.

[12] R.B. Berke, T.Q. Thai, R.J. Rowley, **R.S. Hansen**, "Insights of Correlation Functions in DIC Measurement at Extreme Temperature," ASME International Mechanical Engineering Congress & Exposition, Virtual Conference, Nov. 2020.

[13] T.Q. Thai, R.J. Rowley, P.R. Gradl, **R.S. Hansen**, R.B. Berke, "Competition of Reflected and Emitted Speckle Pattern during DIC Measurements at High Temperature," SEM XIV International Congress, Virtual Conference, Sept 2020.

[14] A.J. Smith, **R.S. Hansen**, T.Q. Thai, R.B. Berke, "Characterizing the Impact of Phase-Angle on Thermo-Mechanical Fatigue Behavior." ASME International Mechanical Engineering Congress & Exposition, Salt Lake City, UT, Nov. 2019.

[15] A.J. Smith, **R.S. Hansen**, T.Q. Thai, R.B. Berke, "The Effect of Phase-Lag on Materials Undergoing Thermo-Mechanical Fatigue." SEM Annual Conference and Exposition on Experimental and Applied Mechanics, Reno, NV, June 2019.
[16] T.Q. Thai, **R.S. Hansen**, A.J. Smith, P. Gradl, R.B. Berke, "Effect of Exposure Time on Ultraviolet DIC at Extreme Temperatures," ASME International Mechanical Engineering Congress & Exposition, Pittsburgh, PA, Nov. 2018.

Posters

[1] **R.S. Hansen**, D.W. Waldram, T.Q. Thai, R.B. Berke "Enhancing Micro-Scale Displacement Measurements Using Super Resolution Digital Image Correlation (SR-DIC)." *ASME International Mechanical Engineering Congress & Exposition*, Virtual Conference, Nov. 2020.
[2] F.B. Van Leeuwen, W.D. Craig, S.R. Jarrett, **R.S. Hansen**, R.B. Berke, "Stereo Digital Image Correlation with Scheimpflug Adjustment," ASME International Mechanical Engineering Congress & Exposition, Virtual Conference, Nov. 2020.
[3] T.Q. Thai, **R.S. Hansen**, A.J. Smith, R.J. Rowley, R.B. Berke, "Camera Sensitivity for Non-Contacting Full-Field Strain Measurement up to 1600°C," *ASME International Mechanical Engineering Congress & Exposition*, Salt Lake City, UT, Nov. 2019.
[4] T.Q. Thai, A.J. Smith, **R.S. Hansen**, R.J. Rowley, R.B. Berke, "Selection of Camera Sensitivity in High Temperature Optical Strain Measurements," *First Annual USU College of Engineering Poster Competition to celebrate Research Week*, Logan, UT, April 2019.

STUDENTS MENTORED

M.S. Students

1. Weston Craig, M.S. student in Mechanical Engineering (current)
    a. MAE M.S. Student Researcher of the Year 2021
2. Steven Jarrett, M.S. student in Mechanical Engineering (current)
3. Adam Smith, M.S. Mechanical Engineering 2020
    a. MAE M.S. Student Researcher of the Year 2020

Undergraduates

1. Brooklyn Beck, B.S. student in Mechanical Engineering (expected graduation May 2023)
2. Maggie Lea, B.S. student in Mechanical Engineering (expected graduation May 2023)
3. Hannah Maxwell, B.S. student in Mechanical Engineering (expected graduation May 2023)
4. Harley Cragun, B.S. student in Biological Engineering (expected graduation May 2023)
5. Micah Estrada, B.S. student in Mechanical Engineering (expected graduation May 2022)
6. Tanner Flitton, B.S. student in Mechanical Engineering (expected graduation May 2022)

7. Fiona Van Leeuwen, B.S. Chemistry and Mechanical Engineering (expected graduation May 2021)
    a. MAE Undergraduate Researcher of the Year 2021
8. Emma Ashby, Mechanical Engineering student 2019-2020
9. Shelby Ames, Mechanical Engineering student 2017-2020
10. Weston Craig, B.S. Mechanical Engineering 2020 ➔ M.S. at USU
11. Katie Burn, B.S. Mechanical Engineering 2019 ➔ M.S. at Purdue
    a. MAE Undergraduate Researcher of the Year 2019
    b. College of Engineering Undergraduate Researcher of the Year 2019
12. Daniel Waldram, B.S. Mechanical Engineering 2018 ➔ M.S. at Univ of Utah
13. Cedale Armstrong, Mechanical Engineering Student 2017-2018

SERVICE AND LEADERSHIP INVOLVEMENTS

- ASME-IMECE Conference Student Event Organizer, 2019
- Treasurer, Utah State University ANS Chapter, 2017-2018
- Full-time Service/Religious Volunteer, United Kingdom, 2012-2014
- Honors Program, Utah State University, 2011-2016